Epigenetic Reprogramming in Mutant IDH1 Glioma Influences Radioresistance And Neural Lineage Differentiation

by

Stephen V. Carney

A dissertation submitted in partial fulfillment
of the requirements for the degree of
Doctor of Philosophy
(Cancer Biology)
in the University of Michigan
2023

Doctoral Committee:

Professor Maria G. Castro, Chair
Associate Professor Alan Boyle
Professor Yali Dou
Associate Professor Jacob Kitzman
Associate Professor Andrew Muntean
Associate Professor Daniel Wahl

Stephen V. Carney

carneyst@umich.edu

ORCID iD: 0000-0001-7786-5158

DEDICATION

To the brain cancer patients that donated their tumors so that this study could explore novel therapeutic targets for the treatment of IDH-mutant glioma.

To my Mom, brother, and extended family that have supported me throughout the years listening to me explain complex ideas about my project even if it sounded like a different language.

To CJ, who encouraged me to continue pushing forward and supporting me through the ups and the downs.

ACKNOWLEDGEMENT

I would like to graciously thank my mentor, Dr. Maria G. Castro, I could never repay you for your support throughout these many years. You provided me with the freedom to explore every avenue that I wanted to pursue. Even when I was deep into the rabbit hole, you were the light leading me out of the tunnel. I admire how invested you are in the success of your trainees, being attentive to their needs and encouraging them to think critically. Thank you for providing me with the opportunity to join the laboratory, which was the foundation I needed to become an independent scientist. I would also like to thank Dr. Pedro Lowenstein, you showed me that someone's passion and their career can truly be one and the same. Your challenging scientific questions during lab meeting made me take a step back and see the bigger picture, because only then could you see things from a different perspective.

To Kaushik, thank you for all your contributions to my manuscript and bringing joy to my life during the challenging times I faced as a graduate student. To Anzar, all the mouse experiments you assisted me with went above and beyond. I would like to thank you both for the countless hours we spent polishing the paper for submission. To Santiago, thank you for assisting me with answering questions that I could not address without your expert guidance. You helped me interpret my results and discern the next steps to my project. To Andrea, I have always been captivated by your passion for science and work-ethic. You were the first one in the lab in the morning and the last to leave in the evening. To Marilu, you have always been a friendly face, inspiring me to tackle each day excited for adventure. To Brandon, thank you for the moments of graduate student solidarity and your support processing crucial data as I neared the finish line. To

Padma, you have been my confidant, my dearest friend, and my cheerleader. You would listen to me ramble on for hours about every new discovery, failed experiment, and the thousands of possibilities that I could come up with. Thank you for being there for me at every stage. To Marta, thank you for handling every loose end around the lab and making sure that our lab ran like a well-oiled machine. To Claire, Ford and Marcus, thank you all for filling the day with laughter and jokes. To Jess, I will remember the many hours we spent learning about DIPG mechanisms and the ways in which we tried to translate the ideas in our mind into figures. To the many lab members, past and present who I met along my journey: Flor, Carl, Dan, Neha, Vivek, Patrick, Mahmoud, Fernando, Mary, Belen, Ayman, Faisal, Carson, Ziwen, and Anna, thank you for making every day fulfilling. To the past students that I had the opportunity to mentor Preethi, Noor, Bhuvna, and Swara, thank you for contributing to the progress of my work and I hope you are moving on to bigger and better things. I would like to especially thank Brandon and Devarshi, you both became my extra pair of hands in the lab and helped make me make tremendous strides with my project.

I would also like to thank the members of my thesis committee-Alan Boyle, Yali Dou, Jacob Kitzman, Andrew Muntean, and Daniel Wahl for their feedback and suggestions throughout our biannual meetings. Thank you, also, to my Post-Baccalaureate Research and Education Program (PREP) mentor, Dr. Anthony Wynshaw-Boris, for preparing me for graduate school and inspiring me to explore new areas of research. To my first Principal Investigator, Dr. Bo Norby, your mentorship started me on this journey to pioneer novel discoveries in biomedical science.

Finally, I would like to thank my family and friends for their overflowing support. I will remember the reassuring conversations and your praises for my success during my last year of graduate school. I could not have made it to the summit without you all.

TABLE OF CONTENTS

LIST OF TABLES

LIST OF FIGURES

LIST OF ABBREVIATIONS

1p/19q codeletion	Co-deletion of the p arm of chromosome 1 and q arm of chromosome 19
2HG	2-hydroxyglutarate
AML	Acute Myeloid Leukemia
α-KG	Alpha-ketoglutarate
ATRX	Alpha-Thalassemia/Mental Retardation, X-linked
BBB	Blood Brain Barrier
BRD4	Bromodomain-containing protein 4
CBTRUS	The Central Brain Tumor Registry of the United States
CDKN2A/B	Cyclin-Dependent Kinase Inhibitor 2 A/B
ChIP-seq	Chromatin Immunoprecipitation and deep sequencing
CIC	Capicua Transcriptional Repressor
CNS	Central Nervous System
CR	Complete Response
EANO	European Association of Neuro-Oncology
EGFR	Epidermal Growth Factor Receptor
GO	Gene Ontology
HDAC1/2	Histone Deacetylase 1 and 2
IDH1	Isocitrate Dehydrogenase 1
IDH2	Isocitrate Dehydrogenase 2
IDG	Isomorphic Diffuse Glioma
IHA	Immortalized Human Astrocytes

IHC	Immunohistochemistry
IHCC	Intrahepatic cholangiocarcinoma
IR	Ionizing Radiation
KO	Knockout
LGG	Low Grade Gliomas
LOH	Loss of heterozygosity
MDS	Myelodysplastic Syndromes
MTD	Maximal Tolerated Dose
mIDH1	Mutant Isocitrate Dehydrogenase I
mR	Minor Response
NuRD	Nucleosome Remodeling and Deacetylase
ORR	Objective response rate
OS	Overall Survival
PARP	Poly ADP-Ribose Polymerase
PDGFA	Platelet Derived Growth Factor Alpha Ligand
PDGFRA	Platelet Derived Growth Factor Receptor Alpha
PFS	Progression-free survival
PMMRDIA	Primary Mismatch Repair Deficient IDH-mutant Astrocytoma
PR	Partial Response
RP2D	Recommended phase II dose
scRNA-seq	Single Cell Ribonucleic Acid sequencing
TCGA	The Cancer Genome Atlas
ZMYND8	Zinc Finger MYND (Myeloid, Nervy and DEAF-1)-type containing 8

Abstract

Traditionally, brain tumors were classified based on clinical attributes like anatomical location, patient's age, and morphologic features. The incorporation of genomics to the World Health Organization (WHO) 2016 central nervous system (CNS) tumor criteria identified distinct molecular subtypes (Louis et al., 2016). Analysis of adult low grade gliomas (LGG) conducted by The Cancer Genome Atlas (TCGA) identified recurrent mutations in the genes encoding isocitrate dehydrogenase 1 (IDH1) and its paralogue IDH2 (Ceccarelli et al., 2016). Patients with IDH-mutant tumors displayed favorable prognosis with a median survival of 6.4 years for astrocytoma and 8 years for oligodendroglioma (Brat et al., 2015). A single amino acid substitutions affecting the arginine 132 in IDH1 or analogous residue arginine 172 in IDH2 alters the catalytic activity of these enzymes to produce an oncometabolite, 2-hydroxyglutarate (2HG). Several studies have shown that cells expressing IDH1/2 mutations establish a hypermethylation phenotype through the competitive inhibition of histone demethylases and DNA hydroxylases by 2HG. These findings suggested that mutant IDH1 (mIDH1) represses epigenetic plasticity by reinforcing the chromatin state of glioma cells restricting their ability to undergo neural differentiation.

Changes in chromatin modifications and transcriptional pathways following the inhibition of mIDH1 have yet to be explored in patient-derived glioma cell cultures that endogenously express mIDH1. The impact of mIDH1-R132H on gliomagenesis was examined in a genetically engineered mouse model, which presented an expansion of stem-like cells at the subventricular zone (Bardella et al., 2016). Based on these findings, we hypothesize that mIDH1 mediates the epigenetic regulation of oncogenic pathways that contribute to therapeutic resistance. We

evaluated the transcriptome and epigenome of a radioresistant mIDH1 glioma cell culture (GCC) treated with mIDH1-specific inhibitor AGI-5198, we observed a global loss of histone mark trimethylation and 1335 genes showed significantly altered expression. We identified Zinc Finger MYND-Type Containing 8 (ZMYND8) as a potential target of mIDH1 reprogramming to confer resistance to irradiation. We provide evidence that ZMYND8 is epigenetically regulated in human mIDH1 GCCs based on a significant decrease in ZMYND8 total protein and loss of H3K4me3 deposition at the ZMYND8 promoter following mIDH1 inhibition. ZMYND8 has been implicated in driving cancer-specific programs through its role in enhancer regulation and recruitment to regions of laser-induced DNA damage. To elucidate the underlying mechanism for ZMYND8 overexpression in mIDH1 glioma, we suppressed ZMYND8 using shRNA knockdown or lentiCRISPRCas9-mediated knockout. We observed a significant decrease in cellular viability in ZMYND8-deficient mIDH1 cells in response to irradiation.

We explored the impact of ZMYND8 loss on the regulation of DNA repair machinery. There was delayed resolution of γH2AX signal 48 hours post-irradiation in ZMYND8 KO mIDH1 GCCs, which could reflect a defect in double stranded break (DSB) repair and an accumulation of DNA damage. Additionally, we targeted newly proposed ZMYND8-interacting partners: Poly ADP-ribose polymerase (PARP) and histone deacetylases 1 and 2 (HDAC1/2) to discern their impact on cellular viability. ZMYND8 KO mIDH1 GCCs were more sensitive to either pamiparib (PARP inhibitor) or panobinostat (pan-HDAC inhibitor) alone or in combination with IR as compared to ZMYND8 wildtype mIDH1 glioma cells. These findings denote a novel role of ZMYND8 in DNA repair and radioresistance of IDH-mutant glioma. We anticipate these findings will provide support for the development of ZMYND8 specific inhibitors, which represents a viable target for the treatment of mIDH1 gliomas.

Chapter 1 Introduction

Adult glioma subtypes and clinical presentation

Diffuse gliomas are the most common malignant neoplasm of the central nervous system (CNS), impacting the lives of young adolescents and elderly adults. The 2022 statistical report from The Central Brain Tumor Registry of the United States (CBTRUS) estimates that 86,335 individuals will be diagnosed with brain and other CNS tumors resulting in the average annual death of 16,606 people (Low et al., 2022). More than half of adult brain tumors are diagnosed as glioblastoma (52.9%) and present with a 5-year survival rate of 6.8% (D. Lin et al., 2021). The second most common is astrocytoma (28%), which can vary in mortality statistics based on the patient's tumor histological grade, where the 5-year survival rate for diffuse astrocytoma (grade 2) was estimated to be 86% and anaplastic astrocytoma (grade 3 and 4) was 45% (Cho et al., 2021). Oligodendroglioma account for 9.3% of adult brain tumor cases and patients have a 5-year survival rate of 74.1%. The highest incidence of brain cancer has been found in non-Hispanic white males younger than 20 years or older than 80 years (D. Lin et al., 2021). The mortality rate for men is 1.58 times more likely than for women. This stark difference in mortality rates between men and women suggested to researchers that sex chromosomal differences could predispose men to developing brain cancer.

Molecular profiling of adult glioma and treatment strategies

The improved availability of whole exome sequencing allowed researchers to identify genetic mutations that drive glioma pathogenesis. In 2008, *Parson et al* analyzed the genomes of 22 glioblastoma samples with the intention to discover genetic alterations that occurred during tumor progression (Parsons et al., 2008). They uncovered a subset of secondary glioblastoma patients that had better overall survival and whose tumors contained a somatic heterozygous point mutation in a gene encoding isocitrate dehydrogenase 1 (IDH1). The most frequent genetic lesions occurred within the active site of the IDH1 enzyme leading to an amino acid substitution of arginine for histidine at residue 132 of the protein (R132H). The following year, this observation was validated in a larger cohort of glioma patients where 142 tumors were shown to have this characteristic IDH1-R132H mutation (Yan et al., 2009). DNA was extracted from a variety of primary tumors obtained from the tissue bank at Duke University's Preston Robert Tisch Brain Center. To determine the mutational status, exon 4 for IDH1 and IDH2 genes were amplified using polymerase chain reaction (PCR) assay and subjected to next-generation sequencing. Pediatric low grade gliomas like ependymoma, medulloblastoma, and subependymal giant-cell astrocytoma were wildtype for both IDH1 and IDH2 (Yan et al., 2009). Non-canonical mutations were observed in IDH1, which included R132C, R132L, R132S and R132G. (Yan et al., 2009). Meanwhile, IDH2 somatic mutations were less frequent and were revealed to express either R172G, R172M, or R172K (Yan et al., 2009).

IDH-mutant gliomas account for roughly 80% of adult low grade glioma (Bai et al., 2016). These tumors can be diagnosed as either astrocytoma, oligodendroglioma, or secondary glioblastoma (newly referred to as grade 4 IDH-mutant astrocytoma) based on histological features (**Table 1.1**) (Ceccarelli et al., 2016). The integration of molecular profiling revealed recurrent

mutations in astrocytoma (ATRX loss and TP53 mutation) and oligodendroglioma (1p19q codeletion and TERT promoter mutation). The presence of a homozygous deletion in cyclin-dependent kinase inhibitor 2A/B (CDKN2A/B) is associated with shorter overall survival and is now classified as a frequent mutation in WHO grade 4 IDH-mutant astrocytoma (Reinhardt et al., 2018). The changes made to the WHO 2021 classification of CNS tumor emphasized the apparent need to reevaluate tumor grading. Two specific aspects were the simplicity of the tumor grading criteria from roman numerals to Arabic numbering and grading within tumor types instead across different molecular groups. In addition, the removal of "anaplastic" as a signifier for grade 3, which defined the presence of mitotic proliferation, necrosis and microvascular proliferation within the tumor biopsy.

IDH-mutant tumors are slow growing, but highly infiltrative and arise predominantly within the frontal lobe. Meanwhile IDH-wildtype tumors were shown to occupy the parietal lobe and to some extent the temporal lobe (Arita et al., 2018). Patients harboring mutations in either IDH1 or IDH2 have a favorable prognosis as compared with high-grade IDH-wildtype glioblastoma. The core pathways found to be deregulated in IDH-wildtype glioblastoma appear to occur as a result of widespread chromosomal changes (**Table 1.1**). This included amplification of tyrosine kinase receptors: EGFR, PDGFRA and MET, and inactivating mutations in cell cycle regulators: TP53, CDKN2A/B, RB1 and PTEN (Brennan et al., 2013; Zhang et al., 2020).

The recent WHO CNS 2021 update identified an epilepsy-associated brain tumor subtype called isomorphic diffuse glioma (IDG), which was IDH-wildtype and considered a benign grade 2 tumor (**Table 1.1**) (Wefers et al., 2020). Copy number analyses of IDG tumors revealed alterations in the myeloblastosis (MYB) transcription factor family: MYBL1 (54%) or MYB (23%). In most cases there appeared to be focal gains of MYBL1 or complex rearrangements

leading to gene fusions that disrupted the intergenic sites of the MYBL1 locus ultimately disrupting the negative regulatory C-myb domain (Wefers et al., 2020). The only recurring gene fusion was *MYBL1-MMP16*, but additional gene partners were identified: -*RAD51B*, -*MAML2*, -*ZFHX4*, and -*TOX* (Wefers et al., 2020). The presence of breakpoints within the MYB resulted in the following gene fusions: *MYB-HMG20A* and *MYB-PCDHGA1* that truncated the C-myb domain and ultimately leading to an overexpression of MYB. DNA methylation data from IDG determined that this group formed its own distinct cluster, but most closely resembled angiocentric glioma, which were shown to express *MYB-QKI* gene fusions (Bandopadhayay et al., 2016). MYBL1/MYB-altered gliomas occurred in patients ranging from 4-50 years of age with a median of 32 years (Wefers et al., 2020). Due to the relatively low incidence rate, clinical recognition by histology alone will not be sufficient and molecular testing will be required to distinguish these patients from other gliomas.

The European Association of Neuro-Oncology (EANO) is a taskforce that provides guidelines for the diagnosis, treatment and follow-up of adult patients with diffuse glioma based on the latest clinical trials (**Table 1.1**) (M. Weller et al., 2021). WHO grade 2 IDH-mutant astrocytoma initially undergo maximal surgical resection followed by the watch-and-wait strategy for patients that are considered low-risk (patients under the age of 40yrs and whose tumors can be entirely resected based on their MRI scans). These patients will still need be monitored for the formation of additional lesions. Meanwhile, those patients considered to be high-risk (over 40 yrs and who have residual disease left after surgery) will receive both RT and chemotherapy. Since these patients tend to be younger in age and receive treatment in the form of ionizing radiation (IR) in combination with the administration of the DNA-alkylating agent temozolomide (TMZ) upon recurrence. The standard-of-care for IDH-mutant grade 3 astrocytoma is IR followed by

maintenance TMZ, but limited improvement has been observed with many patients eventually relapsing. Results from the RTOG trial report demonstrated an improved survival upon tumor recurrence with the addition of polychemotherapy (procarbozine, CCNU, and vincristine: PCV) to IR. Patients diagnosed with IDH-mutant grade 4 astrocytoma are initially treated with IR + TMZ. If the tumor recurs, the patients undergo IR + PCV or bevacizumab (VEGF inhibitor). For IDH-mutant oligodendroglioma grade 2 patients, surgery and monitoring is standard for low-risk oligodendrogliomas, which have the best prognosis of all adult glioma. However, if the patient has high-risk characteristics they will undergo IR + PCV. Meanwhile, IDH-mutant oligodendroglioma grade 3 patients are treated with IR + PCV initially, and both grade 2 and 3 oligodendroglioma patients receive TMZ upon recurrence. For glioblastoma (GBM) patients, the expression of the enzyme methylguanine DNA methyltransferase (MGMT) impacts the efficacy of TMZ treatment (Hegi et al., 2005). GBM are typically treated with both IR + TMZ, unless molecular testing of surgical biopsies has been performed for the MGMT methylation status prior to treatment. It is believed that TMZ will be more efficacious in tumors where MGMT is methylated. If the DNA methylation status of the MGMT locus is known: GBM patient with MGMT unmethylated are recommended to receive IR or if MGMT is methylated the patients are recommended to receive TMZ + IR. With tumor recurrence, GBM can be treated in a variety of manners: palliative care, re-irradiation, surgical resection, bevacizumab, or next-line alkylating chemotherapy.

Temozolomide induces hypermutation and acceleration of glioma progression

Since 2005, TMZ has been the first-line chemotherapeutic agent approved by the FDA for the treatment of recurrent glioblastoma and anaplastic astrocytoma in combination with

Table 1.1 World Health Organization (WHO) classification of adult diffuse glioma and EANO guidelines for treatment

Histological Tumor Type	Age at Time of Diagnosis	WHO 2016 Grading	WHO 2021 Grading	Molecular Markers	DNA Methylation Signature	Current Therapies
Astrocytoma	Adult	II	2	IDH1 or IDH2, ATRX, TP53	G-CIMP high	**At Diagnosis:** low risk (surgical resection (SR) and monitoring (M)) **or** high risk (IR + PCV) **After Recurrence:** Radiation (IR) and Temozolomide (TMZ)
	Adult	III	3	IDH1 or IDH2, ATRX, TP53	G-CIMP high	**At Diagnosis:** SR, IR + TMZ **After Recurrence:** IR + PCV (Procarbozine, CCNU, and vincristine)
	Adult	IV	4	IDH1 or IDH2, ATRX or TERT promoter, TP53, CDKN2A/B, CDK4	G-CIMP high or G-CIMP low	**At Diagnosis:** SR, IR + TMZ **After Recurrence:** repeat IR + PCV or bevacizumab
Oligodendroglioma	Adult	II	2	IDH1 or IDH2, 1p19q codeletion, TERT promoter, CIC, FUBP1, NOTCH1	G-CIMP high	**At Diagnosis:** low risk (SR and M) **or** high risk (IR + PCV) **After Recurrence:** TMZ
	Adult	III	3	IDH1 or IDH2, 1p19q codeletion, TERT promoter, CIC, FUBP1, NOTCH1	G-CIMP high	**At Diagnosis:** SR, IR + PCV **After Recurrence:** TMZ
Glioblastoma	Adult	IV	4	PDGFRA, EGFR, MET, TP53, PTEN, RB1, TERT promoter	G-CIMP low	**At Diagnosis:** TMZ +IR **Molecular testing:** MGMT unmethylated (IR) **or** MGMT is methylated (TMZ +IR) **After Recurrence:** Palliative care, re-irradiation, surgical resection, bevacizumab, **or** next-line alkylating chemotherapy
Isomorphic Diffuse Glioma	Pediatric and Adult	II	2	MYBL1 or MYB gene fusions	G-CIMP low	**At Diagnosis:** SR + M

surgery and radiation (Stupp et al., 2005). This DNA alkylating agent has been the primary standard-of-care for many years due to its lipophilic properties allowing it to cross the blood brain barrier (BBB) and ease of administration due to its oral bioavailability (Baker et al., 1999). TMZ is converted to its active form methyldiazonium cation, which methylates DNA nucleotides specifically at guanine residues creating O^6-methylguanine (O6-MG) (Denny et al., 1994). This indirectly leads to DNA damage by the formation of mutagenic DNA adducts, where O6-MG is mispaired with thymine as opposed to cytosine during the next cycle of DNA replication.

Normally, these lesions can be fixed effectively by the base excision repair (BER) pathway, which is rarely inactivated in GBM (Hombach-Klonisch et al., 2018). However, the expression of the MGMT enzyme can directly repair these DNA lesions and neutralize TMZ-induced cytotoxicity (Zhang et al., 2012). *Hirose et al.* demonstrated that these persistent DNA mismatches result in a cytostatic effect, where the majority of glioma cells arrested at the G2/M phase (Hirose et al., 2001). Unexpectedly, few cells underwent apoptosis instead the majority entered senescence becoming polyploid with an eight nuclei (8n) phenotype (Hirose et al., 2001).

In the clinical setting, the methylation status of the MGMT promoter has become a prognostic factor for determining if a patient's tumor will be sensitive to TMZ therapy. High expression of MGMT mRNA has been linked to TMZ resistance whereas suppression of MGMT transcription by the presence of DNA methylation at CpG islands upstream of the MGMT promoter has been associated with improved TMZ chemotherapeutic response (Kitange et al., 2009). The median overall survival of patients whose tumors were methylated at the MGMT promoter was roughly 22 months compared to 13 months for patients where the MGMT promoter was unmethylated (Hegi et al., 2005). *SongTao et al* examined the relationship between MGMT promoter methylation and IDH-mutational status and found that secondary IDH-mutant

glioblastoma with MGMT methylated promoters had improved survival and decreased progression in response to TMZ (SongTao et al., 2012). Interestingly, 40-55% of IDH-wildtype tumors were MGMT methylated compared to 90-100% of IDH-mutant tumors (Molinaro et al., 2019). These findings support the molecular testing of the MGMT promoter methylation in clinical practice for elderly patients >65 years diagnosed with IDH-wildtype glioblastoma (Baumert et al., 2016).

Nonetheless, *Oldrini et al* identified a discordance between promoter methylation and protein expression of MGMT in a subset of glioma patients that presented with tumor recurrence (Oldrini et al., 2020). The recurrent gliomas carried MGMT genomic rearrangements that replaced the regulatory promoter region of MGMT with a new gene's promoter leading to an overexpression of MGMT (Oldrini et al., 2020). The genomic regions where the breakpoint in MGMT occurred was consistent across tumors located at the boundary of exon 2 just upstream of the MGMT start codon (Oldrini et al., 2020). All the gene fusions occurred in-frame preserving the conserved domains of MGMT. Interestingly, the authors showed that physicians could monitor for these genetic alterations by analyzing MGMT mRNA present in circulating tumor cells from peripheral blood or from tumor-derived extracellular vesicles such as exosomes.

Despite the clinically meaningful progress made by the discovery of TMZ, this therapy unfortunately has been shown to contribute to malignant transformation in a subsets of adult glioma patients. A hypermutation phenotype has been directly linked to TMZ-induced mutagenesis which promotes tumor recurrence and ultimately these patients' tumors become refractory to available treatments. *Johnson et al.* profiled the exomes of 23 paired primary IDH-mutant gliomas and the recurrent tumors resected post-TMZ treatment (Johnson et al., 2014). The authors explored the mutational differences between the initial biopsy and the recurrent tumor to better understand the driver mutations and intratumoral clonality that influenced the tumor's

reemergence (Johnson et al., 2014). Six patients presented with hypermutated (HM) recurrent tumors that were distantly related to the primary tumor acquiring thousands of *de novo* somatic mutations across the genome (Johnson et al., 2014). It's noteworthy that some patients displayed subclonal divergence with each subsequential recurrence possessing a different mutational profile. The majority of these TMZ-induced mutations occurred within the Akt-mTOR signaling pathway including genetic mutations like $PIK3CA^{E542K}$, $PTEN^{A121T,G165R}$, and $MTOR^{S2215F}$ (Johnson et al., 2014). This notion that TMZ might be exerting selective pressure on the evolutionary trajectory of the relapsed tumor, which was also explored in a cohort of IDH-wildtype glioma (Korber et al., 2019). *Körber et al.* demonstrated that only 11% of mutations were shared between the primary to recurrent IDH-wildtype tumors and were frequently found in PTEN, CDKN2A/B, and EGFR. Interestingly a third of patients exhibited clonal TERT promoter mutations, which the authors speculated could be a prerequisite to the rapid regrowth of the tumor (Korber et al., 2019). The authors inferred from a phylogenetic analysis that 72% of recurrent tumors originated from more than one clone existing within the primary tumor.

The progression of low grade IDH-mutant gliomas to high-grade as a result of TMZ monotherapy induced hypermutation was observed in 57% of recurrent LGGs treated at USCF (Yu et al., 2021). The authors defined the presence of hypermutation within the tumor by a mutational burden that exceeded 10 mutations per megabase (Mut/Mb). Upon reoperation, HM IDH-mutant gliomas presented with disseminated disease that spread to ependymal and leptomeningeal regions of the brain and spinal cord. Controversial findings by *Weller et al.* demonstrated that IDH-mutant glioma patients treated with TMZ monotherapy had shorter progression free survival (PFS) rates compared to those that received radiation alone (3.4 vs. 6.2 years) (Weller et al., 2022). Likewise, the NOA-04 randomized phase 3 trial that investigated

radiation vs. chemotherapy alone or in combination with either PCV or TMZ had found that patients treated with TMZ had a shorter time to treatment failure and reduced overall survival (Wick et al., 2016). Nevertheless, these were observational studies of patient survival and we must acknowledge that patients treated with TMZ tend to be older and present with larger tumors, which could also contribute to the worse survival observed.

In tumors that lack MGMT expression, the O6-MG lesions recruit proteins involved in the mismatch repair (MMR) pathway, which attempt to repair the DNA but instead induce mutations by a G:C > A:T nucleotide substitution genetic signature (Cahill et al., 2007). The MutS homolog 2 (MSH2) and MSH6 recognize the O6-MG:T mispaired nucleotides and the endonuclease PMS1 homolog 2 (PMS2) nicks the DNA allowing for the removal of the lesion, which is stabilized by MutL homolog 1 (MLH1) (Acharya et al., 1996; Li & Modrich, 1995). In GBM, MSH6 mutations lead to TMZ resistance (McCord et al., 2020). A newly classified subgroup of IDH-mutant gliomas were found to be inherently TMZ-resistant due to germline or acquired mutations in the MMR pathway. *Suwala et al.* defined this subclass as Primary Mismatch Repair Deficient IDH-mutant Astrocytoma (PMMRDIA), where the authors found hereditary inactivating stop-gain or frameshift mutations in MLH1, MSH2, and MSH6 (Suwala et al., 2021). These patients were diagnosed at a young age (median of 14 years) and presented with the worse median survival observed in IDH-mutant glioma of only 15 months (Suwala et al., 2021). The major genetic differences between the PMMRDIA group and high-grade supratentorial IDH-mutant astrocytoma was the frequency of RB1 mutations (23.5% compared to 4.6% respectively) (Suwala et al., 2021).

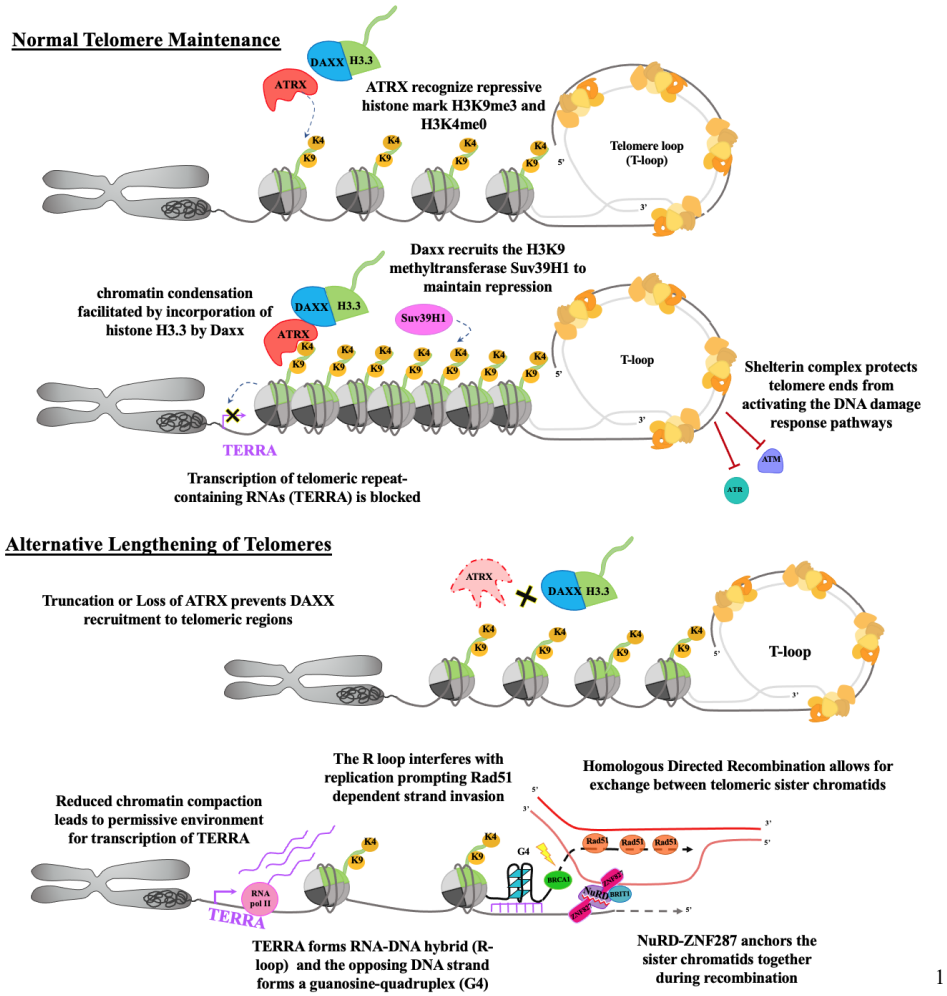

Figure 1.1 Role of ATRX in normal telomere maintenance and the process of Alternative Lengthening of Telomeres (ALT) where ATRX expression is lost by frameshift mutations present in glioma

During normal telomere maintenance, ATRX recognizes repressive histone mark H3K9me3 and H3K4me0 which are found near the end of telomeres. Then ATRX recruits the histone H3 variant (H3.3) chaperone protein DAXX, which incorporates H3.3 onto naked DNA. Based on co-immunoprecipitation studies, Daxx enlists the H3K9 methyltransferase Suv29H1 to deposit methylation marks on the newly incorporated H3.3 histones to maintain the heterochromatin state of the telomeres following mitosis. The degree of chromatin compaction, prevents the expression of the long noncoding transcript of telomeric repeat-containing RNAs (TERRA) . The T-loop is stabilized by the components of the shelterin complex (TRF1,TRF2, POT1, TPP1, RAP1, and TIN2), which protects the telomere ends from activating the DNA damage response pathways. Alternative Lengthening of Telomeres (ALT) pathway occurs independently of telomerase activity instead relies upon homology directed recombination to facilitate telomere extension. Predominantly IDH-mutant gliomas display mutations in ATRX but there are cases in IDH-wildtype glioblastoma, which lead to a loss of ATRX protein expression. DAXX cannot form a stable heterocomplex with ATRX in its absence, thus reduced chromatin compaction allows for transcription of TERRA. TERRA forms RNA-DNA hybrid (R-loop) and the opposing DNA strand forms a guanosine-quadruplex (G4). The R loop interferes with normal replication prompting Rad51 dependent strand invasion to the neighboring sister chromatid. The activation of HDR is stabilized by the NuRD-ZNF287 complex, which anchors the sister chromatids together throughout the exchange.

[1] This figure was originally published in: Haase S, Garcia-Fabiani MB, Carney S, Altshuler D, Núñez FJ, Méndez FM, Núñez F, Lowenstein PR, Castro MG. Mutant ATRX: uncovering a new therapeutic target for glioma. *Expert Opin Ther Targets.* 2018 Jul;22(7):599-613. doi: 10.1080/14728222.2018.1487953.

Alterations in Telomere Maintenance Genes

Inactivating mutations in the chromatin remodeler Alpha-Thalassemia/Mental Retardation, X-linked (ATRX) are prevalent in adult astrocytoma and are known to co-occur with IDH-mutations (Ohba et al., 2020). It is known that loss of ATRX is necessary to trigger alternative lengthening of the telomeres (ALT), a homologous recombination-dependent mechanism that allows tumors cells to extend their telomeres independently of telomerase reverse transcriptase (TERT) expression (**Fig. 1.1**) (Amorim et al., 2016). This mechanism ensures the maintenance of genomic stability allowing cancer cells to divide indefinitely, which contributes to cancer progression (Haase et al., 2018). ATRX functions in a complex with DAXX, which incorporates histone variant H3.3 into heterochromatin (Fan et al., 2019). In the context of brain development, the inactivation of ATRX in embryonic forebrain of mice lead to an increase generation of neural progenitors and migration of early-born neurons (Ritchie et al., 2014). In the absence of ATRX, NPCs displayed premature differentiation, which was attributed to the enhanced asymmetric division of neural progenitor along the subventricular zone (Ritchie et al., 2014). Only when p53 was also lost, could the mitotic defects of ATRX inactivation be rescued (Seah et al., 2008).

Loss of ATRX influences astrocytic lineage and motility

New findings have shown that ATRX also functions as an epigenetic regulator. For this reason, it was hypothesized that ATRX induces oncogenic pathways through the loss of transcriptional repression of distinct gene regions. *Danussi et al* investigated the role of ATRX to induce tumorigenesis in neural precursor cells (NPCs) (Danussi et al., 2018). The authors incorporated the genetic lesions found in astrocytoma into murine neural precursor cells (NPCs). They compared the epigenomic landscape of ATRX+ (wildtype) and ATRX- (knock out) NPCs in

a p53 null mouse background. ATRX was demonstrated to bind to specific transcriptionally active regions in order to alter gene expression in a cell-dependent manner (Danussi et al., 2018). In NPCs, loss of ATRX transcriptionally alters the differentiation profile favoring an astrocytic lineage over neuronal and oligodendrocyte fate, which correlates with the frequency of ATRX inactivating mutations in astrocytoma (Danussi et al., 2018). ATRX loss in NPCs is also correlated with an increased expression of genes involved in cell motility and migratory phenotype in ATRX- NPCs (Danussi et al., 2018). The authors observed that most of the differentially expressed genes on ATRX- NPCs were correlated with genomic loci were ATRX was bound in ATRX+ cells. Altogether, these results demonstrate that ATRX loss not only enhances genomic stability through ALT, but also exerts epigenetic changes that impact neural fate commitment.

Somatic mutations in Capicua Transcriptional Repressor (CIC) drive a bias towards oligodendrocyte precursor cell (OPC) lineage in oligodendroglioma

The major biomarker of oligodendroglioma (ODG) is the partial chromosomal loss of the short arm of chromosome 1 (1p) and the long arm of chromosome 19 (19q), which is referred to as 1p/19q co-deletion (Wesseling & Capper, 2018). Recent explorations into the functional basis for this translocation have concentrated on the genes that reside near the breakpoint. The idea being that this loss of heterozygosity (LOH) would expose putative tumor suppressor genes that influence ODG pathogenesis. Genomic profiling of 34 anaplastic ODGs identified that 53% (18/34) had inactivating mutations in the transcriptional repressor Capicua Transcriptional Repressor (CIC). Missense mutations were predominately found within the high motility group (HMG) domain of CIC, which is responsible for DNA binding (Bettegowda et al., 2011). Despite oligodendrogliomas having a better prognosis, CIC mutated ODGs define an aggressive subset

with a shorter time to contrast enhancement and mean tumor growth based on MRI scans (Gleize et al., 2015).A patient-derived xenograft (PDX) model of an anaplastic ODG expressing CIC was highly invasive, infiltrating into the hippocampus and white matter tracts of the corpus callosum when implanted in mice (Klink et al., 2013).

In order to analyze the role of CIC in neural lineage specification, Yang et al. generated a CIC knockout (Cic-/-) mouse model (Yang et al., 2017). Upon inspection of brains from Cic null mice, the authors observed an aberrant hyperproliferation of a GFAP-expressing population near the SVZ and Olig2-expressing population in the lateral septal nucleus (LSD) (Yang et al., 2017).. These findings indicated an abnormal expansion of an oligodendrocyte precursor cell (OPC) population, potentially providing a link between CIC inactivation and oligodendrocyte differentiation. Cic-/- NSC were able to grow in vitro independent of EGF signaling and under mild hypoxic conditions, while Cic+/+ NSC were not able to survive, indicating that CIC loss confers a proliferative advantage (Yang et al., 2017).. Transcriptome analysis of differentially expressed genes between Cic-/- and Cic+/+ NSCs, revealed that Cic-/- NSCs were unable to progress towards mature oligodendrocytes, but instead remained locked in an OPC-like stem cell niche (Yang et al., 2017). This bias towards an oligodendroglial lineage has been recapitulated by others using conditional Cic knockout murine models (Ahmad et al., 2019). In normal brain, there is a weak nuclear localization of Cic in NSCs and OPCs in contrast to high expression in differentiated neurons and mature oligodendrocytes (Ahmad et al., 2019). Within the postnatal cortex of Cic null mice, there was an expansion of GFAP+ cells and Olig2+Pdgfra+ OPCs. Neurospheres generated from embryonic day 13 (E13) Cic-floxed embryos and transfected with Cre, displayed higher self-renewal and underwent symmetrical cell division in vitro (Ahmad et al., 2019). The authors sought to identify the downstream mediators involved in the glial bias

following Cic loss. With this in mind, the authors focused on a Ets-domain transcription factor, Etv5 which was a known Cic target and overexpressed in ODGs (Ahmad et al., 2019). The overexpression of a dominant-negative form of Etv5 (DNETV) in two primary ODG cultures BT54 and BT88 pushed them towards a mature oligodendrocyte state (Ahmad et al., 2019). Collectively, this data suggests that Cic loss derepresses Ets factors that switch neural fate towards a OPC lineage.

In accordance with CIC's function as a transcriptional repressor acting downstream of RTK/MAPK signaling, *Weissmann et al.* explored how CIC mediates changes to chromatin regulation (Weissmann et al., 2018). The authors demonstrated under basal conditions, CIC binds gene promoter regions and distal enhancers enriched for *TSAATGR* sequences to regulate proliferation. In support of findings from Yang et al, many of these genes have been implicated in MAPK signaling, which is frequently disrupted in many cancers. From affinity purification experiments, it was determined that CIC interacts with histone deacetylating complex SIN3 and HDAC1/2 to remove acetylation marks at gene regions involved in MAPK signaling and specific transcription factors (Weissmann et al., 2018). In a human fetal NSC line G144, ablation of CIC lead to increase histone acetylation at gene regions that encode ID1, CCND1, and SHC3, which have been directly implicated in neural stem cell identity and cell cycle regulation (Weissmann et al., 2018). The CIC feedback mechanism likely prevents the overactivity of the MAPK signaling in normal cells (Weissmann et al., 2018). CIC-mutated oligodendroglioma do not respond to MEK inhibition, thus allowing these cells to grow in growth signal depleted conditions.

Epigenetic reprogramming mediated by the oncometabolite 2-hydroglutarate (2HG)

Isocitrate dehydrogenase enzymes, of which there exist three isoforms are essential in the metabolic process of the Kreb cycle to perform the decarboxylation of isocitrate to α-ketoglutarate. IDH1 is located in the cytoplasm and peroxisomes, whereas IDH2 and IDH3 are present in the mitochondrial matrix. The catalytic activity of IDH enzymes requires the reduction of nicotinamide adenine dinucleotide phosphate ($NADP^+$) as a cofactor. *Parson et al.* demonstrated that mutant IDH1 (mIDH1) lost its normal enzymatic activity to convert isocitrate to α-ketoglutarate (α-KG). Ensuing work by *Dang et al.* explored the impact of mIDH1 on cellular metabolism by profiling metabolites extracted from two glioblastoma cell lines U87MG and LN-18 transfected to express mIDH1 (Dang et al., 2009). The authors demonstrated that mIDH1 results in a new ability of the enzyme to reduce α-KG to 2-hydroxyglutarate (2HG). This challenged the notion that the R132H mutation lead to a loss-of-function, conversely resulted in a neomorphic gain-of-function through the generation of 2HG, a cancer-associated metabolite or oncometabolite.

There are nuclear enzymes that rely upon the availability of α-KG to facilitate their biological function called α-KG dependent dioxygenases. These include the JmjC domain family of histone demethylases (KDM), which remove methyl marks on histones and the TET family of 5-methylcytosine (5mC) hydroxylases that facilitates the removal of methyl groups on DNA nucleotides specifically at CpG islands found at promoters and enhancers (**Fig. 1.2**) (Lu et al., 2012; Xu et al., 2011).

In order to address the underlying mechanism of 2HG, *Xu et al.* proposed that 2HG acted

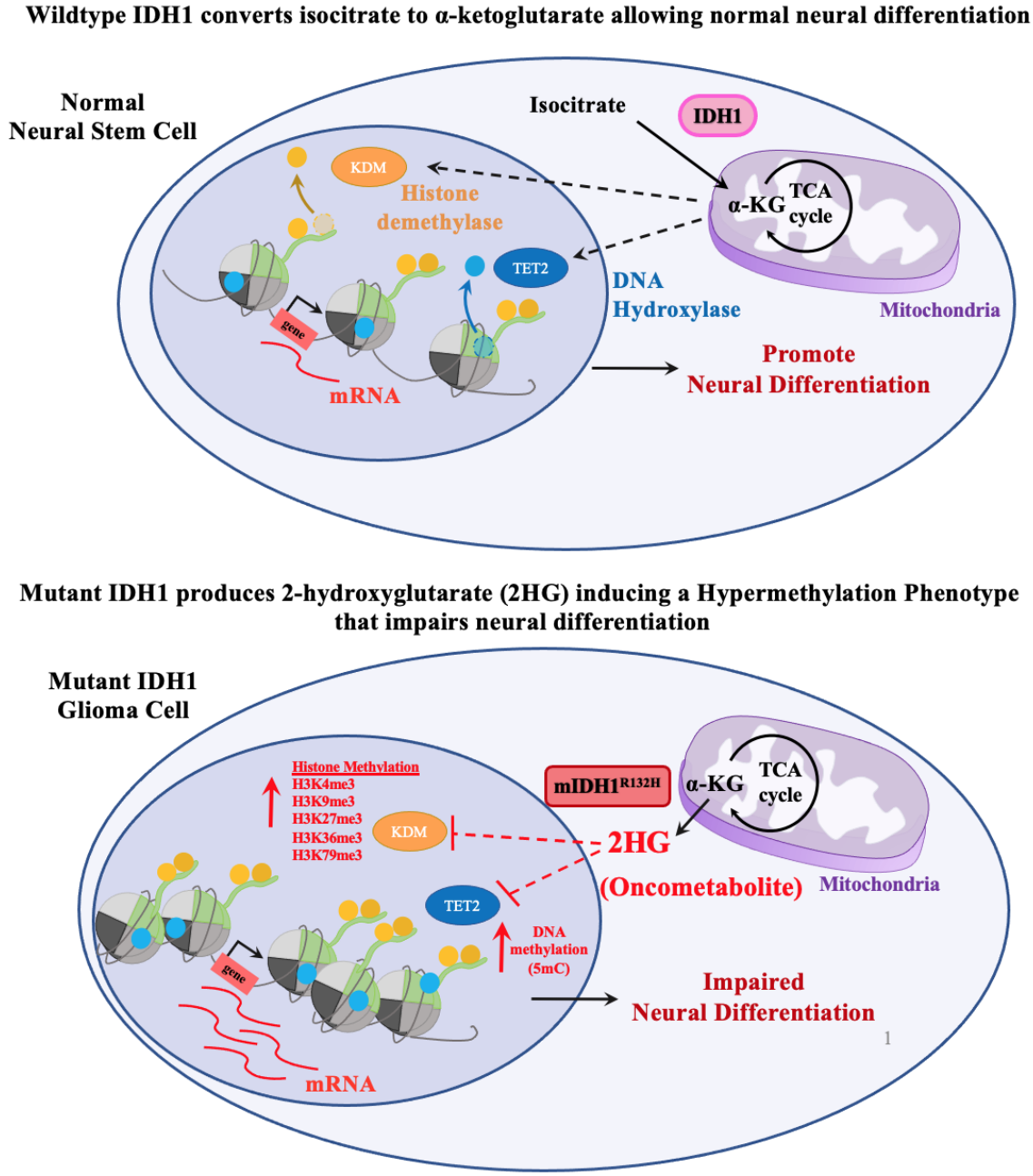

Figure 1.2 Alterations in the metabolism of normal neural stem cells (wildtype IDH1) by acquired mutant IDH1-R132H expression impacts neural lineage by inducing a histone and DNA hypermethylation phenotype in mIDH1 glioma cells

as a competitive inhibitor to α-KG based on their similarity in chemical structure (Xu et al., 2011). The authors exposed a C. elegan histone demethylase (CeKDM7A) to 2HG and examined its ability to remove synthetic methylated H3K9 and H3K27 peptides. At a concentration of 100mM, 2HG completely inhibited the ability of CeKDM7A to remove dimethyl marks on the synthetic histone peptides. Remarkably, 2HG binds within the catalytic core of the CeKDM7A in the same orientation as α-KG, which provided crucial evidence to support its role as an antagonist to α-KG. Also, U87MG cells transiently transfected with mIDH1 displayed elevated histone methylation at active regions marked by H3K4me3 and H3K79me2 as well as repressed regions marked by H3K9me2 and H3K27me3.

mIDH1 establishes DNA hypermethylation, a CpG island methylator phenotype (CIMP)

Although these findings paved the way to elucidate the association between mIDH1 expression and the hypermethylation phenotype, these approaches lacked a dynamic grasp of the global chromatin changes. Several researchers have focused solely on the magnitude of mIDH1 induced hypermethylation instead of visualizing it as a coordinated reorganization targeting specific loci. *Turcan et al.* sought to address whether the distinct CpG island methylator phenotype (CIMP) observed in LGG can be rendered solely by the introduction of IDH1 mutation. The authors transfected immortalized human astrocytes (IHAs) with mIDH1 or wildtype IDH1 (Turcan et al., 2012). Thus producing isogenic lines, where the genomic sequence is the same except for the expression of mIDH1. De novo DNA methylation requires extended periods of time to transpire and retain the epigenomic changes in the context of an *in vitro* model (Ohm et al., 2007). Analysis of the methylome was performed over several passages to allow time for reshaping of the chromatin by mIDH1. The authors identified 30,988 sites differentially methylated in mIDH1 expressing astrocytes, of which 3,141 corresponded to unique promoter regions (Turcan et al.,

2012). These regions were confirmed to originally possess low levels of methylation in the parental line but had subsequently acquired hypermethylation. Additionally, the enrichment of polycomb complex 2 (PRC2) at these targeted loci; which normally associates with repress chromatin regions to deposit H3K27me3, supported the claim that mIDH1 is sufficient to reshape the global methylation landscape (Turcan et al., 2012). The upregulation of a neural stem cell marker Nestin after passage 12 in the mIDH1 expressing astrocytes suggested that mIDH1 reverts the differentiated astrocytes to a neural precursor state.

A shared feature across IDH1/2 mutant cancers showed a high propensity of DNA hypermethylated regions at gene bodies and enhancers, while surprisingly the majority of gene promoters remained hypomethylated (Unruh et al., 2019). Although this finding might imply a universal effect of the IDH-mutation, another study revealed distinct methylome patterns when comparing IDH-mutant tumors to IDH-wildtype tissue matched counterparts. The authors found that 19% of CpG sites were exclusively hypermethylated in IDH-mutant glioma compared to 3% in IDH-mutant AML, 2% in melanoma, and 4% in cholangiocarcinoma (Bledea et al., 2019). CpG methylation can impact nearby genes altering their expression, thus these differentially methylated regions across IDH-mutant cancers may be dependent upon the cellular origin of the cancer. IDH-mutant gliomas displayed the greatest number of biological pathway alterations compared with the other tumor types, specifically the downregulation of tissue development and an upregulation of a subset of DNA repair pathways (Bledea et al., 2019).

The prominent role of mIDH1 in tumor initiation may be distinct from its function in tumor recurrence. *Mazor et al.* reported on six cases of copy number alterations (CNA) at the IDH1 endogenous locus following tumor recurrence (Mazor et al., 2017). These tumors were originally IDH1 mutant but acquired a deletion or an amplification of IDH1 during clonal expansion. As

mentioned prior IDH1 mutations are exclusively heterozygous due to the fact that the production of α-KG by wildtype IDH1 is required for mIDH1 facilitate the conversion of the substrate to 2HG (Luo et al., 2021). Longitudinal assessment of the levels of 2HG by NMR from snap-frozen samples and exome sequencing revealed that either the abundance of mIDH1 or the selection against by loss of heterozygosity promotes lower 2HG levels (Mazor et al., 2017). A related observation was also seen, where in a xenograft isolated from a secondary GBM had retained a mutation in IDH1 but overtime loss the expression during serial transplantation (Mazor et al., 2017). Although the majority of CIMP regions remained repressed, another subset of gene regions had become hypomethylated in the CNA tumor samples (Mazor et al., 2017). This finding suggests a novel area of therapeutic implications to delve into regions that become hypomethylated during malignant transformation.

This shift in DNA methylation occurring in a subset of regulatory regions was also investigated by de Souza et al. (de Souza et al., 2018). The authors performed an immense longitudinal analysis of diffuse gliomas from 77 patients to report on the epigenomic changes occurring as IDH1 mutant tumors typically defined by CIMP high became an aggressive CIMP low subtype (de Souza et al., 2018). The heterogeneity found within CIMP high primary tumors could indicate which patients are at risk of developing a malignant tumor earlier (de Souza et al., 2018). The appearance of CIMP low tumors occurred in 9.5% of all gliomas studied and their methylome profile resembled that of IDH1 wildtype glioblastoma (de Souza et al., 2018).

Insulator dysfunction from loss of CCCTC-binding factor (CTCF) occupancy drives oncogene activation in IDH-mutant glioma

Chromatin is folded into distinct loops called topologically associated domains (TADs), which constrain the regulatory interactions between enhancers and promoters. It has been proposed that these structural scaffolds are established by the binding of CCCTC-binding factor (CTCF) and cohesions to regions of unmethylated DNA. *Flavahan et al*. demonstrated that the increased DNA methylation by mIDH1 disrupts the insulation of topological domains leading to aberrant gene activation (Flavahan et al., 2016). The authors showed that exogenous mIDH1 resulted in the loss of CTCF at the TAD boundary allowing the interaction between a constitutive enhancer with the promoter of a prominent glioma associated oncogene PDGFRA. Interestingly, treatment with the DNA methyltransferase inhibitor 5-azacytidine temporarily reduced DNA methylation at CTCF binding sites, restored TAD separation and caused the downregulation of PDGFRA (Flavahan et al., 2016).

Modrek et al. designed an *in vitro* model of low grade astrocytoma by systematically replicating the sequence of acquired genetic aberrations in human neural stem cells (NSCs) generated from inducible pluripotent stem cells (Modrek et al., 2017). The generation of NSC that ectopically expressed mIDH1 initially, followed by short hairpin knockdown of TP53 (shp53) and lastly shAtrx demonstrated an impaired ability to differentiate into neuronal progenitors by the lack of Tuj1 expression (Modrek et al., 2017). Hypermethylation of CTCF binding sites around the SOX2 locus blocked neural differentiation by diminishing the contacts within the regulatory loop (Modrek et al., 2017). The loss of CTCF occupancy destabilized the chromatin structure altering the chromatin state and ultimately arresting the NSCs within an undifferentiated state (Modrek et al., 2017). These findings support new evidence that chromatin conformation is a

critical step resulting in the absence of neural lineage markers being observed in IDH-mutant glioma.

Reversibility of mIDH1 induced histone hypermethylation

To date, our understanding of the reversibility of histone hypermethylation following loss of mIDH1 activity has been limited to immortalized human astrocytes (IHA) that expressed mIDH1 under a doxycycline (dox) inducible system (Turcan et al., 2018). Notably, IHA-expressing mIDH1 displayed upregulation of stem-like genes: CD24 and PDGFRA, which was accompanied by a transient gain of H3K4me3 at these gene promoter regions suggesting that mIDH1 poises these genes for activation (Turcan et al., 2018). Following dox-withdrawal, methylation at most loci eventually returned to baseline levels either transiently (13.8%) or gradually (62.5%) across cell passages, but 23.7% of regions persisted after loss of mIDH1 (Turcan et al., 2018). These findings suggest that the epigenetic reprogramming mediated by mIDH1 is still not well understood, especially in regard to the contribution of mIDH1 regulation on genes involved in therapeutic resistance.

Development, specificity and early assessment of mIDH1 inhibitors

The epigenetic reprogramming mechanism facilitated by mIDH1 is dependent upon its production of 2HG, which notably our group and others have demonstrated can be reversed through treatment with mIDH1 specific inhibitors (Golub et al., 2019; Kadiyala et al., 2021; Núñez Felipe et al., 2019; Urban et al., 2017) (**Figure 1.3**). A multitude of mIDH1 and mIDH2 specific inhibitors have been developed over the last decade. These drugs vary in chemical structure, mutational specificity, their ability to cross the blood brain barrier, and mechanism of action

(**Table 1.2**) (Tian et al., 2022). The first selective IDH1 inhibitor AGI-5198 was demonstrated to block the production of 2HG by binding the active site of mIDH1. AGI-5198 was also shown to lower 2HG levels *in vivo* in NSG mice implanted with a mIDH1 patient-derived xenograft TS603 (Rohle et al., 2013). This inhibitor preferentially impaired the growth of TS603 human mIDH1 xenografts, potentially through the induced neural differentiation. *Rohle et al.* observed an increased expression of mature oligodendrocyte (NG2, CNP) and astrocyte (GFAP, AQP4, ATP1A2) lineage markers measured by qPCR analysis of the isolated from TS603 xenografts implanted in NSG mice treated orally with 450mg/kg of AGI-5198 (Rohle et al., 2013). Although, AGI-5198 could lower the expression of a neural stem cell marker Nestin in TS603 cells, mIDH1 inhibition was not shown to induce cell death (Rohle et al., 2013).

IDH305 was the next mIDH1 inhibitor to be developed and the first to advance to Phase I assessment. It showed promise for its ability to cross the BBB and targeting mIDH1 via an allosteric site (Cho et al., 2017). When administered to IDH-mutant patients, IDH305 was able to lower 2HG levels by 70% within the tumor after the first week of treatment (Andronesi et al., 2018). The study exposed shifts in the metabolism of the mIDH1 tumors with an observed increase in glutathione and lactate within the tumor in post-treatment scans, suggesting that the tumors might become more aggressive. *Andronesi et al.* observed an increase in Fast fluid-attenuated inversion-recovery (FLAIR) tumor volume following IDH305 treatment potentially an indication of increased tumor growth (Andronesi et al., 2018).

Currently the improved derivatives of AGI-5198: AG-120 and pan-IDH mutant inhibitor AG-881 have been approved by the FDA for the treatment of IDH-mutant cancers. AG-120 has shown great success in AML treatment and has advanced to Phase III (NCT03173248) in

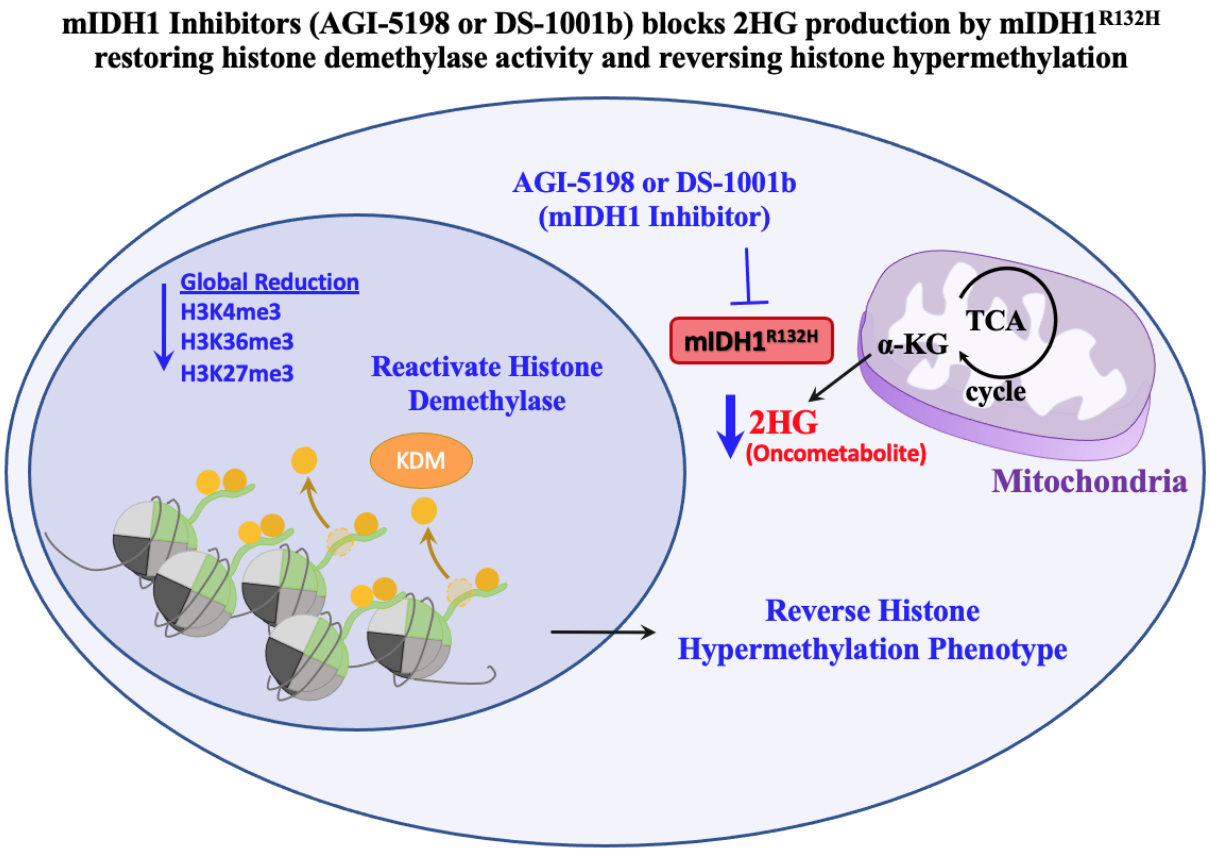

Figure 1.3 Pharmacological inhibition of mIDH1 using AGI-5198 or DS-1001b have been shown to reverse histone hypermethylation through the reduction of 2HG and reactivation of histone demethylase (KDM).

Table 1.2 Development, preclinical evaluation, and clinical trials of pharmacological inhibitors targeting mutant IDH1 and IDH2 in solid tumors and hematologic malignances

Compound	Industry/ Institutional Sponsor	Chemical Backbone Scaffold	*In Vitro* IC_{50}	Mutational Specificity	BBB Permeable	Mechanism of Action	Clinical Trials
AGI-5198	Agios	phenyl-glycine	70-160nM	$IDH1^{R132H}$ $IDH1^{R132C}$	High	Binds to active site of mIDH1 as a competitive inhibitor to α-KG	Not pursued due to metabolic clearance
ML309	Agios	phenyl-glycine	62-96nM	$IDH1^{R132H}$ $IDH1^{R132C}$	None	Binds to mIDH1 after it complexes with NADPH	Not pursued due to low brain permeability
IDH305	Novartis	3-pyrimidin-4-yl-oxazolidin-2-one	18nM	$IDH1^{R132H}$	High	Binds to mIDH1 homodimer in a non-competitive manner leading to an "inactive" conformation	NCT02381886: AML/MDS/Glioma/IHCC
AG-120	Agios	phenyl-glycine	3.5nM	$IDH1^{R132H}$ $IDH1^{R132C}$ $IDH1^{R132G}$ $IDH1^{R132S}$ $IDH1^{R132L}$	Low	Reversible, allosteric competitive inhibitor via Mg^{2+} cofactor binding site	NCT02074839: AML/MDS NCT03173248: AML, AG-120 combined with azacitidine
IDH2-C100	Agios	pyridine-triazine	0.1-1μM	$IDH2^{R140Q}$ $IDH2^{R172K}$	Unknown	Not studied	Not pursued, IDH2-C100 was an analog for AG-221
AG-221	Agios	pyridine-triazine	22nM	$IDH2^{R140Q}$ $IDH2^{R172K}$	None	Non-competitive inhibitor leading to an "inactive" dimer conformation, better agianst $IDH2^{R140Q}$ than $IDH2^{R172K}$	NCT02632708: AML/MDS NCT02577406: AML
AG-6780	Agios	pyridine-triazine	23-170nM	$IDH2^{R140Q}$	Unknown	Binds to mIDH2 dimer interface at the Mg^{2+} allosteric site in a non-competitive inhibitor manner	Not pursued, limited *in vivo* testing and lower binding stability when compared to AG-221
AG-881	Agios	pyridine-triazine	6nM	$IDH1^{R132H}$ $IDH1^{R132C}$ $IDH1^{R132G}$ $IDH1^{R132S}$ $IDH1^{R132L}$ $IDH2^{R140Q}$ $IDH2^{R172K}$	High	Pan-IDH1/2 inhibitor, non-competitive inhibition leading to an "inactive" dimer conformation	NCT03343197: LGG NCT02481154: Solid Tumors, including Glioma NCT02492737: AML/MDS NCT04164901: Recurrent Glioma Grade 2 (INDIGO) NCT05484622: Progressed mIDH1 Astrocytoma, AG-881 combined with Pembrolizumab (anti-PD-1)
BAY1436032	Bayer	benzimidazole	15nM	$IDH1^{R132H}$ $IDH1^{R132C}$ $IDH1^{R132G}$ $IDH1^{R132S}$ $IDH1^{R132L}$	High	Binds to allosteric pocket	NCT03127735: AML NCT02746081: Advanced solid tumors (IHCC, Glioma)

Compound	Industry/ Institutional Sponsor	Chemical Backbone Scaffold	*In Vitro* IC_{50}	Mutational Specificity	BBB Permeable	Mechanism of Action	Clinical Trials
DS-1001b	Daiichi Sankyo	isoxazole	8nM	$IDH1^{R132H}$ $IDH1^{R132C}$	High	Binds to allosteric pocket, reducing mIDH1's affinity for α-KG	NCT03030066: Glioma NCT04458272: Grade 2 Glioma without Chemo/IR
FT-2102	Forma Therapeutics	pyridinone	21-114nM	$IDH1^{R132H}$ $IDH1^{R132C}$	High	Binds mIDH1 monomer, binding allosteric site at dimer interface	NCT02719574:AML/MDS, FT-2102 alone or combined with azacitidine or cytarabine NCT03684811:Solid tumors (IHCC, Glioma)
HMS-101	Dr. Heuser Germany	piperazine and pyrrolidine rings	4-300μM	$IDH1^{R132H}$ $IDH1^{R132C}$ $IDH2^{R140Q}$ $IDH2^{R172K}$	Unknown	Binds an active site in close proxmity to the regulatory segment of the enzyme for binding NADPH, high affinity for mIDH1over mIDH2	Preclinical for AML
MRK-A	Merck	—	5-50nM	$IDH1^{R132H}$ $IDH1^{R132C}$	High	Unknown	Preclinical for Glioma
GSK321	GlaxoSmithKline	aniline	4.6nM	$IDH1^{R132H}$ $IDH1^{R132C}$ $IDH1^{R132G}$	Unknown	Binds to allosteric pocket of homodimer in the presence of $NADP^{+}$	Not pursued due to poor pharmacokinetic properties
LY3410738	Eli Lilly	enamine acrylamide	0.1-1nM	$IDH1^{R132H}$ $IDH1^{R132C}$ $IDH1^{D279N}$	High	Covalently binds to allosteric pocket to inactiviate mIDH1 enzyme (irreversible binding)	NCT04521686: Glioma NCT04603001: AML/MDS/CMML/MPN Experimental Arm C: LY3410738, Venetoclax, and Azacitidine

combination with azacytidine, a DNA methyltransferase inhibitor. Despite AG-120 displaying superior pharmacokinetics to AGI-5198, it is susceptible to transport by the efflux pump p-glycoprotein restricting its brain penetrance (Gottesman et al., 2016). Interestingly, Mellinghoff et al. demonstrated a reduction of 93% in the levels of 2HG present within the cerebral spinal fluid (CSF) of grade 2 and 3 IDH-mutant gliomas treated with AG-120 during the initial clinical reporting (Mellinghoff et al., 2020).

Phase I/II clinical trial results explore the therapeutic potential of mutant IDH1-specific inhibitors in the treatment of recurrent IDH-mutant glioma

LGGs that express IDH-mutations occur in younger patients, who suffer from neurocognitive issues due to the disease. The current treatment strategies for IDH-mutant glioma patients of maximal tumor resection followed by radiation and chemotherapy are not curative. Often these patients experience disease recurrence evident by the appearance of tumor contrast enhancement on T1-weighted MRI brain scans. The utility of mIDH1-specific inhibitors in clinic has relied on the notion that targeting this oncogene at an earlier stage of the disease prior to progression might perhaps delay malignant transformation. The primary objective of these phase I/II studies are to evaluate the safety and tolerability of mIDH1-specific inhibitors and to determine a maximal tolerated dose (MTD) or recommended phase II dose (RP2D) (Mellinghoff et al., 2020). While the secondary objectives are to evaluate the clinical activity as measured by objective response rate (ORR) and progression-free survival (PFS) (Mellinghoff et al., 2020). These responses are designated based on RANO criteria as complete response (CR), partial response (PR) or minor response (mR) (Mellinghoff et al., 2020). A reduction in tumor size is measured by the relative sum of the products of the diameter (SPD) from the on-treatment MRI scans compared to screening baseline from when the patients are enrolled in the trial (Mellinghoff et al., 2020). A

change in SPD with treatment can be classified as CR if there is an absence of detectable tumor, PR for ≥50% SPD change from baseline or mR for ≥25% but ≤50% SPD change from baseline (Mellinghoff et al., 2020).

A glioma cohort of 52 mIDH1 patients (22 with non-enhancing glioma and 30 with enhancing glioma), in which their tumors had recurred following standard therapy were treated with vorasidenib (AG-881, pan-mIDH1/2 inhibitor) once daily initially at 50mg escalated to 300mg for 28-day cycles (Mellinghoff et al., 2020). Preliminary data from this study determined that administration of vorasidenib 50mg/day reduced intratumoral 2HG concentrations by >90%, suggesting an almost complete inhibition of the mIDH1 or mIDH2 enzymes. Dose limiting toxicities (DLT) were observed in patients receiving >100mg of vorasidenib, which was on the basis of elevated alanine and aspartate transaminases (Mellinghoff et al., 2020). The majority of non-enhancing glioma patients (16/22, 72.7%) and enhancing glioma patients (17/30, 56.7%) presented with stable disease, whose tumors showed reductions in SPD <25% with vorasidenib treatment and thus could not be qualified for mR (Mellinghoff et al., 2020). For non-enhancing glioma a ORR of 18% (1 PR, 3 mR) was observed and these patients had a median PFS of 36.8 months (Mellinghoff et al., 2020). This suggests tumor shrinkage is occurring in a subset of non-enhancing glioma patients with treatment with vorasidenib. Meanwhile, there was no indication that vorasidenib has antitumor activity in patients with enhancing tumors at screening and an ORR was not achieved. The aim of the INDIGO trial (NCT04164901) in patients with recurrent grade II non-enhancing mIDH1 glioma is to provide insight into the antitumor activity of vorasidenib during early stages of diagnosis.

Recently published results from the randomized perioperative phase I trials evaluating vorasidenib (AG-881) at 50mg or 10mg daily and ivosidenib (AG-120) at 250mg or 500mg daily

investigated the underlying molecular changes that occur as a result of mIDH-specific inhibition (Mellinghoff et al., 2023). Findings from this exploratory approach examined changes to the transcriptome of tumor biopsies and presence of immune signatures following the vorasidenib and ivosidenib treatment cycles (Mellinghoff et al., 2023). Despite, the tumor:plasma ratio being higher for vorasidenib than ivosidenib, the dosing amount selected for ivosidenib allowed for adequate plasma concentrations to inhibit mIDH1 enzymes within the brain (Mellinghoff et al., 2023). They identified 762 genes that were either induced or repressed in response to 2HG suppression (Mellinghoff et al., 2023). There was a downregulation of "proneural and stemness" associated gene signatures specifically in cell cycle progression (G2M checkpoint, E2F targets, and mitotic spindle), while interferon-α and interferon-γ pathways were the most highly upregulated suggestive of increased immune activation (Mellinghoff et al., 2023). This alluring data presents the possibility that mIDH enzymes might remain active during recurrent disease, considering that lowered 2HG levels were associated with reduced tumor cell proliferation. The ORR for vorasidenib at 50mg was 42.9% (2 PR, 4 mR) and 35.7% ORR for ivosidenib at 500mg (3 PR, 2mR) (Mellinghoff et al., 2023).

Another glioma cohort consisting of 47 patients (15 oligodendroglioma, 32 astrocytoma) participated in a dose-escalation evaluation of DS1001b administered orally at 125-1400mg twice daily for 21-day cycles (Natsume et al., 2023). Thirty patients discontinued with the trial due to disease progression and 8 received ongoing treatment throughout the study (Natsume et al., 2023). The most common adverse effects (AE) were hyperpigmentation resembling a sunburn on the face and forearm (53.2%), diarrhea (46.8%) and pruritus (29.8%) (Natsume et al., 2023). Interestingly, for non-enhancing glioma patients a 33% ORR (2 CR, 4 PR) was achieved and enhancing glioma patients had a 17% ORR (1PR, 3 mR) (Natsume et al., 2023). For the two patients that showed

CR, one was diagnosed as grade 4 IDH-mutant astrocytoma and the other was grade 3 oligodendroglioma. In patients that presented with progressed disease, a salvage surgery was done to measure the intratumoral levels of DS-1001b and 2HG concentration (Natsume et al., 2023). The authors observed a significant reduction in 2HG levels even at 125mg dosing. Currently, DS-1001b is the only brain-penetrable mIDH1 inhibitor to achieve CR in patients. A RP2D has been selected at 250mg to pursue combinatory therapy of DS-1001b with radiotherapy and chemotherapy in IDH-mutant grade 2 glioma.

Olutasidenib (FT-2102) was evaluated in 26 patients at 150mg twice daily for 28-day cycles (de la Fuente et al., 2023). No DLT were observed. Twenty patients discontinued treatment due to disease progression, 1 for AE and 5 remained on treatment (de la Fuente et al., 2023). All patients received prior radiotherapy and most received some form of chemotherapy (23 received TMZ, 9 lomustine, 5 procarbazine, 4 bevacizumab) (de la Fuente et al., 2023). The best response observed was that 40% of patients had stable disease, however only 2 patients had PR (de la Fuente et al., 2023). Interestingly, in patients with non-canonical IDH1 mutations, the patient with R132C had stable disease for >23 months, but the two patients with either R132L or R132G developed disease progression after 1-2 months on treatment (de la Fuente et al., 2023).

What we can infer from these early phase I/II studies is that mIDH1 inhibition appears to decrease the cellular proliferation of mIDH1 gliomas if treated at early stages of disease. However, patients with enhancing glioma at the time of trial screening tend to undergo disease progression when administered mIDH1 inhibitors. It is plausible that upon recurrence, secondary tumors gain mutations in cell cycle regulators that drive accelerated growth, which can bypass the impact of mIDH1 inhibition. The idea that mIDH1 becomes a “passenger” in recurrent tumors has been suggested but remains to be explored?

Modeling mIDH1 pathogenesis in murine models of glioma that endogenously express IDH1-R132H mutation

Early attempts to activate mIDH1 using a conditional knockin allele in the developing brain was hindered by perinatal lethality due to brain hemorrhages and high levels of apoptosis (Sasaki et al., 2012). To prevent adverse effects, *Bardella et al.* generated a tamoxifen-inducible Nestin-Cre restricted the expression of a mIDH1 allele to the subventricular zone of the adult mouse brain (Bardella et al., 2016). Interestingly, the mice developed dilated lateral ventricles surrounded by a hyperproliferating pool of stem-cells and aberrant migration of progenitors into the olfactory bulb (Bardella et al., 2016) Although, the mice formed nodules that infiltrated the brain parenchyma, none developed definitive solid tumors. Nevertheless, mIDH1 expressing progenitors overexpressed genes involved in Wnt, cell cycle, and stem cell maintenance pathways (Bardella et al., 2016). One major fault with this model was the leaky expression of a short RNA Idh1 isoform lacking exon 1 and 2, which resulted in enlarged skulls in mice not crossed with Nestin-Cre (Bardella et al., 2016)

Another model utilized an established RCAS/TVA retroviral vector system to ensure the expression of mIDH1 in specifically neural stem cells (Uhrbom et al., 2005). The RCAS (Replication-Competent Avian Sarcoma-Leukosis Virus LTR with splice acceptor) is derived from the Rous sarcoma virus backbone but can be engineered to express a gene of interest (Orsulic, 2002). Only mouse cells expressing the TVA (tumor virus A receptor) will be infected by the virus allowing integration and expression of the desired oncogenic DNA (Orsulic, 2002) Even though, mIDH1 is not sufficient to induce tumor formation on its own in cooperation with known co-expressed genetic alterations: PDGFA overexpression and loss of *Cdkn2a*, *Atrx*, and *Pten* triggered gliomagenesis *in vivo* (Philip et al., 2018). mIDH1 tumors derived from these mice displayed

reduced 5-hydroxymethylcytosine (5hmC), which is normally formed following the removal of methylation by TET (Philip et al., 2018). A methylation profiling of mIDH1 expressing tumors identified 13,570 regions that were hypermethylated and 2,609 that were hypomethylated compared to wildtype IDH1 expressing tumors (Philip et al., 2018). Considering the robust changes to the chromatin architecture of mIDH1 expressing tumors, the question emerges whether it is possible to restore cellular differentiation processes by inhibiting the production of 2HG.

Our Studies

In an effort to better understand if mIDH1 drives resistance mechanisms to radiotherapy, we performed transcriptomic and epigenomic analyses in a radioresistant human mIDH1 glioma cell culture (GCC). Of the thousands of genes that were dysregulated by mIDH1 inhibition, we identified that the chromatin reader protein Zinc Finger MYND Type Containing 8 (ZMYND8) was significantly repressed. ZMYND8 was known to be recruited to regions of DNA damage and functions in regulating genomic stability at enhancers and telomeres making it an alluring candidate for our investigation. We show that suppression of ZMYND8 by shRNA or CRISPRCas9 mediated genetic knockout sensitizes mIDH1 GCCs to radiotherapy. ZMYND8-interacting partners have recently been proposed as therapeutic targets for the treatment of mIDH1 glioma. Together our study highlights a potential mechanism of therapeutic resistance to radiotherapy that is intrinsic to mIDH1 reprogramming, which converge upon a novel epigenetic vulnerability mechanism to respond to irradiation induced DNA damage.

Chapter 2 Characterization of the Alterations in the Transcriptome and Epigenome After MIDH1 Inhibition in Patient Derived Glioma Cell Culture SF10602

Introduction

Our understanding of the alterations to the transcriptome and epigenome as a result of mIDH1 reprogramming have centered on cellular models where mIDH1 was expressed exogenously (Turcan et al., 2018; Turcan et al., 2012). Or respectively by comparing wildtype vs. mutant IDH1 gliomas, which we know possess drastically different genetic mutations (Bledea et al., 2019). This study aimed to identify genes regulated by mIDH1 in glioma cells derived from an astrocytoma patient (SF10602), in which the mutation was acquired endogenously at the time of tumor initiation. It is thought that mIDH1 serves an initial event to "lock-in" the epigenomic state of neural stem cells and prevent neural differentiation (Rohle et al., 2013).

Pharmacological inhibition of mIDH1 using AGI-5198 induces a transition in neural lineage towards a mature astrocyte and oligodendrocyte transcriptional state. Blocking mIDH1 could potentially disrupting stemness associated pathways leading to the reduced cellular proliferation observed *in vitro* and *in vivo* with PDX models (Rohle et al., 2013). We know that some patients treated with mIDH1-specific inhibitors display remarkable reductions in tumor size. Although, the majority of patients achieve stable disease if treated at early stages of diagnosis (Mellinghoff et al., 2020; Mellinghoff et al., 2023). This study aims to understand if this reversal of histone hypermethylation reconfigures the epigenome in a way that destabilizes pathways involved in radioresistance.

To explore the contribution of mIDH1 to therapeutic resistance to radiotherapy, we utilized a radioresistant mIDH1 GCC SF10602, which underwent malignant transformation after the patient received radiation and TMZ chemotherapy. We found that the gene ZMYND8 was significantly downregulated in SF10602 treated with a mIDH1-specific inhibitor, AGI-5198. Additionally, there was significant loss of active histone mark methylation (H3K4me3) at the promoter locus for ZMYND8 in AGI-5198 treated SF10602. In terms of upregulated genes, we found that replicative stress associated proteins particularly those that occurred at nuclear forks had increased expression in the AGI-5198 treated condition. This suggested to us that certain genes are directly modulated by the hypermethylation of histones induced by mIDH1 reprogramming and directly impacting their mRNA expression. We also evaluated the difference in ZMYND8 nascent RNA expression and chromatin regulation by comparing our genetically engineered mouse models that express NRas, shTP53, shATRX and/or mIDH1-R132H. The mIDH1-expressing neurospheres had enhanced nascent ZMYND8 expression as well as enhanced deposition of H3K4me3 at the promoter regions of the ZMYND8 locus. These findings suggested to us that mIDH1 could be modulating the expression of ZMYND8.

Results

Inhibition of mIDH1 by AGI-5198 leads to the upregulation of replication associated pathways

In this study, we sought to determine radioresistance mechanisms in IDH-mutant gliomas that contribute to glioma cell survival in response to radiotherapy. We utilized a radioresistant patient-derived glioma cell culture SF10602, which retained the endogenous mutations in IDH1-R132H, ATRX and TP53 after adaptation to *in vitro* culture (Jones et al., 2020). In order to identify

pathways altered by mIDH1 inhibition in SF10602, we performed a transcriptomic (RNA-seq) and epigenomic (ChIP-seq) screen (**Fig. 2.1A**) by administering 5μM AGI-5198 every 2 days for 1 week. It has been shown that 2HG is released within the conditioned media of mIDH1 GCC maintained *in vitro* (Tateishi et al., 2015). To confirm that our mIDH1 inhibitor treatment schedule inhibited 2HG production, we collected the conditioned media from untreated and AGI-5198 treated mIDH1 GCCs to analyze the presence of 2HG by liquid chromatogram and mass-spectrometry (LCMS) (**Table 2.1**). We performed a pilot evaluation to determine if the addition of the AGI-5198 every 2 days was sufficient to reduce 2HG production in the SF10602 as compared to the vehicle, Dimethyl sulfoxide (DMSO). (**Fig 2.1B**) We observed a significant reduction of 2HG levels (**Fig. 2.1C**) in three mIDH1 GCCs SF10602, LC1035 and MGG119 following treatment with AGI-5198 or another mIDH1 inhibitor DS-1001b currently in phase II clinical trials (NCT04458272) as compared to the vehicle control DMSO. We performed RNA-seq analysis in triplicate and achieved ~55% aligned reads per sample considering we selected ribo-depletion to capture mature mRNAs and non-coding RNAs (**Table 2.2**). Inhibition of mIDH1 by AGI-5198 resulted in dynamic changes in transcriptional regulation (**Fig. 2.2**), where we observed 1,335 differentially expressed genes consisting of 498 upregulated and 839 downregulated genes based on a log2 fold-change (log_2FC) cut-off greater than ±0.6. We performed a gene set enrichment analysis (GSEA) of these differentially genes altered by mIDH1 inhibition to uncover pathways dependent upon mIDH1 reprogramming
(**Fig. 2.3**). Of the down-regulated gene ontologies (GO) associated with ZMYND8 were involved in transcription factor binding and cellular movement (**Fig. 2.4**). We observe an upregulation of GOs associated with replication (**Fig. 2.5**) specifically Replication Fork (GO:0005657), DNA Replication Initiation (GO:0006270) and Nuclear Replication Fork (GO:0043596). Many of the

genes shared across the replication associated GOs have roles in regulating replication stress facilitated by the stalling and restart of replication forks (**Fig. 2.5**). In addition, the genes that were upregulated following mIDH1 inhibitor treatment function as part of the core replisome or have been associated with responding to replicative stress. This data suggests that blocking 2HG production in mIDH1 GCCs using AGI-5198 induces replicative stress.

Epigenetic Changes following mIDH1 inhibition suggests activation of replicative stress

When cells divide, there must be a strict coordination between transcription and replication to ensure the maintenance of genomic stability. This tightly regulated process is disrupted in cancer cells as a result of oncogene activation (Petropoulos et al., 2019). The destabilization of replication forks or collision events between mediators of transcription and replication can generate DSB. To address replication stress, cells express proteins involved in cell cycle arrest, replication fork restart, and DNA repair to resolve damaged DNA regions (Petropoulos et al., 2019). In order to translate the elevated expression of replication stress genes to their regulation at the chromatin level, we performed chromatin immunoprecipitation and deep sequencing (ChIP-seq) for histone marks associated with active transcription (H3K4me3, H3K36me3), enhancers (H3K4me1, H3K27ac) and transcriptional repression (H3K27me3) in SF10602 in the presence of AGI-5198 (**Fig. 2.6**).

We focused on mediators of the HR pathway, we found ZMYND8 to one of the most significantly downregulated genes following the treatment of SF10602 with AGI-5198 (**Fig. 2.3**). The chromatin reader ZMYND8 has been shown to be recruited to DSB at actively transcribed regions (Gong et al., 2015). Depletion of ZMYND8 by siRNA or knockout impaired the recruitment of RAD51 foci at sites of DNA damage (Gong et al., 2015; Spruijt et al., 2016). We

observed a significant loss of the active histone mark H3K4me3 at three distinct regions (I, II, III) near the promoter of ZMYND8 following mIDH1 inhibition by AGI-5198 (**Fig. 2.7**).

To determine if the upregulation of ZMYND8 was dependent on mIDH1 expression, we assessed nascent transcription by bromouridine sequencing (Bru-seq) within our genetically engineered mouse glioma model comparing mouse tumor NS clones expressing either wtIDH1 (NPA) or mIDH1 (NPAI) (**Fig. 2.8A**). Mouse mIDH1 NS displayed an enhanced transcription rate for *ZMYND8* (1.27-fold), along with HR proteins mediators *RAD50* (1.78-fold), *FANCA* (1.63-fold) and *RAD51* (1.30-fold) compared to the wtIDH1 NS (**Fig. 2.8B**). To determine whether there were differences in the epigenetic regulation of ZMYND8 in the mIDH1 NS compared to wtIDH1 NS, we analyzed H3K4me3 enrichment at the ZMYND8 locus. We found five PePr differential enriched peaks (i-v) that showed significantly higher H3K4me3 enrichment corresponding to ZMYND8 promoter regions across the mIDH1 NS (NPAI C1, C2, C3) versus wtIDH1 NS (NPA C54A, C54B, C2) clones (**Fig. 2.9**). These findings suggest that mIDH1 epigenetically regulates ZMYND8 by increasing H3K4me3 deposition at the promoter leading to enhanced transcription.

Next, we investigated the epigenetic changes that occurred at genes associated with replication stress. We observed elevated H3K27ac deposition at the promoter regions of genes associated with replication following AGI-5198 treatment (**Fig. 2.10A**). The progression of replication forks is facilitated by the unwinding of DNA by the replisome, which is comprised of claspin (CLSPN) and Timeless (TIMELESS) and the tethering of DNA polymerase by proliferating cell nuclear antigen (PCNA) (Gaillard et al., 2015). Methyl methanesulfonate-sensitivity protein 22-like (MMS22L) functions in a complex with Tonsoku Like (TONSL), where it has been shown to be required for replication fork stability by binding newly incorporated histones and aiding in RAD51 loading (Saredi et al., 2016). The flap endonuclease 1 (FEN1)

resolves nicks in DNA that arise during replication (Tsutakawa et al., 2011). The DEAD/H-BOX Helicase 11 (DDX11) facilitates the progression of replication forks by unwinding G-quadraplexes (Cali et al., 2016). The endonuclease V (EXO5) supports replication fork restart and EXO5 expression is correlated with higher mutational burden in solid tumors (Hambarde et al., 2021). Three Prime Repair Exonuclease 1 (TREX1) degrades cytosolic DNA released from the nucleus as a result of chromosomally unstable cells (Mohr et al., 2021). These data suggest that mIDH1 inhibition enhances the activation of replication stress genes marked by elevated deposition of regulatory histone mark H3K27ac at the promoter regions.

When we examined the chromatin regions of genes downregulated with AGI-5198 treatment and were associated with replication, we observed loss of H3K36me3 deposition throughout the promoter and gene body (**Fig. 2.10B**). BTB Domain and CNC Homolog 1 (BACH1) has a role in activating ATR-dependent Chk1 phosphorylation (Gong et al., 2010). Egl-9 Family Hypoxia Inducible Factor 3 (EGLN3) drives ATR-mediated repair under hypoxic conditions (Xie et al., 2012). TP63 regulates transcription at tissue-specific enhancers and conditional ablation of p63 lead to apoptosis of adult neural precursors cells in postnatal mice (Cancino et al., 2015). These data suggest transcriptional suppression of proteins involved in ATR activation following mIDH1 inhibition.

Discussion

The characteristic heterozygous IDH1-R132H mutation produces an oncometablite 2-hydroxyglutarate (2HG) that impairs nuclear enzymes Jumonji-family of histone demethylases and TET2 methylcytosine dioxygenase inducing a IDH-specific hypermethylation phenotype (Turcan et al., 2018; Turcan et al., 2012). By reversing the epigenetic reprogramming elicited by IDH-mutations, we can elucidate how cellular pathways altered by mIDH1 support survival of tumor

cells following radiation. In this study, we sought out to uncover gene targets that displayed alterations in chromatin regulation and gene expression following mIDH1 inhibition, and in turn discern their contribution to radioresistance. We have previously demonstrated that murine tumor neurospheres (NS) harboring mIDH1^{R132H} mutation display differential enrichment of H3K4me3 methylation at genomic regions associated with master regulators of the DNA Damage Response (DDR) (Núñez Felipe et al., 2019).When we inhibited the DNA damage sensor ATM that initiates homologous recombination (HR) pathway or its downstream targets cell cycle checkpoint kinases 1 (Chk1) or 2 (Chk2), we observed enhanced radiosensitization of mIDH1-expressing GCCs. We also showed that pharmacological inhibition of mIDH1-R132H mutation in murine NS reduced mitotic cell proliferation and enhanced the release of Damage Associated Molecular Patterns (Kadiyala et al., 2021). Additionally, administering a mIDH1 specific inhibitor (AGI-5198) in combination with ionizing radiation (IR) to mIDH1 tumor-bearing mice promoted tumor regression and the development of immunological memory (Kadiyala et al., 2021).

We targeted mIDH1 using AGI-5198, which has been shown to decrease the production of 2HG and reverse histone hypermethylation (Rohle et al., 2013). Herein, we evaluated changes in gene expression and epigenetic regulation in a radioresistant mIDH1 patient derived GCC following mIDH1 inhibition. We identified the significant downregulation of the chromatin reader protein, Zinc Finger MYND-Type Containing 8 (ZMYND8, also referred to as RACK7 and PRKCBP1). The connection between ZMYND8 and DNA repair was proposed based on its recruitment to nuclear sites of laser induced DNA damage (Gong et al., 2015). The presence of a bromodomain (BRD)-containing motif encoded within ZMYND8, was shown to recognize acetylated lysine residues, specifically H3K14ac and H4K16ac that are present on post-translational modified (PTM) histones (Savitsky et al., 2016). Recent high resolution crystal

structure analysis of the ZMYND8 protein, explored the putative chromatin reader function of adjacent domains to bind specific histone marks. The plant homeodomain (PHD) recognizes singly methylated lysines (H3K4me1), while the hydrophobic Pro-Trp-Trp-Pro (PWWP) domain recognizes H3K36me2 (Savitsky et al., 2016). These effector domains support early findings that ZMYND8 accumulated at actively transcribed regions where double stranded breaks (DSB) occurred (Gong et al., 2015).

Given that mIDH1-R132H is endogenously expressed in SF10602 and was derived from a patient tumor subjected to radiotherapy, we sought to determine mIDH1-dependent mechanisms that contributed to radioresistance (Jones et al., 2020). We found that ZMYND8 was significantly downregulated following mIDH1 inhibition in the SF10602 treated with AGI-5198. Recent studies have reported that ZMYND8's recruitment to regions of laser-microirradation induced DNA damage is important to facilitate HR DNA repair (Gong et al., 2015; Gong et al., 2017; Spruijt et al., 2016). In doing so, ZMYND8 functions as a beacon to direct the NuRD complex to damaged DNA regions and allow for repression of transcription (Gong et al., 2015; Spruijt et al., 2016). The acetylated histone residues H3K14ac and H4K16ac, which are recognized by ZMYND8, have been shown to be crucial for DNA checkpoint activation and local HR repair of DSB (Horikoshi et al., 2019; Shen et al., 2016). Recent studies have demonstrated preferential vulnerability of mIDH1-expressing glioma models to inhibitors targeting HDAC, which is a component of the NuRD complex (Dow et al., 2021; Sears et al., 2021). Interestingly, mIDH1 glioma cells treated with Panobinostat displayed increased H3K14ac, which is recognized by ZMYND8 (Sears et al., 2021). Our current findings provide evidence that ZMYND8 is epigenetically regulated in human mIDH1 GCCs based on the loss of active histone mark H3K4me3 at the ZMYND8 promoter locus following mIDH1 inhibition. Additionally, our comparison of mouse mIDH1 NS vs. wtIDH1 NS

demonstrated that mouse mIDH1 NS had an enhanced enrichment of H3K4me3 at the ZMYND8 promoter locus by ChIP-seq and increased nascent transcription by Bru-seq. In the context of brain cancer, ZMYND8 has been shown to preferentially bind histone 3.3 point mutant G34R (H3.3G34R) present in pediatric high grade glioma to suppress genes involved in MHC II presentation (Jiao et al., 2020).

Materials and Methods

Cell Culture

Human SF10602 cells (Jones et al., 2020) were grown in NeuroCult NS-A Basal Medium supplemented with 100units/mL antibiotic-antimycotic, 10mL B-27 without vitamin A, 5mL N-2, 100µg/ml Normocin, 20ng/mL FGF, 20ng/mL EGF, and 20ng/mL PDGF-AA. Human MGG119 (Wakimoto et al., 2014) and LC1035 GCCs were grown in Neurobasal media supplemented with 100units/mL antibiotic-antimycotic,10mL B-27, N-2, 100µg/ml normocin, 20ng/mL FGF, 20ng/mL EGF, and 20ng/mL of PDGF-AA. Mouse mIDH1 NS were grown in DMEM-F12 media supplemented with 100units/mL antibiotic-antimycotic, B27, N2, 100µg/mL normocin, 10ng/mL FGF and 10ng/mL EGF. Stable generation of ZMYND8 KO glioma cells were maintained in culture with 10ug/mL puromycin. Glioma cells were dissociated using StemPro Accutase solution and passaged every 4 days for mouse NS and weekly for human glioma cells. Human glioma cells were shared through the following collaborations: Dr. Daniel Cahill laboratory, Harvard Medical School (MGG119) and Dr. Joseph Costello laboratory, UCSF (SF10602). LC1035 were generated in our laboratory through our collaboration with the University of Michigan's Department of Neurosurgery.

Detection of 2HG in conditioned media of mIDH1 GCC following mIDH1 inhibition

The conditioned media was collected from three human mIDH1 GCCs that were untreated, treated with either vehicle (DMSO) or mIDH1 inhibitor (AGI-5198, DS-1001b) for 1 week. Samples were stored at -80°C prior to assessment by liquid chromatography-mass spectrometry (LC-MS). Conditioned media (50 µL) was mixed with 10 µL of internal standard spike-in solution 10 µg/mL of 2-HG-D3 (Sigma-Aldrich) and was homogenized in 1 mL of 80% methanol in aqueous solution. The homogenate was centrifuged at 12000 rpm for 10 min at 4°C, and the supernatant was collected and dried under a stream of nitrogen at 37°C. The extracted sample was then combined with 160 µL of N-(p-toluenesulfonyl)-L-phenylalanyl chloride (TSPC, 2.5 mM in acetonitrile) and 2 µL of pyridine was added and incubated at 37°C for 20 min to derivatize D-2HG. After derivatization the mixture was dried with nitrogen at 37°C and reconstituted in 100 µL of 50% acetonitrile in aqueous solution. The samples were then centrifuged at 12000 RPM for 10 min and the supernatant was collected for quantification.

The quantification of 10µl of derivatized 2-HG was carried out using ultra performance (UP) UPLC-MS (Waters ACQUITY system). The mobile phase consisted of deionized water containing 0.1% formic acid (A) and acetonitrile/methanol (1:1, v/v) containing 0.1% formic acid (B). The gradient started from 70% A and maintained for 1 min, changed to 30% A over 3 min and maintained for 2 min, and finally changed back to 70% A over 0.5 min and held for 1.5 min. The flow rate was 0.5 mL/min, and column temperature was set at 40 °C. The analysis was performed on a Waters ACQUITY UPLC HSS T3 column (1.8 µm, 3.0 × 75 mm) with mass detection at 448.17 (-) for derivatized 2-HG, and at 451.19 (-) for derivatized 2-HG-D3. The 2HG concentration measurements presented in **Fig. 2.1B** can be found in **Table 2.1**.

RNA-sequencing (RNA-seq)

Bulk RNA-Sequencing was performed in collaboration with the University of Michigan (UM) Advanced Genomics Core (AGC), using the NovaSeq-6000 platform for 150-base paired-end reads. Total RNA was isolated from patient-derived mIDH1 GCC SF10602 untreated and AGI-5198-treated using the RNeasy Plus Mini Kit and 100ng of RNA was submitted to the UM AGC. RNA quality was assessed using the TapeStation, samples with an RIN (RNA Integrity Number) of 8 or greater were prepared using Illumina TruSeq mRNA Sample Prep Kit v2. cDNA Library preparation was performed by UM DSC using a ribo-depleted RNA protocol method. Results are from 3 technical replicates per condition; SF10602 untreated or treated with mIDH1 inhibitor AGI-5198 for 1 week. Information pertaining to the number of aligned reads utilized for our RNA-seq analysis can be found in Supplementary Table 1. RNA-Seq dataset generated in this study have been deposited at the NCBI's Gene Expression Omnibus (GEO) with identifier GSE220716.

Bromouridine tagged sequencing (Bru-seq) for nascent RNA expression

These techniques were performed as described previously (*Paulsen et al. 2014*). Briefly, nascent RNA labelling was performed for 30 min at 37°C with 2 mM 5-bromouridine (Sigma-Aldrich, 850187) in conditioned medium. For the BruChase-seq analysis, the bromouridine-containing medium was removed after labelling for 30 min, the plates were rinsed twice in PBS, and then conditioned medium containing 20 mM uridine (Roche, 11934554001) was added. The cells were then incubated for 6 hours at 37°C. At the completion of labelling with or without chase, the cells were lysed in TRIzol (Thermo Fisher Scientific, 15596018), and the Bru-labeled RNA was captured with anti-BrdU antibodies (BD Biosciences, Cat# 555627) conjugated to magnetic beads (Dynabeads goat anti-mouse IgG, Thermo Fisher Scientific, Cat# 11033). The isolated RNA was converted into cDNA libraries and prepared for sequencing using the Illumina TruSeq RNA

Library Preparation Kit v2 (Illumina, RS-122-2001) followed by deep sequencing to around 50 million single-end 50 nucleotide reads.

Bru-seq data analysis

Bioinformatics and data analysis pipeline was implemented using the q pipeline manager (http://sourceforge.net/projects/qppln-mngr/). The bioinformatics programs used, read mapping, genome annotation, and expression scoring were previously described (*Paulsen et al. 2014*) in section 2.4. (Paulsen et al., 2014) Reads per kilobase per million mapped reads (RPKM) values were calculated for individual genes that were at least 300 bp long. For genes with lengths of 30 kb and less, RPKM values were calculated using read counts from the entire gene. For genes longer than 30 kb, an RPKM value was calculated using read counts from the first 30 kb downstream of the TSS. The R package DESeq35 was used to test differential expression of genes where the mean RPKM between samples was greater than 0.5. Significant changes in transcription initiation were defined as follows: adjusted p-values < 0.05; fold change < 1.5.

Bioinformatics analysis of RNA-seq for differential expression

Illumina NovaSeq read files were downloaded to the Sequencing Core storage and concatenated into a single fastq file for each sample. In collaboration with the UM Bioinformatics Core, we checked the quality of the raw reads data for each sample using FastQC (version v0.11.3) to identify features within the data that may indicate quality issues (e.g. low quality scores, over-represented sequences, inappropriate GC content). We aligned reads to the reference genome (UCSC hg19) using Bowtie 2 (RRID:SCR_016368). Expression quantitation was performed with HTSeq (RRID:SCR_005514), set to count non-ambiguously mapped reads only. Data were pre-filtered to remove genes with 0 counts in all samples. Normalization and differential expression

was performed with DESeq (RRID:SCR_000154) which uses a negative binomial generalized linear model. Resultant p-values were corrected for multiple hypotheses using the Benjamini-Hochberg False Discovery Rate (FDR). Genes and transcripts were identified as differentially expressed based on FDR ≤ 0.05, and fold change $\geq \pm 1.5$. The volcano plot was produced using an R base package and encompasses all genes identified by our RNA-seq analysis.

GSEA Enrichment Map and Gene Ontology (GO) Analysis

All 1335 differentially expressed genes between SF10602 treated with AGI-5198 (mIDH1 specific inhibitor) vs. untreated SF10602 were exported to a table with their gene names in the first column and log2-fold change values in the second column, sorted to produce gene ranks. The rank file was used as input to the GSEA (Gene Set Enrichment Analysis), downloaded from the Broad Institute (http://www.gsea-msigdb.org/gsea/login.jsp) (SeqGSEA, RRID:SCR_005724). The Broad Institute MSigDB includes the complete Gene Ontology (GO) (c5.all.v7.5.1.symbols.gmt), which we used as the input Knowledgebase. GSEA was run with 2000 permutations and gene set size range restricted to between 0 and 200 genes. An enrichment map was generated using the Cytoscape Platform (v3.9.1), which requires the rank and gmt file along with the positive/negative GSEA results. Each circle represents an individual GO term, and the size of the circle represents the number of genes within that set. The color of the circle signifies the directionality of expression in the mIDH1 inhibitor treated (AGI-5198) compared to untreated, where red is upregulated in AGI-5198-treated compared to untreated while blue is downregulated. We included all differentially enriched GO pathways that had a p-value<0.01 and FDR<0.05 as shown in Supplementary Figure S1. The enrichment score plots for Replication Fork, DNA Replication Initiation and Nuclear Replication Fork are shown in Figure 1E, which are images provides in the GSEA Pre-ranking report.

Chromatin immunoprecipitation and deep sequencing (ChIP-seq)

SF10602 were cultured in the presence of 5μM AGI-5198 (mIDH1 inhibitor) or the vehicle (DMSO) for 10 days prior to isolation for chromatin immunoprecipitation (ChIP). Modifications to laboratory native ChIP-seq protocol as previously described previously (Mendez et al., 2018; Núñez Felipe et al., 2019) were as follows: 1.) increased cell number per histone mark IP from $1x10^6$ to $3x10^6$, 2.) increased histone mark antibody concentration to 2μg, 3.) extended Dynabead A/G incubation to 6hrs, and 4.) doubled Dynabead A/G concentration. ChIP-Seq dataset generated in this study have been deposited at the NCBI's Gene Expression Omnibus (GEO) with identifier GSE220715.

Data Availability

There are no limitations on data availability. The ChIP-Seq dataset generated in this study can be acquired through NCBI's Gene Expression Omnibus (GEO) with identifier GSE220715. The RNA-Seq dataset generated in this study can be acquired through NCBI's Gene Expression Omnibus (GEO) with identifier GSE220716. All other data generated within this study are available via the supplementary data files; cells and plasmids will be freely distributed upon request from the corresponding author, Maria G Castro.

Figures

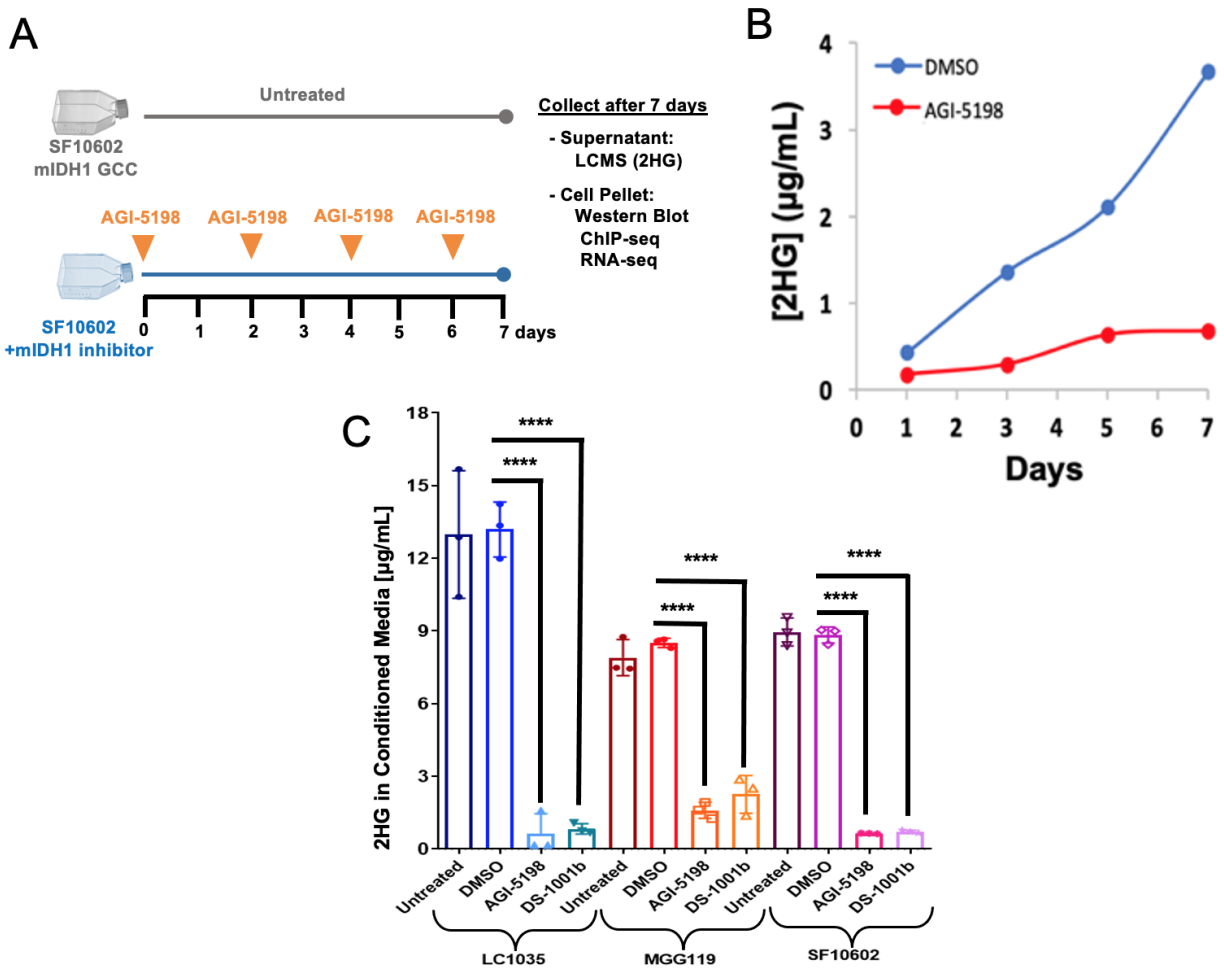

Figure 2.1 Pharmacological inhibition of mIDH1^{R132H}-expressing human glioma cell cultures with either AGI-5198 or DS-1001b blocks the production of 2-hydroxyglutarate (2HG)

(A) Experimental schematic of downstream analyses comparing untreated SF10602 human glioma cell culture (GCC) that endogenously express the R132H mutation in isocitrate dehydrogenase 1 (mIDH1) with cells treated with 5µM AGI-5198 (a mIDH1 specific inhibitor). After 1 week, the supernatant was collected for liquid chromatogram and mass spectrometry (LCMS) and cell pellet was utilized for transcriptomic (RNA-sequencing), epigenomic (ChIP-sequencing) and protein (Western blot) analysis. (B) Pilot study to evaluate the levels of 2HG by LCMS over time in the condition media of SF10602 treated with vehicle DMSO (blue) or AGI-5198 (red). (C) Representative histogram displays the liquid chromatography and mass spectrometry (LC/MS) measurement in microgram per microliter (µg/mL) of 2-hydroxyglutarate (2HG), an oncometabilite produced by mIDH1, present within the conditioned media of three patient-derived mIDH1 GCCs [LC1035, MGG119 and SF10602]. Samples were collected from untreated, vehicle treated (DMSO), mIDH1 inhibitor (AGI-5198, competitive) or mIDH1 inhibitor in phase II (DS-1001b, allosteric). Errors bars represent standard error of mean (SEM) from independent biological replicates (n=3). **** $P < 0.0001$; unpaired t test.

Table 2.1 Liquid chromatography and mass spectrometry (LC-MS) measurements of 2HG in the conditioned media of mIDH1 glioma cell cultures (GCCs) untreated (DMSO) or treated with mIDH1 inhibitors (AGI-5198 or DS-1001b)

Sample No.	Description	peak 2-HG	peak IS	peak ratio	2HG concentration in media (μg/mL)
1	LC1035 untreated	84082	18402	4.569	10.412
2	LC1035 untreated	98294	14207	6.919	15.681
3	LC1035 untreated	102169	18033	5.666	12.871
4	LC1035 DMSO	98077	16669	5.884	13.360
5	LC1035 DMSO	93593	14914	6.276	14.239
6	LC1035 DMSO	101767	19314	5.269	11.982
7	LC1035 AGI-5198	5327	8415	0.633	1.586
8	LC1035 AGI-5198	0	3190	0.000	Not detected
9	LC1035 AGI-5198	0	4771	0.000	Not detected
10	LC1035 DS1001b	2855	7035	0.406	1.076
11	LC1035 DS1001b	1293	5047	0.256	0.741
12	LC1035 DS1001b	1583	6898	0.229	0.681
13	MGG119 untreated	74182	22734	3.263	7.483
14	MGG119 untreated	71517	22027	3.247	7.447
15	MGG119 untreated	76175	19877	3.832	8.760
16	MGG119 DMSO	85330	22540	3.786	8.655
17	MGG119 DMSO	78987	21778	3.627	8.299
18	MGG119 DMSO	87528	23313	3.754	8.585
19	MGG119 AGI-5198	6987	14282	0.489	1.263
20	MGG119 AGI-5198	9609	12208	0.787	1.931
21	MGG119 AGI-5198	11453	17832	0.642	1.607
22	MGG119 DS1001b	4744	8727	0.544	1.385
23	MGG119 DS1001b	26212	21626	1.212	2.884
24	MGG119 DS1001b	20024	19133	1.047	2.513
25	SF10602 untreated	139089	33203	4.189	9.560
26	SF10602 untreated	154172	39452	3.908	8.929
27	SF10602 untreated	151356	41217	3.672	8.401
28	SF10602 DMSO	162124	41125	3.942	9.006
29	SF10602 DMSO	151718	38309	3.960	9.047
30	SF10602 DMSO	146837	39775	3.692	8.445
31	SF10602 AGI-5198	8477	41397	0.205	0.626
32	SF10602 AGI-5198	9937	45339	0.219	0.658
33	SF10602 AGI-5198	9403	43612	0.216	0.650
34	SF10602 DS1001b	8181	36855	0.222	0.664
35	SF10602 DS1001b	12106	44059	0.275	0.783
36	SF10602 DS1001b	10549	43158	0.244	0.714
37	plain media (MGG119/LC1035) media	0	7851	0	Not detected
38	plain media (SF10602 media)	0	7984	0	Not detected

Table 2.2 RNA sequencing performed on ribo-depleted total RNA samples to capture mature RNAs and non-coding RNAs

Sample ID	Description	Number of fragments (2 reads per side)	Number of aligned reads	Percent reads aligned	aligned reads percent duplicates	aligned reads not multi- mapped or discordant
Sample_130939	Untreated SF10602 rep1	54,467,387	60,255,501	55	25.18	27,582,011
Sample_130940	Untreated SF10602 rep2	49,159,298	48,925,554	50	23.68	22,431,351
Sample_130941	Untreated SF10602 rep3	51,769,590	58,220,882	56	25.39	26,813,994
Sample_130942	Mutant IDH1 inhibitor rep1	49,790,214	53,857,970	54	25.23	24,706,207
Sample_130943	Mutant IDH1 inhibitor rep2	52,332,347	58,386,172	56	25.92	26,662,389
Sample_130944	Mutant IDH1 inhibitor rep3	41,863,074	48,099,917	57	24.67	21,962,991

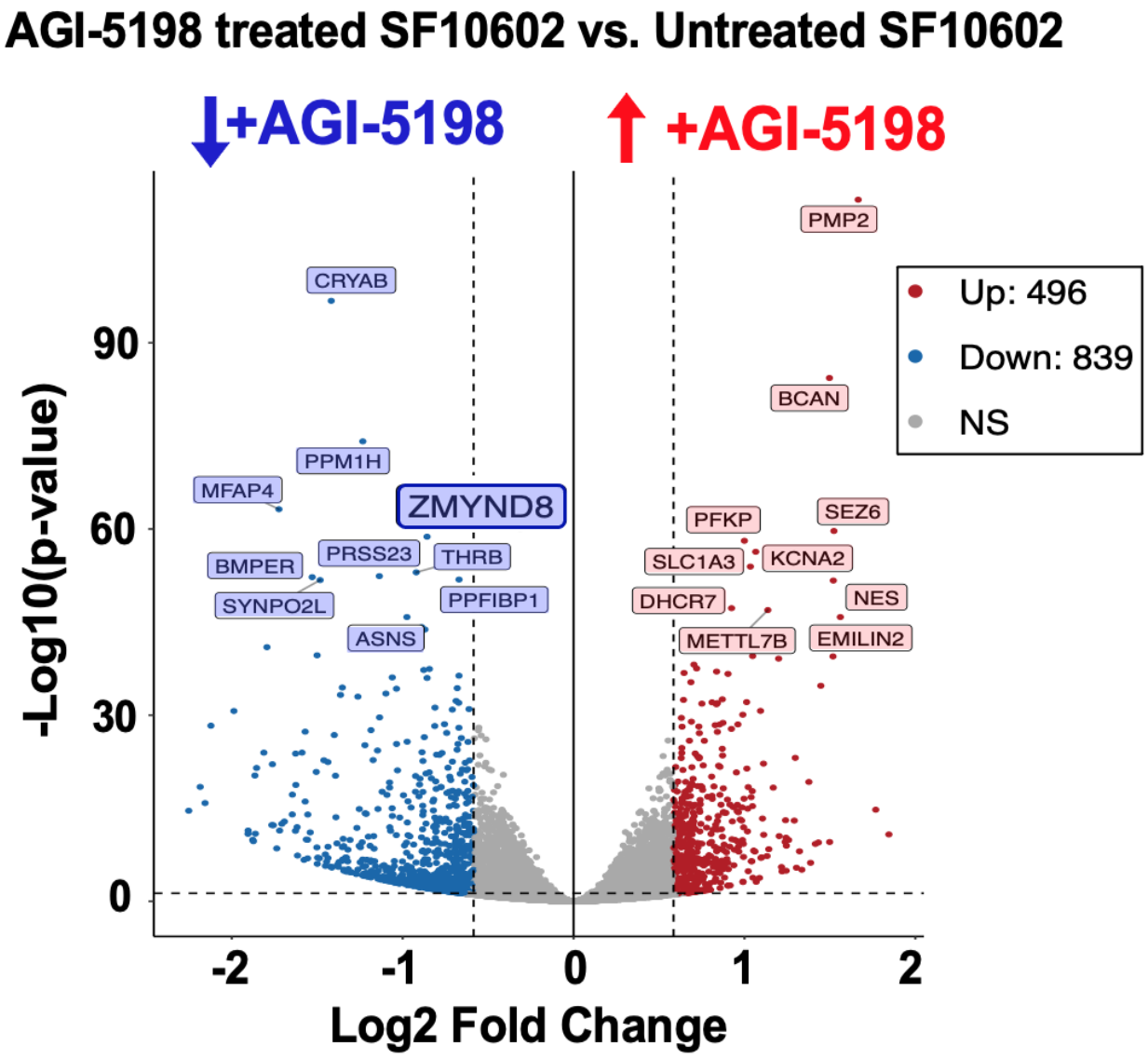

Figure 2.2 Differential gene expression analysis from SF10602 treated with AGI-5198 vs. untreated SF10602

Volcano plot of differentially expressed genes (DEG) based on RNA-seq analysis comparing AGI-5198 treated SF10602 vs. untreated. The x-axis represents that log2-fold change in gene expression of SF10602 treated with AGI-5198 relative to untreated and the y-axis represents the significance of that change based on the inverse log10 of the p-value. Each dot represents a individual gene. Genes found to be downregulated in AGI-5198 treated mIDH1 GCCs vs. untreated are shown in blue, up-regulated in red, or no statistically significant (NS) difference in grey.

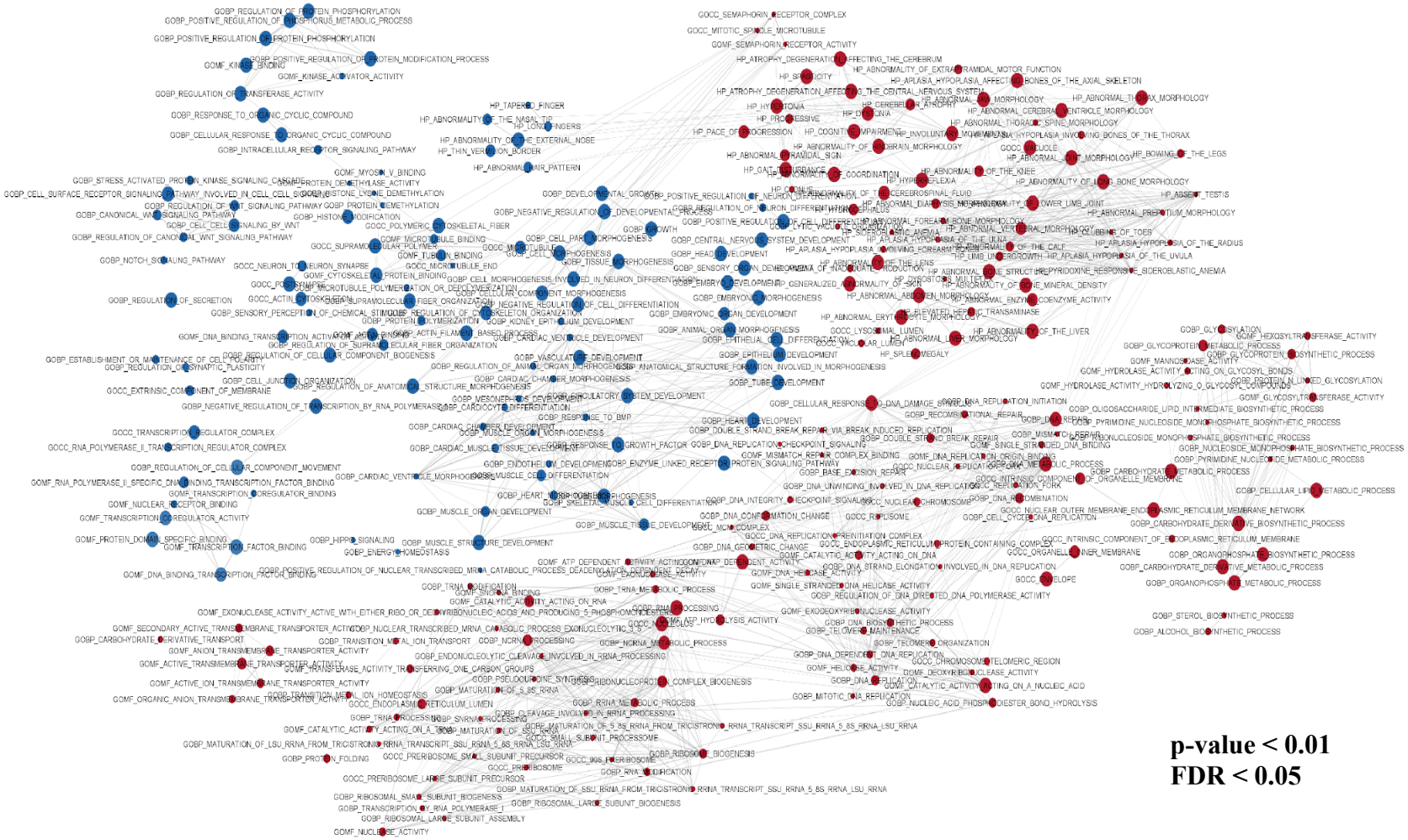

Figure 2.3 Cytoscape enrichment map of gene ontologies (GO) differential enriched in SF10602 treated with AGI-5198 vs. untreated.

GSEA pathway analysis of DEGs in AGI-5198 treated mIDH1 GCC SF10602 vs untreated. Circles represent distinct GOs and their sizes reflect the number of enriched genes within a GO. The cut-off used for defining DEG was log 2-fold change (Log2C)>±0.6, p-value<0.01, false discovery rate (FDR)<0.05. Related GOs are linked by edges in gray for shared genes that have function within multiple pathways. The node color refers to the statistically significant DE genes in AGI-5198 treated vs untreated SF10602 where upregulated GOs are shown in red and downregulated GOs are shown in blue. Image was generated using Enrichment Map Plug-in on Cytoscape 3.9.1.

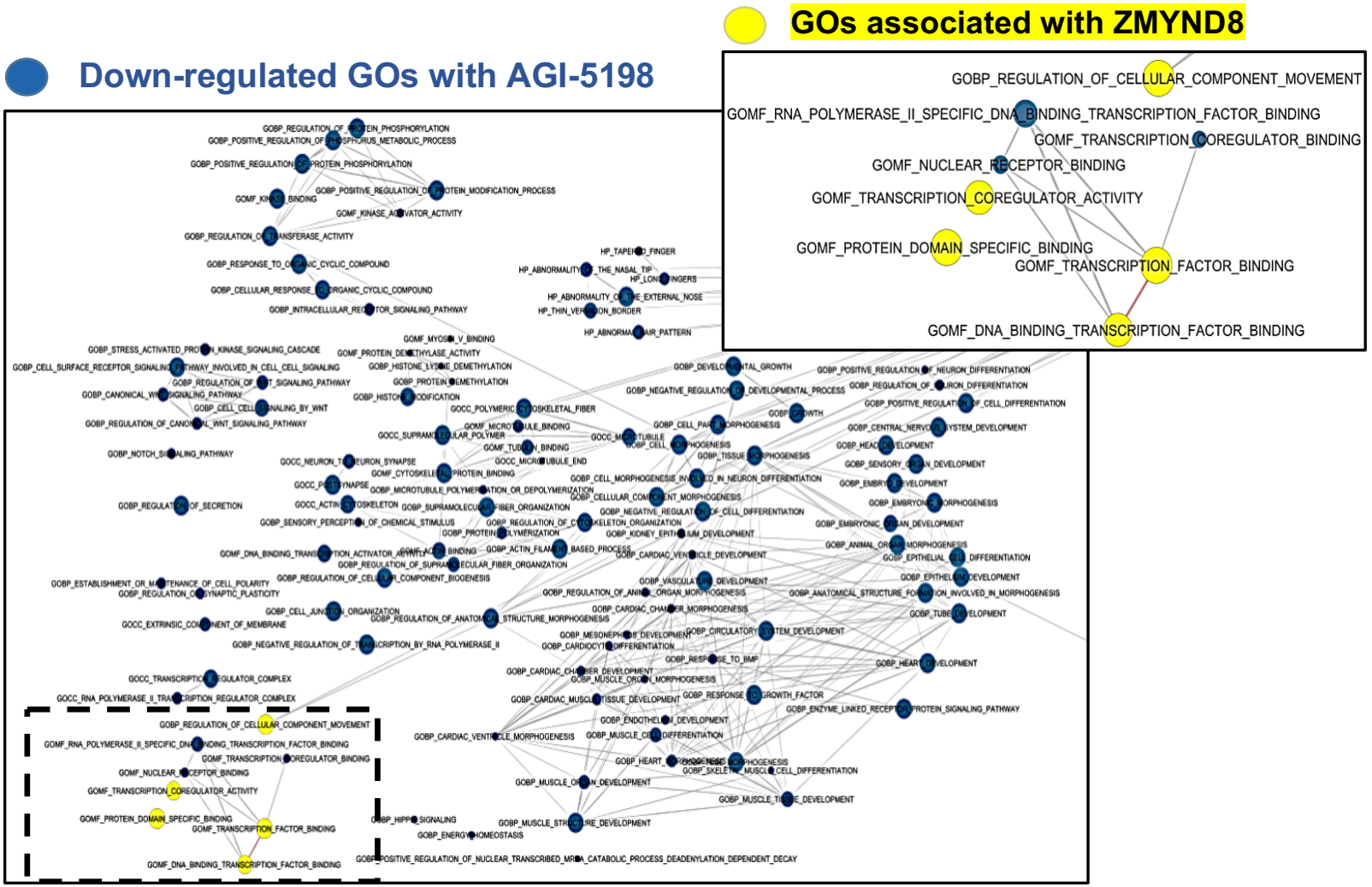

Figure 2.4 Downregulated GOs following mIDH1 inhibition in SF10602 treated with AGI-5198, highlighting ZMYND8 associated GOs

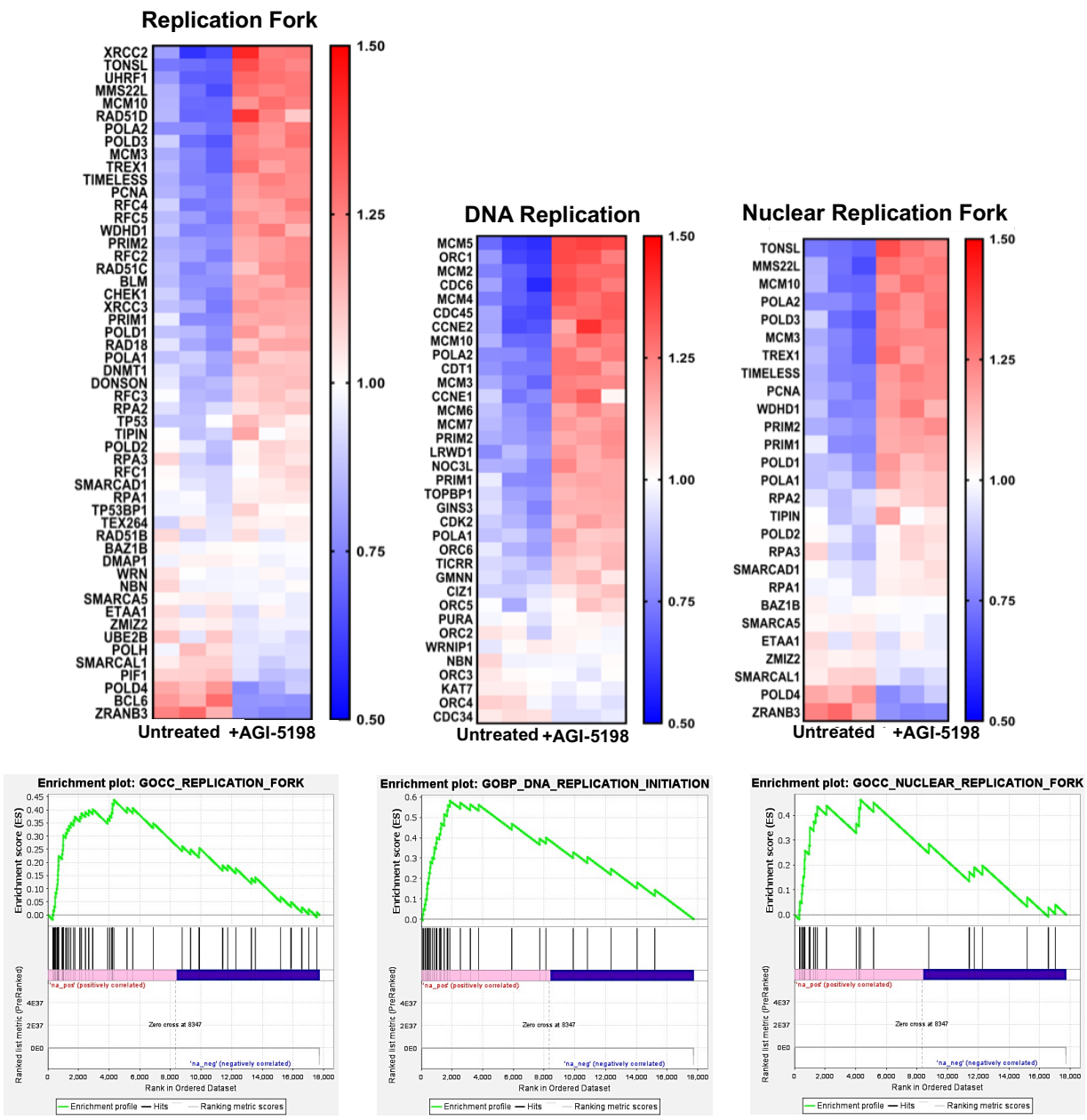

Figure 2.5 Heatmap of upregulated Gene Ontologies associated with replication found to be upregulated with AGI-5198 treatment and the corresponding genes

Heatmap depicting the relevant GOs related to DNA replication initiation and replication forks that were upregulated in AGI-5198 treated GCCs compared to untreated. The corresponding GSEA enrichment plot is adjacent, where the green line represents the enrichment score for a given GO as the analysis proceeds along the rank list of DEG.

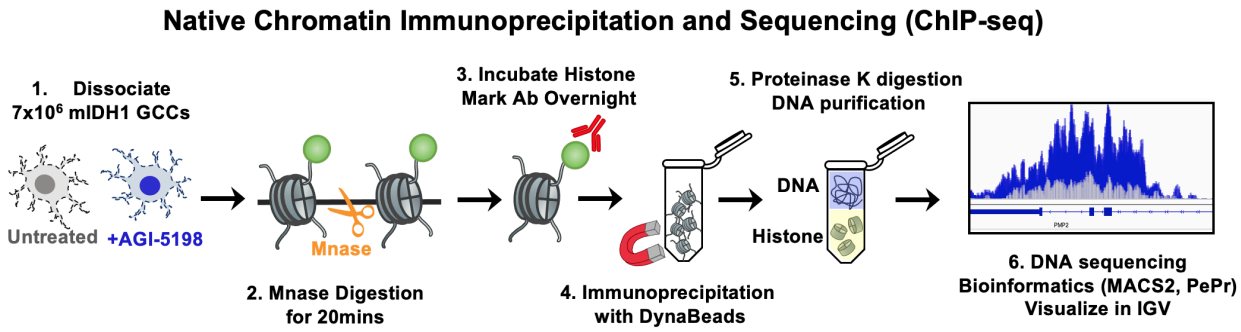

Figure 2.6 Workflow for native chromatin immunoprecipitation and sequencing (ChIP-seq) to profile genome wide changes to histone mark modification after mIDH1 inhibition

SF10602 were cultured as untreated or treated with AGI-5198 (mIDH1 inhibitor) for 1 week, then the mIDH1 GCCs were dissociated with StemPro accutase for 5mins and then 7 million cells were isolated for chromatin immunopreciptation. The cell suspension was incubated for 20 minutes with Micrococcal nuclease (Mnase) to digest unbound DNA and generate mononucleosomes. Chromatin suspension was incubated overnight with histone mark specific antibodies in separated aliquots (H3K4me1, H3K4me3, H3K27ac, H3K27me3, and H3K36me3). The next day, samples were washed then incubated for 3-4 hours with Dynabeads to concentrate histone marked chromatin. These samples were then digested with proteinase K at 55ºC to degrade histone protein and release DNA into solution. DNA was purified using Qiagen kit and then submitted for DNA sequencing. Data analysis was performed using MACS2 and PePr to create bigwig files that could be visualized on the Integrative Genome Viewer (IGV).

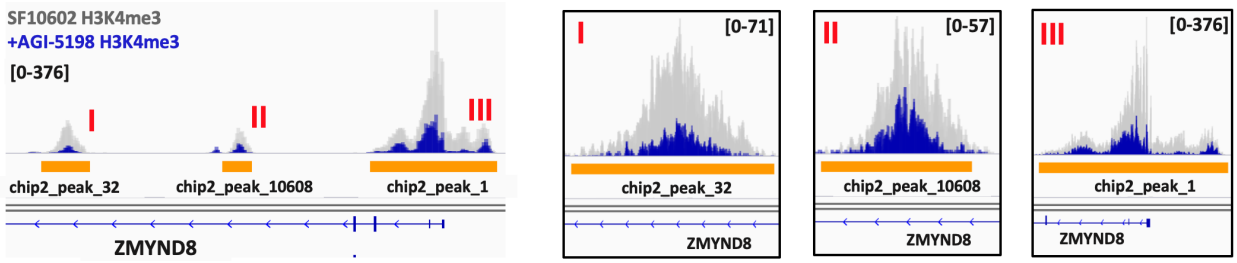

Figure 2.7 Reduction in histone 3 lysine 4 trimethylation (H3K4me3) deposition at the ZMYND8 locus when mIDH1 is inhibited by AGI-5198 in human GCC SF10602

Integrative Genomics Viewer (IGV) image displays overlapping tracks comparing the H3K4me3 occupancy in specific genomic regions near the ZMYND8 promoter in untreated SF10602 (grey, two replicates) and AGI-5198 treated (dark blue, two replicates). The y-axis represents the number of immunoprecipitated fragments for a given histone mark normalized to the total number of reads per sample and mapped to the human genome reference (hg19) along the x-axis. Regions that display significant changes in histone mark deposition based on peak-calling prioritization pipeline (PePr) comparison between SF10602 untreated vs. AGI-5198 treated SF10602 are represented by orange bars and red roman numerals signify distinct regions that are expanded to the right.

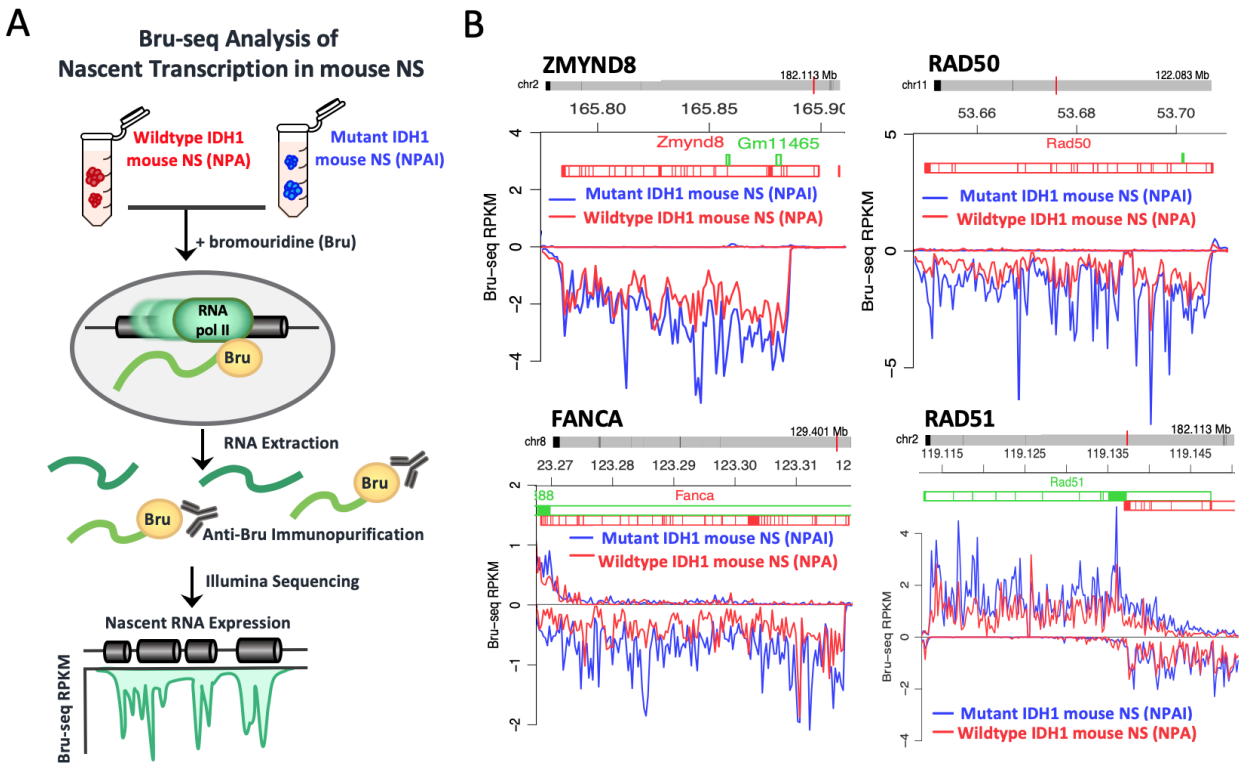

Figure 2.8 Bromouridine sequencing (Bru-seq) quantification of nascent RNA expression of ZMYND8 and other homologous recombination (HR) repair protein in mutant IDH1 vs. wildtype IDH1 mouse glioma model

(A) Diagram of Bru-seq assay to quantify the rate of nascent transcription in reads per kilobase of transcript per million reads mapped (RPKM) based on bromouridine labelled RNAs comparing wtIDH1 (red) vs. mIDH1 mouse NS (blue). (B) Bru-seq traces show differential transcriptional rates (<1.2fold ; P <0.05) of DNA repair genes ZMYND8, RAD50, FANCA and RAD51 in mIDH1 (blue, n=12) compared to wtIDH1 NS (red, n=3).

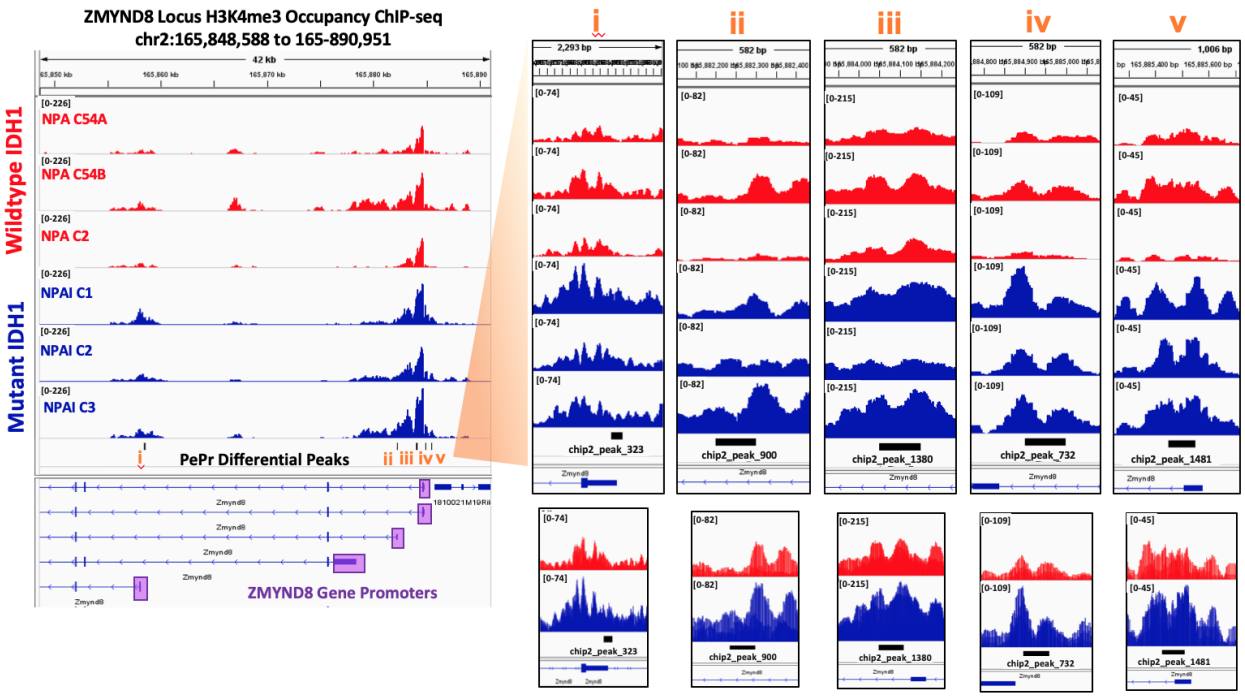

Figure 2.9 Enhanced H3K4me3 deposition at ZMYND8 promoters in mouse neurospheres expressing mIDH1 (NPA1) vs. wtIDH1 (NPA)

Integrative Genome Viewer (IGV) image displays ChIP-seq tracks of H3K4me3 enrichment at the ZMYND8 promoter region in wtIDH1 NS vs. mIDH1 NS. Differential enriched peaks (i-v, black bars) in mIDH1 NS vs wtIDH1 are displayed as separated tracks, while overlapped tracks are shown below. (n = 3 biological replicates per group).

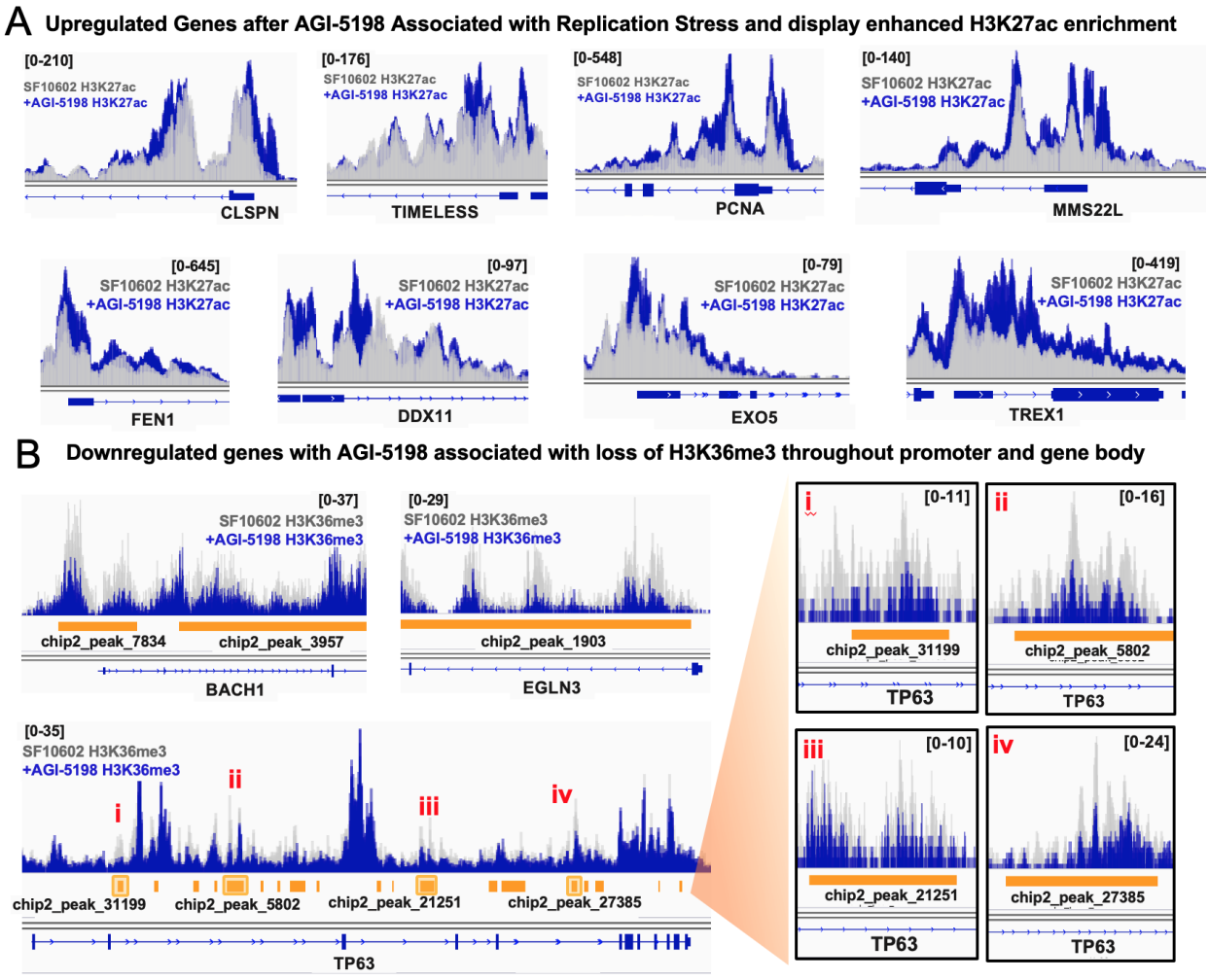

Figure 2.10 Replication stress associated genes upregulated with mIDH1 inhibition display enhanced H3K27ac at the promoter region, while histone mark H3K36me3 was reduced in enrichment in genes downregulated by mIDH1 inhibition associated with ATR mediated repair

(**A**) IGV screenshots of H3K27ac deposition at the promoters of specific genes associated with replication stress. (**B**) IGV screenshots of H3K36me3 deposition throughout the promoter and gene body, where select regions that lost H3K36me3 deposition by PePr calling at TP63 locus are indicated by yellow squares.

Chapter 3 ZMYND8 Regulation and Targeting in MIDH1 Patient Derived GCCs and Mouse NS

Introduction

Radioresistance mechanisms contributing to tumor recurrence in IDH1-mutant glioma have focused on mutational differences between the primary vs. recurrent tumors. Our laboratory has demonstrated that mIDH1 inhibition sensitizes mIDH1 GCCs to radiation. We previously showed that the homologous recombination (HR) pathway is rewired in mIDH1 glioma cell cultures through the enhanced active histone mark H3K4me3 deposition at the promoters of DNA repair proteins, which we showed to be mediated by mIDH1 reprogramming (Núñez Felipe et al., 2019). This supports the survival of mIDH1 glioma following radiotherapy. Pharmacological inhibition of either ATM (KU60019) or Chk1/2 (AZD7762) DNA repair regulators improves overall survival of mIDH1 tumor bearing mice. Herein we target the chromatin reader protein ZMYND8, whose expression was shown to be significantly suppressed by mIDH1 inhibition. ZMYND8 has roles in HR mediated DNA repair, where it is recruited to regions of laser microirradiation and facilitates transcriptional silencing at these areas of DNA damage. Utilizing shRNA knockdown or lentiviral CRISPR knockout (KO) of ZMYND8, we observed a reduction in cellular viability of mIDH1 GCCs to IR. We observed that DDR proteins were elevated after IR in the ZMYND8 KO compared to ZMYND8 WT. We believe that the loss of ZMYND8 potentially cause the cells to acquire more DNA damage through their reduced ability to recognize regions of DNA damage or facilitate the repair of IR-induced damage.

Results

Inhibiting mIDH1 suppresses expression of ZMYND8

Epigenetic regulation of a gene is defined by the patterns of specific histone modifications at the genomic locus and correlates with chromatin accessibility and gene expression. H3K4me3 is enriched at sites of poised and actively transcribed regions, which highlights the activity of genes that govern cell-specific networks. We sought to determine if the significant reduction of H3K4me3 at the ZMYND8 promoter following AGI-5198 treatment in the SF10602 would lead to a decrease in protein expression. We included two additional human mIDH1 GCCs (MGG119, LC1035) to evaluate if the inhibition of mIDH1 lead to a decrease in ZMYND8 gene expression across mIDH1 GCCs derived from separate patients. We performed western blotting (WB) for ZMYND8 in three human mIDH1 GCCs treated with AGI-5198 (**Fig. 3.1A**). We observed a significant reduction of ZMYND8 protein expression in the MGG119 ($p<0.0001$), SF10602 ($p<0.0001$) and LC1035 ($p<0.0001$) following AGI-5198 treatment (**Fig. 3.1B**). To confirm that this modulation of ZMYND8 protein expression was consistent with mIDH1 inhibition, we treated the human mIDH1 GCCs with DS-1001b (**Fig. 3.1C**). We observed a significant reduction of ZMYND8 expression in the MGG119 ($p < 0.05$), SF10602 ($p < 0.0001$) and LC1035 ($p < 0.01$) after DS-1001b treatment (**Fig. 3.1D**). Considering that western blots are representative of the bulk sample, we performed immunohistochemistry for ZMYND8 on paraffin-embedded human mIDH1 NS pre-treated with AGI-5198. This allowed us to determine the impact of mIDH1 inhibition on ZMYND8 expression at the individual cell level (**Fig. 3.2A**). We observed a significant reduction in the percentage of ZMYND8 positive nuclei in the SF10602 ($p< 0.001$) and LC1035 ($p < 0.0001$) pre-treated with AGI-5198 compared the DMSO treated (**Fig. 3.2B**). We analyzed the nuclear IHC staining of ZMYND8 using Quantitative Pathology & Bioimage

Analysis (QuPath) to define the number of ZMYND8 positive cells per frame (**Fig. 3.3A**). Pre-treatment of LC1035 with DS-1001b prompted a similar reduction in the percentage of ZMYND8 positive nuclei (**Fig. 3.3B**). These data demonstrate that mIDH1 epigenetically regulates ZMYND8 protein expression, which is suppressed by mIDH1 inhibition.

Inhibition of mIDH1 promotes the expression of replication stress proteins shown to be upregulated in IDH-wildtype GCCs compared to IDH-mutant GCCs

The reproducible reduction of ZMYND8 protein expression following mIDH1 inhibition led us to explore whether the decrease in ZMYND8 coincided with changes in proteins involved in replication stress (**Fig. 3.4**). To address this, we collected protein from SF10602 that were untreated, treated with vehicle (DMSO) or 5μM AGI-5198 every 2 days for 1 week. First, we investigated the protein expression of TREX1, an exonuclease that sequesters ssDNA fragments generated from aberrant replication and has been shown to be recruited to stalled replication forks (**Fig. 3.4A**) (Yang et al., 2007). We observed a significant increase in TREX1 protein expression in SF10602 treated with AGI-5198 when compared to DMSO treated cells ($p < 0.05$) (**Fig. 3.4B**). Next, we evaluated the expression of PCNA and TIMELESS, which are known to be co-expressed during S phase (**Fig. 3.4C**) (Yoshizawa-Sugata & Masai, 2007). We observed a significant increase in PCNA protein expression in SF10602 treated with AGI-5198 ($p < 0.01$) compared to untreated cells, and a modest increase ($p < 0.05$) in DMSO-treated cells (**Fig. 3.4D**). Similarly, we found TIMELESS to be significantly increased following AGI-5198 treatment ($p < 0.001$) compared to untreated SF10602. In order to maintain the structural stability of stalled replication forks, Timeless forms a complex with Tipin to prevent the disassembly of the replisome (Yoshizawa-Sugata & Masai, 2007). These findings suggest that mIDH1 inhibition induces genomic instability mediated by an increase in replication stress protein expression.

These findings were also confirmed in mIDH1 MGG119 GCCs that were untreated, treated with vehicle (DMSO), or 5μM AGI-5198 every 2 days for 1 week. Protein was extracted and the expression of PCNA and TIMELESS was determined using western blot analysis (**Fig. 3.5**). We observed a significant increase in PCNA protein expression in MGG119 cells treated with AGI-5198 compared to DMSO-treated cells ($p < 0.0001$) (**Fig 3.5A-B**). We observed a significant increase in TIMELESS protein expression in MGG119 treated with AGI-5198 compared to DMSO-treated cells ($p < 0.01$) (**Fig. 3.5C-D**).

We further validated our findings using both wt-IDH1 mouse NS and mIDH1 mouse NS. Protein was extracted and the expression of ZMYND8, TREX1, PCNA, and TIMELESS was determined using western blot analysis (**Fig. 3.6**). We observed a significant decrease in ZMYND8 protein expression in wt-IDH1 mouse NS ($p < 0.0001$) compared to mIDH1 mouse NS (**Fig. 3.6A-B**). We observed a significant increase in TREX1 protein expression in wt-IDH1 mouse NS ($p < 0.0001$) compared to mIDH1 mouse NS (**Fig. 3.6C-D**). Furthermore, we observed a significant increase in both PCNA ($p < 0.0001$) and TIMELESS ($p < 0.01$) protein expression in wt-IDH1 mouse NS compared to mIDH1 mouse NS (**Fig. 3.6E-H**).

Suppression of ZMYND8 by shRNA or CRISPRCas9 mediated genetic knockout (KO) enhances the radiosensitivity of mIDH1 GCCs

Based on the role of ZMYND8 in transcriptional repression at sites of DSB, we hypothesized that it might promote resistance to IR-induced DNA damage in mIDH1 GCCs. We began by targeting the human and mouse isoforms of ZMYND8 using short-hairpin (shRNA) knockdown that we cloned into our pT2-plasmid backbone (**Fig. 3.7**) (Calinescu et al., 2015; Koschmann et al., 2016). The oligonucleotide sequences that contributed to the greatest reduction in total protein ZMYND8 expression have the for shRNA region marked in red (**Table 3.1**). To

confirm that the pT2-shZMYND8-GFP plasmids we designed could reduce ZMYND8 protein expression, we transfected HEK293 cells with pT2-shZMYND8-GFP plasmids targeting the human gene and NIH-3T3 cells for the mouse isoform in combination with the sleeping beauty transposase (SB) plasmid to improve the integration efficiency. We performed WB analysis 3 days post-transfection and observed a reduction in ZMYND8 expression in HEK293 transfected with human sh2-ZMYND8 and mouse sh4-ZMYND8 plasmids in NIH3T3 (**Fig. 3.8**).

Next, we generated stable ZMYND8 shRNA knockdown clones in two mIDH1 GCCs, SF10602 and MGG119. (**Fig 3.9A**). After purifying the GFP+ population by flow cytometry, we assessed ZMYND8 protein expression by WB in the MGG119 and SF10602 (**Fig 3.9B-C**). We observed a significant reduction of ZMYND8 protein expression by 75% in the MGG119 and 60% in the SF10602 compared to non-transfected (**Fig 3.9D-E**). Survival of mIDH1 GCCs expressing the shZMYND8-GFP plasmids was assessed 3 days post-irradiation exposure. MGG119 expressing the shZMYND8-GFP plasmids showed reduced cellular viability in response to escalating doses of radiation with a half maximal inhibitory concentration (IC_{50}) of 9.5Gy (**Fig 3.9F**). SF10602 expressing shZMYND8-GFP plasmids displayed a significant reduction in cellular viability but a IC_{50} was not reached at single radiation doses up to 20Gy (**Fig 3.9G**). These data suggest that suppression of ZMYND8 expression in mIDH1 GCC enhances their susceptibility to ionizing radiation.

Next, we ablated the expression of ZMYND8 using lentiviral CRISPRv2 vector expressing Cas9 and ZMYND8 guide RNAs (sgRNA) to generate ZMYND8 KO mIDH1 GCC clones (**Fig. 3.10A**) (Wang et al., 2021). After lentiviral incubation and puromycin selection, loss of ZMYND8 was evaluated by WB in the SF10602, MGG119 and NPAI mouse mIDH1 NS (**Fig. 3.10B, 3.10C, and 3.10D respectively**). We observed a significant reduction in cellular viability 3 days post-IR

in the ZMYND8 KO compared to ZMYND8 WT mIDH1 GCCs. The SF10602 ZMYND8 KO had an IC_{50} of 7.5Gy compared to SF10602 ZMYND8 WT where an IC_{50} was not reached (**Fig. 3.10E**). The MGG119 ZMYND8 KO had an IC_{50} of 16.8Gy compared to MGG119 ZMYND8 WT where an IC_{50} was not reached (**Fig. 3.10F**). The NPAI ZMYND8 KO exhibited an IC_{50} of 2.8Gy versus the NPAI ZMYND8 WT where an IC_{50} was not reached. (**Fig. 3.10G**). These data indicate ZMYND8 contributes to the survival of mIDH1 GCCs in response to radiation.

ZMYND8 KO mIDH1 GCCs are defective in resolving IR induced DNA damage and undergo activation of cell cycle arrest

To further examine the relationship between ZMYND8 and DDR signaling, we analyzed the activation of HR proteins at the indicated time points following 20Gy IR in SF10602 ZMYND8 WT and SF10602 ZMYND8 KO cells by WB (**Fig. 3.11A**). The HR pathway maintains genomic integrity by first sensing DNA damage, recruiting DNA repair mediators to the region and inducing cell cycle arrest (**Fig. 3.11B**). Gamma histone H2AX (γH2AX) has been used to assess DNA damage following IR but can also indicate genomic instability in the form of replication stress (Banath et al., 2010; Mah et al., 2010). We validated the loss of ZMYND8 expression in the SF10602 ZMYND8 KO (**Fig. 3.12A**) and quantified the changes in ZMYND8 expression within the SF10602 ZMYND8 WT post-IR (**Fig. 3.12B**). We observed sustained γH2AX signal in SF10602 ZMYND8 KO compared with SF10602 ZMYND8 WT following IR (**Fig. 3.12C**). SF10602 ZMYND8 KO display higher basal γH2AX signal in the non-irradiated (NR) control when compared with SF10602 ZMYND8 WT (**Fig. 3.12C**). The greatest difference in γH2AX expression relative to loading control (tubulin) was present at 24hrs post-IR ($p < 0.001$) (**Fig. 3.12C**). This delayed resolution of γH2AX signal may reflect a defect in the efficiency of DSB repair or an accumulation of DNA damage in the SF10602 ZMYND8 KO following IR. ATM is

a master regulator of HR repair and undergoes autophosphorylation at serine 1981 (pATM), which actives ATM by dissociating it from a dimer to a monomer form (So et al., 2009). We observed enhanced activation of pATM in the SF10602 ZMYND8 KO compared to SF10602 ZMYND8 WT in response to IR (**Fig. 3.12D**). The greatest difference in pATM activation relative to β-actin was present at 30mins post-IR ($p < 0.001$) (**Fig. 3.12E**). DNA damage acquired during IR interrupts cell cycle progression through the activation of checkpoint kinases Chk1 and Chk2 to allow accurate DNA repair fidelity. As a safeguard, Chk1 triggers G2/M arrest in response to IR-induced DNA damage, its phosphorylation at serine 345 (pChk1) by ATR signifies impaired replication control (Wilsker et al., 2008). We observed extended activation of pChk1 relative to Chkl in SF10602 ZMYND8 KO compared to SF10602 ZMYND8 WT in response to IR (**Fig. 3.12D**). While the SF10602 ZMYND8 WT show a return of pChk1 to NR levels at 48hrs post-IR ($p < 0.0001$), the SF10602 ZMYND8 KO display prolonged activation of pChk1 (**Fig. 3.12F**).

Next, we evaluated phosphorylation of Rad51 at threonine 309 (pRad51), which is mediated by activated Chk1. Rad51 promotes genomic stability by binding to ssDNA to stabilize replication forks in order to protect under-replicated DNA regions during mitosis (Adolph et al., 2021; Wassing et al., 2021; Wolf et al., 2016). Additionally, Rad51 is recruited to DSB regions where it cooperates with HR proteins to promote strand invasion (Wassing et al., 2021). We observed elevated relative expression of pRad/Rad51 in SF10602 ZMYND8 KO compared to SF10602 ZMYND8 WT beginning at 4hrs post-IR ($p < 0.05$) which was most significantly elevated after 48hrs post IR ($p < 0.0001$) (**Fig. 3.12G**). Chk2 is phosphorylated on threonine 68 (pChk2) by ATM in order to induce G2/M arrest. We observed significant increase in the relative pChk2/Chk2 level in the SF10602 ZMYND8 KO compared to the SF10602 ZMYND8 WT beginning at 30mins post-IR ($p < 0.0001$) (**Fig. 3.12I**). While the SF10602 ZMYND8 WT show

a return of pChk2 to NR levels at 24hrs post-IR ($p < 0.0001$), the SF10602 ZMYND8 KO display prolonged activation of pChk2 (**Fig. 3.12I**). These findings suggest that ZMYND8 plays an important role in DDR, which is mediated by the mobilization of DDR proteins to repair IR-induced DNA damage and regulation of cell cycle progression.

Discussion

We observed a significant reduction in ZMYND8 protein expression in three patient-derived mIDH1 GCC after treatment with AGI-5198 or DS-1001b. Additionally, inhibition of mIDH1 in SF10602 increased expression of genes associated with replication stress and genomic instability. Timeless has been shown to accumulate at regions of DNA damage tracks induced by laser-microirradiation and its retention at damaged chromatin is dependent on the presence of PARP but not its activity (Xie et al., 2015; Young et al., 2015). Cancer cells undergo persistent DNA replication stress as a result of aberrant cell cycle progression. Timeless has been shown to stabilize replication forks and contribute to sister chromatid cohesion for maintenance of genomic integrity (Leman et al., 2010; Rageul et al., 2020). In cervical cancer models, the overexpression of Timeless has been proposed to function in response to replication stress driven by oncogene activation (Bianco et al., 2019). TREX1 is known to function as a 3'-5' DNA exonuclease to degrade ssDNA or mispaired DNA duplexes that arise from the repair of DNA lesions and aberrant replication (Mohr et al., 2021; Wolf et al., 2016). The elevated expression of Timeless and TREX1 following mIDH1 inhibition in SF10602 could be an indication of enhanced genomic stress. We observed lower total protein levels for TREX1, TIMELESS and PCNA in our mouse mIDH1 GCCs (NPAI) compared to our IDH1-wildtype NS (NPA).

By selectively suppressing ZMYND8 expression in human mIDH1 GCCs by the means of shRNA knockdown or genetic knockout using lenti-CRISPRCas9, we observed a significant

decrease in cellular viability in response to IR. In support of the role of ZMYND8 in genomic integrity, loss of ZMYND8 in triple-negative breast cancer cells lead to an increase in micronuclei formation along with chromosome aberrations including dicentric chromosomes and DNA breaks evaluated by metaphase spreads (Wang et al., 2021). A potential mechanism contributing to this induction of genomic instability, could be the result of overactivation of enhancers following the loss of ZMYND8 (Shen et al., 2016). A recent study mapping transcription-mediated DSB in breast cancer revealed that RAD51 localized to super-enhancers to stabilize DNA damage occurring due to hyper-transcription (Hazan et al., 2019). In our time-course assessment of HR repair protein activation following IR, total Rad51 appeared to be increased beginning at 30mins post IR in the SF10602 ZMYND8 KO vs. SF10602 ZMYND8 WT. We observed a robust activation of p-ATM beginning at 30mins after IR and remained elevated up to 24hrs after IR in the SF10602 ZMYND8 KO compared to SF10602 ZMYND8 WT. SF10602 ZMYND8 KO displayed prolonged activation of pChk2, while the SF10602 ZMYND8 WT showed a return to baseline 24hrs post-IR. We hypothesize that loss of ZMYND8 impairs the resolution of DSB induced by IR, which leads to extended cell cycle arrest mediated by pChk2. It has been proposed that ZMYND8 functions in transcriptional silencing of active transcription to allow for repair of DNA damage by HR proteins (Gong et al., 2015). We hypothesize that when exposed to irradiation ZMYND8 KO cells accumulate more DNA damage and thus DDR proteins are upregulated to response to the damage (Gong et al., 2015).

Materials and Methods

Embedding mIDH1 GCC NS for Immunohistochemistry

Following 1 week treatment with vehicle (DMSO) or 5μM mIDH1 inhibitor (AGI-5198), mIDH1 NS were transferred to 15 mL conical and allowed to settle by gravity. The supernatant was removed by manual pipetting and mIDH1 NS were suspended gently in 4% PFA for overnight incubation to fix and retain neurosphere morphology. The next day mIDH1 NS were washed thrice in PBS buffer. Autoclaved 4% low-melting agarose was cooled to 43°F on bead bath. In order to embed mIDH1 NS in agarose, cells were transferred to 1.5mL microcentrifuge tube and 200μl of agarose was added over top of the NS. A wooden skewer was used to evenly distribute mIDH1 NS before immediately transferring to ice. Agarose cone containing mIDH1 NS was removed and processed at Histology core for paraffin sectioning. Representative sections of mIDH1 NS were made at 5μm thickness and transferred to microscope slides. Immunohistochemistry (IHC) was performed by heating slides to 60°C for 20mins to assist in remove of paraffin. NS slides were deparaffinized and rehydrated. Permeabilization of NS was performed using TBS-0.025% Triton-X (TBS-TX) for 20 min. Antigen retrieval was performed at 96°C with citrate buffer (10mM sodium citrate, 0.05% Tween-20, pH 6) for an additional 20 min. Once cooled to room temperature (RT), sections were outlined with hydrophobic barrier pen, washed thrice (3min washes) with TBS-TX and blocked with 10% horse serum (HS) for 1hr at RT. IHC sections were incubated in primary antibody ZMYND8 (1:2000) diluted in 5% HS TBS-TX overnight in 4°C cold room. The following day, sections were washed with TBS and incubated with biotinylated secondary antibody goat anti-rabbit (1:1000) for 1hr at RT. Next, slides were washed thrice in TBS and incubated with Vectastain ABC reagent for 30mins covered by aluminum foil. Following TBS

wash, slides were developed using Betazoid DAB Chromogen kit (Biocare BDB2004) for 1-2mins at RT.

pT2-shZMYND8-GFP plasmid construction

These plasmids were generated by excising the micro-30a loop from the pT2-shATRX-GFP (Addgene #124259) via overnight restriction enzyme digestion with XhoI and EcoRI at 37ºC. The backbone pT2-GFP DNA was purified using the QIAquick Gel Extraction Kit (Cat No: 28706). Oligonucleotide sequences consisting of short hairpin (sh) that target exon 12 of the human ZMYND8 gene or exon 24 in the mouse ZYMND8 gene were ligated using T4 DNA ligase protocol (NEB M0202). The ligated pT2-shZMYND8-GFP plasmid was transformed into competent *E Coli* (NEB C2984H) and single colonies were expanded for DNA isolation using the QIAprep spin miniprep kit (Cat No: 27104). Cloned sites were confirmed by DNA sanger sequencing.

Generation of ZMYND8 knockdown tumor cell lines

Stable transfection of pT2-shZMYND8-GFP was performed using electroporation combined with sleeping-beauty transposon system integration *in vitro*. Human mIDH1 primary glioma cell cultures, SF10602 and MGG119 were dissociated to single cells and $1x10^6$ cells were collected. Glioma cell pellets were resuspended in Lonza Nucleofector (V4XP-3024) P3 buffer solution and nucleofected on the 4D-Nucleofector system (Cat No: AAF-1002B) along with pT2-shZMYND8-GFP (1.5ug) and Sleeping beauty transpose-luciferase (Cat No.20207 Addgene, 0.5ug) plasmids. Cells were transferred to laminin-coated plates and detection of green fluorescent cells was observed the next day by fluorescence microscopy. Isolation of GFP-positive glioma cells was performed 3-4 weeks after nucleofection in order to allow for higher enrichment. Expanded

mIDH1 GCCs expressing shZMYND8 were sorted again to isolate the top 25% of GFP-expressing glioma cells. Knockdown of ZMYND8 expression was confirmed by western blot.

Lentiviral particle generation

Second generation lentiviral particles were packaged using HEK293T cells, which were seeded at 5 million cells and incubated with plasmid transfection mix containing 80µl of jetPRIME solution, 2 mL of PEG, envelope (10µg), package (15µg) and lentiCRISPR-V2-ZMYND8 (20µg) plasmid provided by Dr. Weibo Lou at UTSW. (Wang et al. 2021 Cancer Research) Lentiviral particles were purified from conditioned media by centrifuging at 30,000 rpm for 2hrs. After ultra-centrifugation, the concentrated lentiviral particles were resuspended in 1 mL of ice-cold PBS under gentle agitation 25rpm at 4^{o}C for 1hr. Lentiviral particle solution was aliquoted into cryo-safe microcentrifuge tubes and stored at -80^{o}C for later use.

Intracranial mIDH1 glioma model

All animal studies were conducted according to guidelines approved by the IACUC of the University of Michigan (protocols PRO00009578 and PRO00009546). All animals were housed in an AAALAC-accredited animal facility and were monitored daily. Studies did not discriminate by sex; both male and females were used. The strains of mice used in the study were C57BL/6 (the Jackson Laboratory, strain no. 000664) and CD8-KO (the Jackson Laboratory, strain no. B6.129S2-Cd8atm1Mak/J, stock no. 002665).

Our laboratory has modelled mIDH1 low grade glioma by integrating oncogenic plasmid DNA into the neural stem cells present within the developing brain of post-natal mice utilizing the sleeping beauty (SB) transposon system. The mIDH1 glioma cells endogenous express IDH1-R132H along with genetic lesions that drive oncogenesis through NRAS^{G12V} and simulate tumor

suppressor loss by ATRX and TP53 short hairpin knockdown. Tumor NS were derived from endogenous mIDH1 tumors that were adapted to *in vitro* culture and could be reimplanted into immunocompetent C57BL6 (The Jackson Laboratory, C57BL/6J Strain# 000664) mice for preclinical experiments in this study. Intracranial surgeries were performed by stereotactically injecting 50,000 mIDH1 NS into the right striatum using a 22-gauge Hamilton syringe with the following coordinates: 1.0 mm anterior, 2.5mm lateral and 3.0mm deep from the bregma suture line.

Generation of human and mouse ZMYND8 KO glioma cells

Human mIDH1 primary glioma cell cultures SF10602 and MGG119 were seeded at $2x10^5$ cells per well of laminin coated 6-well plate. The following day, cell culture media was removed and cells were incubated directly with lentiviral particles for 10mins. Media was changed after 3 days of lentiviral transfection and cells were expanded for another week prior to puromycin selection. Loss of ZMYND8 expression was confirmed by western blot.

Quantitative Pathology & Bioimage Analysis Software Analysis

QuPath v0.3.2(actively developed at the University of Edinburgh) is open-source software for bioimage analysis and digital pathology. Positive cell detection command allows to classify cells as either positive or negative, using DAB optical density mean and a single threshold. This command allows to detect 'objects'(cells) in the selected field, and the percentage of representation of each cluster (negative and positive, in this case). Between 13-17 fields (containing 3-4 neurospheres sections each) were quantified per treatment group. Same parameters were employed for the detection of all the fields for every sample. Percentage of DAB-stained positive cells over total number of cells per fields was quantified. (Threshold: SF10302: 0.2; LC1035: 0.3).

Western blot and radiation sensitivity *in vitro*

Mouse NS (NPA-C54B: wt-IDH1, NPAI: mIDH1) and human mIDH1 GCCs (SF10602 and MGG119) were seeded at density of 5.0 x 10^6 cells into 75-cm2 flasks containing NSC media. After 24 hours, mouse NS and human GCCs were treated with 5Gy and 20Gy radiation, respectively. After an additional 48 hours, cell lysates were prepared by incubating glioma cells with RIPA lysis buffer (MilliporeSigma, Cat# R0278) and 1X Halt™ protease and Phosphatase inhibitor cocktail, EDTA-free (100X) (Thermo Scientific, Cat# 78441) on ice for 15 minutes. Resulting cell lysates were centrifuged at 14000 RPM at 4°C for 15 minutes and supernatants were collected to determine protein concentration in comparison to standard bovine serum albumin (BSA) protein concentrations through bicinchoninic acid assay (BCA) (Pierce, 23227). For electrophoretic separation of proteins, 20 µg of total protein were resuspended in loading buffer (10% sodium dodecyl sulfate, 20% glycerol, and 0.1% bromophenol blue) and samples were heated at 95°C for 5mins to denature protein and later loaded onto a 4-12% Bis-Tris gel (Thermo Fisher Scientific, NuPAGE, NP0322BOX). Proteins from the gel were transferred to 0.2 µm nitrocellulose membrane (Bio-Rad, Cat# 1620112) and blocked with 5% bovine serum albumin (BSA) in TBS-0.1% Tween-20. After blocking, membranes were incubated with primary anti-phospho γH2AX (1:1000) (Cell Signaling Technologies, Cat# 9718S), anti-γH2AX (1:1000) (Cell Signaling Technologies, Cat# 2595S), primary antibody ZMYND8 (1:2000) (Bethyl Laboratories, Cat# A302-089A), primary antibody TIMELESS (1:1000) (Bethyl Laboratories, Cat.# A300-960A), primary antibody PCNA (1:1000) (Cell Signaling Technologies, Cat# 2586T), primary antibody TREX1 (1:1000) (Abcam, Cat# ab185228), primary antibody BRD4 (1:1000) (Cell Signaling Technology, Cat# 83375B), primary antibody HDAC1 (1:1000) (Cell Signaling Technology, Cat# 2062S), primary antibody HDAC2 (1:1000) (Cell Signaling Technology, Cat#

57156S), Vinculin (1:3000) (Thermo Fisher Scientific, Cat# 7000062) or β-tubulin antibodies (1:4000) (Sigma-Aldrich, Cat# A1978) overnight at 4°C. The next day, blots were washed with TBS-0.1% tween-20 and incubated with secondary (1:4000) antibodies [Dako, Agilent Technologies, goat anti-rabbit 1:4000 (Cat# P0448), rabbit anti-mouse 1:4000 (Cat# P0260)] for one hour at room temperature. Blots were washed several times again with TBS-0.1% tween-2.0 Enhanced chemiluminescence reagents were used to detect the signals following the manufacturer's instructions (SuperSignal West Femto, Thermo Fisher Scientific, Cat# 34095) and visualized under Bio-Rad gel imaging software. Band intensities were quantified using ImageJ (RRID:SCR_003070).

Figures

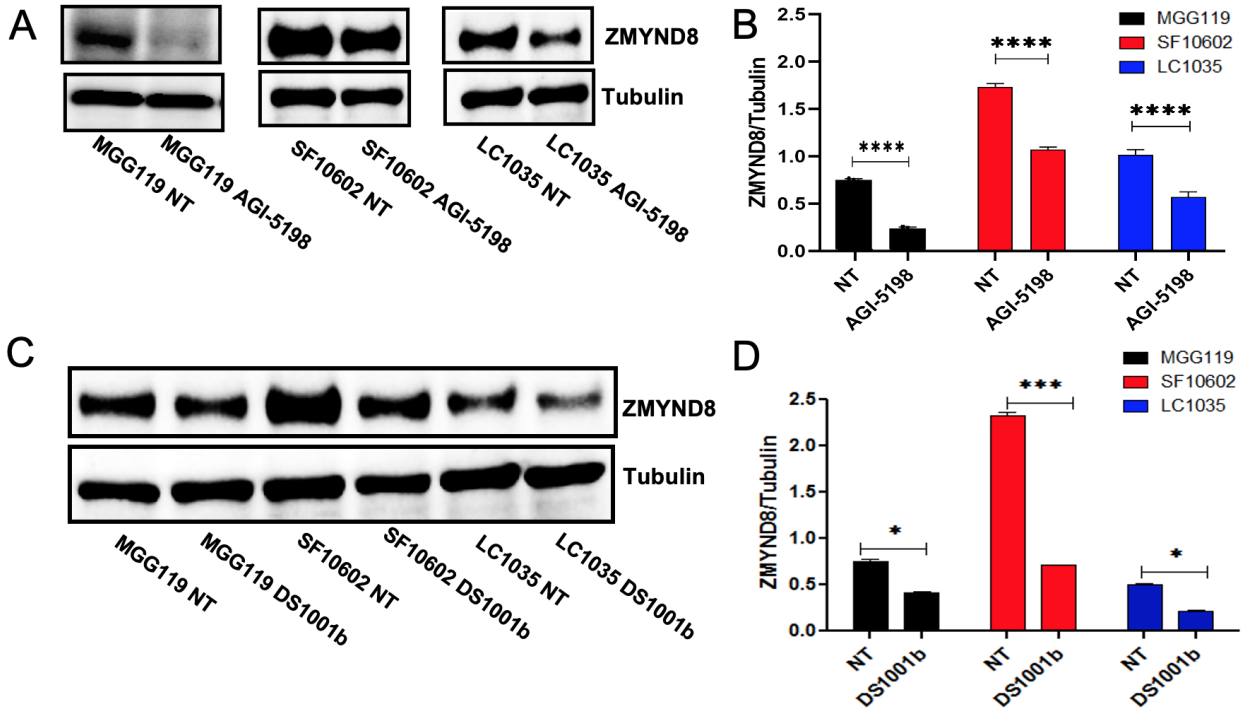

Figure 3.1 Decreased ZMYND8 protein expression following mIDH1 inhibitor treatment (AGI-5198, DS-1001b) in three separate human mIDH1 GCCs

(A) Representative western blot for ZMYND8 protein expression in three human mIDH1 GCCs that were non-treated (NT) or AGI-5198-treated (mIDH1 inhibitor) for 1 week. (B) ImageJ densiometric quantification of ZMYND8 protein expression based relative to loading control (tubulin) for each of the mIDH1 GCCs either NT or AGI-5198 treated: MGG119 (black), SF10602 (red), and LC1035 (blue). (C) Representative western blot for ZMYND8 protein expression in three human mIDH1 GCCs that were NT or DS1001b treated (clinical mIDH1 inhibitor) for 1 week. (D) ImageJ densiometric quantification of ZMYND8 protein expression following DS1001b treatment compared to NT. Errors bars represent SEM from independent biological replicates (n=3). * $P<0.05$, *** $P<0.001$, **** $P < 0.0001$; two-tailed t test.

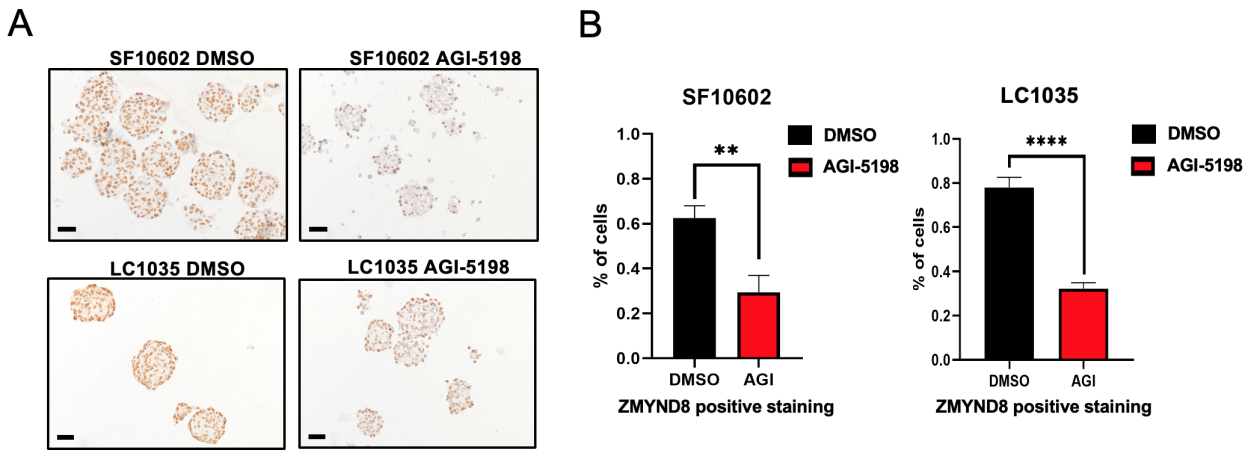

Figure 3.2 Immunohistochemistry (IHC) staining of embedded mIDH1 human neurospheres treated with vehicle (DMSO) or mIDH1 inhibitor (AGI-5198)

(A) Immunohistochemistry (IHC) staining of sectioned paraffin-embedded human mIDH1 GCCs treated with vehicle (DMSO) or mIDH1 inhibitor (AGI-5198). (B) Representative Quantitative Pathology & Bioimage Analysis (QuPath) of IHC slides to identify the percentage of ZMYND8 positive staining (Diaminobenzidine (DAB) optical density > 0.4) for 12 representative frames. Representative Quantitative Pathology & Bioimage Analysis (QuPath) of IHC slides to identify the percentage of ZMYND8 positive staining (Diaminobenzidine (DAB) optical density > 0.4) for 12 representative frames. Errors bars represent SEM from independent microscope fields (n=12). ** P<0.01, **** P < 0.0001; two-tailed t test.

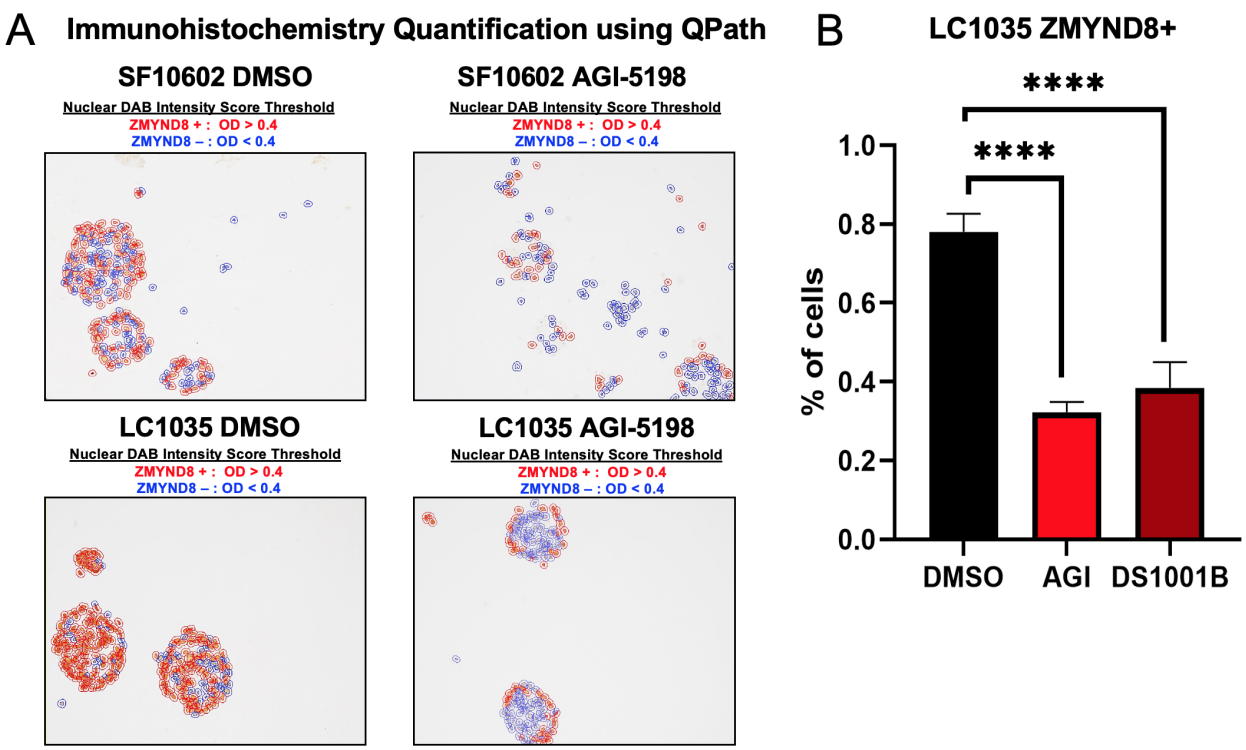

Figure 3.3 IHC quantification of nuclear staining for ZMYND8 expression in human mIDH1 neurospheres treated with either DMSO or AGI-5198 prior to fixation

(A) Immunohistochemistry (IHC) staining of sectioned paraffin-embedded human mIDH1 GCCs treated with vehicle (DMSO) or mIDH1 inhibitor (AGI-5198). (B) Representative Quantitative Pathology & Bioimage Analysis (QuPath) of IHC slides to identify the percentage of ZMYND8 positive staining (Diaminobenzidine (DAB) optical density > 0.4) for 12 representative frames. Errors bars represent SEM from independent microscope fields (n=12). **** $P < 0.0001$; two-tailed t test

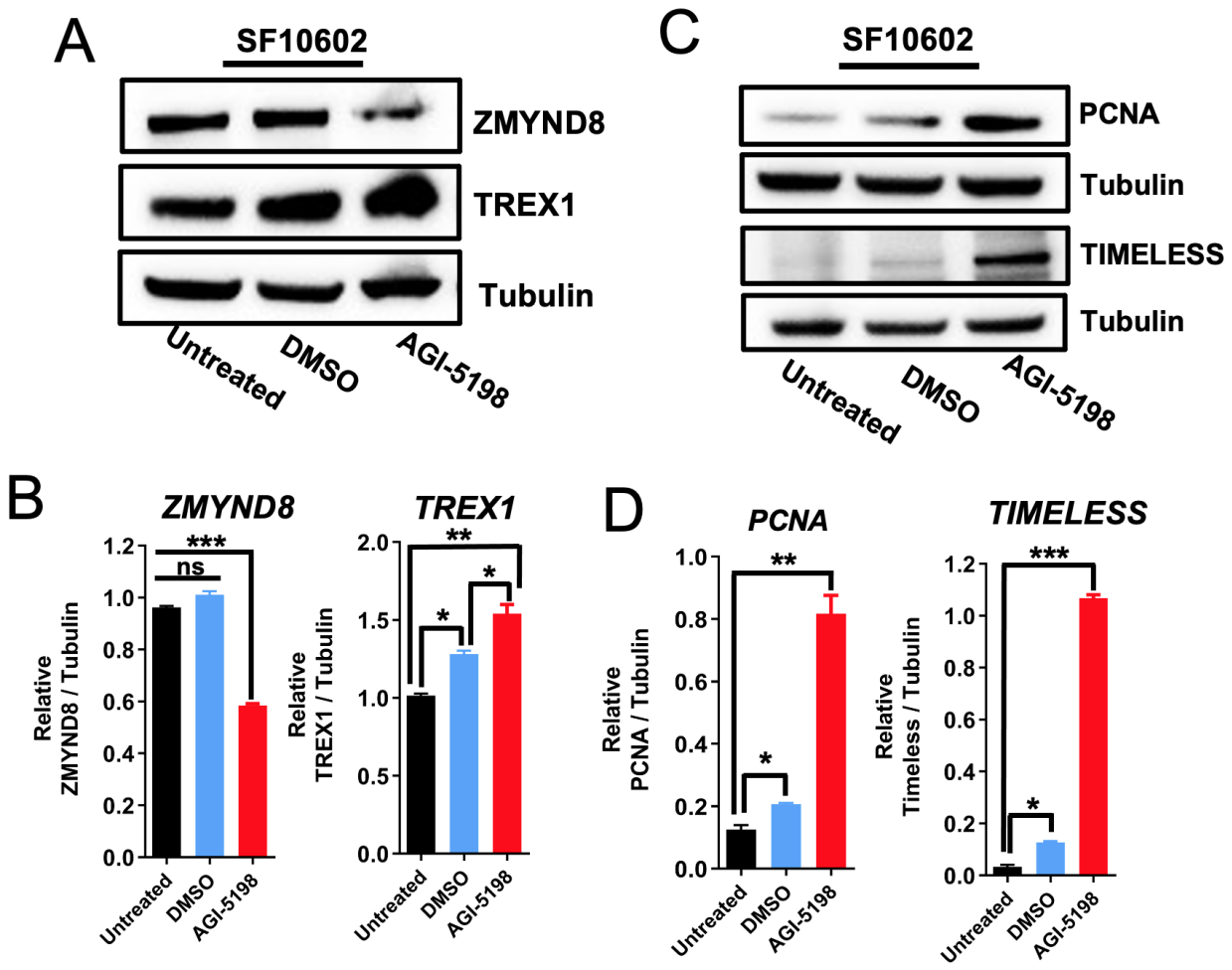

Figure 3.4 Assessment of replication stress associated proteins (PCNA, TIMELESS) and genomic instability (TREX1) following treatment of SF10602 with AGI-5198

(A) Western blot analysis shows ZMYND8 and TREX1 expression in SF10602 mIDH1 GCC either untreated, DMSO, or AGI-5198 treatment for 1 week with tubulin as a loading control. (B) ImageJ densiometric quantification of the western blot for ZMYND8 and TREX1. (C) Western blot analysis shows PCNA and TIMELESS expression in SF10602 either untreated, DMSO, or AGI-5198 treatment for 1 week with tubulin as a loading control. (D) ImageJ densiometric quantification of the western blot for PCNA and TIMELESS. Errors bars represent SEM from independent biological replicates (n=3). ns: not statistically significant, * P<0.05, ** P<0.01, *** P<0.001; two-tailed t test.

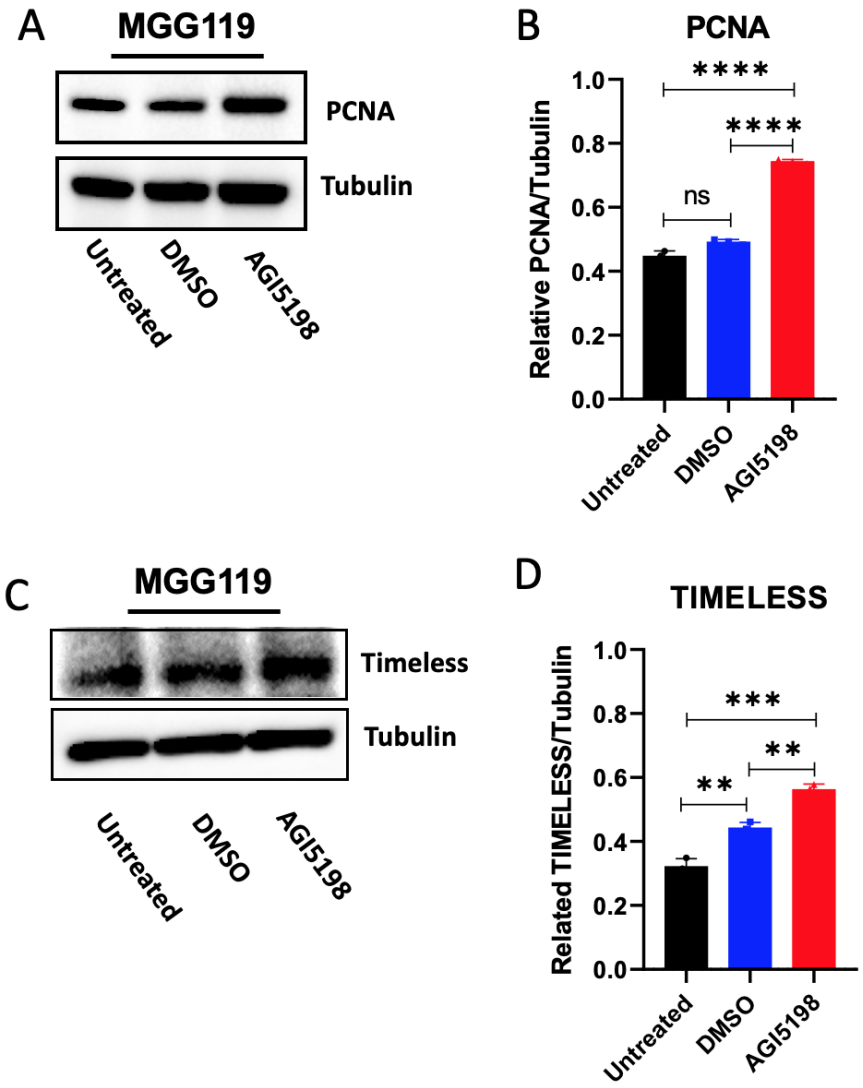

Figure 3.5 Human mIDH1 GCC MGG119 treated with a mIDH1 inhibitor (AGI-5198) exhibits an increased expression of genes associated with genomic instability

Western blot analysis showing (**A, B**) PCNA and (**C, D**) TIMELESS expression in MGG119 mIDH1 GCC either untreated, DMSO, or AGI-5198 treatment for 1 week with tubulin as a loading control. ImageJ densitometric quantification of the western blot for PCNA, and TIMELESS. Errors bars represent SEM from independent biological replicates (n=3). ns-not significant, **p<0.01, ***p<0.001, ****p<0.0001; unpaired t test.

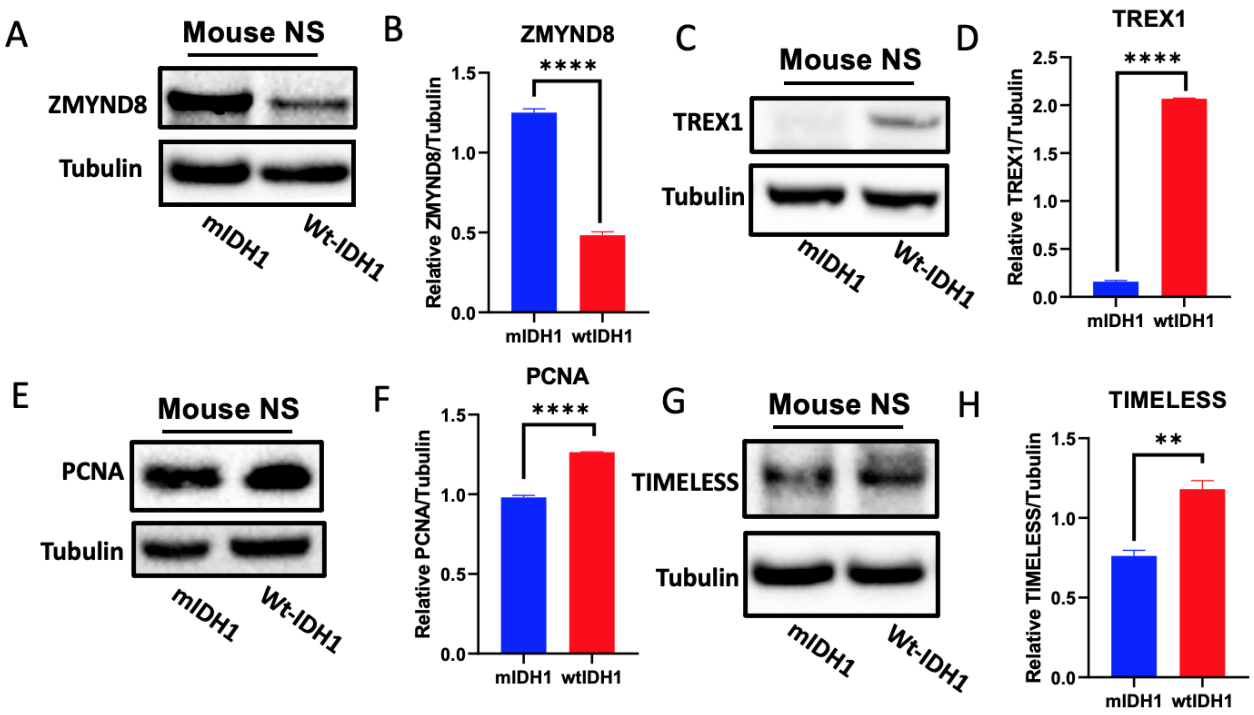

Figure 3.6 mIDH1 glioma cells exhibit enhanced ZMYND8 expression and lower levels of expression of replication stress related proteins

Western blot analysis showing (**A, B**) ZMYND8, (**C, D**) TREX1, (**E, F**) PCNA, and (**G, H**) TIMELESS expression in mIDH1 cells (NPAI) and wt-IDH1 cells (NPA-C54B) with tubulin as a loading control. ImageJ densitometric quantification of the western blot for ZMYND8, TREX1, PCNA, and TIMELESS. Errors bars represent SEM from independent biological replicates (n=3). ** $p<0.01$, **** $p<0.0001$; unpaired t test.

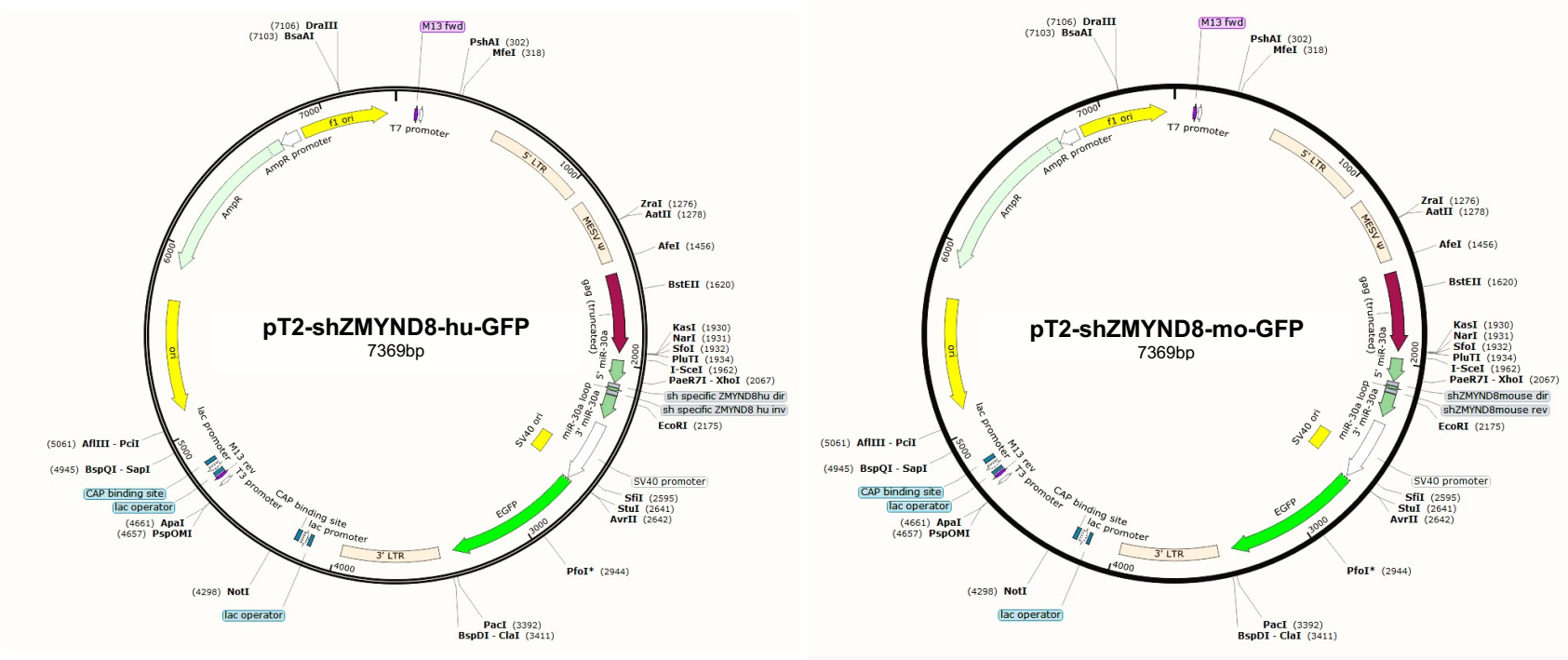

Figure 3.7 Plasmid maps for the cloned short hairpin RNA (shRNA) oligonucleotides targeting ZMYND8 (shZMYND8) isoforms for human and mouse

Diagram of the plasmids utilized to knockdown expression of ZMYND8 in human (pT2-shZMYND8-hu-GFP) or mouse (pT2-shZMYND8-mo-GFP) cells.

Table 3.1 Corresponding shRNA sequences highlighted in red for sh2-ZMYND8 (human) and sh4-ZMYND8 (mouse).

shRNA Oligos	DNA Oligonucleotide Sequences targeting ZMYND8
Human sh2-ZMYND8 F	TCGAGAAGGTATATTGCTGTTGACAGTGAGCGCCGGATTTCCTTGTCGGATATTAGTGAAGCCACAG ATGTAATATCCGACAAGGAAATCCGGTGCCTACTGCCTCGG
Human sh2-ZMYND8 R	AATTCCGAGGCAGTAGGCACCGGATTTCCTTGTCGGATATTACATCTGTGGCTTCACTAATATCCGA CAAGGAAATCCGGCGCTCACTGTCAACAGCAATATACCTTC
Mouse sh4-ZMYND8 F	TCGAGAAGGTATATTGCTGTTGACAGTGAGCGGCCAAACACTTTAGGTGTAAGTAGTGAAGCCACA GATGTACTTACACCTAAAGTGTTTGGCTGCCTACTGCCTCGG
Mouse sh4-ZMYND8 R	AATTCCGAGGCAGTAGGCAGCCAAACACTTTAGGTGTAAGTACATCTGTGGCTTCACTACTTACACC TAAAGTGTTTGGCCGCTCACTGTCAACAGCAATATACCTTC

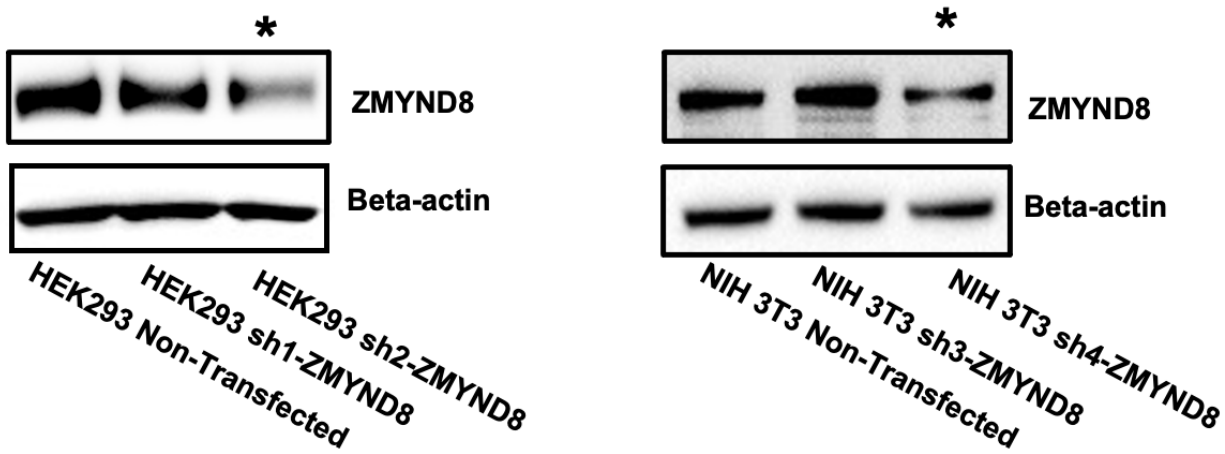

Figure 3.8 Western Blot results following transfection of human HeK293 and mouse NIH3T3 cells with shZMYND8 knockdown plasmids

Western blot assessing ZMYND8 expression in human HEK293 and mouse NIH3T3 cells 3 days after jet-prime transfection with ZMYND8 knockdown plasmid. Asterisk denotes the shZMYND8 plasmids selected.

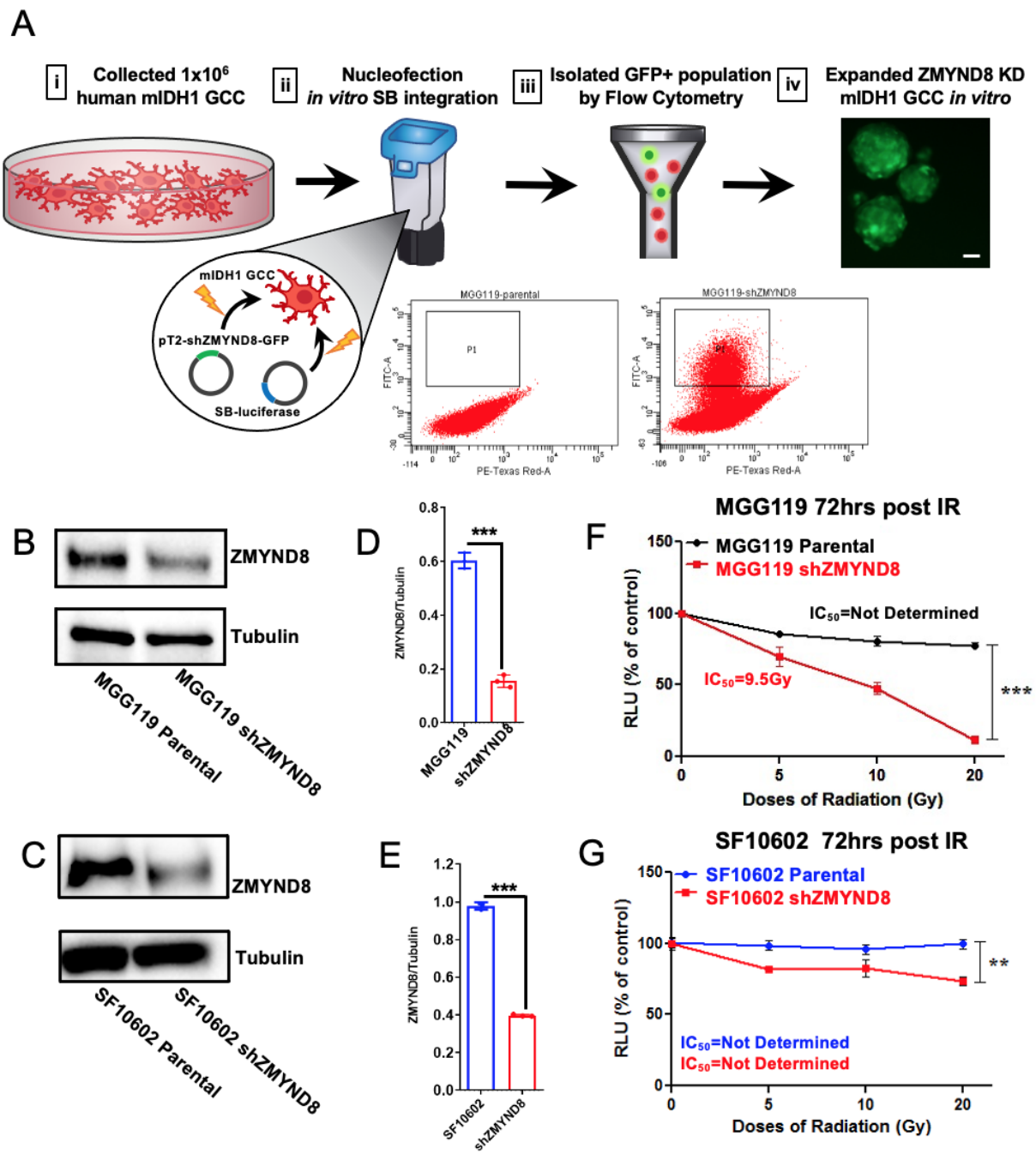

Figure 3.9 Generation of shZMYND8 knockdown mIDH1 GCCs

(A) Illustration of the nucleofection procedure to generate stable shZMYND8 knockdown clones of the human mIDH1 GCCs (SF10602, MGG119). i) $1x10^6$ human mIDH1 GCCs were collected. ii) mIDH1 GCCs were suspended in nucleofection solution containing pT2-shZMYND8-GFP (knockdown plasmid) and sleeping beauty luciferase (SB-luciferase) plasmid to integrate shZMYND8 knockdown plasmid using Lonza nucleofector system. iii) Isolated green fluorescent protein expressing cells (GFP+) by flow cytometry. iv) expanded the stable shZMYND8 cells. (B) Western blot for ZMYND8 expression in MGG119 non-transfected (parental) vs. shZMYND8 and (C) histogram quantification of ZMYND8 relative to Tubulin. (D) CellTiter-Glo assay to assess cellular viability 72hrs post-IR comparing MGG119 parental (black) vs. MGG119 shZMYND8 (red). (E) Western blot for ZMYND8 expression in SF10602 non-transfected (parental) vs. shZMYND8 and (F) histogram quantification of ZMYND8 relative to Tubulin. (G) Cellular viability 72hrs post-IR in SF10602 parental vs. shZMYND8. Errors bars represent standard error of mean (SEM) from independent biological replicates (n=3). ** $p<0.01$, *** $p<0.001$; unpaired t test.

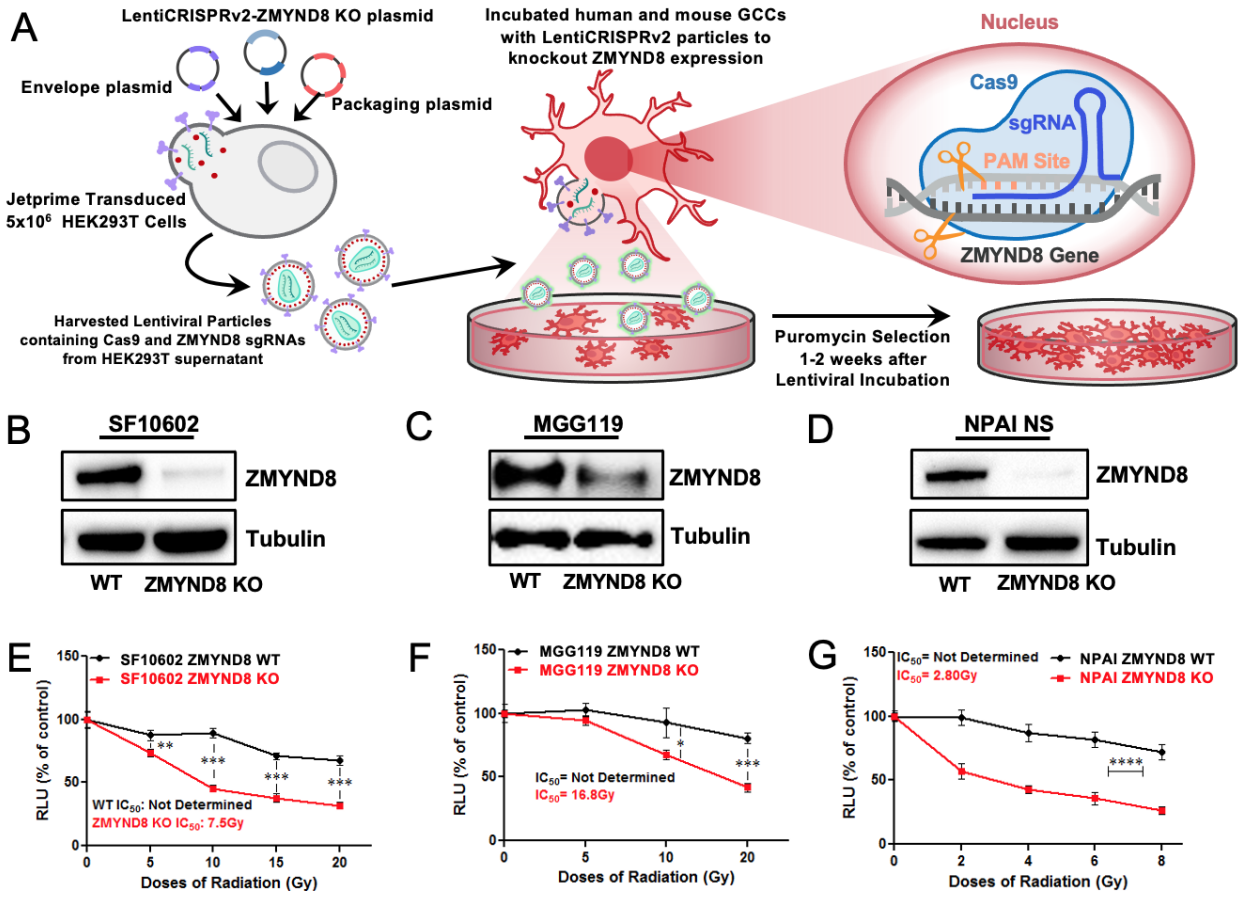

Figure 3.10 ZMYND8 KO GCCs display reduced viability to irradiation

(A) Experimental model in which ZMYND8 lentiviral particles were generated to knockout (KO) ZMYND8 expression in human and mouse GCCs mediated by CRISPR-Cas9-sgRNAs. ZMYND8 KO GCCs were selected based on resistance to 10μg/mL puromycin for 1 week in mouse mIDH1 GCCs and 2 weeks for human mIDH1 GCCs. Representative western blot quantification of ZMYND8 KO for (B) SF10602, (D) MGG119 and (F) NPAI mouse NS. Cellular viability of ZMYND8 wildtype (WT, shown by black line) vs. ZMYND8 KO, represented by the red line, was assessed 72 hours after irradiation (IR) exposure using CellTiter-Glo assay in the (C) SF10602, (E) MGG119 and (G) NPAI. Results are expressed in relative luminescence units (RLU) to control non-irradiated (0 Gy) cells.

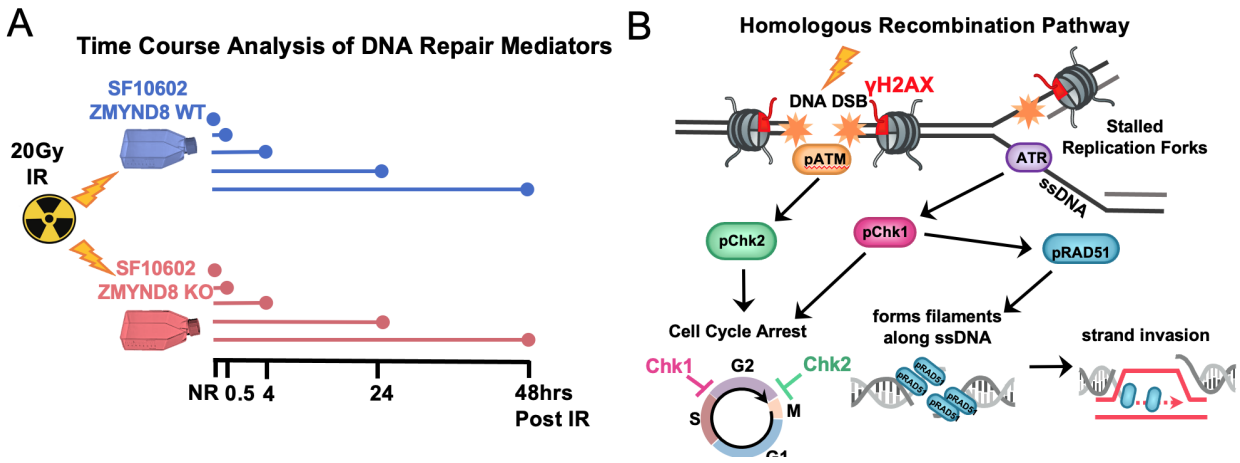

Figure 3.11 Temporal evaluation of DNA Repair protein expression that are involved in HR in SF10602 ZMYND8 Wildtype (WT) compared to SF10602 ZMYND8 KO

(A). Diagram of the time course analysis of DNA repair proteins expressed in SF10602 ZMYND8 WT (blue) vs. SF10602 ZMYND8 KO (red) exposed to a single dose of 20Gy IR and protein was collected from non-irradiated (NR) cells and at 0.5, 4, 24, and 48 hours post IR exposure. (B) Model of irradiation (lighting blot) induced activation of the homologous recombination (HR) pathway including downstream HR mediators.

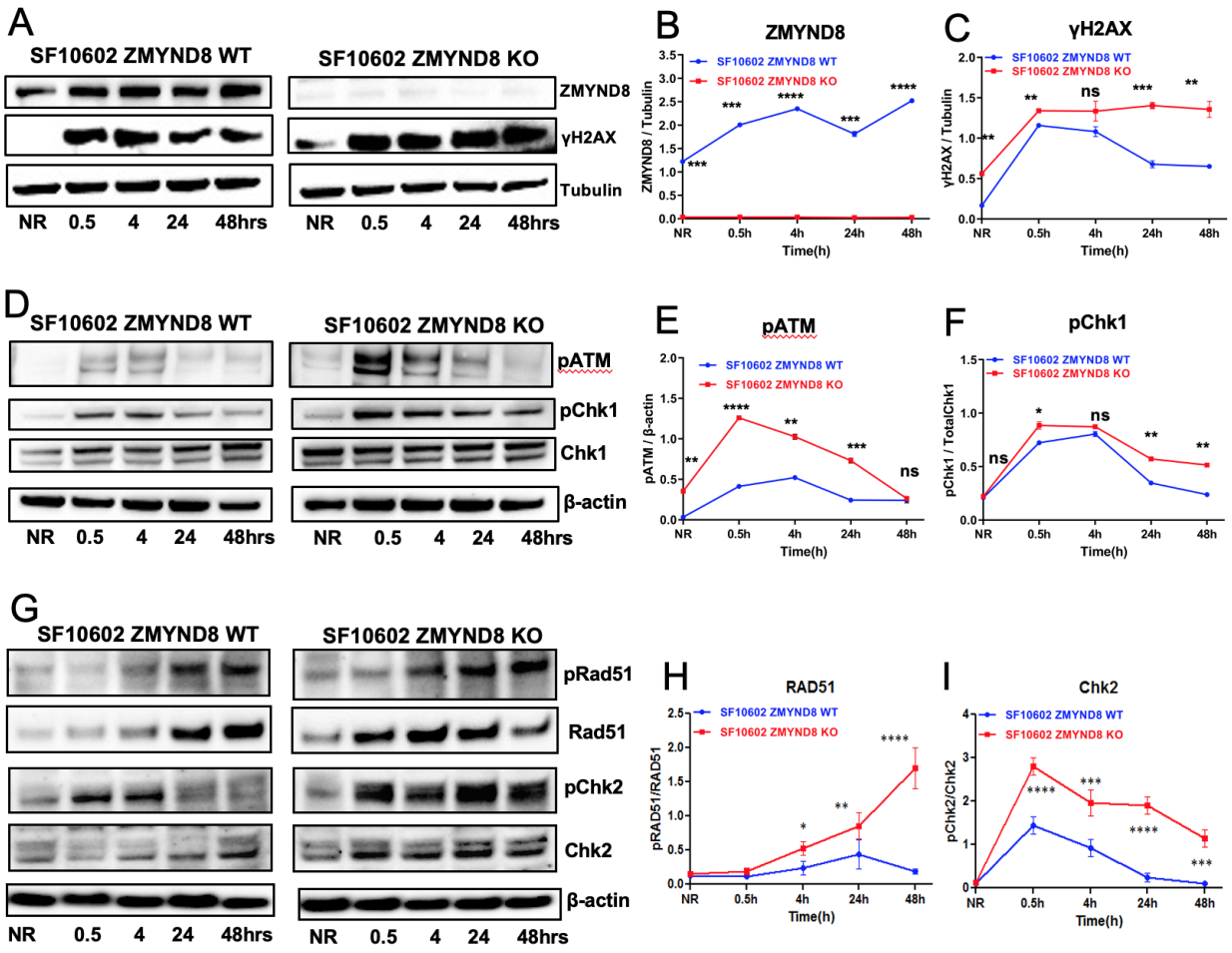

Figure 3.12 ZMYND8 KO mIDH1 GCCs are defective in resolving IR induced DNA damage and undergo prolonged activation of cell cycle arrest

(A) Representative western blot for ZMYND8 and γH2AX expression in SF10602 ZMYND8 WT vs.SF10602 ZMYND8 KO at the indicated conditions described in IR time course diagram. (B) Line graph represents the quantification of ZMYND8 expression relative to tubulin in SF10602 ZMYND8 WT (blue) vs. SF10602 KO (red) from 0 (NR) to 48hrs post IR. (C) Line graph represents the quantification of yH2AX relative to tubulin. (D) Representative western blot for phosphorylated ATM (pATM) and Chk1 (pChk1) expression and their respective nonphosphorylated (ATM and Chk1) proteins relative to β-actin. Line graph represents the quantification of (E) pATM expression relative to β-actin and (F) pChk1 expression relative to Chk1. (G) Representative western blot for phosphorylated Rad51 (pRad51) and Chk2 (pChk2) expression and their respective nonphosphorylated (Rad51 and Chk2) proteins relative to β-actin. Line graph represents the quantification of (H) pRad51 expression relative to Rad51 and (I) pChk2 expression relative to Chk2. Error bars represent SEM from independent biological replicates. (n=3) * P<0.05, ** P<0.01, *** P<0.001, **** P < 0.0001; two-tailed t test.

Chapter 4 Targeting ZMYND8-interacting Partners and the Generation of a PDGFRA-driven Mouse Model of MIDH1 Glioma

Introduction

Despite IDH-mutant glioma patients displaying a prolonged period between initial diagnosis to tumor recurrence as compared to GBM, these patients will experience tumor relapse after radiotherapy and chemotherapy (Yu et al., 2021). Previous studies aimed at characterizing the role of mIDH1 in susceptibility to irradiation focused solely on introducing mIDH1 exogenously to available glioma cell lines, which do not harbor the same genetic lesions present in mIDH1 gliomas (Wang et al., 2014). We generated a genetically engineered mouse model of mIDH1 glioma that was initiated through the introduction of the oncogenic mutation PDGFRA-D842V, which drives the MAPKK pathway independent of growth factor ligand. The proneural genetic signature that is defined by expression of SOX, OLIG2, and PDGFRA has been associated with mIDH1 gliomas (Saito et al., 2019).

Gain-of-function mutations in PDGFRA frequently occur in IDH-wildtype GBM, but these alterations are less common in IDH-mutant tumors. *Flavahan et al.* performed 3-dimensional chromosome conformation capture (3C) to examine looping interactions at the PDGFRA locus in an IDH-mutant BT142 gliomasphere derived from an oligoastrocytoma (Flavahan et al., 2016). With the goal of identifying regulatory elements that might underlie PDGFRA upregulation in IDH-mutant glioma, the authors identified the FIP1LI enhancer to be strongly associated with the PDGFRA promoter in BT142 glioma cells (Flavahan et al., 2016). As compared to wildtype-IDH1 EGFR-amplified glioma cell GSC6, this interaction did not occur due to a CTCF binding site

creating a boundary between the FIP1L1 enhancer with PDGFRA promoter (Flavahan et al., 2016). This CTCF motif exhibited a 5-fold increase in DNA methylation in the BT142 as compared to GSC6, which suggested that mIDH1 could be disrupting the boundary of chromatin looping to drive PDGFRA oncogene activation by preventing CTCF binding to specific DNA regions (Flavahan et al., 2016). Another study, where mIDH1 was exogenously expressed in immortalized human astrocytes (IHA) found enhanced H3K4me3 deposition at the PDGFRA promoter (Turcan et al., 2018). Therefore, we pursued generating a mouse model where PDGFRA was constitutively activated to understand its contribution to gliomagenesis in our murine model and to evaluate if knocking out ZMYND8 enhanced the susceptibility to irradiation.

ZMYND8 has been shown to form a complex with chromatin reader proteins like BRD4 and HDAC, which we targeted using pharmacological inhibitors to determine their contribution to the radiosensitivity observed in the ZMYND8 KO mIDH1 GCCs compared ZMYND8 WT. We observed an additive effect of targeting BRD4 (JQ1, I-BET-762) or HDAC (Panobinostat) on decreasing the survival of ZMYND8 KO mIDH1 GCCs to radiotherapy. We did not observe a correlated upregulation of BRD4 or HDAC1 or HDAC2 in IDH-mutant glioma compared to IDH-wildtype glioma, suggesting that the regulation of BRD4 and HDAC1/2 does not occur in the same manner as ZMYND8. It is likely, that the increased susceptibility of ZMYND8 KO to BRD4 and HDAC inhibitors functions independently of their function at the chromatin level.

Treatment of human mIDH1 GCCs *in vitro* with TMZ results in a marked increase in PAR polymers and occurs within the first hour after exposure (Tateishi et al., 2017). The recruitment of ZMYND8 to regions of DNA damage has been shown to be dependent upon the presence of PARP (Spruijt et al., 2016). Several groups have shown that mIDH1 GCCs are sensitive to PARP inhibitors when combined with irradiation. PARP inhibitors like veliparib and pamiparib trap

PARP onto DNA and prevent its polymerization (Kim & Nam, 2022). This convergence of ZMYND8, PARP, and HDAC to occur at regions of DNA damage propose a potential epigenetic vulnerability that requires further investigation.

Results

Murine model of mIDH1 glioma driven by constitutive activation of Platelet Derived Growth Factor Receptor mutation D842V ($PDGFRA^{D842V}$) and loss of TP53 and ATRX

Amplified expression of PDGFRA has been found in 9.9% of LGG, and was more frequently observed in diffuse astrocytoma (16.3%) as compared to oligodendroglioma (2.6%) (Motomura et al., 2013). We developed a second mIDH1 mouse glioma model using the $PDGFRA^{D842V}$ plasmid to constitutively activate the receptor tyrosine kinase (RTK)-RAS-PI3K pathway (**Fig. 4.1A**). We induced brain tumors in two experimental groups: wtIDH1 (RPA: $PDGFRA^{D842V}$, shP53, and shATRX) and mIDH1 (RPAI: $PDGFRA^{D842V}$, shP53, shATRX, and $mIDH1^{R132H}$). The MS of mice in the RPAI group was 172 days post-injection (DPI), which was significantly greater compared to RPA group with an MS of 92 DPI; $p<0.0023$, Mantel-Cox test (**Fig. 4.1B**).

We generated the RPAI NS from a resected sleeping-beauty tumor 158 DPI, and integration of oncogenic plasmids was assessed by fluorescence microscopy (**Fig. 4.2A-B**). Additionally, we demonstrated that the RPAI NS was able to generate tumors in mice and confirmed expression of mIDH1 using a specific antibody for the R132H mutation and ATRX loss by IHC (**Fig. 4.2C**). WB analysis of RPAI NS treated with AGI-5198 revealed a decrease in global histone mark lysine trimethylation for H3K4me3, H3K27me3 and H3K36me3, but there was no change in global H3K27ac expression (**Fig. 4.3A**). After we confirmed the loss of ZMYND8 in RPAI ZMYND8 KO by WB analysis (**Fig. 4.3B**), we assessed their viability in response to IR.

The RPAI ZMYND8 KO exhibited an IC_{50} of 4.0Gy versus the RPAI ZMYND8 WT with an IC_{50} of 8.1Gy (**Fig. 4.3C**). This finding further supports the importance of ZMYND8 in survival of mIDH1-expression glioma cells to IR independent of the oncogenic driver mutation.

Murine mIDH1 glioma models display sensitivity to BRD4 and HDAC inhibitors and ZMYND8 KO show a greater decrease in cell viability compared to ZMYND8 WT

To begin to examine the mechanisms by which ZMYND8 contributes to genomic stability, we inhibited two newly described ZMYND8-interacting partners BRD4 and HDAC. We sought to investigate if BRD4 and HDAC cooperate with ZMYND8 to mediate the response to irradiation. We evaluated the sensitivity of our two mouse mIDH1 NS, NPAI ZMYND8 WT versus NPAI ZMYND8 KO and RPAI ZMYND8 WT versus RPAI ZMYND8 KO to two bromodomain and extraterminal domain inhibitors (BETi): JQ1 and I-BET-762, which also target BRD2 and BRD3 in addition to BRD4 (**Fig. 4.4A**). We also assessed the sensitivity of our mouse mIDH1 NS to the pan-histone deacetylase inhibitor Panobinostat, which targets Class I, II and IV HDACs (**Fig. 4.4B**). We observed an enhanced vulnerability of NPAI ZMYND8 KO to JQ1 treatment ($p < 0.0001$) with an IC_{50} of 0.18μM versus the NPAI ZMYND8 WT where an IC_{50} was not reached (**Fig. 4.5A**). The RPAI ZMYND8 KO had a reduced viability to JQ1 ($p < 0.01$) with an IC_{50} of 0.51μM versus the RPAI ZMYND8 WT with an IC_{50} of 0.97μM (**Fig. 4.5B**). The NPAI ZMYND8 KO displayed reduced cellular viability to I-BET-762 ($p < 0.0001$) with an IC_{50} of 0.335μM versus the NPAI ZMYND8 WT where an IC_{50} was not reached (**Fig. 4.5C**). The RPAI ZMYND8 KO displayed reduced viability to I-BET-762 ($p < 0.0001$) with an IC_{50} of 0.001μM versus the RPAI ZMYND8 WT with an IC_{50} of 0.19μM (Fig. 4.5D). Both mouse NPAI NS displayed sensitivity to Panobinostat ($p < 0.0001$), with NPAI ZMYND8 WT having an IC_{50} of 0.0340μM versus NPAI ZMYND8 KO with an IC_{50} of 0.0075μM (**Fig. 4.5E**). Similarly, both RPAI NS showed sensitivity

to Panobinostat ($p < 0.0001$), with RPAI ZMYND8 KO having an IC_{50} of 0.0082μM versus RPAI ZMYND8 WT with an IC_{50} of 0.41μM (**Fig. 4.5F**). We found that the NPAI ZMYND8 KO were more sensitive to BRD4 and HDAC inhibition compared to the NPAI ZMYND8 WT, which was also confirmed in the RPAI ZMYND8 KO versus RPAI ZMYND8 WT. The ZMYND8 KO mIDH1 GCCs exhibited higher levels of radiosensitization when IR was delivered in combination with either BRD4 or HDAC inhibition (**Fig. 4.4C**). Collectively, this data suggests the inhibition of epigenetic modulators BRD4 or HDAC in combination with IR further reduced the cellular viability of ZMYND8 KO mIDH1 GCCs.

Our results demonstrate that the changes in the sensitivity to BRD4 and HDAC inhibitors on ZMYND8-KO cells are directly related to the loss of ZMYND8 and not to changes on the expression of BRD4 and HDAC. Also, the expression of BRD4, HDAC1, and HDAC2 do not show a correlation with the expression levels of ZMYND8 (**Fig. 4.6A-I**).

These findings were further confirmed through mIDH1 MGG119 GCCs which were untreated, treated with vehicle (DMSO), or 5 μM AGI-5198 every 2 days for 1 week. Protein was extracted and the expression of HDAC1, HDAC2, and BRD4 was determined using western blot analysis (Supplementary Figure S12). We observed no significant difference in HDAC1 and HDAC2 protein expression between all three experimental groups (**Fig. 4.7A-D**). We observed a slight increase in the expression of BRD4 in MGG119 treated with AGI-5198 when compared with DMSO-treated cells ($p < 0.01$), however, this difference was not considered biologically meaningful (**Fig. 4.8A-B**).

In vivo impact of radiation on mIDH1 ZMYND8-WT and mIDH1 ZMYND8-KO mouse models

Tumor-bearing mice were irradiated with a dose of 2Gy/day for 5 days each cycle (20 Gy total) for both experimental groups (**Fig 4.9A-B**). Tumor burden was confirmed using IVIS bioluminescence and radiation treatment started 10 days post tumor implantation. We observed a minor increase in the median survival mIDH1 (MS=18 days) vs. mIDH1+IR (MS=22 days) in the group with mIDH1 tumors (p=0.0045) (**Fig 4.9C**). The efficacy of radiation was more significant in mIDH1/ZMYND8 KO (MS=25 days) vs. mIDH1/ZMYND8KO+IR (MS=34 days) tumors (p=0.0084) (**Fig 4.9D**).

ZMYND8 KO mIDH1 GCCs are more susceptible to PARP inhibition

Considering the elevated expression of DDR proteins following IR in ZMYND8 KO GCCs compared to ZMYND8 WT GCCs, we wondered if this resulted from an impaired resolution of DNA damage due to intrinsic genomic stress occurring within the ZMYND8 KO GCCs. We speculated that loss of ZMYND8 would increase the susceptibility of mIDH1 GCCs to chemicals that promote genotoxic stress. To evaluate this, we targeted PARP, an initial sensor of DNA lesions specifically at single-stranded DNA breaks (SSB) (**Fig. 4.10**). PARP1 and PARP2 catalyze a reaction that utilizes NAD+ to attach negatively charged poly(ADP-ribose) polymers to various target proteins, including itself, to signal the recruitment of DNA repair proteins to the region. We choose to utilize Pamiparib, a selective PARP1/2 inhibitor which prevents PARP from binding to DNA, thus preventing the formation of PARP-DNA complexes which allow for the persistence of unrepaired SSB (**Fig. 4.10**) (Li et al., 2020). The PARP-DNA adducts create a barrier at replication forks, resulting in fork collapse and the formation of DSBs (**Fig. 4.10**) (Li et al., 2020). We observed a significant reduction ($p < 0.001$) in cellular viability of the SF10602 ZMYND8 KO to

increasing doses of Pamiparib with an IC_{50} of 12.6μM versus the SF10602 ZMYND8 WT with an IC_{50} of 88.5 μM (**Fig. 4.11A**). When we combined Pamiparib with 20Gy IR, we observed enhanced therapeutic response in the SF10602 ZMYND8 KO compared to the SF10602 ZMYND8 WT (**Fig. 4.11B**). The sensitivity of SF10602 to Pamiparib +IR was further enhanced by the loss of ZMYND8, where this combination was also supported in the MGG119 (**Fig. 4.12A-B**). Next, we evaluated the response of our mouse mIDH1 GCCs to PARP inhibition; we observed a significant reduction in cellular viability of NPAI ZMYND8 KO to Pamiparib alone with an IC_{50} of 4.9μM versus the NPAI ZMYND8 WT with an IC_{50} of 50.5μM (**Fig. 4.11C**). We also validated the response to Pamiparib in a second mIDH1 model (RPAI) *in vitro* presented in **Fig. 4.12C-D**, which determines the efficacy of PARP inhibition and irradiation comparing mIDH1 ZMYND8 WT vs. mIDH1 ZMYND8 KO cells. Comparably, RPAI ZMYND8 KO glioma cells displayed a significant reduction in cellular viability when treated with Pamiparib (IC_{50} = 2.0μM; $p < 0.0001$) vs. RPAI ZMYND8 WT glioma cells (IC_{50} = 44.7μM) (**Fig. 4.12C**). In the combination of Pamiparib and 6Gy IR, we similarly observed an enhanced therapeutic response in the NPAI ZMYND8 KO compared to the NPAI ZMYND8 WT (**Fig. 4.11D**). Additionally, the combination of Pamiparib with IR (6 Gy) significantly ($p < 0.01$) reduced cellular viability of RPAI ZMYND8 KO glioma cells compared to RPAI ZMYND8 WT glioma cells at all concentration of Pamiparib used (**Fig. 4.12D**). The recruitment of ZMYND8 to regions of DNA damage has been proposed to be mediated by PARP (Spruijt et al., 2016). These data suggest that PARP could function upstream of ZMYND8. To translate these findings to *in vivo*, we implanted 50,000 NPAI ZMYND8 WT GCCs in immunocompetent C57BL6 mice and confirmed tumor burden based on IVIS bioluminescence signal at 10 days post implantation (dpi). Tumor bearing mice were administered saline or Pamiparib (1mg/mL) and with/out IR, as indicated in **Fig. 4.13A**. We observed a 1.7-fold

($p < 0.05$) increase in the MS of mice in the Pamiparib + IR group (MS: 55dpi) when compared to IR alone (MS: 38 dpi) or Pamiparib alone (MS:34 dpi) (Fig. 6G). When compared to the control mice that received saline (MS:29 dpi), mice in the Pamiparib + IR group displayed a 1.9-fold ($p<0.01$) increase in MS (**Fig. 4.13B**). We did not observe a significant difference in viability in response to AGI-5198 treatment in NPAI ZMYND8 WT versus ZMYND8 KO, but when combined with IR we observed a modest reduction in viability $p<0.05$ (**Fig. 4.13C**). The enhanced sensitivity of mIDH1 GCCs to IR after the genetic knockout of ZMYND8, or treatment with HDAC or PARP inhibitors, propose a novel vulnerability of mIDH1 GCCs to respond to IR-induced DNA damage. We speculate that the loss of transcriptional repression mediated by ZMYND8's recruitment of NuRD or ZMYND8 recognition of DNA damaged regions marked by PARP leads to defective HR repair in mIDH1 GCCs (**Fig. 4.13D**).

To address whether ZMYND8 expression varied across LGG patients based on IDH1 mutation status, we analyzed publicly available RNA-seq data from the The Cancer Genome Atlas (TCGA) LGG dataset (**Fig. 4.14A**). We observed a significant increase ($p<0.05$) in log2-normalized ZMYND8 expression in mIDH1 LGG versus wtIDH1 LGG. When we stratified the overall survival (OS) of LGG patient into low- or high-ZMYND8 expression groups, we found that high-ZMYND8 mIDH1 LGG were associated with poor clinical outcome with a median OS of 6.3yrs as compared with low-ZMYND8 mIDH1 LGG with a median OS of 7.9yrs (**Fig. 4.14B**). There was no significant difference found within wtIDH1 LGGs, where high-ZMYND8 wtIDH1 LGGs had a median OS of 1.7yrs compared with 2.0yrs in low-ZMYND8 wtIDH1 LGGs. This significant discrepancy in OS found amongst mIDH1 LGGs ($p<0.0001$), indicates that a subset of mIDH1 glioma overexpress ZMYND8 and of which present with poor patient outcome. Considering that upon recurrence IDH-mutated gliomas present as high-grade, we analyzed

Kaplan Meier survival for median ZMYND8 expression along with mIDH1 status from the Chinese Glioma Genome Atlas (CGGA) for primary and secondary GBM (**Fig. 4.14C-F**). There was no significant discrepancy in median OS found amongst CGGA primary (**Fig. 4.14C**) or secondary (**Fig. 4.14D**) wtIDH1 GBM based on ZMYND8 median expression. We observed a shortening in median OS within primary (**Fig. 4.14E**, $p < 0.0014$) and secondary (**Fig. 4.14F**, $p < 0.0027$) mIDH1 GBM high-ZMYND8 compared to low-ZMYND8 patient tumors.

We performed serum biochemistry analysis of liver and kidney metabolites in the animals receiving Pamiparib, or Pamiparib + IR treatment compared with animals in the saline treatment group. There was no significant difference observed in the serum level of kidney (creatinine, blood urea nitrogen) and liver (aminotransferase, aspartate aminotransferase) metabolites tested in animals treated with Pamiparib, or Pamiparib + IR treatment compared to saline treatment group (**Fig. 4.15A-H**).

Histopathological analysis of liver sections to inspect the potential toxicity of the Pamiparib+IR treatment revealed that the liver tissue sections had no differences in the hepatocytes, stromal central, and portal areas between the control saline and the treatment group (**Fig. 4.16A-B**).

Discussion

Inhibition of epigenetic regulators BRD4 and HDAC further reduced the cellular viability of ZMYND8 KO mIDH1 GCCs. Recent work in AML showed that ZMYND8 recruitment to enhancers was mediated by BRD4 (Cao et al., 2021). The oncogenic programs regulated by BRD4 to support cancer cell survival were downregulated in AMLs when ZMYND8 was depleted (Cao et al., 2021). Inhibition of BRD4 using JQ1 was shown to abolish ZMYND8 occupancy at enhancers (Cao et al., 2021). There is compelling evidence that BRD4 functions at replication

forks, where it associates with several complexes involved in chromatin remodeling (MMS22L, TONSL) and replication (POLA2, POLD3), which we also observed to be upregulated in our RNA-seq analysis (Wessel et al., 2019). Additionally, inhibition of BRD4 either by siRNA knockdown or JQ1 treatment has been shown to induce DNA damage marked by increased γH2AX foci formation (Bowry et al., 2018). Loss of BRD4 induces replicative stress via the deregulation of transcription and in response RAD51 is recruited to damaged DNA regions to suppress replication (Lam et al., 2020).

Traditionally, BRD4 inhibitors like JQ1 compete with the acetyl lysine recognition binding site on BRD4 preventing its ability to facilitate oncogenic transcription at enhancers leading to a suppression of cancer cell growth and apoptosis (Chapuy et al., 2013). More recently, degradation of BRD4 has been shown to induce endogenous DNA damage in cancer cells undergoing replication marked by an increase in γH2AX foci (Edwards et al., 2020). It is likely that the differences in cellular viability of mouse mIDH1 ZMYND8 KO and ZMYND8 WT treated with JQ1/I-BET-762 could be the result of enhanced DNA damage facilitated by inhibition of BRD4 in ZMYND8 KO cells. Treatment of mIDH1 tumor cells with the HDAC inhibitor Vorinostat lead to a suppression of Rad51 and Brca1 expression, along with an increase in cleaved PARP (Dow et al., 2021). HDAC inhibitors have been shown to increase histone acetylation (H3K9, H3K18, H3K56, H4K8, H4K16) and induce senescence mediated by p21 and p27 (Lin et al., 2019). It has been proposed that the hyperacetylation of histone prevents chromatin condensation, a necessary step for DNA repair. While also downregulating the expression of key DNA repair proteins like Ku70, DNA-Pkc, and Rad51 (Carrier, 2013). HDAC inhibitors exhibit broad antineoplastic effects mediated by the induction of apoptosis, cell cycle arrest and inhibition of DNA repair machinery. Our data suggest that the susceptibility of mIDH1 glioma cells to either BRD4 or HDAC inhibitors

is dependent on the expression of ZMYND8. Our data also suggests that BRD4 or HDAC expression levels are not correlated with the levels of ZMYND8 expression.

PARP functions as an early sensor of DNA damage and has been shown to rapidly deposit poly-ADP ribose chains (PARylation) at newly generated DNA DSB within milliseconds (Caron et al., 2019). The recruitment of ZMYND8 to laser-induced DSB was shown to be dependent upon the presence of PARylation (Spruijt et al., 2016). Surprisingly, we observed that ZMYND8 WT mIDH1 glioma cells were sensitive to Pamiparib treatment, but ZMYND8 KO mIDH1 glioma cells displayed a further decrease in cellular viability. Recent studies have observed enhanced sensitivity of IDH-mutant glioma to PARP inhibition using preclinical mouse models and human glioma stem cell lines (Lu et al., 2017; Wang et al., 2020). Pamiparib (BGB-290) in combination with TMZ is currently being evaluated clinically for the treatment of IDH1/2 mutant grade I-IV Gliomas (NCT03749187) and recurrent gliomas with IDH1/2 mutations (NCT03914742). Moreover, our data shows that ZMYND8 functions alongside PARP to signal the repair of IR induced DNA damage.

PARP inhibitors and antibodies that inhibit immune checkpoints, like CTLA-4, PD-1 and PD-L1 are currently being evaluated in clinical trials for ovarian, breast, prostate, lung, urothelial, and gastrointestinal cancers (Vikas et al., 2020). In preclinical models of breast cancer, PARP inhibitors have been shown to upregulate the expression of PD-L1 (Jiao et al., 2017). To date, clinical trials in recurrent IDH-mutant glioma are recruiting patients to evaluate PARP inhibitors alone and in combination with chemotherapeutic agents like temozolomide and carboplatin (Sim et al., 2022). Also, the combination of Olaparib, a PARP inhibitor, and durvalumab, a PD-L1 antibody, is currently being investigated in patients with recurrent IDH-mutated high-grade glioma (Ramos et al., 2021).

To our knowledge, a direct connection between ZMYND8 regulation at the chromatin level within mIDH1 glioma has not previously been described. However, we found that high ZMYND8 expressing mIDH1 LGG patient tumors exhibited a shorter median OS as compared with low ZMYND8 expressing mIDH1 LGG.

In summary, by examining the alterations to the epigenome and biological pathways following mIDH1 inhibition, we provide novel evidence that ZMYND8 is epigenetically regulated by mIDH1 reprogramming in patient derived mIDH1 GCCs and in our genetically engineered mouse mIDH1 glioma model. In addition, our data shows that ZMYND8 supports the survival of human mIDH1 GCCs and mouse mIDH1 NS in response to radiation through its role in contributing to DNA repair and genomic stability. Genetic ablation of ZMYND8 in combination with epigenetic inhibitors against PARP, HDAC, and BRD4 further reduces the cellular viability of mIDH1 GCCs to IR induced DNA damage. We anticipate these findings will provide support for the development of ZMYND8 specific inhibitors, which represents a viable target for the treatment of mIDH1 gliomas.

Materials and Methods

Platelet Derived Growth Factor Receptor Mutant D842V ($PDGFR^{D842V}$)-driven mouse mIDH1 glioma neurospheres

We have generated an additional mIDH1 glioma model (RPAI) driven by platelet derived growth factor receptor alpha mutation ($PDGFRA^{D842V}$) to promote constituent activation of the MAPK pathway, which have been shown to induce tumors in diffuse intrinsic pontine glioma (DIPG) models (Patel et al., 2020). These mouse glioma cells endogenous express IDH1-R132H, along with ATRX and TP53 short hairpin knockdown to simulate the molecular genetic lesions that

define the molecular features of astrocytoma. Tumor NS were derived from endogenous mIDH1 tumors that were adapted to *in vitro* culture and could be reimplanted into NSG mice to demonstrate the ability to form tumors.

In vitro dose-response and evaluation of radiosensitivity using PARP inhibitor

To assess the susceptibility of both ZMYND8 WT and ZMYND8 KO generated in mouse mIDH1 NS and human mIDH1 GCCs to PARP inhibitor (PARPi), we used Pamiparib (BGB-290) (SelleckChem, Cat# S8592), a PARPi for our study. Herein, both the cells were plated at a density of 1500 cells per well in 96-well plates (Fisher, 12-566-00) 24h prior to treatment. We used 5 wells per inhibitor dose evaluated for each cell type. We evaluated 8 concentrations of inhibitor in serial dilutions (e.g., 1μM, 3μM, 10μM, 30μM, 50μM, 100μM) and were added to each well for each dilution evaluated. Cells were then incubated for 3 days and viability was assessed using CellTiter-Glo assay (Promega, Cat# G7572) following manufacturer's protocol. Moveover to assess the radiosensitization, cells were then incubated with either Pamiparib alone or in combination with radiation at their respective IC_{50} doses for 72h in triplicate wells per condition. Cells were pre-treated with PARPi 2h prior to irradiation with 6Gy and 20Gy of radiation for mouse neurospheres and human glioma cells respectively. Resulting luminescence was read with the Enspire Multimodal Plate Reader (Perkin Elmer). Data was represented graphically using the GraphPad Prism 7 (RRID:SCR_002798) using sigmoidal regression model which allows the determination of IC_{50} values and statistical significance was determined by one-way ANOVA followed by Tukey's test for multiple comparisons.

Tumor implantation and inhibition of DNA damage response *in vivo*

NPAI ZMYND8-WT GCCs (50,000 cells) were implanted in immunocompetent C57BL6 (The Jackson Laboratory, C57BL/6J Strain# 000664) mice. Mice were anesthetized using ketamine (75mg/kg, I.P) and dexmedetomidine (0.5mg/kg, I.P) before stereotactic implantation with cells in the right striatum. The coordinates for implantation were 1.0 mm anterior and 2.0 mm lateral from the bregma, and 3.5 mm ventral from the dura. Neurospheres were injected at a rate of 1 μL/min. Mice were given a combination of buprenorphine (0.1mg/kg, S.C) and carprofen (5mg/kg, S.C) for analgesia. Tumor burden was confirmed based on IVIS bioluminescence signal at 10 days post-implantation (dpi), and the mice were divided into 4 groups: i. Saline; ii. Pamiparib injected (1mg/mL); iii. IR treated; and iv. Pamiparib+IR. Mice were administered with 10 mg/Kg of Pamiparib, dissolved in 10% (2-hydroxypropyl)- β-cyclodextrin (Sigma Aldrich, Cat# H107-5G), and injected in a volume of 200 uL, 5 days per week for two weeks. Mice were lightly anesthetized with isoflurane and placed under a copper Orthovoltage source, with the irradiation beam directed to the brain, while the body was shielded by iron collimators. A dose of 2 Gy per irradiation session was given 5 days per week for two weeks, for a total of 20 Gy. Irradiation treatment was given to the mice at the University of Michigan Radiation Oncology Core.

Histone Extraction

To assess changes in histone modifications in RPAI NS treated with either vehicle (DMSO) or mIDH1 inhibitor (AGI-5198) (MedKoo Biosciences, Inc. Cat# 406264), we collected histone extracts using the Histone Purification Mini Kit (Active Motif, Cat# 40026). We performed WB analysis using 10μg histone protein and assessed global histone mark modifications for H3K4me3 (Diagenode, Cat# C15410003-50), H3K27me3 (Diagenode, Cat# C15410195), H3K27ac

(Diagenode, Cat# C15410196) and H3K36me3 (Diagenode, Cat# C15410192) relative to total histone 3 (Cell Signaling, Cat# 9715S).

The Cancer Genome Atlas (TCGA) and Chinese Glioma Genome Atlas (CGGA) Analysis

Low Grade Glioma patient clinical annotation and RNA-seq data from the NCI Genomic Data Commons (GDC) repository were downloaded using the TCGAbiolinks package (Colaprico et al., 2016). All CGGA data were downloaded from the Chinese Glioma Genome Atlas (http://www.cgga.org.cn/) (Chinese Glioma Genome Atlas, RRID:SCR_018802) (Zhao et al., 2021). mRNA expression levels were normalized and ZMYND8 expression was compared between wtIDH1 and mIDH1 samples using a Log-rank test. The relationship between patients' overall survival and the levels of ZMYND8 were identified by the R packages "survminer" and "survival".

Human single cell-RNA-sequencing (scRNA-seq)

Human glioma scRNA seq was performed and analyzed as previously described. (Alghamri et al., 2021) The data has been deposited in NCBI's Gene Expression Omnibus (GEO, RRID:SCR_005012) with identifier (GSE152277). Briefly, freshly isolated primary tumor tissue was kept in DMEM/F12 media (Gibco). Tissue was cut into small pieces until a homogenous solution was obtained. The cell suspension was passed through 70 μm strainer to remove debris and connective tissue, lysed with RBC's lysis buffer (Biolegend), and passed through dead cells removal column (Miltenyi Biotec). 3' single cell libraries were generated using the 10X Genomics Chromium Controller following the manufacturer's protocol for 3' V3.1 chemistry with NextGEM Chip G reagents (10X Genomics). Final library quality was assessed using the Tapestation 4200 (Agilent), and libraries were quantified by Kapa qPCR (Roche). Pooled libraries were subjected

to 150 bp paired-end sequencing according to the manufacturer's protocol (Illumina NovaSeq 6000). Raw sequencing data files were converted to fastq files and aligned to the human reference genome using the Cell Ranger Pipeline (10X Genomics). The data were clustered and gene expression were analyzed using the Seurat R package.

Efficacy of radiation in mIDH1 ZMYND8-WT vs. mIDH1 ZMYND8-KO glioma bearing mice

CD8 knock-out mice (The Jackson Laboratories, B6.129S2-Cd8^{atm1Mak}/J, Strain# 002665) were anesthetized using ketamine (75mg/kg, I.P) and dexmedetomidine (0.5mg/kg, LP) prior to stereotactic implantation with 50,000 NPAI & NPAI ZMYNDKO cells in the right striatum. We used CD8 KO mice for this experiment to eliminate the impact of the adaptive immune system in the efficacy of radiation. The coordinates for implantation were 1.0 mm anterior and 2.0 mm lateral from the bregma and 3.5 mm ventral from the dura. Neurospheres were injected at a rate of 1 μL/min. Mice were given a combination of buprenorphine (0.1mg/kg, S.C) and carprofen (5mg/kg, S.C) for analgesia. Ten days' post tumor cell implantation, mice were subjected to ionizing irradiation (IR) using a dose of 2 Gy, 5 days per week for two weeks, for a total of 20 Gy of IR. Mice were lightly anaesthetized with isoflurane. Mice were placed under a copper Orthovoltage source, with the irradiation beam directed to the brain, the body of the mouse was shielded by iron collimators. Irradiation treatment was given to mice at the University of Michigan Radiation Oncology Core.

Serum Chemistry

Blood was collected from the submandibular vein from mIDH1glioma bearing mice and transferred to serum separation tubes (Biotang). Samples were incubated at room temperature for

60mins to allow for blood coagulation. Tubes were then centrifuged at 2000 rpm (400 x g) for 15 minutes and serum was collected from the tubes. Complete serum chemistry for all samples was assessed by the Veterinary Core Facility at the University of Michigan Medical School.

Liver Hematoxylin & Eosin (H&E) staining in experimental mouse groups

Livers were embedded in paraffin for histological analysis, 5µm thick sections were generated using the microtome system and sections were stained using H&E as described below. Sectioned livers were de-paraffinized by placing them for 10 min in a 60 °C oven and then transferring them at 5 min intervals through a series of three slide containers filled with xylene. the slides were Hydrated through a series of ethanol baths: 100% ethanol for 2 min, repeat once, 95% ethanol for 2 min, repeat once, 70% ethanol for 2 min and then transferred to water. The slides were stained by dipping them in a slide container filled with Harris Hematoxylin for 2 min. Rinse in tap water until water is clear. Dip slides twice into bluing solution (0.1% Sodium Bicarbonate). Let slides stand in tap water for 2 min, then transfer to 80% ethanol for 2 min. After, the slides were dipped in a container filled with Eosin for 5 min. Dehydrate slides in a series of ethanol baths (80% ethanol 3-4 dips, 95% ethanol 2 min, repeat once, 100% ethanol 2 min, repeat once). Clear with 3 consecutive baths of xylene, 3 min each. Coverslip with a xylene-based mounting medium and let dry on a flat surface at room temperature until ready for imaging. Store at room temperature. Brightfield images were acquired employing an Olympus MA BX53 microscope.

Figures

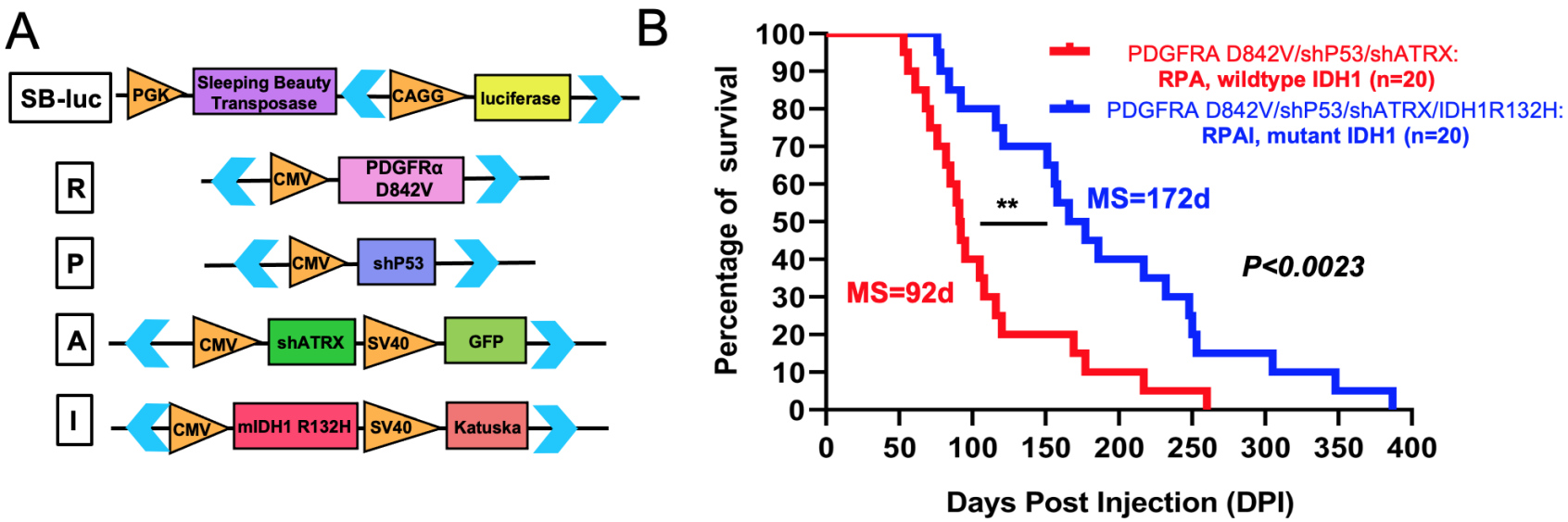

Figure 4.1 Generation of PDGFRαD842V-driven mouse glioma model using SB transposase system

(A) Schematic representation of sleeping beauty transposase (SB) luciferase (luc) and oncogenic DNA plasmids used to develop gliomas in mice. Blue arrows indicate position of inverted and direct repeat sequences recognized by SB for integration, which flank oncogenic DNA sequences that encode for constitutively active PDGFRA D842V receptor, shP53, shATRX-GFP and mIDH1 R132H-Katuska [RPAI]. (B) Kaplan-Meier survival curves for mice bearing wtIDH1 (RPA, n=20) or mIDH1 (RPAI, n=20) gliomas (**$P < 0.01$, Mantel-Cox test).

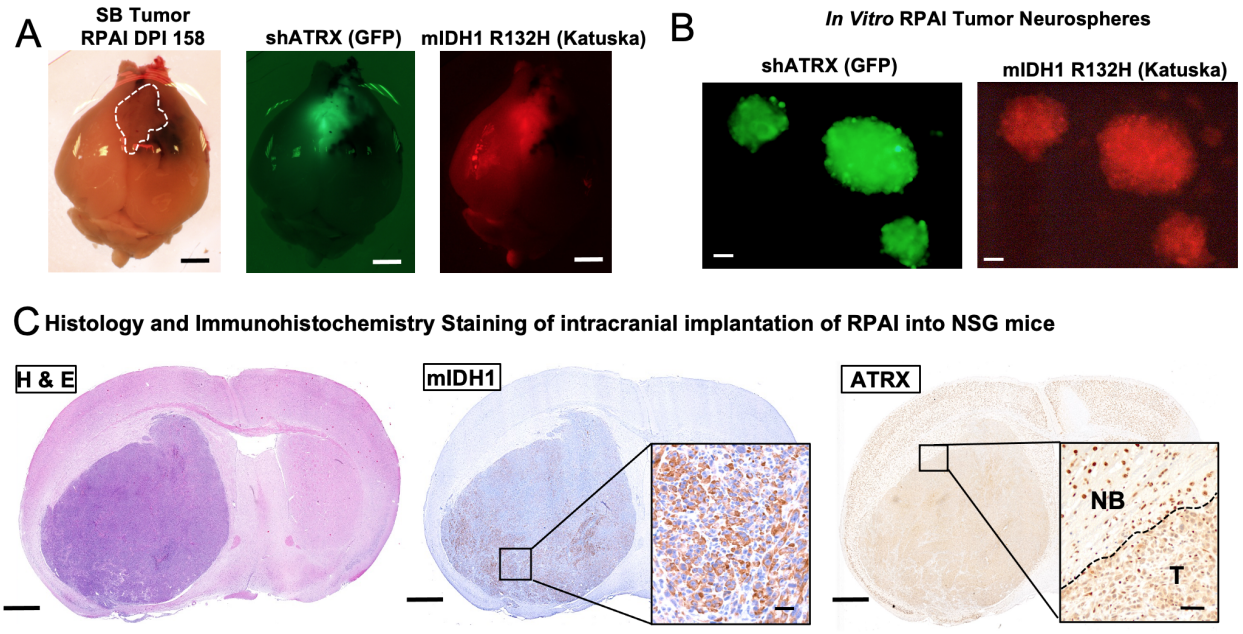

Figure 4.2 Fluorescent imaging and histological confirmation of genetic lesions (shATRX-GFP and mIDH1R132H-Katsuska) in primary sleeping beauty (SB) derived tumor, neurospheres maintained *in vitro* and reimplanted into NSG mice to determine tumor burden *in vivo*

(A) Representative mouse brain of SB RPAI tumor (dotted outline)158 days post injection (DPI) with fluorescence microscopic images of GFP corresponding to shATRX-GFP plasmid integration and Katuska (red) fluorescence corresponding to mIDH1-R132H. Scale bar: 2mm. (B) Fluorescence microscopic images of *in vitro* tumor neurospheres generated from SB-tumor. Scale bar is 500µm. (C) Hematoxylin and eosin (H&E) histological stain of NSG mouse brain tumor which was intracranially implanted with RPAI NS. Brain tissue was stained by IHC for mIDH1 and ATRX. Brain section scale bar: 1mm, mIDH1 IHC scale bar: 20µm, ATRX IHC scale bar: 50µm with the tumor boundary defined by dotted line, NB-normal brain, T-tumor tissue.

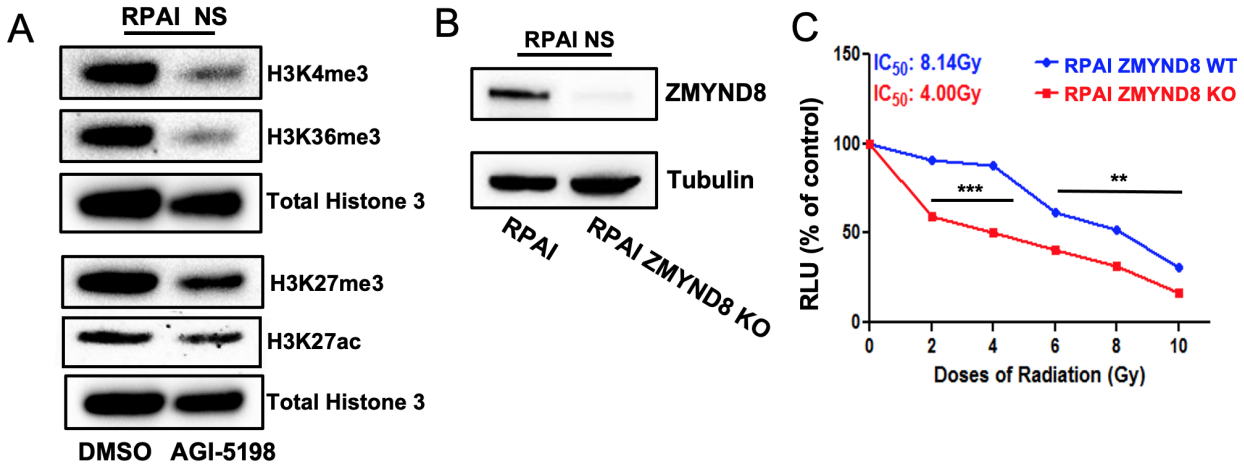

Figure 4.3 Reversal of histone mark hypermethylation in murine mIDH1 NS (RPAI) treated with AGI-5198 and increased sensitivity to IR in RPAI ZMYND8 KO vs. RPAI ZMYND8 WT

(A) Western blot representative of changes in histone mark (H3K4me3, H3K36me3, H3K27me3, H3K27ac) protein expression in RPAI NS treated with either DMSO or AGI-5198 for 1 week. (B) Western blot of ZMYND8 expression in RPAI vs. RPAI ZMYND8 KO and (C) Cellular viability 72hrs post-IR in RPAI vs. RPAI ZMYND8 KO. Errors bars represent standard error of mean (SEM) from independent biological replicates (n=3). ** $p<0.01$, *** $p<0.001$; unpaired t test.

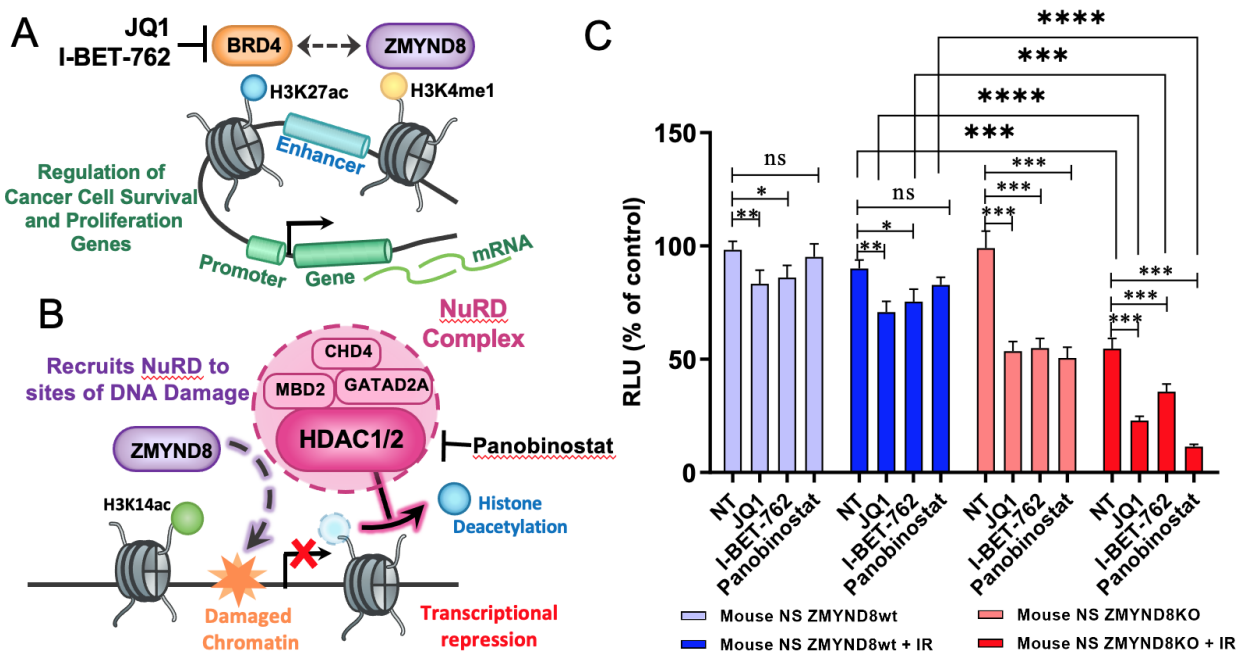

Figure 4.4 Inhibiting ZMYND8-interacting partners Bromodomain-containing protein 4 (BRD4) and Histone deacetylase 1/2 (HDAC1/2) enhances the susceptibility of NPAI ZMYND8 KO to IR relative to NPAI ZMYND8 WT

(H) Working model of ZMYND8-interacting partner Bromodomain-containing protein 4 (BRD4), where ZMYND8 is recruited to enhancer regions marked by H3K4me1 and contributes to the regulation of cancer cell survival and proliferation associated genes. BRD4 inhibitors, JQ1and I-BET-762, can disrupt this interaction. (I) Working model of ZMYND8-interacting partner HDAC1/2 (histone deacetylase 1/2); a component of the Nucleosome Remodeling and Histone Deacetylase (NuRD) complex , where ZMYND8 binds H3K14ac residues present at damaged chromatin regions and recruits HDAC along with other NuRD subunits:MDB2, CHD4, and GATAD2A. Panobinostat inhibits HDAC1/2 and prevents histone deacetylation mediated by HDAC1/2, which is required for transcriptional repression at regions of DNA damage. (J) Representative bar graph of cellular viability measured in RLU, which shows the effect of BRD4 (JQ1, I-BET-762) or HDAC (Panobinostat) inhibition alone (-IR) or in combination with irradiation (+IR) in mouse NPAI ZMYND8 wt in blue vs. NPAI ZMYND8 KO in red. Errors bars represent SEM from independent biological replicates (n=3). ns-not significant, * P<0.05, ** P<0.01, *** P<0.001, **** P < 0.0001; two-tailed t test.

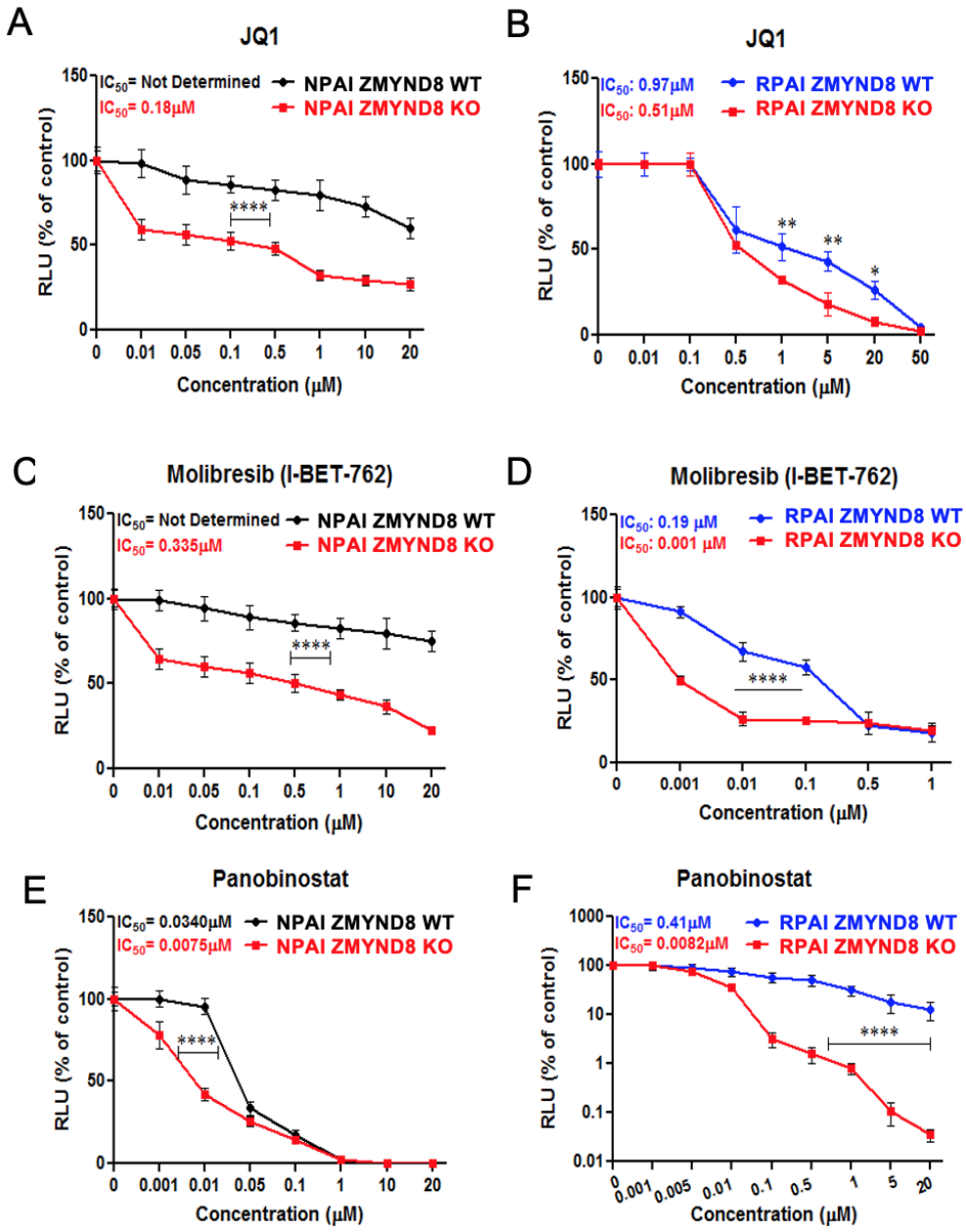

Figure 4.5 ZMYND8 KO mouse mIDH1 NS display reduced viability in response to epigenetic inhibitors targeting BRD4 and HDAC compared to ZMYND8 WT NS

The impact of epigenetic inhibitors targeting BRD4 (JQ1, I-BET-762) and HDAC (Panobinostat) on *in vitro* cellular viability was assessed in two mIDH1 mouse NS comparing parental (ZMYND8 WT) vs. ZMYND8 KO isogenic clones. Cellular viability was determined based on CellTiter-Glo Assay measured in relative luminescence unit (RLU) compared to non-treated controls. (A) Mouse NS harboring NRasG12V, shP53, shATRX, mIDH1R132H mutations [NPAI] ZMYND8 WT (black) vs. ZMYND8 KO (red) treated with JQ1 for 72hrs. (B) Mouse NS harboring PDGFRαD842V, shP53, shATRX, mIDH1-R132H mutations [RPAI] NS expressing ZMYND8 WT (blue) vs. ZMYND8 KO (red) treated with JQ1 for 72hrs. (C) Cellular viability of NPAI ZMYND8 WT vs. ZMYND8 KO treated with I-BET-762 for 72hrs. (D) Cellular viability of RPAI ZMYND8 WT vs. ZMYND8 KO treated with I-BET-762 for 72hrs. (E) Cellular viability of NPAI ZMYND8 WT vs. ZMYND8 KO treated with Panobinostat for 72hr. (F) Cellular viability of RPAI ZMYND8 WT vs. ZMYND8 KO treated with Panobinostat for 72hrs with RLU represented in log scale. The data are representative of three independent biological replicates and error bars denote the SEM of samples performed in triplicate. *p<0.05, **p<0.01, ***p<0.001, ****p<0.0001; unpaired t test

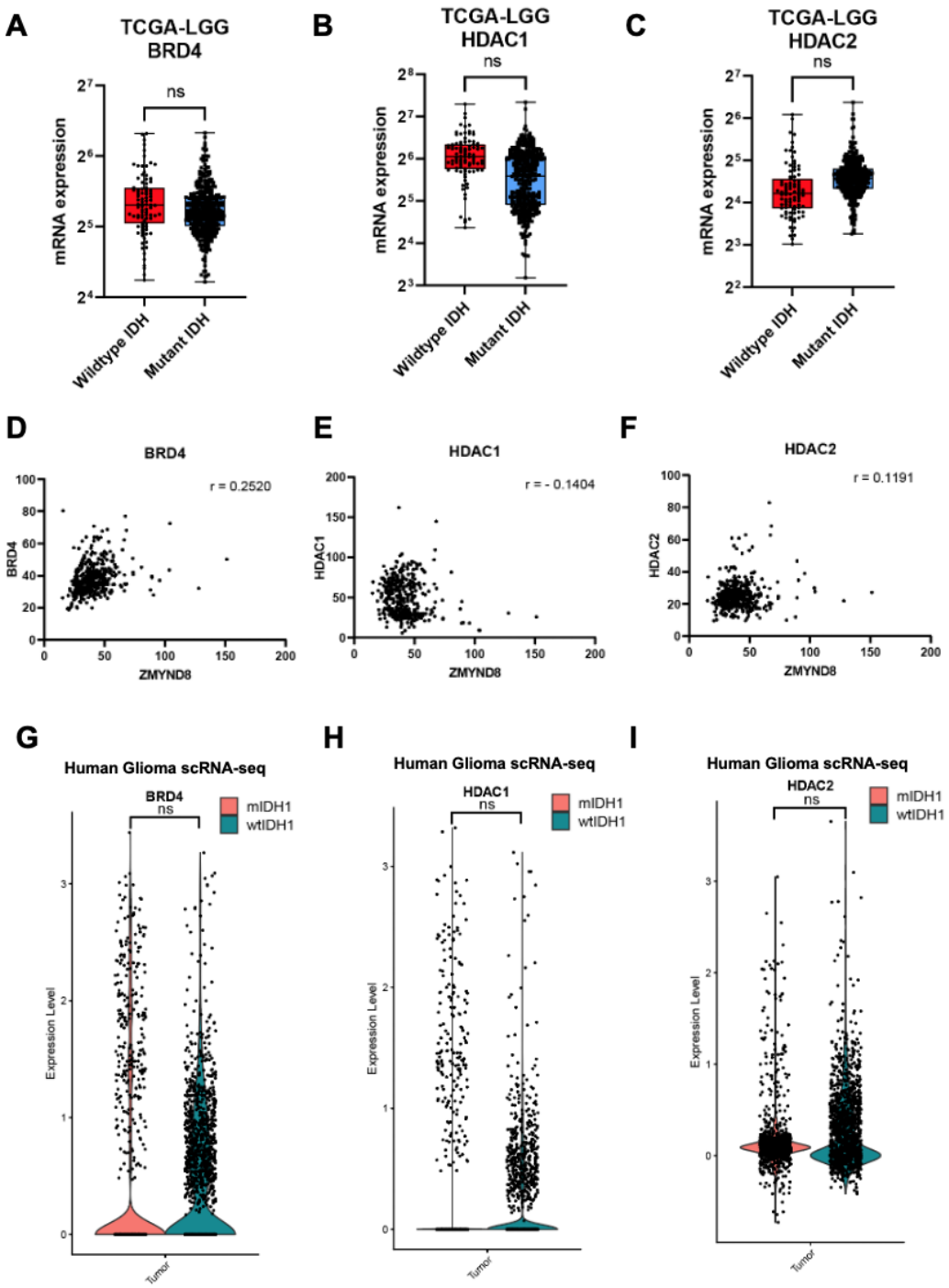

Figure 4.6 No correlation or alterations in gene expression for BRD4 and HDAC1/2 based on mIDH status or ZMYND8 expression in LGG tumors and scRNA-seq from glioma patients.

(A) Analysis of RNA-seq data obtained from TCGA to quantify BRD4 mRNA in LGG with wtIDH1 or mIDH1. (B) Analysis of RNA-seq data obtained from TCGA to quantify HDAC1 mRNA in LGG with wtIDH1 or mIDH1. C) Analysis of RNA-seq data obtained from TCGA to quantify HDAC2 mRNA in LGG with wtIDH1 or mIDH1. n.s.: not significant, unpaired t-test. (D-F) Correlation between ZMYND8 expression and BRD4, HDAC1 and HDAC2 from TCGA-LGG database with mIDH1. (D)BRD4 (E) HDAC1 (F) HDAC2 was illustrated in scatter plot from TCGA dataset. R value represents the statistical results of the Pearson correlation analysis. (G-I) Human glioma scRNA seq was analyzed for the expression of BRD4, HDAC1 and HDAC2 in wtIDH1 and mIDH1 glioma tumor cells. Violin plots represent the expression of (G) BRD4 (H) HDAC1 (I) HDAC2. ns.: not significant, unpaired t-test.

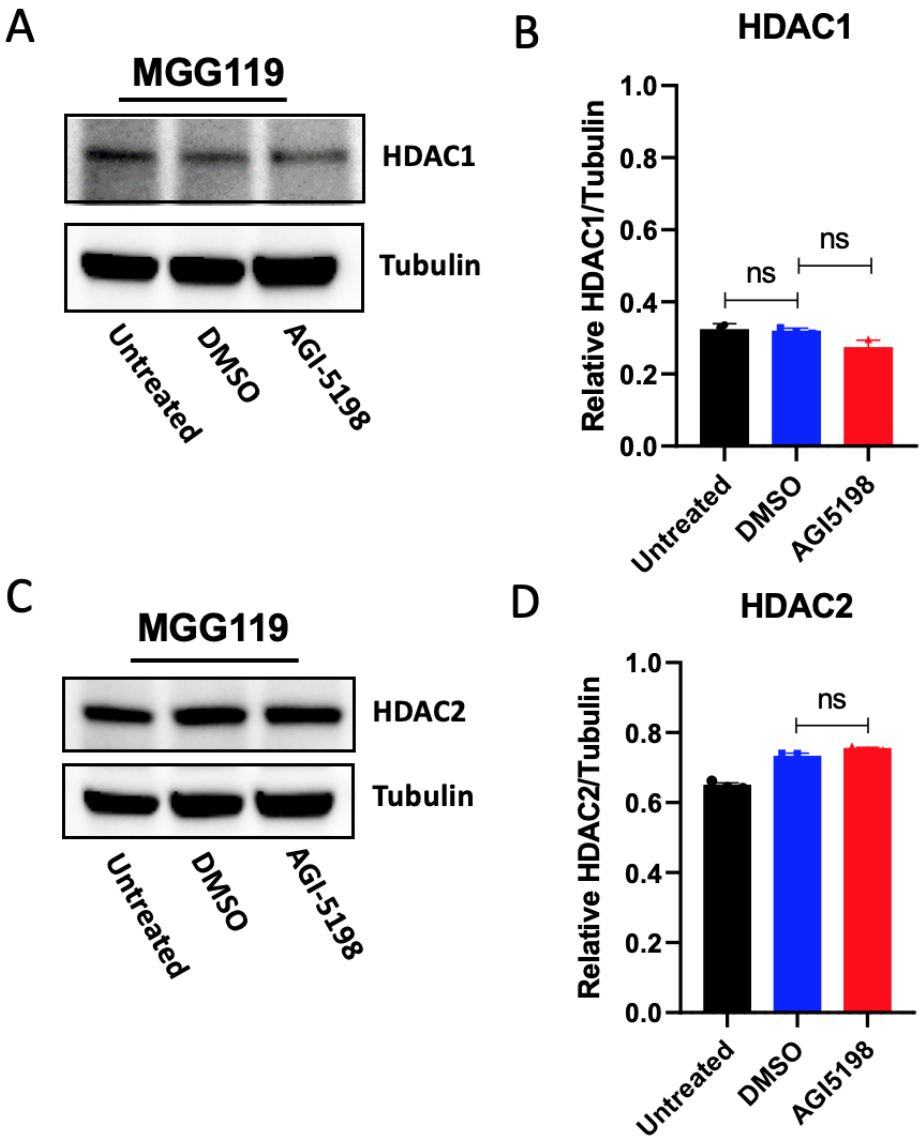

Figure 4.7 Protein expression of HDAC1 and HDAC2 is unaffected by mIDH1 inhibition in human mIDH1 GCC MGG119

Human mIDH1 GCCs treated with a mIDH1 inhibitor (AGI-5198) shows no correlation with HDAC1 and HDAC2 expression Western blot analysis showing (A, B) HDAC and (C, D) HDAC2 expression in MGG119 mIDH1 GCC either untreated, DMSO, or AGI-5198 treatment for 1 week with tubulin as a loading control. ImageJ densitometric quantification of the western blot for HDAC1 and HDAC2. Errors bars represent SEM from independent biological replicates (n=3). ns-not significant; unpaired t test.

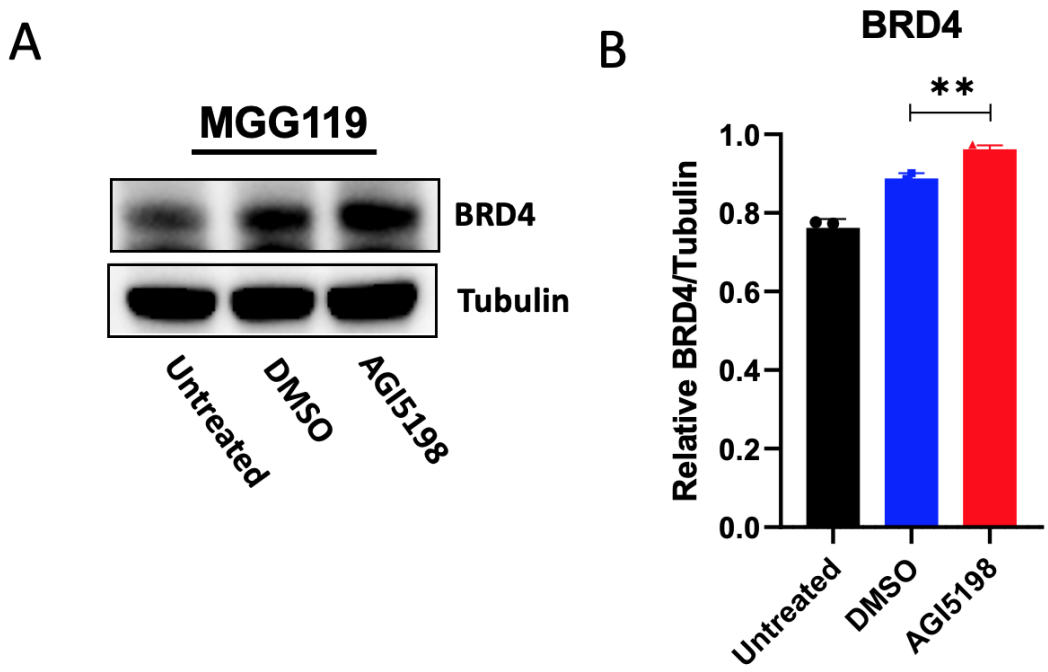

Figure 4.8 Protein expression of BRD4 is increased by mIDH1 inhibition in human mIDH1 GCC MGG119

Human mIDH1 GCCs treated with a mIDH1 inhibitor (AGI-5198) shows slight increase in BRD4 expression by Western blot analysis. (A, B) BRD4 expression in MGG119 mIDH1 GCC either untreated, DMSO, or AGI-5198 treatment for 1 week with tubulin as a loading control. ImageJ densitometric quantification of the western blot for BRD4. Errors bars represent SEM from independent biological replicates (n=3). ** $p < 0.01$; unpaired t test.

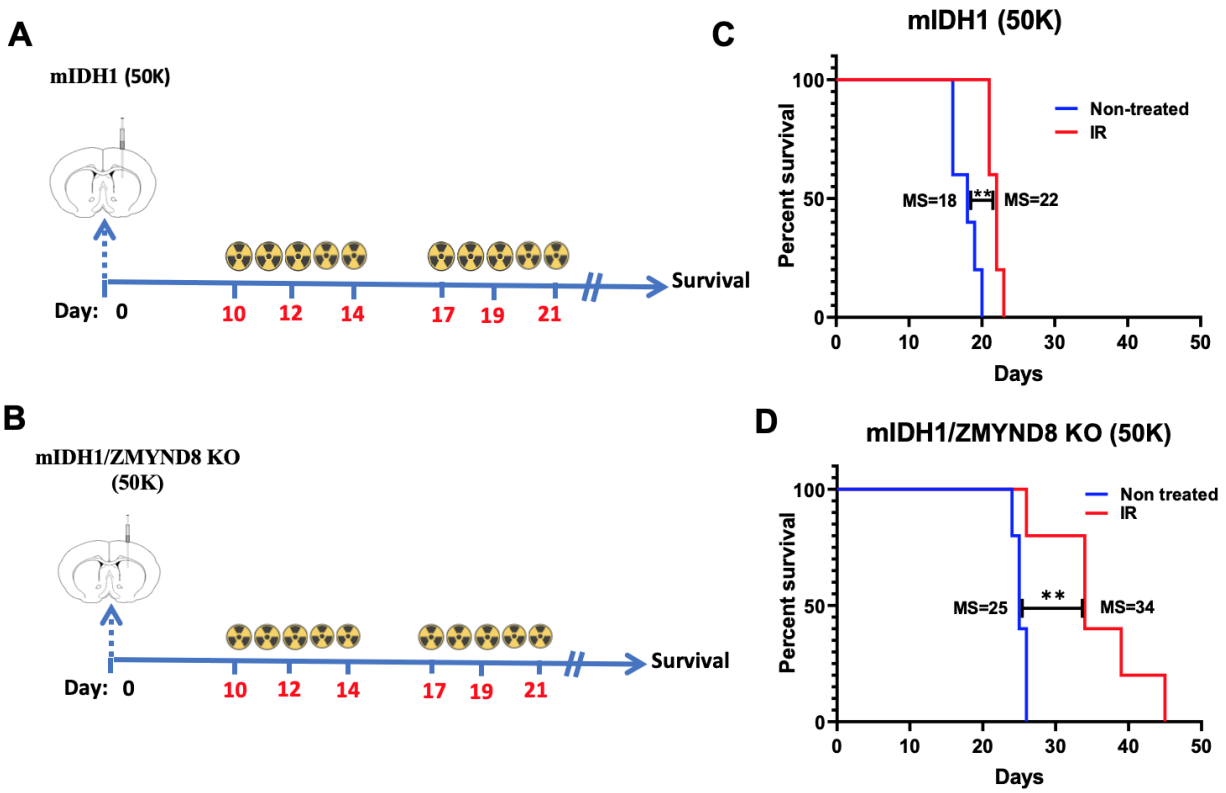

Figure 4.9 Efficacy of radiation therapy on orthotopic mIDH1 and mIDH1 ZMYND8 KO glioma models

Ten days after implantation of 50,000 (A) mIDH1 & (C) mIDH1/ZMYND8 KO NS, animals were randomly divided into 2 groups: (i)Non-treated, (ii) IR received 2Gy/day for 5 days each cycle (20 Gy total). Mice were monitored for tumor burden and euthanized at symptomatic stages to track survival. (B) Kaplan-Meier survival curve: Increase in the median survival (4 days) is seen in the group treated with ionizing irradiation in mIDH1 tumor-bearing mice (p=0.0045). *p<0.05, **p<0.01; log-rank Mantel-Cox test. (D) Kaplan-Meier survival curve: Significant increase in the median survival (9 days) is observed in the treated group in mIDH1/ZMYND8 KO tumor-bearing mice (p= 0.0084). *p<0.05, **p<0.01; log-rank Mantel-Cox test.

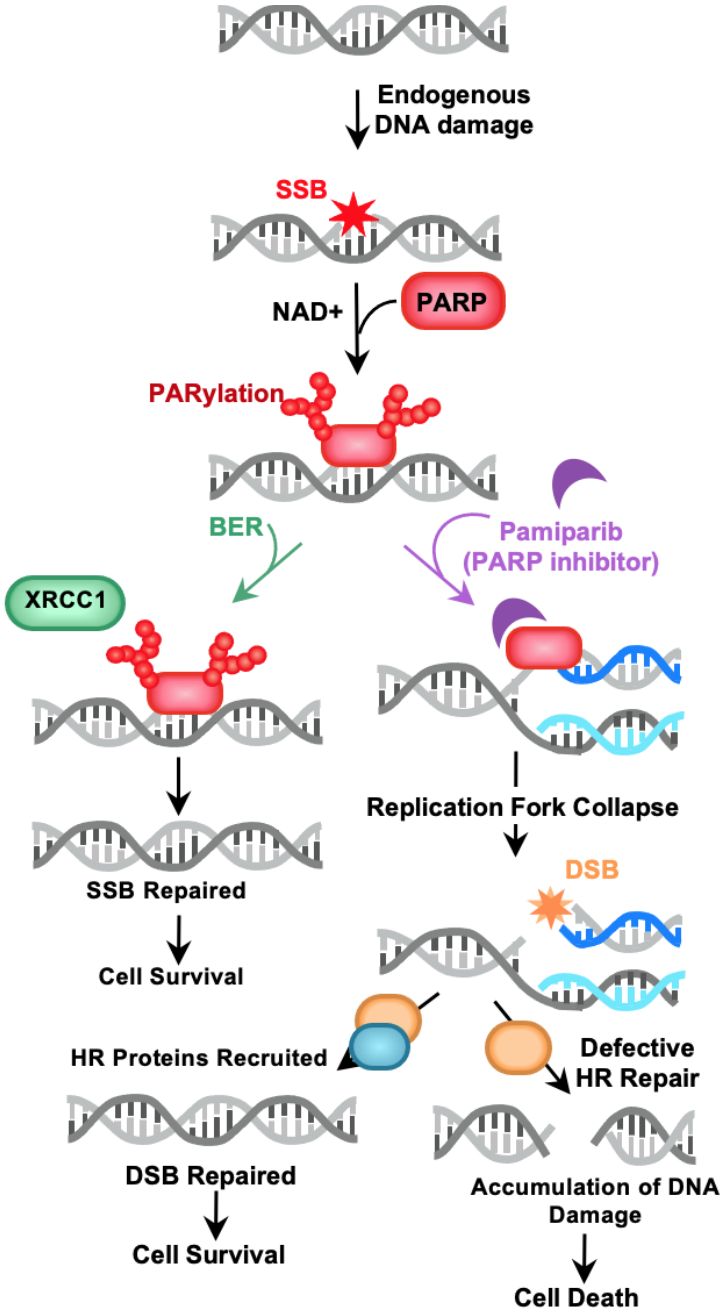

Figure 4.10 Schematic of PARP inhibition on DNA repair pathways

Proposed mechanism of PARP's repair of single stranded breaks (SSB), which occur as a results of endogenous DNA damage in proliferating cells. PARP1/2 catalyze a reaction that utilizes nicotinamide adenine dinucleotide (NAD+) to add poly(ADP-ribose) polymers to itself and signals the recruitment of proteins involved in base excision repair (BER) like XRCC1 to resolve the SSB. Pamiparib (PARP inhibitor) block PARylation and trap PARP onto DNA, resulting in the formation of double stranded breaks (DSB) at collapsed replication forks. Cells that can successfully recruit HR proteins can repair the DSB.

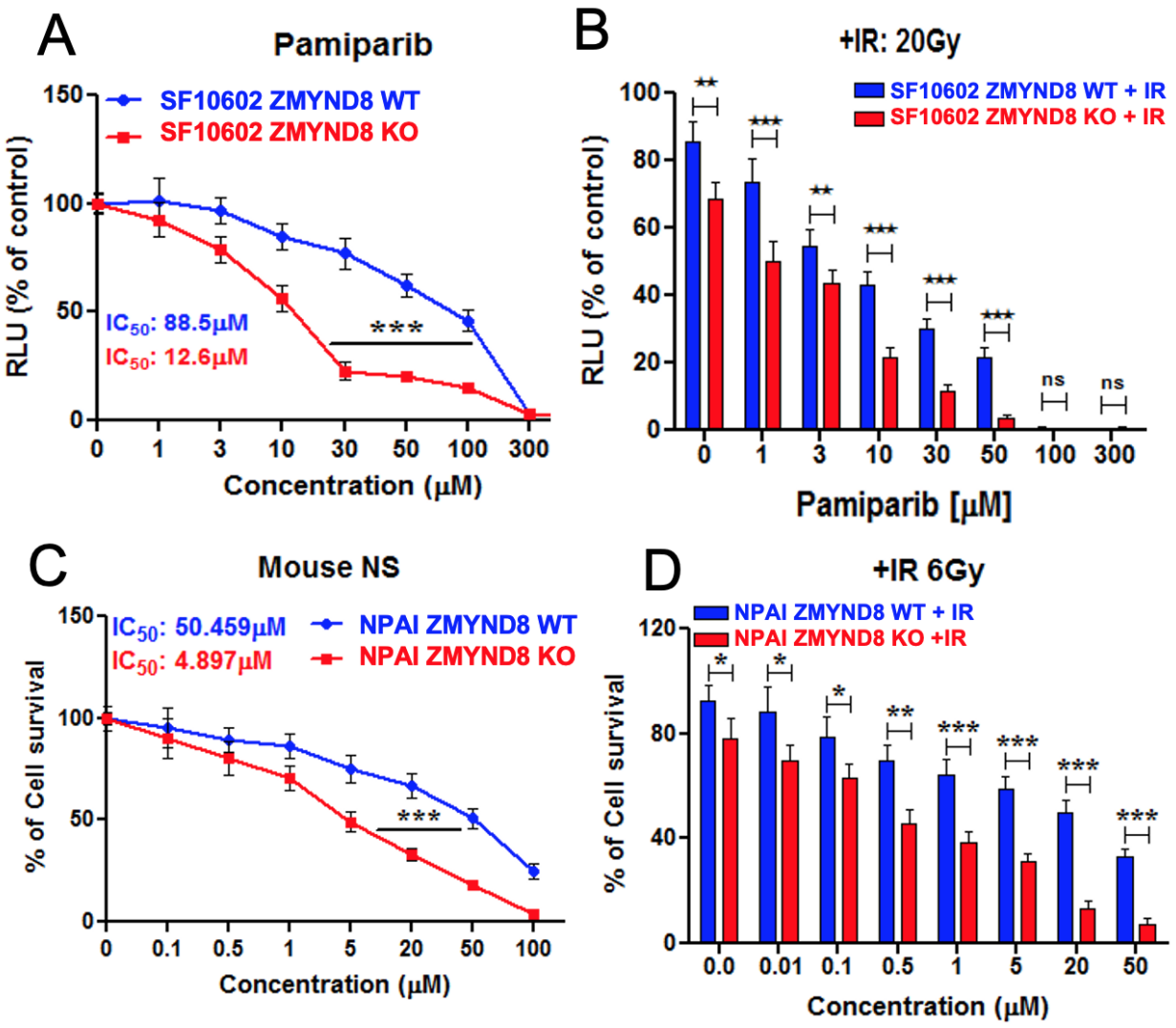

Figure 4.11 ZMYND8 KO display enhanced sensitivity to PARP inhibitor (Pamiparib)

(A) Pamiparib dose response curve to evaluate the impact of PARP inhibition on SF10602 ZMYND8 WT (blue) vs. SF10602 ZMYND8 KO (red). Two-tailed t-test (B) Cell viability assay shows the effect of Pamiparib + Irradiation (IR 20Gy) on cell proliferation in SF10602 ZMYND8 WT vs. SF10602 ZMYND8 KO measured in RLU relative to control non-treated. Two-tailed t-test (C) Pamiparib dose response curve from mouse NPAI mIDH1 GCCs ZMYND8 WT (blue) vs. NPAI ZMYND8 KO (red). Two-tailed t-test (D) Cell viability assay shows the effect of Pamiparib + IR 6Gy on cell proliferation in NPAI ZMYND8 WT (blue) vs. NPAI ZMYND8 KO (red) measured in RLU relative to control IR alone (0µM Pamiparib). Two-tailed t-test

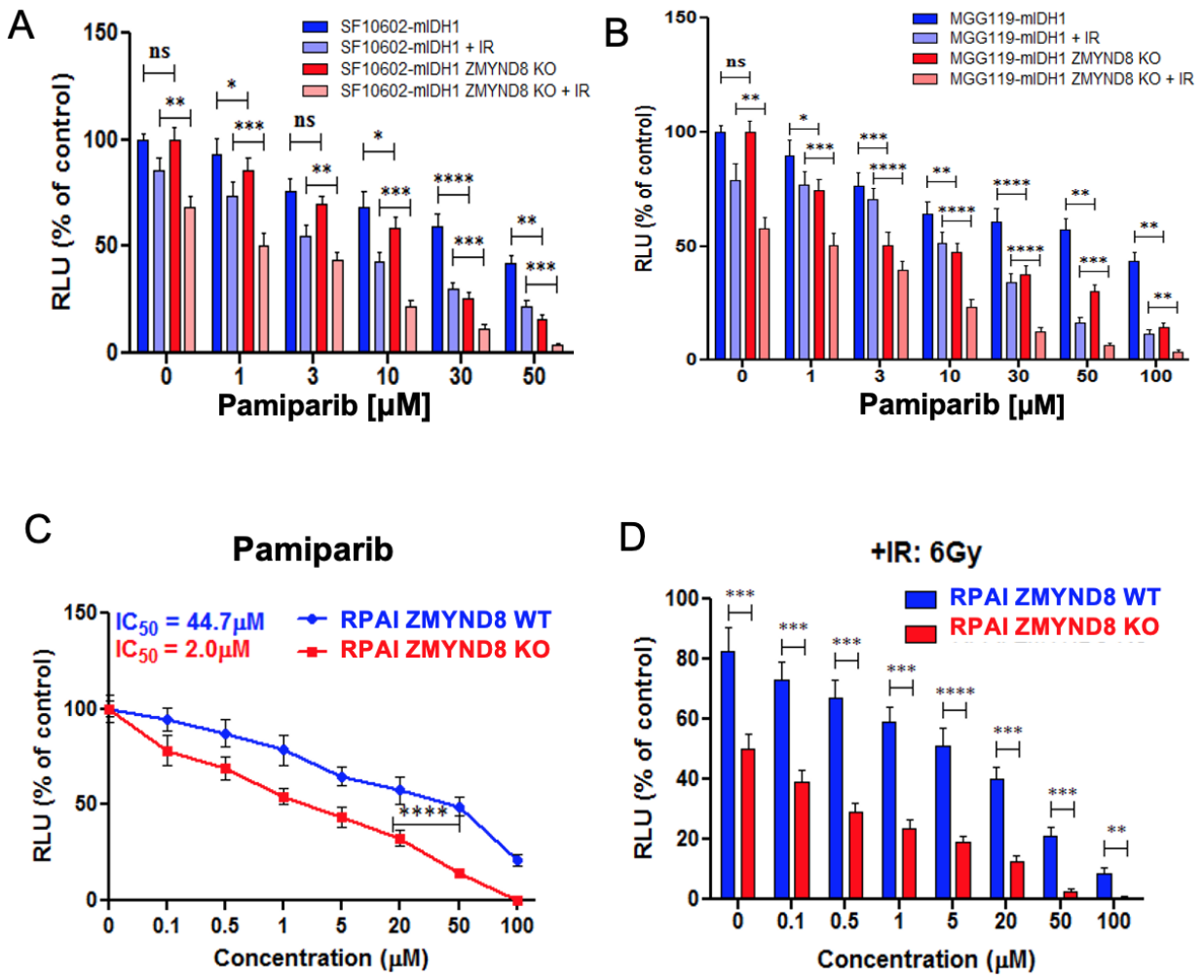

Figure 4.12 Combination of ZMYND8 KO and Parp inhibition reduces cellular viability of mIDH1 human and mouse GCCs

Representative histogram displays the effect of increased doses of Pamiparib (PARP inhibitor) alone or in combination with IR on cellular viability after 72hrs between (A) SF10602 ZMYND8 WT (dark blue) vs. SF10602 ZMYND8 WT + IR (light blue) vs SF10602 ZMYND8 KO (red) vs. SF10602 ZMYND8 KO +IR (pink) and (B) MGG119 ZMYND8 WT (dark blue) vs. MGG119 ZMYND8 WT + IR (light blue) vs. MGG119 ZMYND8 KO (dark red) vs. MGG119 ZMYND8 KO +IR (light red). Errors bars represent SEM from independent biological replicates (n=3). Not significant (ns), *p<0.05, **p<0.01, ***p<0.001, ****p<0.0001; Multiple t test (C) Pamiparib dose response curve in RPAI ZMYND8 WT (blue) vs. RPAI ZMYND8 KO (red) to assess cellular viability measured by RLU relative to non-treated control. (D) Cell viability assay shows the effect of Pamiparib + IR 6Gy on cell proliferation in RPAI ZMYND8 WT vs. RPAI ZMYND8 KO measured in RLU relative to control non-treated. Errors bars represent SEM from independent biological replicates (n=3) **p<0.01, ***p<0.001, ****p<0.0001; unpaired t test.

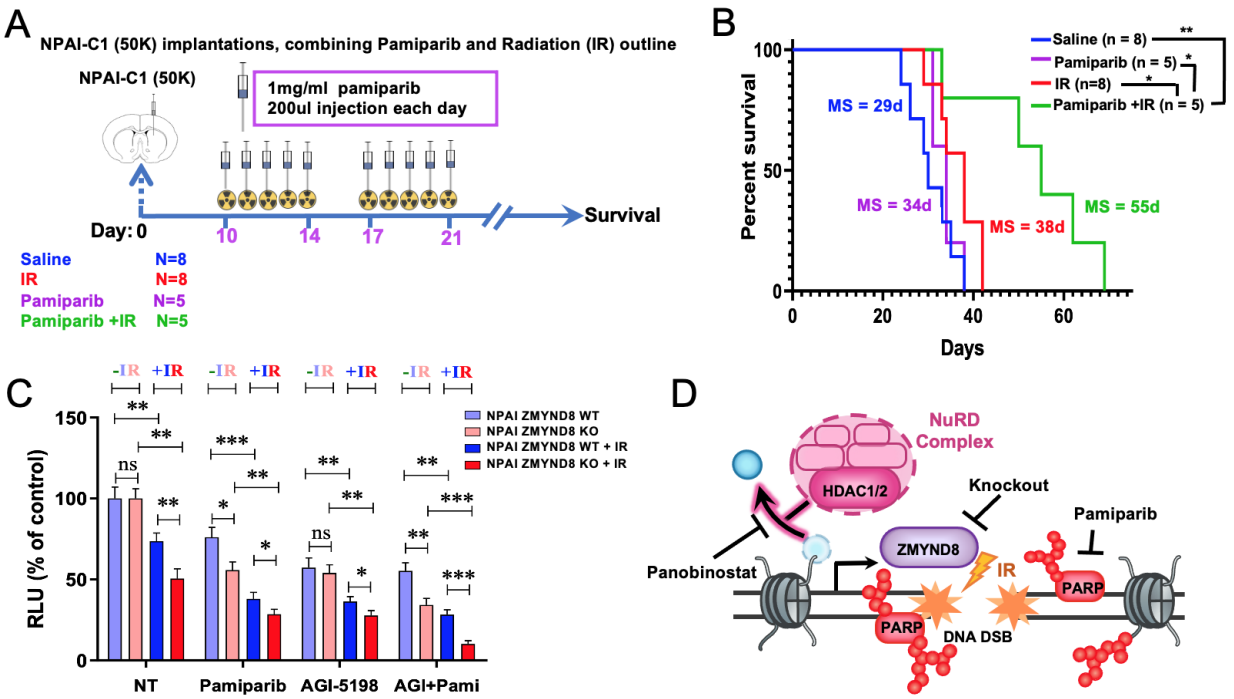

Figure 4.13 In vivo evaluation of PARP inhibition alone or in combination with IR or AGI-5198 presents a novel epigenetic vulnerability of mIDH1 glioma

(A) Preclinical design for testing the impact of PARP inhibitor (Pamiparib) on the response to IR in an orthotopic glioma model. Ten days after implantation of 50,000 NPAI NS, animals were randomly divided into 4 groups: (i) saline, (ii) IR received 2Gy/day for 5 days each cycle (20Gy total) starting 10 days post implantation (dpi) (iii) pamiparib delivered intraperitoneal (1mg/mL injection) 5 days on and 2 days off for 2 weeks, (iv) pamiparib + IR. Mice were monitored for tumor burden and euthanized at symptomatic stages to track survival to treatment. (B) Kaplan-Meier survival curve of NPAI ZMYND8 WT tumor bearing mice treated with or without 6Gy (n=8) in the presence or absence of Pamiparib (n=5). *$P < 0.05$, **$P < 0.01$; log-rank Mantel-Cox test. (C) Impact of mIDH1 inhibition (AGI-5198) and Pamiparib alone or in combination on the cellular viability of NPAI ZMYND8 WT and NPAI ZMYND8 KO in the presence (+IR) or absence (-IR) of irradiation. Errors bars represent SEM from independent biological replicates (n=3). ns-not significant, *P<0.05, **P<0.01, ***P<0.001; Multiple t-test was used (D) Working model in which targeting ZMYND8 by genetic knockout or treatment with HDAC or PARP inhibition exposes a epigenetic vulnerability of mIDH1 GCCs to IR induced DNA damage.

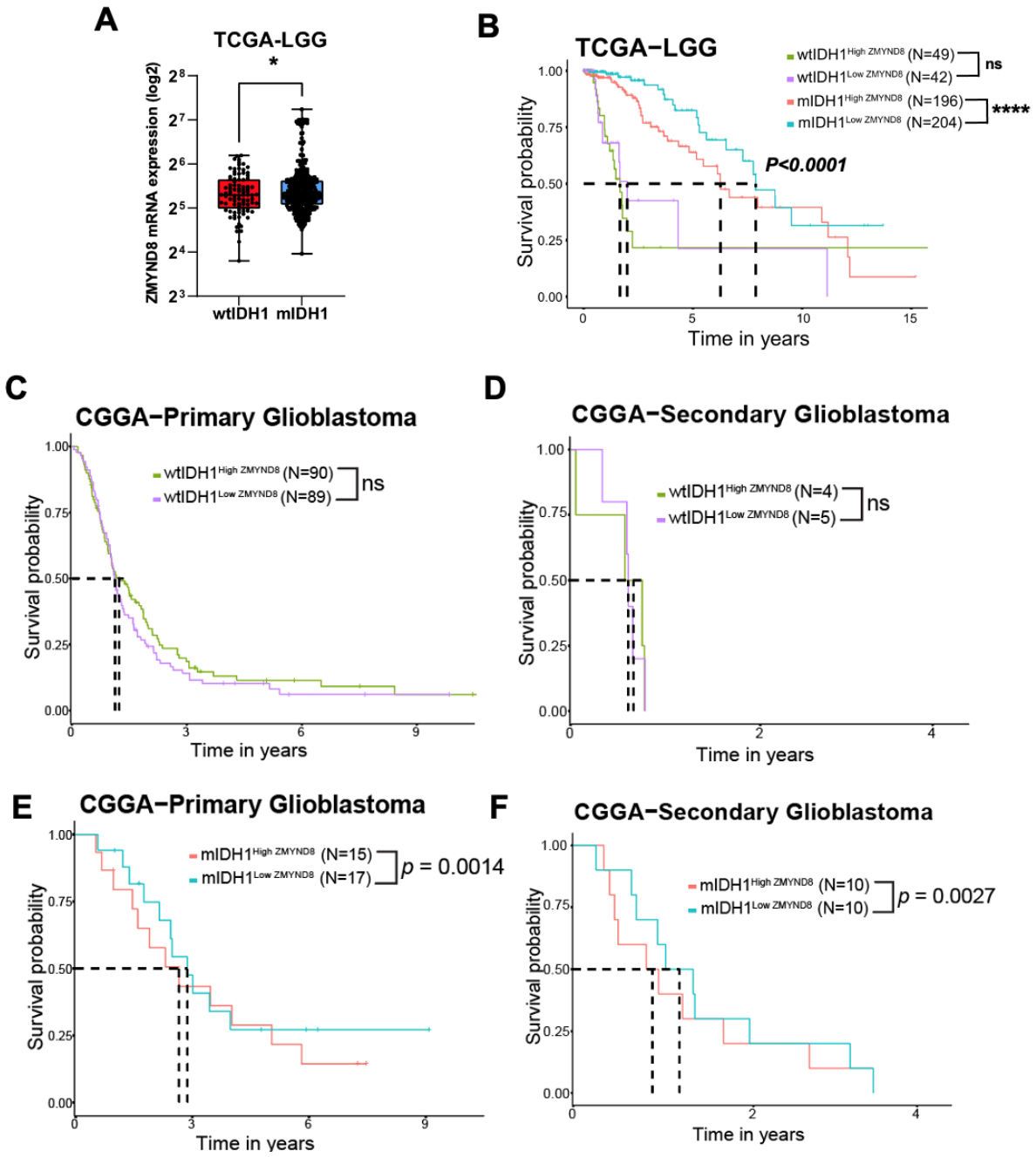

Figure 4.14 ZMYND8 is overexpressed in a subset of mIDHa glioma that is associated with poor clinical outcome in these patients

(A) Analysis of normalized log2 ZMYND8 mRNA expression levels in human Lower Grade Glioma (LGG) patients from The Cancer Genome Analysis (TCGA) LGG dataset segregated based on IDH1 mutational status as either wildtype IDH1 (wtIDH1) or mutant IDH1 (mIDH1). *p<0.05, unpaired t test. (B) Kaplan-Meier survival analysis using the log-rank test for TCGA LGG patients for whom IDH1 mutational status and prognosis data were available. Patients were subdivided by median expression level of ZMYND8 and IDH1 status: wtIDH1 high ZMYND8 (green), wtIDH1 low ZMYND8 (purple), mIDH1 high ZMYND8 (red) and mIDH1 low ZMYND8 (blue). ****p<0.0001; log-rank test. (C) Kaplan-Meier survival analysis of CGGA-Primary Glioblastoma wtIDH1 patients with high and low ZMYND8 expression. (D) Kaplan-Meier survival analysis of CGGA-Secondary Glioblastoma wtIDH1 patients with high and low ZMYND8 expression. (E) Kaplan-Meier survival analysis of CGGA-Primary Glioblastoma mIDH1 patients with high and low ZMYND8 expression. (F) Kaplan-Meier survival analysis of CGGA-Secondary Glioblastoma mIDH1 patients with high and low ZMYND8 expression. ns: not significant, log-rank test.

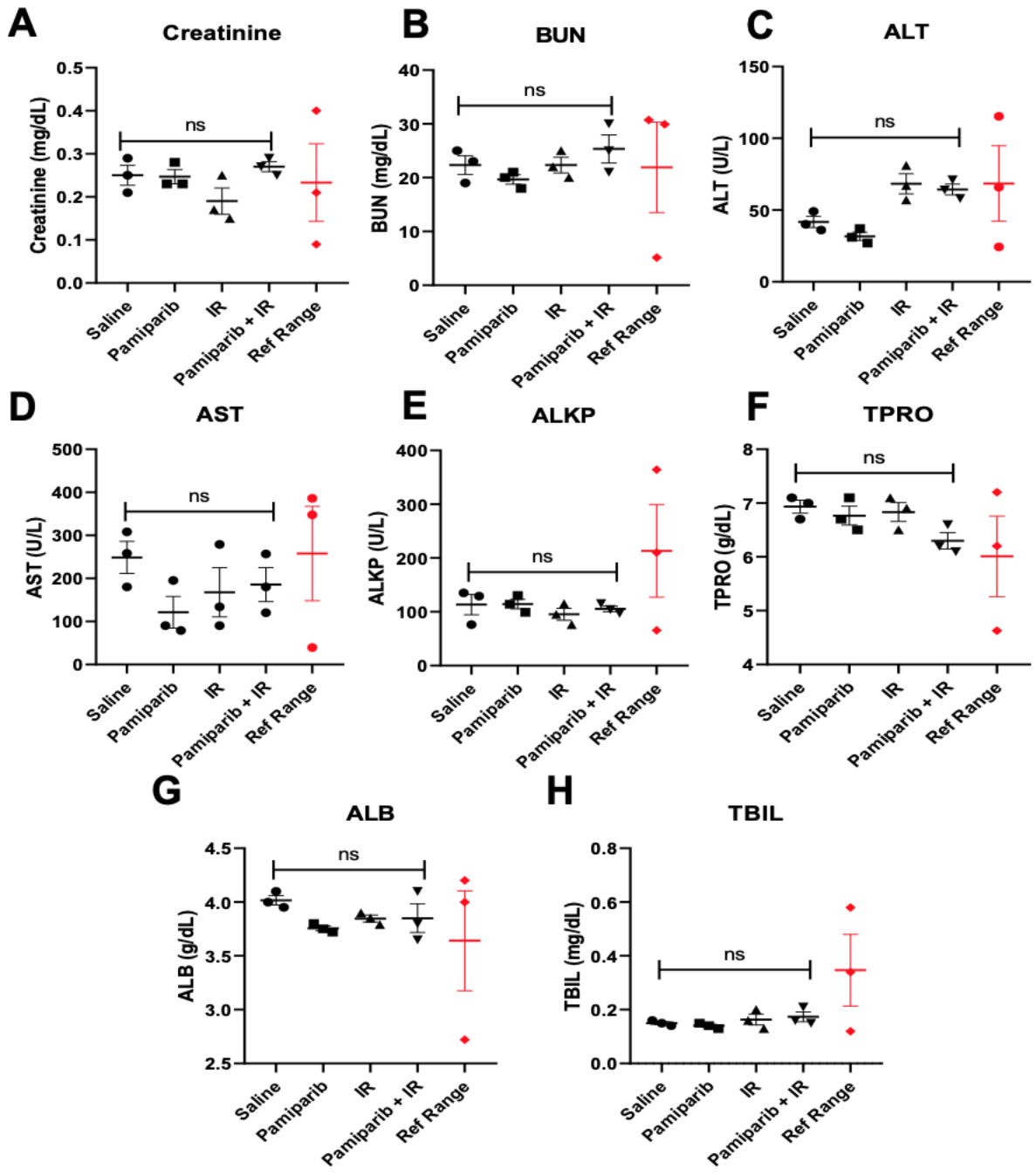

Figure 4.15 Biochemical analysis of mouse serum following Pamiparib treatment in combination with IR

mIDH1 tumor bearing mice treated with Pamiparib in combination with radiation (IR) exhibit normal serum biochemical parameters compared to saline treated control. Serum was collected from tumor bearing mice treated with saline, pamiparib, IR or pamiparib + IR. For each treatment group levels of (A) Creatinine, (B) blood urea nitrogen (BUN), (C) Alanine transaminase (ALT), (D) Aspartate transaminase (AST), (E) Alkaline phosphatase (ALKP), (F)Total Protein (TPRO), (G) Albumin, (H) Total Bilirubin (TBIL) were quantified. The reference range is indicated in red. The levels of different serum biochemical parameters between the treatment groups were compared and were found non-significant, $p > 0.05$ (n=3 biological replicates)

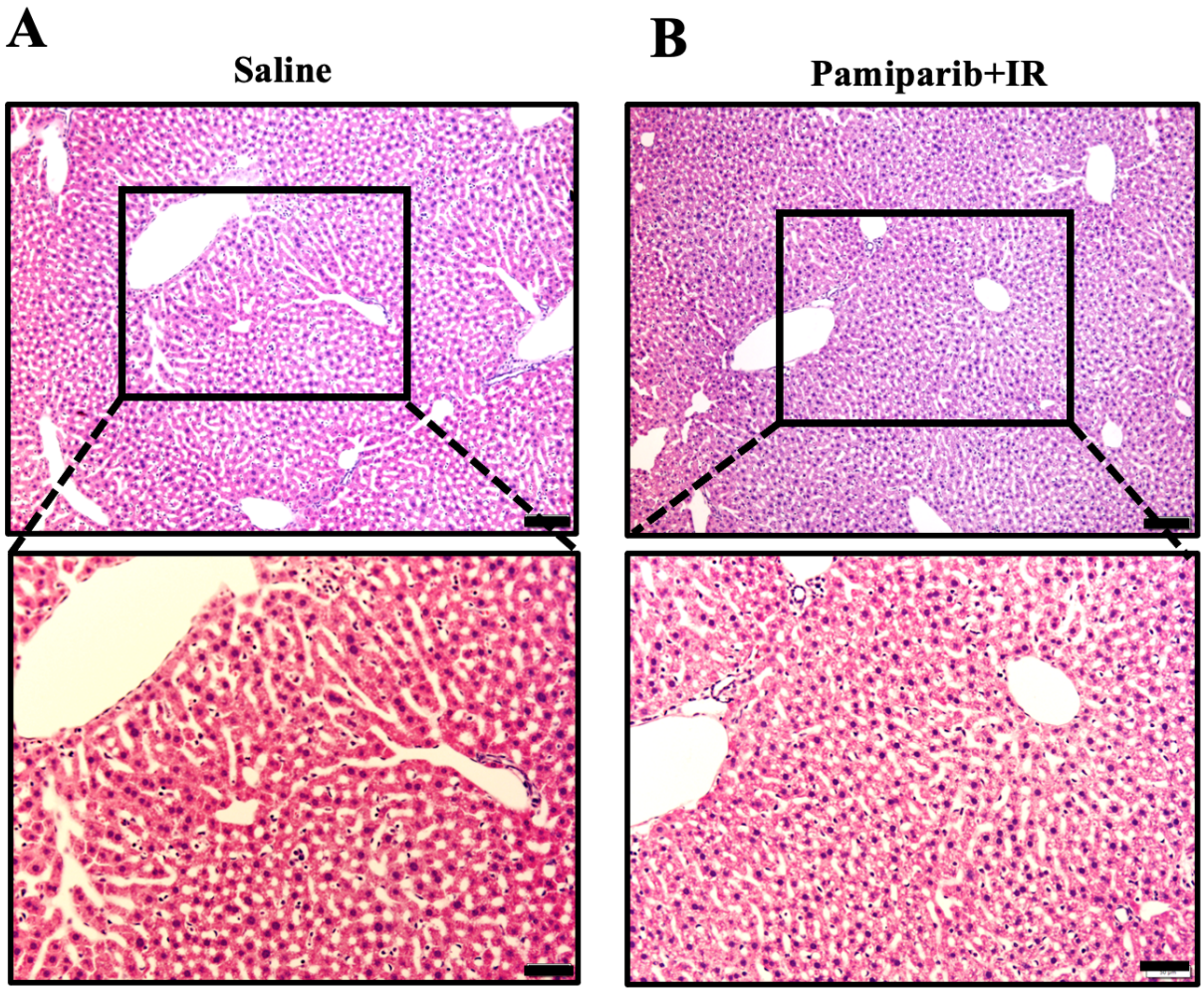

Figure 4.16 Histopathological assessment of livers from tumor-bearing mice treated with Pamiparib + IR

H&E staining of 5μm paraffin-embedded liver sections from (A) Saline, (B) Pamiparib + IR treatment group. The top panel represents the low magnification (10X), and the bottom panel represents the high magnification (20X). High-magnification panels indicate areas delineated in the low-magnification panels. Histology performed on resected livers following treatment of mIDH1 tumor-bearing mice. Representative images from a single experiment consisting of independent biological replicates are displayed. Black scale bars = 100μm (10X), 50μm (20X).

Chapter 5 Discussion and Future Directions

Summary

Mutant isocitrate dehydrogenase 1 (mIDH1) alters the epigenetic regulation of chromatin, leading to a hypermethylation phenotype in adult glioma (**Chapter 1; Figs. 1.2 and 1.3**). This work focuses on identifying gene targets epigenetically dysregulated by mIDH1 to confer therapeutic resistance to ionizing radiation (IR). We evaluated changes in the transcriptome and epigenome in a radioresistant mIDH1 patient-derived glioma cell culture (GCC) following treatment with an mIDH1 specific inhibitor AGI-5198 (**Chapter 2**; **Fig. 2.1A, Table 2.2 and Fig. 2.6**). We identified Zinc Finger MYND-Type Containing 8 (ZMYND8) as potential target of mIDH1 reprogramming (**Chapter 2; Figs. 2.2, and 2.7-2.9**). Inhibition of mIDH1 lead to an upregulation of gene networks involved in replication stress (**Chapter 2; Figs. 2.5 and 2.10**). We found that the expression of ZMYND8, a regulator of DNA damage response was decreased in three patient-derived mIDH1 GCCs after treatment with AGI-5198 (**Chapter 3; Figs. 3.1-3.3**). We suppressed ZMYND8 expression by shRNA knockdown and genetic knockout (KO) in mIDH1 glioma cells then assessed cellular viability to IR (**Chapter 3; Figs. 3.7-3.8, 3.9A and Table 3.1**). Loss of ZMYND8 expression sensitized mIDH1 GCCs to radiotherapy marked by decreased cellular viability(**Chapter 3; Figs. 3.9B-G and 3.10**). Following IR, mIDH1 glioma cells with ZMYND8 knockout (KO) exhibit significant phosphorylation of ATM and sustained γH2AX activation. (**Chapter 3; Figs. 3.11A and 3.12**). We assessed the sensitivity of mIDH1 GCCS to pharmacological inhibition of ZMYND8-interacting partners: HDAC, BRD4, and PARP (**Chapter 4; Figs. 4.4-4.5, 4.11)**. ZMYND8 KO mIDH1 GCCs were further responsive to IR

when treated with either BRD4 or HDAC inhibitors **Chapter 4; Figs. 4.12**). PARP inhibition further enhanced the efficacy of radiotherapy in ZMYND8 KO mIDH1 glioma cells **Chapter 4; Fig. 4.13B**). These findings indicate the impact of ZMYND8 in the maintenance of genomic integrity and repair of IR-induced DNA damage in mIDH1 glioma.

Translational Relevance

The evaluation of mIDH1 inhibitors in phase I clinical trials for the treatment of IDH-mutant glioma have demonstrated that these drugs are well-tolerated and safe to be given for long periods of time (Natsume et al., 2022; Vo et al., 2022). Nevertheless, the majority of patients treated with mIDH1 inhibitors achieve stable disease but only a few patients show partial responses in terms of reduced tumor volume with treatment. Although this response may be due to decreased tumor cell proliferation, mIDH1 inhibitors do not delay tumor growth for all patients (Huang et al., 2019; Pusch et al., 2017). This study explores potential gene targets regulated by mIDH1 reprogramming to provide new avenues for targeting therapeutic resistance to radiotherapy observed in mIDH1 glioma. We demonstrate changes in epigenetic regulation of ZMYND8 by mIDH1 in a radioresistant mIDH1 GCC SF10602, which had the highest expression relative to the other mIDH1 GCCs used in this study. *Xiao et al.* evaluated this association of ZMYND8 in IDH-mutant glioma by performing IHC staining in 104 glioma patient biopsies. Notably, only a subset of astrocytoma (27.3%) showed high ZMYND8 expression compared to 64.3% in oligodendroglioma and 57.9% in glioblastoma (preprint, doi:10.21203/rs.3.rs-2112846/v1). There was lower expression of ZMYND8 in normal brain. The authors suggest that ZMYND8 could be a prognostic marker to screen patients that might present with more aggressive disease, considering

that patients with high ZMYND8 expressing tumors had a median OS of ~23 months compared to ~38 months in low ZMYND8 tumors.

IDH-mutant gliomas have been shown to undergo malignant transformation and present as high-grade following treatment with TMZ. The best course of treatment is PCV for IDH-mutant oligodendroglioma providing a median PFS of 9.1 yrs compared to 3.6 yrs for patients treated with TMZ (J. Weller et al., 2021). However, patients treated with PCV will eventually succumb to disease. It is likely that we must reevaluate the use of DNA-alkylating chemotherapy in the treatment of IDH-mutant glioma. The original perspective was that creating more DNA damage will slow the tumors, but instead we have found that this causes the tumors to recur as a result of the gained mutations induced by TMZ treatment.

Our compelling findings provide insight into a novel epigenetic vulnerability of mIDH1 GCCs to respond to DNA damage that relies upon overexpression of ZMYND8 for the tumor cells to survive. We anticipate that the development of ZMYND8 specific inhibitors could provide a different angle to target radioresistance in mIDH1 glioma.

Limitations and Perspective

The first whole genome sequencing of cancer was performed in 2008, which paved the way for the identification of genetic mutations that initiate cancer formation (Ley et al., 2008). The era of mutation-targeted therapies emerged, which could subdue the pathways cancer cells hijack to maintain their proliferation and resist current therapies. In **Chapter 1**, we explore the clinical presentation of IDH-mutant glioma and the pioneering studies that discerned the molecular rewiring of metabolism and epigenetic regulation by IDH1 mutation. We discuss the multitude of mIDH1-specific inhibitors that have been developed and their impact on patient survival in phase I/II trials for the treatment of recurrent mIDH1 glioma. The consensus is that the majority of

mIDH1 glioma patients achieving stable disease on treatment with mIDH1 inhibitors but some achieve partial or even complete responses measured by a significant reduction in tumor volume or absence of residual tumor by MRI scans respectively. The cellular processes that influences this difference in patient responses still need to be further investigated.

How mIDH1 inhibitors influence therapeutic response to radiotherapy has been modelled in mice and patient derived mIDH1 GCCs by our laboratory (Kadiyala et al., 2021; Nunez et al., 2019). Herein we aimed to examine how mIDH1 modulates gene expression to confer resistance to radiation and determine gene targets that are dependent upon mIDH1 reprogramming. In **Chapter 2**, we performed transcriptomic and epigenomic analysis of an mIDH1 GCC SF10602 after *in vitro* inhibition of mIDH1 using AGI-5918. This radioresistant mIDH1 GCCs was derived from a secondary recurrent tumor biopsy taken after the patient was treated with TMZ + IR and TMZ monotherapy (Jones et al., 2020). Previous work investigating genetic drivers to malignant transformation have focused on acquired mutations and clonal divergence after TMZ treatment. Our study identified ZMYND8 as a potential epigenetic target of mIDH1 reprogramming. We observed a reduction of ZMYND8 transcripts after mIDH1 inhibition in the SF10602 mIDH1 GCC, which we believed to be mediated by a decrease of active histone mark H3K4me3 deposition at the promoter region. The potential regulators of ZMYND8 have not been identified. We did not determine what transcription factors (TF) or chromatin regulators could account for the suppression of ZMYND8 expression independent of the reversal of histone hypermethylation by mIDH1 inhibition. It is likely that ZMYND8 is a stem-cell marker, which is induced to maintain genomic stability in highly proliferative cells. We know that mIDH1 inhibition induces neural differentiation and the loss of specific neural stem cell TFs should be investigated in future studies.

In **Chapter 3**, we correlated changes in ZMYND8 protein expression with mIDH1 inhibition and an upregulation of replication stress associated proteins: PCNA and TIMELESS. We hypothesized that the decrease in cellular proliferation exhibited by mIDH1 GCCs treated with mIDH1 specific inhibitors could be the result of decrease in ZMYND8 expression. We did observe a significant reduction in ZMYND8 protein across three mIDH1 GCCs treated with two mIDH1 inhibitors, which target mIDH1 through different mechanisms (AGI-5198:competitive, DS1001b:allosteric). ZMYND8 KO mIDH1 GCCs have reduced viability to increased dosages of irradiation, which we believe to be mediated by defective resolution of DNA damage and induction of cell cycle arrest as a result. Several studies have shown that mild replicative stress promote genomic instability and arrested cells acquire high levels of genomic aberrations. One limitation of this work is that we evaluated cellular viability after 48hours post-IR, and later timepoints should be conducted after 1-2 weeks post-IR to determine if the ZMYND8 KO cells recover from IR-induced damage. We associated the increased DNA damage in the SF10602 ZMYND8 KO with the prolonged presence of γH2AX protein expression 48hrs post-IR. Alternatively, we could have performed a comet assay to visually quantify DNA breaks and determine if they were unresolved in the ZMYND8 KO. Besides the proposed role of ZMYND8 in establishing a repressive environment to facilitate the repair of DNA, ZMYND8 appears to have a role at regulating enhancer activity. ZMYND8 KO breast cancer cells display overactivation of super-enhancers marked by elevated deposition of H3K4me3 at these regions and elevated transcription of the nearby genes that they regulate. ZMYND8 has been suggested to have activator function, where it could modulate RNA polymerase pausing at regulatory regions, potentially through its interaction with BRD4, TEF-b, or DOTL1.

In Chapter 4, we evaluate the contribution of ZMYND8-interacting partners on the survival of mIDH1 GCCs: BRD4, HDAC, PARP, which have recently been shown to reduce proliferation of mIDH1 GCCs by our study and by several independent laboratories (Bai et al., 2016; Sears et al., 2021; Wang et al., 2020). The convergence of these proteins through their association of ZMYND8, proposed to us that ZMYND8 plays a crucial role in responding to genomic stability and regulation of transcription. We found that ZMYND8 KO have enhanced sensitivity to pharmacological inhibition of BRD4 (JQ1, I-BET-762), HDAC (Panobinostat), and PARP (pamiparib). PARP is specifically required for the recruitment of ZMYND8 to regions of DNA damage (Spruijt et al., 2016). PARP inhibitors trap PARP onto DNA, which could promote the recruitment of ZMYND8 to these regions to still allow for the cascade of DNA repair to occur.

Inhibition of mIDH1 and ZMYND8 loss alters the tumor-immune microenvironment

Immune checkpoint inhibitors have been shown to be ineffective as a monotherapy in the treatment of IDH-mutant glioma. A comprehensive characterization of the expression of immunological markers in IDH-mutant compared to IDH-wildtype glioma suggests that IDH-mutant gliomas are "immune-cold". There is reduced infiltration of T cells into the tumor microenvironment along with a decreased expression of immune-checkpoint markers (PD-L1, PD1, CTLA-4, TIM3, LAG3) within the tumor biopsies with the lowest expression being found in IDH-mutant codel and moderate levels in IDH-mutant non-codel relative to IDH-wildtype glioma that showed high expression (W. Lin et al., 2021). Our laboratory demonstrated that the expression of PD-L1 was upregulated following treatment of mIDH1-tumor bearing mice with AGI-5198 delivered via nanoparticles *in vivo* and contributed to an increase infiltration of T cells when combined with anti-PDL1 blockade (Kadiyala et al., 2021). The combination of AG-120

(ivosidenib) and nivolumab (anti-PD1) are currently being evaluated in a Phase II clinical trial for IDH-mutant glioma (NCT04056910).

We and other groups have shown that the oncometabolite 2HG accumulates at fairly high levels within the mIDH1 tumors. This secreted 2HG has been shown to suppress T cell proliferation by decreasing the activity of NFAT, a calcium-dependent transcription factor that regulates critical T cell cytokines like interleukin-2 (IL-2) (Bunse et al., 2018). T cells exposed to exogenous 2HG had decreased mitochondrial ATP production resulting in lower T-cell receptor signaling by phospholipase C, gamma 1 (PLC-γ1) which repressed T cell proliferation (Bunse et al., 2018). The combination of PD-1 blockade and mIDH1 inhibitor BAY1436032 provided a 20% survival in GL261-S/MAR-IDH1R132H mouse model potentially reversing the immunosuppression asserted by 2HG (Bunse et al., 2018). Recently, another group found that tumor derived 2HG that is taken up by T cells alters their metabolism. They found that the glycolytic enzyme lactate dehydrogenase (LDH) was inhibited by 2HG resulting in a decrease in cytotoxic CD8+ T cell signatures and impaired interferon-γ (IFN-γ) signaling (Notarangelo et al., 2022). The compelling finding from the recent vorasidenib trials suggests that inflammatory immune activation occurs within IDH-mutant patient treated with mIDH1 inhibitors (Mellinghoff et al., 2023). There was elevated expression of interferon stimulated genes (OAS1, OAS2) within patient biopsies on mIDH1 inhibitor treatment (Mellinghoff et al., 2023). Future studies should explore the composition of the immune microenvironment in mIDH1 patients prior to therapy and on-treatment across mIDH1 inhibitors. The question remains, does this early intervention with mIDH1 inhibitor treatment reverse the suppression of T cell activation and what are the mechanisms involved?

Work by our collaborator, Dr. Weibo Luo laboratory found that ZMYND8 contributes to the maintenance of genomic stability in triple-negative breast cancer and prevents the activation of the cGAS-STING pathway, which functions as a DNA damage sensor for the innate immune system (Wang et al., 2021). The authors report an upregulation of PD-L2, IFN-β, and other interferon-stimulated genes (ISG) in ZMYND8 KO vs. ZMYND8 WT breast cancer cells (Wang et al., 2021). The loss of ZMYND8 promoted the infiltration of $CD4^+$ and $CD8^+$ T cells into the tumor microenvironment in a syngeneic mouse model of breast cancer contributing to the reduced tumor burden in ZMYND8 KO bearing animals (Wang et al., 2021). Pertaining to this observation, when we implanted ZMYND8 KO glioma cells into C57BL6 mice, these tumors were rejected within 2-3 weeks post-implantation (data not shown). We hypothesize that this could be the result of immune activation to the ZMYND8 KO glioma cells specifically T cell-mediated considering that these tumors were able to continue growing in $CD8^{-/-}$ mice. We plan to evaluate this phenomenon in future studies to determine changes in the immune microenvironment with ZMYND8 loss.

Overexpression of ZMYND8 was found across multiple cancer types suggesting it could be essential to maintain the proliferation of cancer stem cells

In a murine colorectal cancer (CRC) model, ZMYND8 was identified by the depletion of sgRNAs targeting the gene in a CRISPR-Cas9 screening of 441 epigenetic regulators (Pan et al., 2021). *Pan et al.* utilized organoids-derived from intestinal stem cells (ISC) defined by the expression of Leucine Rich Repeat Containing G Protein-Coupled Receptor 5 ($Lgr5^+$) regulator (Pan et al., 2021). ZMYND8 knockdown restricted the ability of ISCs to form enteroids *in vitro*, potential as a result of slowed growth in anchorage-independent conditions regulators (Pan et al.,

2021). This decreased proliferation could also be the result of a reduced cancer stem cell potential with ZMYND8 loss (Pan et al., 2021). There was a reduction in the frequency of stemness markers ALDH1^{+} and CD44^{high} cells in ZMYND8-depleted ISCs (Pan et al., 2021). The Lgr5^{+} ISCs present in the crypts of mouse colon were shown to express high levels of ZMYND8. Using a CRC transgenic model (Villin^{CRE}; APC$^{min/+}$; ZMYND8f$^{fl/fl}$), ZMYND8 was genetically knockout during cancer initiation regulators (Pan et al., 2021). The authors observed that the ZMYND8 KO mice had a significant reduction in the number polyps of which there were far fewer and the lesions were smaller in size (Pan et al., 2021).

A recent publication from our collaborator Dr. Weibo Luo, details their use of two conditional knockout (cKO) ZMYND8 mouse models, MMTV-PyMT/MMTV-CRE/ZMYND8$^{fl/fl}$ and MMTV/-PyMT/K14-CRE/ZMYND8$^{fl/fl}$ to isolate breast cancer stem cells (BCSC) from the mammary gland and control when ZMYND8 was ablated (Luo et al., 2022). These ZMYND8 cKO mice had lower total number of tumors, decreased tumor weight and absence of metastatic spread of BCSCs to the lung (Luo et al., 2022). Expression of ZMYND8 increased from primary to secondary mammospheres and Lin^{-}CD90^{-}ALDH^{high} BCSCs MMTV-PyMT tumors displayed higher expression of ZMYND8 compared to the ALDH^{low} population (Luo et al., 2022).

In three hepatocellular carcinoma models (HuH7, SNU449, PLC-PRF5), ZMYND8 shRNA knockdown lead to a decrease in cellular migration in transwell assay, colony formation potential, increased apoptosis, and inhibited tumor growth *in vivo* (Choi et al., 2021).

I organized the transport of ZMYND8$^{fl/fl}$ mice, which were provided by Dr. Andrew Knutson at the University of Hawaii (pre-print, doi.org/10.1101/2022.10.06.510015). This transgenic model would allow us to knockout ZMYND8 expression during tumor initiation or *ex*

vivo in tumor neurosphere cultures. I began breeding ZMYND8 $^{fl/fl}$ mice with NestinCre^{ER} mice, which would allow us to knockout ZMYND8 expression in the neural stem cells that line the lateral ventricles. Mouse embryos where ZMYND8 was ubiquitously loss was found to be embryonic lethal. Thus, I selected to conditionally knockout ZMYND8 *in vitro*, which would allow us to generate SB-tumors that we could then abolish ZMYND8 expression using hydroxytamoxifen (4-OHT) and have isogenic controls to compare to. This work is ongoing and will likely be taken over by another graduate or postdoctoral trainee.

ZMYND8 has been linked to telomere maintenance through its role in stabilizing RAD51 associated protein 1 (RAD51AP1)

Alternative lengthening of telomeres (ALT) is facilitated by homology-directed repair (HDR), where RAD51 associated protein 1 (RAD51AP1) stabilizes R-loop HR intermediates formed by telomere repeat containing RNAs (TERRA) that prevent DNA breaks at telomere ends (Kaminski et al., 2022). ZMYND8 knockdown by small interference RNA (siRNA) in osteosarcoma U2OS cell line lead to a significant increase in the percentage of micronuclei, fragile telomeres and telomeric R-loops (Kaminski et al., 2022). ZMYND8-deficient cells showed impaired RAD51AP1 localization to telomeric DSBs. RAD51AP1 has been known to restrict RNA polymerase 2 (RNAPII) progression to prevent transcription-replication collisions (TRC) from occurring and ultimately DNA damage (Kaminski et al., 2022). The authors suggests that ZMYND8 establishes a repressive chromatin state that assists in RAD51AP1-mediated RNAPII pausing to allow for the repair of telomere ends (Kaminski et al., 2022). It would be interesting to explore the relationship between ATRX loss and ZMYND8 expression given that these proteins each contribute to the ALT mechanism.

REFERENCES

Acharya, S., Wilson, T., Gradia, S., Kane, M. F., Guerrette, S., Marsischky, G. T., Kolodner, R., & Fishel, R. (1996). hMSH2 forms specific mispair-binding complexes with hMSH3 and hMSH6. *Proc Natl Acad Sci U S A*, *93*(24), 13629-13634. https://doi.org/10.1073/pnas.93.24.13629

Adolph, M. B., Mohamed, T. M., Balakrishnan, S., Xue, C., Morati, F., Modesti, M., Greene, E. C., Chazin, W. J., & Cortez, D. (2021). RADX controls RAD51 filament dynamics to regulate replication fork stability. *Mol Cell*, *81*(5), 1074-1083 e1075. https://doi.org/10.1016/j.molcel.2020.12.036

Ahmad, S. T., Rogers, A. D., Chen, M. J., Dixit, R., Adnani, L., Frankiw, L. S., Lawn, S. O., Blough, M. D., Alshehri, M., Wu, W., Marra, M. A., Robbins, S. M., Cairncross, J. G., Schuurmans, C., & Chan, J. A. (2019). Capicua regulates neural stem cell proliferation and lineage specification through control of Ets factors. *Nat Commun*, *10*(1), 2000. https://doi.org/10.1038/s41467-019-09949-6

Alghamri, M. S., McClellan, B. L., Avvari, R. P., Thalla, R., Carney, S., Hartlage, M. S., Haase, S., Ventosa, M., Taher, A., & Kamran, N. (2021). G-CSF secreted by mutant IDH1 glioma stem cells abolishes myeloid cell immunosuppression and enhances the efficacy of immunotherapy. *Science advances*, *7*(40), eabh3243.

Amorim, J. P., Santos, G., Vinagre, J., & Soares, P. (2016). The Role of ATRX in the Alternative Lengthening of Telomeres (ALT) Phenotype. *Genes (Basel)*, *7*(9). https://doi.org/10.3390/genes7090066

Andronesi, O. C., Arrillaga-Romany, I. C., Ly, K. I., Bogner, W., Ratai, E. M., Reitz, K., Iafrate, A. J., Dietrich, J., Gerstner, E. R., Chi, A. S., Rosen, B. R., Wen, P. Y., Cahill, D. P., & Batchelor, T. T. (2018). Pharmacodynamics of mutant-IDH1 inhibitors in glioma patients probed by in vivo 3D MRS imaging of 2-hydroxyglutarate. *Nat Commun*, *9*(1), 1474. https://doi.org/10.1038/s41467-018-03905-6

Arita, H., Kinoshita, M., Kawaguchi, A., Takahashi, M., Narita, Y., Terakawa, Y., Tsuyuguchi, N., Okita, Y., Nonaka, M., Moriuchi, S., Takagaki, M., Fujimoto, Y., Fukai, J., Izumoto, S., Ishibashi, K., Nakajima, Y., Shofuda, T., Kanematsu, D., Yoshioka, E., Kodama, Y., Mano, M., Mori, K., Ichimura, K., & Kanemura, Y. (2018). Lesion location implemented magnetic resonance imaging radiomics for predicting IDH and TERT promoter mutations in grade II/III gliomas. *Sci Rep*, *8*(1), 11773. https://doi.org/10.1038/s41598-018-30273-4

Bai, H., Harmancı, A. S., Erson-Omay, E. Z., Li, J., Coşkun, S., Simon, M., Krischek, B., Özduman, K., Omay, S. B., Sorensen, E. A., Turcan, Ş., Bakırcığlu, M., Carrión-Grant, G., Murray, P. B., Clark, V. E., Ercan-Sencicek, A. G., Knight, J., Sencar, L., Altınok, S., Kaulen, L. D., Gülez, B., Timmer, M., Schramm, J., Mishra-Gorur, K., Henegariu, O., Moliterno, J., Louvi, A., Chan, T. A., Tannheimer, S. L., Pamir, M. N., Vortmeyer, A. O., Bilguvar, K., Yasuno, K., & Günel, M. (2016). Integrated genomic characterization of IDH1-mutant glioma malignant progression. *Nat Genet*, *48*(1), 59-66. https://doi.org/10.1038/ng.3457

Baker, S. D., Wirth, M., Statkevich, P., Reidenberg, P., Alton, K., Sartorius, S. E., Dugan, M., Cutler, D., Batra, V., Grochow, L. B., Donehower, R. C., & Rowinsky, E. K. (1999). Absorption, metabolism, and excretion of 14C-temozolomide following oral administration to patients with advanced cancer. *Clin Cancer Res*, *5*(2), 309-317. https://www.ncbi.nlm.nih.gov/pubmed/10037179

Banath, J. P., Klokov, D., MacPhail, S. H., Banuelos, C. A., & Olive, P. L. (2010). Residual gammaH2AX foci as an indication of lethal DNA lesions. *BMC Cancer*, *10*, 4. https://doi.org/10.1186/1471-2407-10-4

Bandopadhayay, P., Ramkissoon, L. A., Jain, P., Bergthold, G., Wala, J., Zeid, R., Schumacher, S. E., Urbanski, L., O'Rourke, R., Gibson, W. J., Pelton, K., Ramkissoon, S. H., Han, H. J., Zhu, Y., Choudhari, N., Silva, A., Boucher, K., Henn, R. E., Kang, Y. J., Knoff, D., Paolella, B. R., Gladden-Young, A., Varlet, P., Pages, M., Horowitz, P. M., Federation, A., Malkin, H., Tracy, A. A., Seepo, S., Ducar, M., Van Hummelen, P., Santi, M., Buccoliero, A. M., Scagnet, M., Bowers, D. C., Giannini, C., Puget, S., Hawkins, C., Tabori, U., Klekner, A., Bognar, L., Burger, P. C., Eberhart, C., Rodriguez, F. J., Hill, D. A., Mueller, S., Haas-Kogan, D. A., Phillips, J. J., Santagata, S., Stiles, C. D., Bradner, J. E., Jabado, N., Goren, A., Grill, J., Ligon, A. H., Goumnerova, L., Waanders, A. J., Storm, P. B., Kieran, M. W., Ligon, K. L., Beroukhim, R., & Resnick, A. C. (2016). MYB-QKI rearrangements in angiocentric glioma drive tumorigenicity through a tripartite mechanism. *Nat Genet*, *48*(3), 273-282. https://doi.org/10.1038/ng.3500

Bardella, C., Al-Dalahmah, O., Krell, D., Brazauskas, P., Al-Qahtani, K., Tomkova, M., Adam, J., Serres, S., Lockstone, H., Freeman-Mills, L., Pfeffer, I., Sibson, N., Goldin, R., Schuster-Boeckler, B., Pollard, P. J., Soga, T., McCullagh, J. S., Schofield, C. J., Mulholland, P., Ansorge, O., Kriaucionis, S., Ratcliffe, P. J., Szele, F. G., & Tomlinson, I. (2016). Expression of Idh1(R132H) in the Murine Subventricular Zone Stem Cell Niche Recapitulates Features of Early Gliomagenesis. *Cancer Cell*, *30*(4), 578-594. https://doi.org/10.1016/j.ccell.2016.08.017

Baumert, B. G., Hegi, M. E., van den Bent, M. J., von Deimling, A., Gorlia, T., Hoang-Xuan, K., Brandes, A. A., Kantor, G., Taphoorn, M. J. B., Hassel, M. B., Hartmann, C., Ryan, G., Capper, D., Kros, J. M., Kurscheid, S., Wick, W., Enting, R., Reni, M., Thiessen, B., Dhermain, F., Bromberg, J. E., Feuvret, L., Reijneveld, J. C., Chinot, O., Gijtenbeek, J. M. M., Rossiter, J. P., Dif, N., Balana, C., Bravo-Marques, J., Clement, P. M., Marosi, C., Tzuk-Shina, T., Nordal, R. A., Rees, J., Lacombe, D., Mason, W. P., & Stupp, R. (2016). Temozolomide chemotherapy versus radiotherapy in high-risk low-grade glioma (EORTC 22033-26033): a randomised, open-label, phase 3 intergroup study. *Lancet Oncol*, *17*(11), 1521-1532. https://doi.org/10.1016/S1470-2045(16)30313-8

Bettegowda, C., Agrawal, N., Jiao, Y., Sausen, M., Wood, L. D., Hruban, R. H., Rodriguez, F. J., Cahill, D. P., McLendon, R., Riggins, G., Velculescu, V. E., Oba-Shinjo, S. M., Marie, S. K., Vogelstein, B., Bigner, D., Yan, H., Papadopoulos, N., & Kinzler, K. W. (2011). Mutations in CIC and FUBP1 contribute to human oligodendroglioma. *Science*, *333*(6048), 1453-1455. https://doi.org/10.1126/science.1210557

Bianco, J. N., Bergoglio, V., Lin, Y. L., Pillaire, M. J., Schmitz, A. L., Gilhodes, J., Lusque, A., Mazieres, J., Lacroix-Triki, M., Roumeliotis, T. I., Choudhary, J., Moreaux, J., Hoffmann, J. S., Tourriere, H., & Pasero, P. (2019). Overexpression of Claspin and Timeless protects cancer cells from replication stress in a checkpoint-independent manner. *Nat Commun*, *10*(1), 910. https://doi.org/10.1038/s41467-019-08886-8

Bledea, R., Vasudevaraja, V., Patel, S., Stafford, J., Serrano, J., Esposito, G., Tredwin, L. M., Goodman, N., Kloetgen, A., Golfinos, J. G., Zagzag, D., Weigelt, B., Iafrate, A. J., Sulman, E. P., Chi, A. S., Dogan, S., Reis-Filho, J. S., Chiang, S., Placantonakis, D., Tsirigos, A., & Snuderl, M. (2019). Functional and topographic effects on DNA methylation in IDH1/2 mutant cancers. *Sci Rep*, *9*(1), 16830. https://doi.org/10.1038/s41598-019-53262-7

Bowry, A., Piberger, A. L., Rojas, P., Saponaro, M., & Petermann, E. (2018). BET Inhibition Induces HEXIM1- and RAD51-Dependent Conflicts between Transcription and Replication. *Cell Rep*, *25*(8), 2061-2069 e2064. https://doi.org/10.1016/j.celrep.2018.10.079

Brat, D. J., Verhaak, R. G., Aldape, K. D., Yung, W. K., Salama, S. R., Cooper, L. A., Rheinbay, E., Miller, C. R., Vitucci, M., Morozova, O., Robertson, A. G., Noushmehr, H., Laird, P. W., Cherniack, A. D., Akbani, R., Huse, J. T., Ciriello, G., Poisson, L. M., Barnholtz-Sloan, J. S., Berger, M. S., Brennan, C., Colen, R. R., Colman, H., Flanders, A. E., Giannini, C., Grifford, M., Iavarone, A., Jain, R., Joseph, I., Kim, J., Kasaian, K., Mikkelsen, T., Murray, B. A., O'Neill, B. P., Pachter, L., Parsons, D. W., Sougnez, C., Sulman, E. P., Vandenberg, S. R., Van Meir, E. G., von Deimling, A., Zhang, H., Crain, D., Lau, K., Mallery, D., Morris, S., Paulauskis, J., Penny, R., Shelton, T., Sherman, M., Yena, P., Black, A., Bowen, J., Dicostanzo, K., Gastier-Foster, J., Leraas, K. M., Lichtenberg, T. M., Pierson, C. R., Ramirez, N. C., Taylor, C., Weaver, S., Wise, L., Zmuda, E., Davidsen, T., Demchok, J. A., Eley, G., Ferguson, M. L., Hutter, C. M., Mills Shaw, K. R., Ozenberger, B. A., Sheth, M., Sofia, H. J., Tarnuzzer, R., Wang, Z., Yang, L., Zenklusen, J. C., Ayala, B., Baboud, J., Chudamani, S., Jensen, M. A., Liu, J., Pihl, T., Raman, R., Wan, Y., Wu, Y., Ally, A., Auman, J. T., Balasundaram, M., Balu, S., Baylin, S. B., Beroukhim, R., Bootwalla, M. S., Bowlby, R., Bristow, C. A., Brooks, D., Butterfield, Y., Carlsen, R., Carter, S., Chin, L., Chu, A., Chuah, E., Cibulskis, K., Clarke, A., Coetzee, S. G., Dhalla, N., Fennell, T., Fisher, S., Gabriel, S., Getz, G., Gibbs, R., Guin, R., Hadjipanayis, A., Hayes, D. N., Hinoue, T., Hoadley, K., Holt, R. A., Hoyle, A. P., Jefferys, S. R., Jones, S., Jones, C. D., Kucherlapati, R., Lai, P. H., Lander, E., Lee, S., Lichtenstein, L., Ma, Y., Maglinte, D. T., Mahadeshwar, H. S., Marra, M. A., Mayo, M., Meng, S., Meyerson, M. L., Mieczkowski, P. A., Moore, R. A., Mose, L. E., Mungall, A. J., Pantazi, A., Parfenov, M., Park, P. J., Parker, J. S., Perou, C. M., Protopopov, A., Ren, X., Roach, J., Sabedot, T. S., Schein, J., Schumacher, S. E., Seidman, J. G., Seth, S., Shen, H., Simons, J. V., Sipahimalani, P., Soloway, M. G., Song, X., Sun, H., Tabak, B., Tam, A., Tan, D., Tang, J., Thiessen, N., Triche, T., Jr., Van Den Berg, D. J., Veluvolu, U., Waring, S., Weisenberger, D. J., Wilkerson, M. D., Wong, T., Wu, J., Xi, L., Xu, A. W., Yang, L., Zack, T. I., Zhang, J., Aksoy, B. A., Arachchi, H., Benz, C., Bernard, B.,

Carlin, D., Cho, J., DiCara, D., Frazer, S., Fuller, G. N., Gao, J., Gehlenborg, N., Haussler, D., Heiman, D. I., Iype, L., Jacobsen, A., Ju, Z., Katzman, S., Kim, H., Knijnenburg, T., Kreisberg, R. B., Lawrence, M. S., Lee, W., Leinonen, K., Lin, P., Ling, S., Liu, W., Liu, Y., Liu, Y., Lu, Y., Mills, G., Ng, S., Noble, M. S., Paull, E., Rao, A., Reynolds, S., Saksena, G., Sanborn, Z., Sander, C., Schultz, N., Senbabaoglu, Y., Shen, R., Shmulevich, I., Sinha, R., Stuart, J., Sumer, S. O., Sun, Y., Tasman, N., Taylor, B. S., Voet, D., Weinhold, N., Weinstein, J. N., Yang, D., Yoshihara, K., Zheng, S., Zhang, W., Zou, L., Abel, T., Sadeghi, S., Cohen, M. L., Eschbacher, J., Hattab, E. M., Raghunathan, A., Schniederjan, M. J., Aziz, D., Barnett, G., Barrett, W., Bigner, D. D., Boice, L., Brewer, C., Calatozzolo, C., Campos, B., Carlotti, C. G., Jr., Chan, T. A., Cuppini, L., Curley, E., Cuzzubbo, S., Devine, K., DiMeco, F., Duell, R., Elder, J. B., Fehrenbach, A., Finocchiaro, G., Friedman, W., Fulop, J., Gardner, J., Hermes, B., Herold-Mende, C., Jungk, C., Kendler, A., Lehman, N. L., Lipp, E., Liu, O., Mandt, R., McGraw, M., McLendon, R., McPherson, C., Neder, L., Nguyen, P., Noss, A., Nunziata, R., Ostrom, Q. T., Palmer, C., Perin, A., Pollo, B., Potapov, A., Potapova, O., Rathmell, W. K., Rotin, D., Scarpace, L., Schilero, C., Senecal, K., Shimmel, K., Shurkhay, V., Sifri, S., Singh, R., Sloan, A. E., Smolenski, K., Staugaitis, S. M., Steele, R., Thorne, L., Tirapelli, D. P., Unterberg, A., Vallurupalli, M., Wang, Y., Warnick, R., Williams, F., Wolinsky, Y., Bell, S., Rosenberg, M., Stewart, C., Huang, F., Grimsby, J. L., Radenbaugh, A. J., & Zhang, J. (2015). Comprehensive, Integrative Genomic Analysis of Diffuse Lower-Grade Gliomas. *N Engl J Med*, *372*(26), 2481-2498. https://doi.org/10.1056/NEJMoa1402121

Brennan, C. W., Verhaak, R. G., McKenna, A., Campos, B., Noushmehr, H., Salama, S. R., Zheng, S., Chakravarty, D., Sanborn, J. Z., Berman, S. H., Beroukhim, R., Bernard, B., Wu, C. J., Genovese, G., Shmulevich, I., Barnholtz-Sloan, J., Zou, L., Vegesna, R., Shukla, S. A., Ciriello, G., Yung, W. K., Zhang, W., Sougnez, C., Mikkelsen, T., Aldape, K., Bigner, D. D., Van Meir, E. G., Prados, M., Sloan, A., Black, K. L., Eschbacher, J., Finocchiaro, G., Friedman, W., Andrews, D. W., Guha, A., Iacocca, M., O'Neill, B. P., Foltz, G., Myers, J., Weisenberger, D. J., Penny, R., Kucherlapati, R., Perou, C. M., Hayes, D. N., Gibbs, R., Marra, M., Mills, G. B., Lander, E., Spellman, P., Wilson, R., Sander, C., Weinstein, J., Meyerson, M., Gabriel, S., Laird, P. W., Haussler, D., Getz, G., Chin, L., & Network, T. R. (2013). The somatic genomic landscape of glioblastoma. *Cell*, *155*(2), 462-477. https://doi.org/10.1016/j.cell.2013.09.034

Bunse, L., Pusch, S., Bunse, T., Sahm, F., Sanghvi, K., Friedrich, M., Alansary, D., Sonner, J. K., Green, E., Deumelandt, K., Kilian, M., Neftel, C., Uhlig, S., Kessler, T., von Landenberg, A., Berghoff, A. S., Marsh, K., Steadman, M., Zhu, D., Nicolay, B., Wiestler, B., Breckwoldt, M. O., Al-Ali, R., Karcher-Bausch, S., Bozza, M., Oezen, I., Kramer, M., Meyer, J., Habel, A., Eisel, J., Poschet, G., Weller, M., Preusser, M., Nadji-Ohl, M., Thon, N., Burger, M. C., Harter, P. N., Ratliff, M., Harbottle, R., Benner, A., Schrimpf, D., Okun, J., Herold-Mende, C., Turcan, S., Kaulfuss, S., Hess-Stumpp, H., Bieback, K., Cahill, D. P., Plate, K. H., Hanggi, D., Dorsch, M., Suva, M. L., Niemeyer, B. A., von Deimling, A., Wick, W., & Platten, M. (2018). Suppression of antitumor T cell immunity by the oncometabolite (R)-2-hydroxyglutarate. *Nat Med*, *24*(8), 1192-1203. https://doi.org/10.1038/s41591-018-0095-6

Cahill, D. P., Levine, K. K., Betensky, R. A., Codd, P. J., Romany, C. A., Reavie, L. B., Batchelor, T. T., Futreal, P. A., Stratton, M. R., Curry, W. T., Iafrate, A. J., & Louis, D. N. (2007). Loss of the mismatch repair protein MSH6 in human glioblastomas is associated with

tumor progression during temozolomide treatment. *Clin Cancer Res*, *13*(7), 2038-2045. https://doi.org/10.1158/1078-0432.CCR-06-2149

Cali, F., Bharti, S. K., Di Perna, R., Brosh, R. M., Jr., & Pisani, F. M. (2016). Tim/Timeless, a member of the replication fork protection complex, operates with the Warsaw breakage syndrome DNA helicase DDX11 in the same fork recovery pathway. *Nucleic Acids Res*, *44*(2), 705-717. https://doi.org/10.1093/nar/gkv1112

Calinescu, A. A., Nunez, F. J., Koschmann, C., Kolb, B. L., Lowenstein, P. R., & Castro, M. G. (2015). Transposon mediated integration of plasmid DNA into the subventricular zone of neonatal mice to generate novel models of glioblastoma. *J Vis Exp*(96). https://doi.org/10.3791/52443

Cancino, G. I., Fatt, M. P., Miller, F. D., & Kaplan, D. R. (2015). Conditional ablation of p63 indicates that it is essential for embryonic development of the central nervous system. *Cell Cycle*, *14*(20), 3270-3281. https://doi.org/10.1080/15384101.2015.1087618

Cao, Z., Budinich, K. A., Huang, H., Ren, D., Lu, B., Zhang, Z., Chen, Q., Zhou, Y., Huang, Y. H., Alikarami, F., Kingsley, M. C., Lenard, A. K., Wakabayashi, A., Khandros, E., Bailis, W., Qi, J., Carroll, M. P., Blobel, G. A., Faryabi, R. B., Bernt, K. M., Berger, S. L., & Shi, J. (2021). ZMYND8-regulated IRF8 transcription axis is an acute myeloid leukemia dependency. *Mol Cell*, *81*(17), 3604-3622 e3610. https://doi.org/10.1016/j.molcel.2021.07.018

Caron, M. C., Sharma, A. K., O'Sullivan, J., Myler, L. R., Ferreira, M. T., Rodrigue, A., Coulombe, Y., Ethier, C., Gagne, J. P., Langelier, M. F., Pascal, J. M., Finkelstein, I. J., Hendzel, M. J., Poirier, G. G., & Masson, J. Y. (2019). Poly(ADP-ribose) polymerase-1 antagonizes DNA resection at double-strand breaks. *Nat Commun*, *10*(1), 2954. https://doi.org/10.1038/s41467-019-10741-9

Carrier, F. (2013). Chromatin Modulation by Histone Deacetylase Inhibitors: Impact on Cellular Sensitivity to Ionizing Radiation. *Mol Cell Pharmacol*, *5*(1), 51-59. https://www.ncbi.nlm.nih.gov/pubmed/24648865

Ceccarelli, M., Barthel, F. P., Malta, T. M., Sabedot, T. S., Salama, S. R., Murray, B. A., Morozova, O., Newton, Y., Radenbaugh, A., Pagnotta, S. M., Anjum, S., Wang, J., Manyam, G., Zoppoli, P., Ling, S., Rao, A. A., Grifford, M., Cherniack, A. D., Zhang, H., Poisson, L., Carlotti, C. G., Jr., Tirapelli, D. P., Rao, A., Mikkelsen, T., Lau, C. C., Yung, W. K., Rabadan, R., Huse, J., Brat, D. J., Lehman, N. L., Barnholtz-Sloan, J. S., Zheng, S., Hess, K., Rao, G., Meyerson, M., Beroukhim, R., Cooper, L., Akbani, R., Wrensch, M., Haussler, D., Aldape, K. D., Laird, P. W., Gutmann, D. H., Network, T. R., Noushmehr, H., Iavarone, A., & Verhaak, R. G. (2016). Molecular Profiling Reveals Biologically Discrete Subsets and Pathways of Progression in Diffuse Glioma. *Cell*, *164*(3), 550-563. https://doi.org/10.1016/j.cell.2015.12.028

Chapuy, B., McKeown, M. R., Lin, C. Y., Monti, S., Roemer, M. G., Qi, J., Rahl, P. B., Sun, H. H., Yeda, K. T., Doench, J. G., Reichert, E., Kung, A. L., Rodig, S. J., Young, R. A., Shipp, M. A., & Bradner, J. E. (2013). Discovery and characterization of super-enhancer-associated dependencies in diffuse large B cell lymphoma. *Cancer Cell*, *24*(6), 777-790. https://doi.org/10.1016/j.ccr.2013.11.003

Cho, U., Yang, S. H., & Yoo, C. (2021). Estimation of the occurrence rates of IDH1 and IDH2 mutations in gliomas and the reconsideration of IDH-wildtype anaplastic astrocytomas: an institutional experience. *J Int Med Res*, *49*(6), 3000605211019258. https://doi.org/10.1177/03000605211019258

Cho, Y. S., Levell, J. R., Liu, G., Caferro, T., Sutton, J., Shafer, C. M., Costales, A., Manning, J. R., Zhao, Q., Sendzik, M., Shultz, M., Chenail, G., Dooley, J., Villalba, B., Farsidjani, A., Chen, J., Kulathila, R., Xie, X., Dodd, S., Gould, T., Liang, G., Heimbach, T., Slocum, K., Firestone, B., Pu, M., Pagliarini, R., & Growney, J. D. (2017). Discovery and Evaluation of Clinical Candidate IDH305, a Brain Penetrant Mutant IDH1 Inhibitor. *ACS Med Chem Lett*, *8*(10), 1116-1121. https://doi.org/10.1021/acsmedchemlett.7b00342

Choi, S., Lee, K. W., Koh, H. H., Park, S., Yeo, S. Y., Joh, J. W., Choi, M. S., Kim, S. H., Park, C. K., & Ha, S. Y. (2021). Validation of ZMYND8 as a new treatment target in hepatocellular carcinoma. *J Cancer Res Clin Oncol*, *147*(12), 3517-3534. https://doi.org/10.1007/s00432-021-03768-3

Colaprico, A., Silva, T. C., Olsen, C., Garofano, L., Cava, C., Garolini, D., Sabedot, T. S., Malta, T. M., Pagnotta, S. M., Castiglioni, I., Ceccarelli, M., Bontempi, G., & Noushmehr, H. (2016). TCGAbiolinks: an R/Bioconductor package for integrative analysis of TCGA data. *Nucleic Acids Res*, *44*(8), e71. https://doi.org/10.1093/nar/gkv1507

Dang, L., White, D. W., Gross, S., Bennett, B. D., Bittinger, M. A., Driggers, E. M., Fantin, V. R., Jang, H. G., Jin, S., Keenan, M. C., Marks, K. M., Prins, R. M., Ward, P. S., Yen, K. E., Liau, L. M., Rabinowitz, J. D., Cantley, L. C., Thompson, C. B., Vander Heiden, M. G., & Su, S. M. (2009). Cancer-associated IDH1 mutations produce 2-hydroxyglutarate. *Nature*, *462*(7274), 739-744. https://doi.org/10.1038/nature08617

Danussi, C., Bose, P., Parthasarathy, P. T., Silberman, P. C., Van Arnam, J. S., Vitucci, M., Tang, O. Y., Heguy, A., Wang, Y., Chan, T. A., Riggins, G. J., Sulman, E. P., Lang, F. F., Creighton, C. J., Deneen, B., Miller, C. R., Picketts, D. J., Kannan, K., & Huse, J. T. (2018). Atrx inactivation drives disease-defining phenotypes in glioma cells of origin through global epigenomic remodeling. *Nat Commun*, *9*(1), 1057. https://doi.org/10.1038/s41467-018-03476-6

de la Fuente, M. I., Colman, H., Rosenthal, M., Van Tine, B. A., Levacic, D., Walbert, T., Gan, H. K., Vieito, M., Milhem, M. M., Lipford, K., Forsyth, S., Guichard, S. M., Mikhailov, Y., Sedkov, A., Brevard, J., Kelly, P. F., Mohamed, H., & Monga, V. (2023). Olutasidenib (FT-2102) in patients with relapsed or refractory IDH1-mutant glioma: A multicenter, open-label, phase Ib/II trial. *Neuro Oncol*, *25*(1), 146-156. https://doi.org/10.1093/neuonc/noac139

de Souza, C. F., Sabedot, T. S., Malta, T. M., Stetson, L., Morozova, O., Sokolov, A., Laird, P. W., Wiznerowicz, M., Iavarone, A., Snyder, J., deCarvalho, A., Sanborn, Z., McDonald, K. L., Friedman, W. A., Tirapelli, D., Poisson, L., Mikkelsen, T., Carlotti, C. G., Jr., Kalkanis, S., Zenklusen, J., Salama, S. R., Barnholtz-Sloan, J. S., & Noushmehr, H. (2018). A Distinct DNA Methylation Shift in a Subset of Glioma CpG Island Methylator Phenotypes during Tumor Recurrence. *Cell Rep*, *23*(2), 637-651. https://doi.org/10.1016/j.celrep.2018.03.107

Denny, B. J., Wheelhouse, R. T., Stevens, M. F., Tsang, L. L., & Slack, J. A. (1994). NMR and molecular modeling investigation of the mechanism of activation of the antitumor drug temozolomide and its interaction with DNA. *Biochemistry*, *33*(31), 9045-9051. https://doi.org/10.1021/bi00197a003

Dow, J., Krysztofiak, A., Liu, Y., Colon-Rios, D. A., Rogers, F. A., & Glazer, P. M. (2021). Vulnerability of IDH1-Mutant Cancers to Histone Deacetylase Inhibition via Orthogonal Suppression of DNA Repair. *Mol Cancer Res*, *19*(12), 2057-2067. https://doi.org/10.1158/1541-7786.MCR-21-0456

Edwards, D. S., Maganti, R., Tanksley, J. P., Luo, J., Park, J. J. H., Balkanska-Sinclair, E., Ling, J., & Floyd, S. R. (2020). BRD4 Prevents R-Loop Formation and Transcription-Replication Conflicts by Ensuring Efficient Transcription Elongation. *Cell Rep*, *32*(12), 108166. https://doi.org/10.1016/j.celrep.2020.108166

Fan, H. C., Chen, C. M., Chi, C. S., Tsai, J. D., Chiang, K. L., Chang, Y. K., Lin, S. Z., & Harn, H. J. (2019). Targeting Telomerase and ATRX/DAXX Inducing Tumor Senescence and Apoptosis in the Malignant Glioma. *Int J Mol Sci*, *20*(1). https://doi.org/10.3390/ijms20010200

Flavahan, W. A., Drier, Y., Liau, B. B., Gillespie, S. M., Venteicher, A. S., Stemmer-Rachamimov, A. O., Suva, M. L., & Bernstein, B. E. (2016). Insulator dysfunction and oncogene activation in IDH mutant gliomas. *Nature*, *529*(7584), 110-114. https://doi.org/10.1038/nature16490

Gaillard, H., Garcia-Muse, T., & Aguilera, A. (2015). Replication stress and cancer. *Nat Rev Cancer*, *15*(5), 276-289. https://doi.org/10.1038/nrc3916

Gleize, V., Alentorn, A., Connen de Kerillis, L., Labussiere, M., Nadaradjane, A. A., Mundwiller, E., Ottolenghi, C., Mangesius, S., Rahimian, A., Ducray, F., network, P., Mokhtari, K., Villa, C., & Sanson, M. (2015). CIC inactivating mutations identify aggressive subset of 1p19q codeleted gliomas. *Ann Neurol*, *78*(3), 355-374. https://doi.org/10.1002/ana.24443

Golub, D., Iyengar, N., Dogra, S., Wong, T., Bready, D., Tang, K., Modrek, A. S., & Placantonakis, D. G. (2019). Mutant Isocitrate Dehydrogenase Inhibitors as Targeted Cancer Therapeutics. *Front Oncol*, *9*, 417. https://doi.org/10.3389/fonc.2019.00417

Gong, F., Chiu, L. Y., Cox, B., Aymard, F., Clouaire, T., Leung, J. W., Cammarata, M., Perez, M., Agarwal, P., Brodbelt, J. S., Legube, G., & Miller, K. M. (2015). Screen identifies bromodomain protein ZMYND8 in chromatin recognition of transcription-associated DNA damage that promotes homologous recombination. *Genes Dev*, *29*(2), 197-211. https://doi.org/10.1101/gad.252189.114

Gong, F., Clouaire, T., Aguirrebengoa, M., Legube, G., & Miller, K. M. (2017). Histone demethylase KDM5A regulates the ZMYND8-NuRD chromatin remodeler to promote DNA repair. *J Cell Biol*, *216*(7), 1959-1974. https://doi.org/10.1083/jcb.201611135

Gong, Z., Kim, J. E., Leung, C. C., Glover, J. N., & Chen, J. (2010). BACH1/FANCJ acts with TopBP1 and participates early in DNA replication checkpoint control. *Mol Cell*, *37*(3), 438-446. https://doi.org/10.1016/j.molcel.2010.01.002

Gottesman, M. M., Lavi, O., Hall, M. D., & Gillet, J. P. (2016). Toward a Better Understanding of the Complexity of Cancer Drug Resistance. *Annu Rev Pharmacol Toxicol*, *56*, 85-102. https://doi.org/10.1146/annurev-pharmtox-010715-103111

Haase, S., Garcia-Fabiani, M. B., Carney, S., Altshuler, D., Nunez, F. J., Mendez, F. M., Nunez, F., Lowenstein, P. R., & Castro, M. G. (2018). Mutant ATRX: uncovering a new therapeutic target for glioma. *Expert Opin Ther Targets*, *22*(7), 599-613. https://doi.org/10.1080/14728222.2018.1487953

Hambarde, S., Tsai, C. L., Pandita, R. K., Bacolla, A., Maitra, A., Charaka, V., Hunt, C. R., Kumar, R., Limbo, O., Le Meur, R., Chazin, W. J., Tsutakawa, S. E., Russell, P., Schlacher, K., Pandita, T. K., & Tainer, J. A. (2021). EXO5-DNA structure and BLM interactions direct DNA resection critical for ATR-dependent replication restart. *Mol Cell*, *81*(14), 2989-3006 e2989. https://doi.org/10.1016/j.molcel.2021.05.027

Hazan, I., Monin, J., Bouwman, B. A. M., Crosetto, N., & Aqeilan, R. I. (2019). Activation of Oncogenic Super-Enhancers Is Coupled with DNA Repair by RAD51. *Cell Rep*, *29*(3), 560-572 e564. https://doi.org/10.1016/j.celrep.2019.09.001

Hegi, M. E., Diserens, A. C., Gorlia, T., Hamou, M. F., de Tribolet, N., Weller, M., Kros, J. M., Hainfellner, J. A., Mason, W., Mariani, L., Bromberg, J. E., Hau, P., Mirimanoff, R. O., Cairncross, J. G., Janzer, R. C., & Stupp, R. (2005). MGMT gene silencing and benefit from temozolomide in glioblastoma. *N Engl J Med*, *352*(10), 997-1003. https://doi.org/10.1056/NEJMoa043331

Hirose, Y., Berger, M. S., & Pieper, R. O. (2001). p53 effects both the duration of G2/M arrest and the fate of temozolomide-treated human glioblastoma cells. *Cancer Res*, *61*(5), 1957-1963. https://www.ncbi.nlm.nih.gov/pubmed/11280752

Hombach-Klonisch, S., Mehrpour, M., Shojaei, S., Harlos, C., Pitz, M., Hamai, A., Siemianowicz, K., Likus, W., Wiechec, E., Toyota, B. D., Hoshyar, R., Seyfoori, A., Sepehri, Z., Ande, S. R., Khadem, F., Akbari, M., Gorman, A. M., Samali, A., Klonisch, T., & Ghavami, S. (2018). Glioblastoma and chemoresistance to alkylating agents: Involvement of apoptosis, autophagy, and unfolded protein response. *Pharmacol Ther*, *184*, 13-41. https://doi.org/10.1016/j.pharmthera.2017.10.017

Horikoshi, N., Sharma, D., Leonard, F., Pandita, R. K., Charaka, V. K., Hambarde, S., Horikoshi, N. T., Gaur Khaitan, P., Chakraborty, S., Cote, J., Godin, B., Hunt, C. R., & Pandita, T. K. (2019). Pre-existing H4K16ac levels in euchromatin drive DNA repair by homologous recombination in S-phase. *Commun Biol*, *2*, 253. https://doi.org/10.1038/s42003-019-0498-z

Huang, J., Yu, J., Tu, L., Huang, N., Li, H., & Luo, Y. (2019). Isocitrate Dehydrogenase Mutations in Glioma: From Basic Discovery to Therapeutics Development. *Front Oncol*, *9*, 506. https://doi.org/10.3389/fonc.2019.00506

Jiao, F., Li, Z., He, C., Xu, W., Yang, G., Liu, T., Shen, H., Cai, J., Anastas, J. N., Mao, Y., Yu, Y., Lan, F., Shi, Y. G., Jones, C., Xu, Y., Baker, S. J., Shi, Y., & Guo, R. (2020). RACK7 recognizes H3.3G34R mutation to suppress expression of MHC class II complex components and their delivery pathway in pediatric glioblastoma. *Sci Adv*, *6*(29), eaba2113. https://doi.org/10.1126/sciadv.aba2113

Jiao, S., Xia, W., Yamaguchi, H., Wei, Y., Chen, M. K., Hsu, J. M., Hsu, J. L., Yu, W. H., Du, Y., Lee, H. H., Li, C. W., Chou, C. K., Lim, S. O., Chang, S. S., Litton, J., Arun, B., Hortobagyi, G. N., & Hung, M. C. (2017). PARP Inhibitor Upregulates PD-L1 Expression and Enhances Cancer-Associated Immunosuppression. *Clin Cancer Res*, *23*(14), 3711-3720. https://doi.org/10.1158/1078-0432.CCR-16-3215

Johnson, B. E., Mazor, T., Hong, C., Barnes, M., Aihara, K., McLean, C. Y., Fouse, S. D., Yamamoto, S., Ueda, H., Tatsuno, K., Asthana, S., Jalbert, L. E., Nelson, S. J., Bollen, A. W., Gustafson, W. C., Charron, E., Weiss, W. A., Smirnov, I. V., Song, J. S., Olshen, A. B., Cha, S., Zhao, Y., Moore, R. A., Mungall, A. J., Jones, S. J. M., Hirst, M., Marra, M. A., Saito, N., Aburatani, H., Mukasa, A., Berger, M. S., Chang, S. M., Taylor, B. S., & Costello, J. F. (2014). Mutational analysis reveals the origin and therapy-driven evolution of recurrent glioma. *Science*, *343*(6167), 189-193. https://doi.org/10.1126/science.1239947

Jones, L. E., Hilz, S., Grimmer, M. R., Mazor, T., Najac, C., Mukherjee, J., McKinney, A., Chow, T., Pieper, R. O., Ronen, S. M., Chang, S. M., Phillips, J. J., & Costello, J. F. (2020). Patient-derived cells from recurrent tumors that model the evolution of IDH-mutant glioma. *Neurooncol Adv*, *2*(1), vdaa088. https://doi.org/10.1093/noajnl/vdaa088

Kadiyala, P., Carney, S. V., Gauss, J. C., Garcia-Fabiani, M. B., Haase, S., Alghamri, M. S., Nunez, F. J., Liu, Y., Yu, M., Taher, A., Nunez, F. M., Li, D., Edwards, M. B., Kleer, C. G., Appelman, H., Sun, Y., Zhao, L., Moon, J. J., Schwendeman, A., Lowenstein, P. R., & Castro, M. G. (2021). Inhibition of 2-hydroxyglutarate elicits metabolic reprogramming and mutant IDH1 glioma immunity in mice. *J Clin Invest*, *131*(4). https://doi.org/10.1172/JCI139542

Kaminski, N., Wondisford, A. R., Kwon, Y., Lynskey, M. L., Bhargava, R., Barroso-Gonzalez, J., Garcia-Exposito, L., He, B., Xu, M., Mellacheruvu, D., Watkins, S. C., Modesti, M., Miller, K. M., Nesvizhskii, A. I., Zhang, H., Sung, P., & O'Sullivan, R. J. (2022). RAD51AP1 regulates ALT-HDR through chromatin-directed homeostasis of TERRA. *Mol Cell*, *82*(21), 4001-4017 e4007. https://doi.org/10.1016/j.molcel.2022.09.025

Kitange, G. J., Carlson, B. L., Schroeder, M. A., Grogan, P. T., Lamont, J. D., Decker, P. A., Wu, W., James, C. D., & Sarkaria, J. N. (2009). Induction of MGMT expression is associated with temozolomide resistance in glioblastoma xenografts. *Neuro Oncol*, *11*(3), 281-291. https://doi.org/10.1215/15228517-2008-090

Klink, B., Miletic, H., Stieber, D., Huszthy, P. C., Campos Valenzuela, J. A., Balss, J., Wang, J., Schubert, M., Sakariassen, P. O., Sundstrom, T., Torsvik, A., Aarhus, M., Mahesparan, R., von Deimling, A., Kaderali, L., Niclou, S. P., Schrock, E., Bjerkvig, R., & Nigro, J. M. (2013). A novel, diffusely infiltrative xenograft model of human anaplastic oligodendroglioma with

mutations in FUBP1, CIC, and IDH1. *PLoS One*, *8*(3), e59773. https://doi.org/10.1371/journal.pone.0059773

Kim, D., & Nam, H. J. (2022). PARP Inhibitors: Clinical Limitations and Recent Attempts to Overcome Them. *Int J Mol Sci*, *23*(15). https://doi.org/10.3390/ijms23158412

Korber, V., Yang, J., Barah, P., Wu, Y., Stichel, D., Gu, Z., Fletcher, M. N. C., Jones, D., Hentschel, B., Lamszus, K., Tonn, J. C., Schackert, G., Sabel, M., Felsberg, J., Zacher, A., Kaulich, K., Hubschmann, D., Herold-Mende, C., von Deimling, A., Weller, M., Radlwimmer, B., Schlesner, M., Reifenberger, G., Hofer, T., & Lichter, P. (2019). Evolutionary Trajectories of IDH(WT) Glioblastomas Reveal a Common Path of Early Tumorigenesis Instigated Years ahead of Initial Diagnosis. *Cancer Cell*, *35*(4), 692-704 e612. https://doi.org/10.1016/j.ccell.2019.02.007

Koschmann, C., Calinescu, A. A., Nunez, F. J., Mackay, A., Fazal-Salom, J., Thomas, D., Mendez, F., Kamran, N., Dzaman, M., Mulpuri, L., Krasinkiewicz, J., Doherty, R., Lemons, R., Brosnan-Cashman, J. A., Li, Y., Roh, S., Zhao, L., Appelman, H., Ferguson, D., Gorbunova, V., Meeker, A., Jones, C., Lowenstein, P. R., & Castro, M. G. (2016). ATRX loss promotes tumor growth and impairs nonhomologous end joining DNA repair in glioma. *Sci Transl Med*, *8*(328), 328ra328. https://doi.org/10.1126/scitranslmed.aac8228

Lam, F. C., Kong, Y. W., Huang, Q., Vu Han, T. L., Maffa, A. D., Kasper, E. M., & Yaffe, M. B. (2020). BRD4 prevents the accumulation of R-loops and protects against transcription-replication collision events and DNA damage. *Nat Commun*, *11*(1), 4083. https://doi.org/10.1038/s41467-020-17503-y

Leman, A. R., Noguchi, C., Lee, C. Y., & Noguchi, E. (2010). Human Timeless and Tipin stabilize replication forks and facilitate sister-chromatid cohesion. *J Cell Sci*, *123*(Pt 5), 660-670. https://doi.org/10.1242/jcs.057984

Ley, T. J., Mardis, E. R., Ding, L., Fulton, B., McLellan, M. D., Chen, K., Dooling, D., Dunford-Shore, B. H., McGrath, S., Hickenbotham, M., Cook, L., Abbott, R., Larson, D. E., Koboldt, D. C., Pohl, C., Smith, S., Hawkins, A., Abbott, S., Locke, D., Hillier, L. W., Miner, T., Fulton, L., Magrini, V., Wylie, T., Glasscock, J., Conyers, J., Sander, N., Shi, X., Osborne, J. R., Minx, P., Gordon, D., Chinwalla, A., Zhao, Y., Ries, R. E., Payton, J. E., Westervelt, P., Tomasson, M. H., Watson, M., Baty, J., Ivanovich, J., Heath, S., Shannon, W. D., Nagarajan, R., Walter, M. J., Link, D. C., Graubert, T. A., DiPersio, J. F., & Wilson, R. K. (2008). DNA sequencing of a cytogenetically normal acute myeloid leukaemia genome. *Nature*, *456*(7218), 66-72. https://doi.org/10.1038/nature07485

Li, G. M., & Modrich, P. (1995). Restoration of mismatch repair to nuclear extracts of H6 colorectal tumor cells by a heterodimer of human MutL homologs. *Proc Natl Acad Sci U S A*, *92*(6), 1950-1954. https://doi.org/10.1073/pnas.92.6.1950

Li, H., Liu, Z. Y., Wu, N., Chen, Y. C., Cheng, Q., & Wang, J. (2020). PARP inhibitor resistance: the underlying mechanisms and clinical implications. *Mol Cancer*, *19*(1), 107. https://doi.org/10.1186/s12943-020-01227-0

Lin, C. L., Tsai, M. L., Lin, C. Y., Hsu, K. W., Hsieh, W. S., Chi, W. M., Huang, L. C., & Lee, C. H. (2019). HDAC1 and HDAC2 Double Knockout Triggers Cell Apoptosis in Advanced Thyroid Cancer. *Int J Mol Sci*, *20*(2). https://doi.org/10.3390/ijms20020454

Lin, D., Wang, M., Chen, Y., Gong, J., Chen, L., Shi, X., Lan, F., Chen, Z., Xiong, T., Sun, H., & Wan, S. (2021). Trends in Intracranial Glioma Incidence and Mortality in the United States, 1975-2018. *Front Oncol*, *11*, 748061. https://doi.org/10.3389/fonc.2021.748061

Lin, W., Qiu, X., Sun, P., Ye, Y., Huang, Q., Kong, L., & Lu, J. J. (2021). Association of IDH mutation and 1p19q co-deletion with tumor immune microenvironment in lower-grade glioma. *Mol Ther Oncolytics*, *21*, 288-302. https://doi.org/10.1016/j.omto.2021.04.010

Louis, D. N., Perry, A., Reifenberger, G., von Deimling, A., Figarella-Branger, D., Cavenee, W. K., Ohgaki, H., Wiestler, O. D., Kleihues, P., & Ellison, D. W. (2016). The 2016 World Health Organization Classification of Tumors of the Central Nervous System: a summary. *Acta Neuropathol*, *131*(6), 803-820. https://doi.org/10.1007/s00401-016-1545-1

Low, J. T., Ostrom, Q. T., Cioffi, G., Neff, C., Waite, K. A., Kruchko, C., & Barnholtz-Sloan, J. S. (2022). Primary brain and other central nervous system tumors in the United States (2014-2018): A summary of the CBTRUS statistical report for clinicians. *Neurooncol Pract*, *9*(3), 165-182. https://doi.org/10.1093/nop/npac015

Lu, C., Ward, P. S., Kapoor, G. S., Rohle, D., Turcan, S., Abdel-Wahab, O., Edwards, C. R., Khanin, R., Figueroa, M. E., Melnick, A., Wellen, K. E., O'Rourke, D. M., Berger, S. L., Chan, T. A., Levine, R. L., Mellinghoff, I. K., & Thompson, C. B. (2012). IDH mutation impairs histone demethylation and results in a block to cell differentiation. *Nature*, *483*(7390), 474-478. https://doi.org/10.1038/nature10860

Lu, Y., Kwintkiewicz, J., Liu, Y., Tech, K., Frady, L. N., Su, Y. T., Bautista, W., Moon, S. I., MacDonald, J., Ewend, M. G., Gilbert, M. R., Yang, C., & Wu, J. (2017). Chemosensitivity of IDH1-Mutated Gliomas Due to an Impairment in PARP1-Mediated DNA Repair. *Cancer Res*, *77*(7), 1709-1718. https://doi.org/10.1158/0008-5472.CAN-16-2773

Luo, M., Bao, L., Chen, Y., Xue, Y., Wang, Y., Zhang, B., Wang, C., Corley, C. D., McDonald, J. G., Kumar, A., Xing, C., Fang, Y., Nelson, E. R., Wang, J. E., Wang, Y., & Luo, W. (2022). ZMYND8 is a master regulator of 27-hydroxycholesterol that promotes tumorigenicity of breast cancer stem cells. *Sci Adv*, *8*(28), eabn5295. https://doi.org/10.1126/sciadv.abn5295

Luo, S., Zhu, S., Liao, J., Zhang, Y., Hou, X., Luo, T., Zhao, E., Xu, J., Pang, L., Liang, X., Xiao, Y., & Li, X. (2021). IDH clonal heterogeneity segregates a subgroup of non-1p/19q codeleted gliomas with unfavourable clinical outcome. *Neuropathol Appl Neurobiol*, *47*(3), 394-405. https://doi.org/10.1111/nan.12671

Mah, L. J., El-Osta, A., & Karagiannis, T. C. (2010). gammaH2AX: a sensitive molecular marker of DNA damage and repair. *Leukemia*, *24*(4), 679-686. https://doi.org/10.1038/leu.2010.6

Mazor, T., Chesnelong, C., Pankov, A., Jalbert, L. E., Hong, C., Hayes, J., Smirnov, I. V., Marshall, R., Souza, C. F., Shen, Y., Viswanath, P., Noushmehr, H., Ronen, S. M., Jones, S. J. M., Marra, M. A., Cairncross, J. G., Perry, A., Nelson, S. J., Chang, S. M., Bollen, A. W., Molinaro, A. M., Bengtsson, H., Olshen, A. B., Weiss, S., Phillips, J. J., Luchman, H. A., & Costello, J. F. (2017). Clonal expansion and epigenetic reprogramming following deletion or amplification of mutant IDH1. *Proc Natl Acad Sci U S A*, *114*(40), 10743-10748. https://doi.org/10.1073/pnas.1708914114

McCord, M., Steffens, A., Javier, R., Kam, K. L., McCortney, K., & Horbinski, C. (2020). The efficacy of DNA mismatch repair enzyme immunohistochemistry as a screening test for hypermutated gliomas. *Acta Neuropathol Commun*, *8*(1), 15. https://doi.org/10.1186/s40478-020-0892-2

Mellinghoff, I. K., Ellingson, B. M., Touat, M., Maher, E., De La Fuente, M. I., Holdhoff, M., Cote, G. M., Burris, H., Janku, F., Young, R. J., Huang, R., Jiang, L., Choe, S., Fan, B., Yen, K., Lu, M., Bowden, C., Steelman, L., Pandya, S. S., Cloughesy, T. F., & Wen, P. Y. (2020). Ivosidenib in Isocitrate Dehydrogenase 1-Mutated Advanced Glioma. *J Clin Oncol*, *38*(29), 3398-3406. https://doi.org/10.1200/JCO.19.03327

Mellinghoff, I. K., Lu, M., Wen, P. Y., Taylor, J. W., Maher, E. A., Arrillaga-Romany, I., Peters, K. B., Ellingson, B. M., Rosenblum, M. K., Chun, S., Le, K., Tassinari, A., Choe, S., Toubouti, Y., Schoenfeld, S., Pandya, S. S., Hassan, I., Steelman, L., Clarke, J. L., & Cloughesy, T. F. (2023). Vorasidenib and ivosidenib in IDH1-mutant low-grade glioma: a randomized, perioperative phase 1 trial. *Nat Med*. https://doi.org/10.1038/s41591-022-02141-2

Mendez, F. M., Nunez, F. J., Zorrilla-Veloz, R. I., Lowenstein, P. R., & Castro, M. G. (2018). Native Chromatin Immunoprecipitation Using Murine Brain Tumor Neurospheres. *J Vis Exp*(131). https://doi.org/10.3791/57016

Modrek, A. S., Golub, D., Khan, T., Bready, D., Prado, J., Bowman, C., Deng, J., Zhang, G., Rocha, P. P., Raviram, R., Lazaris, C., Stafford, J. M., LeRoy, G., Kader, M., Dhaliwal, J., Bayin, N. S., Frenster, J. D., Serrano, J., Chiriboga, L., Baitalmal, R., Nanjangud, G., Chi, A. S., Golfinos, J. G., Wang, J., Karajannis, M. A., Bonneau, R. A., Reinberg, D., Tsirigos, A., Zagzag, D., Snuderl, M., Skok, J. A., Neubert, T. A., & Placantonakis, D. G. (2017). Low-Grade Astrocytoma Mutations in IDH1, P53, and ATRX Cooperate to Block Differentiation of Human Neural Stem Cells via Repression of SOX2. *Cell Rep*, *21*(5), 1267-1280. https://doi.org/10.1016/j.celrep.2017.10.009

Mohr, L., Toufektchan, E., von Morgen, P., Chu, K., Kapoor, A., & Maciejowski, J. (2021). ER-directed TREX1 limits cGAS activation at micronuclei. *Mol Cell*, *81*(4), 724-738 e729. https://doi.org/10.1016/j.molcel.2020.12.037

Molinaro, A. M., Taylor, J. W., Wiencke, J. K., & Wrensch, M. R. (2019). Genetic and molecular epidemiology of adult diffuse glioma. *Nat Rev Neurol*, *15*(7), 405-417. https://doi.org/10.1038/s41582-019-0220-2

Motomura, K., Mittelbronn, M., Paulus, W., Brokinkel, B., Keyvani, K., Sure, U., Wrede, K., Nakazato, Y., Tanaka, Y., Nonoguchi, N., Pierscianek, D., Kim, Y. H., Mariani, L., Vital, A., Perry, A., & Ohgaki, H. (2013). PDGFRA gain in low-grade diffuse gliomas. *J Neuropathol Exp Neurol*, *72*(1), 61-66. https://doi.org/10.1097/NEN.0b013e31827c4b5b

Natsume, A., Arakawa, Y., Narita, Y., Sugiyama, K., Hata, N., Muragaki, Y., Shinojima, N., Kumabe, T., Saito, R., Motomura, K., Mineharu, Y., Miyakita, Y., Yamasaki, F., Matsushita, Y., Ichimura, K., Ito, K., Tachibana, M., Kakurai, Y., Okamoto, N., Asahi, T., Nishijima, S., Yamaguchi, T., Tsubouchi, H., Nakamura, H., & Nishikawa, R. (2022). The first-in-human phase I study of a brain penetrant mutant IDH1 inhibitor DS-1001 in patients with recurrent or progressive IDH1-mutant gliomas. *Neuro Oncol*. https://doi.org/10.1093/neuonc/noac155

Natsume, A., Arakawa, Y., Narita, Y., Sugiyama, K., Hata, N., Muragaki, Y., Shinojima, N., Kumabe, T., Saito, R., Motomura, K., Mineharu, Y., Miyakita, Y., Yamasaki, F., Matsushita, Y., Ichimura, K., Ito, K., Tachibana, M., Kakurai, Y., Okamoto, N., Asahi, T., Nishijima, S., Yamaguchi, T., Tsubouchi, H., Nakamura, H., & Nishikawa, R. (2023). The first-in-human phase I study of a brain-penetrant mutant IDH1 inhibitor DS-1001 in patients with recurrent or progressive IDH1-mutant gliomas. *Neuro Oncol*, *25*(2), 326-336. https://doi.org/10.1093/neuonc/noac155

Notarangelo, G., Spinelli, J. B., Perez, E. M., Baker, G. J., Kurmi, K., Elia, I., Stopka, S. A., Baquer, G., Lin, J. R., Golby, A. J., Joshi, S., Baron, H. F., Drijvers, J. M., Georgiev, P., Ringel, A. E., Zaganjor, E., McBrayer, S. K., Sorger, P. K., Sharpe, A. H., Wucherpfennig, K. W., Santagata, S., Agar, N. Y. R., Suva, M. L., & Haigis, M. C. (2022). Oncometabolite d-2HG alters T cell metabolism to impair CD8(+) T cell function. *Science*, *377*(6614), 1519-1529. https://doi.org/10.1126/science.abj5104

Núñez Felipe, J., Mendez Flor, M., Kadiyala, P., Alghamri Mahmoud, S., Savelieff Masha, G., Garcia-Fabiani Maria, B., Haase, S., Koschmann, C., Calinescu, A.-A., Kamran, N., Saxena, M., Patel, R., Carney, S., Guo Marissa, Z., Edwards, M., Ljungman, M., Qin, T., Sartor Maureen, A., Tagett, R., Venneti, S., Brosnan-Cashman, J., Meeker, A., Gorbunova, V., Zhao, L., Kremer Daniel, M., Zhang, L., Lyssiotis Costas, A., Jones, L., Herting Cameron, J., Ross James, L., Hambardzumyan, D., Hervey-Jumper, S., Figueroa Maria, E., Lowenstein Pedro, R., & Castro Maria, G. (2019). IDH1-R132H acts as a tumor suppressor in glioma via epigenetic up-regulation of the DNA damage response. *Science Translational Medicine*, *11*(479), eaaq1427. https://doi.org/10.1126/scitranslmed.aaq1427

Ohba, S., Kuwahara, K., Yamada, S., Abe, M., & Hirose, Y. (2020). Correlation between IDH, ATRX, and TERT promoter mutations in glioma. *Brain Tumor Pathol*, *37*(2), 33-40. https://doi.org/10.1007/s10014-020-00360-4

Ohm, J. E., McGarvey, K. M., Yu, X., Cheng, L., Schuebel, K. E., Cope, L., Mohammad, H. P., Chen, W., Daniel, V. C., Yu, W., Berman, D. M., Jenuwein, T., Pruitt, K., Sharkis, S. J., Watkins, D. N., Herman, J. G., & Baylin, S. B. (2007). A stem cell-like chromatin pattern may predispose tumor suppressor genes to DNA hypermethylation and heritable silencing. *Nat Genet*, *39*(2), 237-242. https://doi.org/10.1038/ng1972

Oldrini, B., Vaquero-Siguero, N., Mu, Q., Kroon, P., Zhang, Y., Galan-Ganga, M., Bao, Z., Wang, Z., Liu, H., Sa, J. K., Zhao, J., Kim, H., Rodriguez-Perales, S., Nam, D. H., Verhaak, R. G. W., Rabadan, R., Jiang, T., Wang, J., & Squatrito, M. (2020). MGMT genomic rearrangements contribute to chemotherapy resistance in gliomas. *Nat Commun*, *11*(1), 3883. https://doi.org/10.1038/s41467-020-17717-0

Orsulic, S. (2002). An RCAS-TVA-based approach to designer mouse models. *Mamm Genome*, *13*(10), 543-547. https://doi.org/10.1007/s00335-002-4003-4

Pan, Q., Zhong, S., Wang, H., Wang, X., Li, N., Li, Y., Zhang, G., Yuan, H., Lian, Y., Chen, Q., Han, Y., Guo, J., Liu, Q., Qiu, T., Jiang, J., Li, Q., Tan, M., Yin, H., Peng, J., Xiao, Y., & Qin, J. (2021). The ZMYND8-regulated mevalonate pathway endows YAP-high intestinal cancer with metabolic vulnerability. *Mol Cell*, *81*(13), 2736-2751 e2738. https://doi.org/10.1016/j.molcel.2021.04.009

Parsons, D. W., Jones, S., Zhang, X., Lin, J. C., Leary, R. J., Angenendt, P., Mankoo, P., Carter, H., Siu, I. M., Gallia, G. L., Olivi, A., McLendon, R., Rasheed, B. A., Keir, S., Nikolskaya, T., Nikolsky, Y., Busam, D. A., Tekleab, H., Diaz, L. A., Jr., Hartigan, J., Smith, D. R., Strausberg, R. L., Marie, S. K., Shinjo, S. M., Yan, H., Riggins, G. J., Bigner, D. D., Karchin, R., Papadopoulos, N., Parmigiani, G., Vogelstein, B., Velculescu, V. E., & Kinzler, K. W. (2008). An integrated genomic analysis of human glioblastoma multiforme. *Science*, *321*(5897), 1807-1812. https://doi.org/10.1126/science.1164382

Patel, S. K., Hartley, R. M., Wei, X., Furnish, R., Escobar-Riquelme, F., Bear, H., Choi, K., Fuller, C., & Phoenix, T. N. (2020). Generation of diffuse intrinsic pontine glioma mouse models by brainstem-targeted in utero electroporation. *Neuro Oncol*, *22*(3), 381-392. https://doi.org/10.1093/neuonc/noz197

Paulsen, M. T., Veloso, A., Prasad, J., Bedi, K., Ljungman, E. A., Magnuson, B., Wilson, T. E., & Ljungman, M. (2014). Use of Bru-Seq and BruChase-Seq for genome-wide assessment of the synthesis and stability of RNA. *Methods*, *67*(1), 45-54. https://doi.org/10.1016/j.ymeth.2013.08.015

Petropoulos, M., Champeris Tsaniras, S., Taraviras, S., & Lygerou, Z. (2019). Replication Licensing Aberrations, Replication Stress, and Genomic Instability. *Trends Biochem Sci*, *44*(9), 752-764. https://doi.org/10.1016/j.tibs.2019.03.011

Philip, B., Yu, D. X., Silvis, M. R., Shin, C. H., Robinson, J. P., Robinson, G. L., Welker, A. E., Angel, S. N., Tripp, S. R., Sonnen, J. A., VanBrocklin, M. W., Gibbons, R. J., Looper, R. E., Colman, H., & Holmen, S. L. (2018). Mutant IDH1 Promotes Glioma Formation In Vivo. *Cell Rep*, *23*(5), 1553-1564. https://doi.org/10.1016/j.celrep.2018.03.133

Pusch, S., Krausert, S., Fischer, V., Balss, J., Ott, M., Schrimpf, D., Capper, D., Sahm, F., Eisel, J., Beck, A. C., Jugold, M., Eichwald, V., Kaulfuss, S., Panknin, O., Rehwinkel, H., Zimmermann, K., Hillig, R. C., Guenther, J., Toschi, L., Neuhaus, R., Haegebart, A., Hess-Stumpp, H., Bauser, M., Wick, W., Unterberg, A., Herold-Mende, C., Platten, M., & von Deimling, A. (2017). Pan-mutant IDH1 inhibitor BAY 1436032 for effective treatment of IDH1

mutant astrocytoma in vivo. *Acta Neuropathol*, *133*(4), 629-644. https://doi.org/10.1007/s00401-017-1677-y

Rageul, J., Park, J. J., Zeng, P. P., Lee, E. A., Yang, J., Hwang, S., Lo, N., Weinheimer, A. S., Scharer, O. D., Yeo, J. E., & Kim, H. (2020). SDE2 integrates into the TIMELESS-TIPIN complex to protect stalled replication forks. *Nat Commun*, *11*(1), 5495. https://doi.org/10.1038/s41467-020-19162-5

Ramos, R., Climans, S. A., Adile, A., Ghiassi, P., Baker, S., Phillips, M. J., Zadeh, G., Chen, E. X., & Mason, W. P. (2021). Combination olaparib and durvalumab for patients with recurrent IDH-mutated gliomas. *Journal of Clinical Oncology*, *39*(15_suppl), e14026-e14026. https://doi.org/10.1200/JCO.2021.39.15_suppl.e14026

Reinhardt, A., Stichel, D., Schrimpf, D., Sahm, F., Korshunov, A., Reuss, D. E., Koelsche, C., Huang, K., Wefers, A. K., Hovestadt, V., Sill, M., Gramatzki, D., Felsberg, J., Reifenberger, G., Koch, A., Thomale, U. W., Becker, A., Hans, V. H., Prinz, M., Staszewski, O., Acker, T., Dohmen, H., Hartmann, C., Mueller, W., Tuffaha, M. S. A., Paulus, W., Hess, K., Brokinkel, B., Schittenhelm, J., Monoranu, C. M., Kessler, A. F., Loehr, M., Buslei, R., Deckert, M., Mawrin, C., Kohlhof, P., Hewer, E., Olar, A., Rodriguez, F. J., Giannini, C., NageswaraRao, A. A., Tabori, U., Nunes, N. M., Weller, M., Pohl, U., Jaunmuktane, Z., Brandner, S., Unterberg, A., Hanggi, D., Platten, M., Pfister, S. M., Wick, W., Herold-Mende, C., Jones, D. T. W., von Deimling, A., & Capper, D. (2018). Anaplastic astrocytoma with piloid features, a novel molecular class of IDH wildtype glioma with recurrent MAPK pathway, CDKN2A/B and ATRX alterations. *Acta Neuropathol*, *136*(2), 273-291. https://doi.org/10.1007/s00401-018-1837-8

Ritchie, K., Watson, L. A., Davidson, B., Jiang, Y., & Berube, N. G. (2014). ATRX is required for maintenance of the neuroprogenitor cell pool in the embryonic mouse brain. *Biol Open*, *3*(12), 1158-1163. https://doi.org/10.1242/bio.20148730

Rohle, D., Popovici-Muller, J., Palaskas, N., Turcan, S., Grommes, C., Campos, C., Tsoi, J., Clark, O., Oldrini, B., Komisopoulou, E., Kunii, K., Pedraza, A., Schalm, S., Silverman, L., Miller, A., Wang, F., Yang, H., Chen, Y., Kernytsky, A., Rosenblum, M. K., Liu, W., Biller, S. A., Su, S. M., Brennan, C. W., Chan, T. A., Graeber, T. G., Yen, K. E., & Mellinghoff, I. K. (2013). An inhibitor of mutant IDH1 delays growth and promotes differentiation of glioma cells. *Science*, *340*(6132), 626-630. https://doi.org/10.1126/science.1236062

Saito, N., Hirai, N., Aoki, K., Sato, S., Suzuki, R., Hiramoto, Y., Fujita, S., Nakayama, H., Hayashi, M., Sakurai, T., & Iwabuchi, S. (2019). Genetic and Lineage Classification of Glioma-Initiating Cells Identifies a Clinically Relevant Glioblastoma Model. *Cancers (Basel)*, *11*(10). https://doi.org/10.3390/cancers11101564

Saredi, G., Huang, H., Hammond, C. M., Alabert, C., Bekker-Jensen, S., Forne, I., Reveron-Gomez, N., Foster, B. M., Mlejnkova, L., Bartke, T., Cejka, P., Mailand, N., Imhof, A., Patel, D. J., & Groth, A. (2016). H4K20me0 marks post-replicative chromatin and recruits the TONSL-MMS22L DNA repair complex. *Nature*, *534*(7609), 714-718. https://doi.org/10.1038/nature18312

Sasaki, M., Knobbe, C. B., Itsumi, M., Elia, A. J., Harris, I. S., Chio, II, Cairns, R. A., McCracken, S., Wakeham, A., Haight, J., Ten, A. Y., Snow, B., Ueda, T., Inoue, S., Yamamoto, K., Ko, M., Rao, A., Yen, K. E., Su, S. M., & Mak, T. W. (2012). D-2-hydroxyglutarate produced by mutant IDH1 perturbs collagen maturation and basement membrane function. *Genes Dev*, *26*(18), 2038-2049. https://doi.org/10.1101/gad.198200.112

Savitsky, P., Krojer, T., Fujisawa, T., Lambert, J. P., Picaud, S., Wang, C. Y., Shanle, E. K., Krajewski, K., Friedrichsen, H., Kanapin, A., Goding, C., Schapira, M., Samsonova, A., Strahl, B. D., Gingras, A. C., & Filippakopoulos, P. (2016). Multivalent Histone and DNA Engagement by a PHD/BRD/PWWP Triple Reader Cassette Recruits ZMYND8 to K14ac-Rich Chromatin. *Cell Rep*, *17*(10), 2724-2737. https://doi.org/10.1016/j.celrep.2016.11.014

Seah, C., Levy, M. A., Jiang, Y., Mokhtarzada, S., Higgs, D. R., Gibbons, R. J., & Berube, N. G. (2008). Neuronal death resulting from targeted disruption of the Snf2 protein ATRX is mediated by p53. *J Neurosci*, *28*(47), 12570-12580. https://doi.org/10.1523/JNEUROSCI.4048-08.2008

Sears, T. K., Horbinski, C. M., & Woolard, K. D. (2021). IDH1 mutant glioma is preferentially sensitive to the HDAC inhibitor panobinostat. *J Neurooncol*, *154*(2), 159-170. https://doi.org/10.1007/s11060-021-03829-0

Shen, H., Xu, W., Guo, R., Rong, B., Gu, L., Wang, Z., He, C., Zheng, L., Hu, X., Hu, Z., Shao, Z. M., Yang, P., Wu, F., Shi, Y. G., Shi, Y., & Lan, F. (2016). Suppression of Enhancer Overactivation by a RACK7-Histone Demethylase Complex. *Cell*, *165*(2), 331-342. https://doi.org/10.1016/j.cell.2016.02.064

Sim, H. W., Galanis, E., & Khasraw, M. (2022). PARP Inhibitors in Glioma: A Review of Therapeutic Opportunities. *Cancers (Basel)*, *14*(4). https://doi.org/10.3390/cancers14041003

So, S., Davis, A. J., & Chen, D. J. (2009). Autophosphorylation at serine 1981 stabilizes ATM at DNA damage sites. *J Cell Biol*, *187*(7), 977-990. https://doi.org/10.1083/jcb.200906064

SongTao, Q., Lei, Y., Si, G., YanQing, D., HuiXia, H., XueLin, Z., LanXiao, W., & Fei, Y. (2012). IDH mutations predict longer survival and response to temozolomide in secondary glioblastoma. *Cancer Sci*, *103*(2), 269-273. https://doi.org/10.1111/j.1349-7006.2011.02134.x

Spruijt, C. G., Luijsterburg, M. S., Menafra, R., Lindeboom, R. G., Jansen, P. W., Edupuganti, R. R., Baltissen, M. P., Wiegant, W. W., Voelker-Albert, M. C., Matarese, F., Mensinga, A., Poser, I., Vos, H. R., Stunnenberg, H. G., van Attikum, H., & Vermeulen, M. (2016). ZMYND8 Co-localizes with NuRD on Target Genes and Regulates Poly(ADP-Ribose)-Dependent Recruitment of GATAD2A/NuRD to Sites of DNA Damage. *Cell Rep*, *17*(3), 783-798. https://doi.org/10.1016/j.celrep.2016.09.037

Stupp, R., Mason, W. P., van den Bent, M. J., Weller, M., Fisher, B., Taphoorn, M. J., Belanger, K., Brandes, A. A., Marosi, C., Bogdahn, U., Curschmann, J., Janzer, R. C., Ludwin, S. K., Gorlia, T., Allgeier, A., Lacombe, D., Cairncross, J. G., Eisenhauer, E., Mirimanoff, R. O., European Organisation for, R., Treatment of Cancer Brain, T., Radiotherapy, G., & National Cancer Institute of Canada Clinical Trials, G. (2005). Radiotherapy plus concomitant and

adjuvant temozolomide for glioblastoma. *N Engl J Med*, *352*(10), 987-996. https://doi.org/10.1056/NEJMoa043330

Suwala, A. K., Stichel, D., Schrimpf, D., Kloor, M., Wefers, A. K., Reinhardt, A., Maas, S. L. N., Kratz, C. P., Schweizer, L., Hasselblatt, M., Snuderl, M., Abedalthagafi, M. S. J., Abdullaev, Z., Monoranu, C. M., Bergmann, M., Pekrun, A., Freyschlag, C., Aronica, E., Kramm, C. M., Hinz, F., Sievers, P., Korshunov, A., Kool, M., Pfister, S. M., Sturm, D., Jones, D. T. W., Wick, W., Unterberg, A., Hartmann, C., Dodgshun, A., Tabori, U., Wesseling, P., Sahm, F., von Deimling, A., & Reuss, D. E. (2021). Primary mismatch repair deficient IDH-mutant astrocytoma (PMMRDIA) is a distinct type with a poor prognosis. *Acta Neuropathol*, *141*(1), 85-100. https://doi.org/10.1007/s00401-020-02243-6

Tateishi, K., Wakimoto, H., Iafrate, A. J., Tanaka, S., Loebel, F., Lelic, N., Wiederschain, D., Bedel, O., Deng, G., Zhang, B., He, T., Shi, X., Gerszten, R. E., Zhang, Y., Yeh, J. J., Curry, W. T., Zhao, D., Sundaram, S., Nigim, F., Koerner, M. V. A., Ho, Q., Fisher, D. E., Roider, E. M., Kemeny, L. V., Samuels, Y., Flaherty, K. T., Batchelor, T. T., Chi, A. S., & Cahill, D. P. (2015). Extreme Vulnerability of IDH1 Mutant Cancers to NAD+ Depletion. *Cancer Cell*, *28*(6), 773-784. https://doi.org/10.1016/j.ccell.2015.11.006

Tateishi, K., Higuchi, F., Miller, J. J., Koerner, M. V. A., Lelic, N., Shankar, G. M., Tanaka, S., Fisher, D. E., Batchelor, T. T., Iafrate, A. J., Wakimoto, H., Chi, A. S., & Cahill, D. P. (2017). The Alkylating Chemotherapeutic Temozolomide Induces Metabolic Stress in IDH1-Mutant Cancers and Potentiates NAD(+) Depletion-Mediated Cytotoxicity. *Cancer Res*, *77*(15), 4102-4115. https://doi.org/10.1158/0008-5472.CAN-16-2263

Tian, W., Zhang, W., Wang, Y., Jin, R., Wang, Y., Guo, H., Tang, Y., & Yao, X. (2022). Recent advances of IDH1 mutant inhibitor in cancer therapy. *Front Pharmacol*, *13*, 982424. https://doi.org/10.3389/fphar.2022.982424

Tsutakawa, S. E., Classen, S., Chapados, B. R., Arvai, A. S., Finger, L. D., Guenther, G., Tomlinson, C. G., Thompson, P., Sarker, A. H., Shen, B., Cooper, P. K., Grasby, J. A., & Tainer, J. A. (2011). Human flap endonuclease structures, DNA double-base flipping, and a unified understanding of the FEN1 superfamily. *Cell*, *145*(2), 198-211. https://doi.org/10.1016/j.cell.2011.03.004

Turcan, S., Makarov, V., Taranda, J., Wang, Y., Fabius, A. W. M., Wu, W., Zheng, Y., El-Amine, N., Haddock, S., Nanjangud, G., LeKaye, H. C., Brennan, C., Cross, J., Huse, J. T., Kelleher, N. L., Osten, P., Thompson, C. B., & Chan, T. A. (2018). Mutant-IDH1-dependent chromatin state reprogramming, reversibility, and persistence. *Nat Genet*, *50*(1), 62-72. https://doi.org/10.1038/s41588-017-0001-z

Turcan, S., Rohle, D., Goenka, A., Walsh, L. A., Fang, F., Yilmaz, E., Campos, C., Fabius, A. W., Lu, C., Ward, P. S., Thompson, C. B., Kaufman, A., Guryanova, O., Levine, R., Heguy, A., Viale, A., Morris, L. G., Huse, J. T., Mellinghoff, I. K., & Chan, T. A. (2012). IDH1 mutation is sufficient to establish the glioma hypermethylator phenotype. *Nature*, *483*(7390), 479-483. https://doi.org/10.1038/nature10866

Uhrbom, L., Kastemar, M., Johansson, F. K., Westermark, B., & Holland, E. C. (2005). Cell type-specific tumor suppression by Ink4a and Arf in Kras-induced mouse gliomagenesis. *Cancer Res*, *65*(6), 2065-2069. https://doi.org/10.1158/0008-5472.CAN-04-3588

Unruh, D., Zewde, M., Buss, A., Drumm, M. R., Tran, A. N., Scholtens, D. M., & Horbinski, C. (2019). Methylation and transcription patterns are distinct in IDH mutant gliomas compared to other IDH mutant cancers. *Sci Rep*, *9*(1), 8946. https://doi.org/10.1038/s41598-019-45346-1

Urban, D. J., Martinez, N. J., Davis, M. I., Brimacombe, K. R., Cheff, D. M., Lee, T. D., Henderson, M. J., Titus, S. A., Pragani, R., Rohde, J. M., Liu, L., Fang, Y., Karavadhi, S., Shah, P., Lee, O. W., Wang, A., McIver, A., Zheng, H., Wang, X., Xu, X., Jadhav, A., Simeonov, A., Shen, M., Boxer, M. B., & Hall, M. D. (2017). Assessing inhibitors of mutant isocitrate dehydrogenase using a suite of pre-clinical discovery assays. *Sci Rep*, *7*(1), 12758. https://doi.org/10.1038/s41598-017-12630-x

Vikas, P., Borcherding, N., Chennamadhavuni, A., & Garje, R. (2020). Therapeutic Potential of Combining PARP Inhibitor and Immunotherapy in Solid Tumors. *Front Oncol*, *10*, 570. https://doi.org/10.3389/fonc.2020.00570

Vo, A. H., Ambady, P., & Spencer, D. (2022). The IDH1 inhibitor ivosidenib improved seizures in a patient with drug-resistant epilepsy from IDH1 mutant oligodendroglioma. *Epilepsy Behav Rep*, *18*, 100526. https://doi.org/10.1016/j.ebr.2022.100526

Wakimoto, H., Tanaka, S., Curry, W. T., Loebel, F., Zhao, D., Tateishi, K., Chen, J., Klofas, L. K., Lelic, N., Kim, J. C., Dias-Santagata, D., Ellisen, L. W., Borger, D. R., Fendt, S. M., Vander Heiden, M. G., Batchelor, T. T., Iafrate, A. J., Cahill, D. P., & Chi, A. S. (2014). Targetable signaling pathway mutations are associated with malignant phenotype in IDH-mutant gliomas. *Clin Cancer Res*, *20*(11), 2898-2909. https://doi.org/10.1158/1078-0432.CCR-13-3052

Wang, X. W., Labussiere, M., Valable, S., Peres, E. A., Guillamo, J. S., Bernaudin, M., & Sanson, M. (2014). IDH1(R132H) mutation increases U87 glioma cell sensitivity to radiation therapy in hypoxia. *Biomed Res Int*, *2014*, 198697. https://doi.org/10.1155/2014/198697

Wang, Y., Luo, M., Chen, Y., Wang, Y., Zhang, B., Ren, Z., Bao, L., Wang, Y., Wang, J. E., Fu, Y. X., Luo, W., & Wang, Y. (2021). ZMYND8 Expression in Breast Cancer Cells Blocks T-Lymphocyte Surveillance to Promote Tumor Growth. *Cancer Res*, *81*(1), 174-186. https://doi.org/10.1158/0008-5472.CAN-20-1710

Wang, Y., Wild, A. T., Turcan, S., Wu, W. H., Sigel, C., Klimstra, D. S., Ma, X., Gong, Y., Holland, E. C., Huse, J. T., & Chan, T. A. (2020). Targeting therapeutic vulnerabilities with PARP inhibition and radiation in IDH-mutant gliomas and cholangiocarcinomas. *Sci Adv*, *6*(17), eaaz3221. https://doi.org/10.1126/sciadv.aaz3221

Wassing, I. E., Graham, E., Saayman, X., Rampazzo, L., Ralf, C., Bassett, A., & Esashi, F. (2021). The RAD51 recombinase protects mitotic chromatin in human cells. *Nat Commun*, *12*(1), 5380. https://doi.org/10.1038/s41467-021-25643-y

Wefers, A. K., Stichel, D., Schrimpf, D., Coras, R., Pages, M., Tauziede-Espariat, A., Varlet, P., Schwarz, D., Soylemezoglu, F., Pohl, U., Pimentel, J., Meyer, J., Hewer, E., Japp, A., Joshi, A., Reuss, D. E., Reinhardt, A., Sievers, P., Casalini, M. B., Ebrahimi, A., Huang, K., Koelsche, C., Low, H. L., Rebelo, O., Marnoto, D., Becker, A. J., Staszewski, O., Mittelbronn, M., Hasselblatt, M., Schittenhelm, J., Cheesman, E., de Oliveira, R. S., Queiroz, R. G. P., Valera, E. T., Hans, V. H., Korshunov, A., Olar, A., Ligon, K. L., Pfister, S. M., Jaunmuktane, Z., Brandner, S., Tatevossian, R. G., Ellison, D. W., Jacques, T. S., Honavar, M., Aronica, E., Thom, M., Sahm, F., von Deimling, A., Jones, D. T. W., Blumcke, I., & Capper, D. (2020). Isomorphic diffuse glioma is a morphologically and molecularly distinct tumour entity with recurrent gene fusions of MYBL1 or MYB and a benign disease course. *Acta Neuropathol*, *139*(1), 193-209. https://doi.org/10.1007/s00401-019-02078-w

Weissmann, S., Cloos, P. A., Sidoli, S., Jensen, O. N., Pollard, S., & Helin, K. (2018). The Tumor Suppressor CIC Directly Regulates MAPK Pathway Genes via Histone Deacetylation. *Cancer Res*, *78*(15), 4114-4125. https://doi.org/10.1158/0008-5472.CAN-18-0342

Weller, J., Katzendobler, S., Blobner, J., Thiele, F., Becker, H., Quach, S., Egensperger, R., Niyazi, M., Suchorska, B., Thon, N., Weller, M., & Tonn, J. C. (2022). Limited efficacy of temozolomide alone for astrocytoma, IDH-mutant, CNS WHO grades 2 or 3. *J Neurooncol*, *160*(1), 149-158. https://doi.org/10.1007/s11060-022-04128-y

Weller, J., Katzendobler, S., Karschnia, P., Lietke, S., Egensperger, R., Thon, N., Weller, M., Suchorska, B., & Tonn, J. C. (2021). PCV chemotherapy alone for WHO grade 2 oligodendroglioma: prolonged disease control with low risk of malignant progression. *J Neurooncol*, *153*(2), 283-291. https://doi.org/10.1007/s11060-021-03765-z

Weller, M., van den Bent, M., Preusser, M., Le Rhun, E., Tonn, J. C., Minniti, G., Bendszus, M., Balana, C., Chinot, O., Dirven, L., French, P., Hegi, M. E., Jakola, A. S., Platten, M., Roth, P., Ruda, R., Short, S., Smits, M., Taphoorn, M. J. B., von Deimling, A., Westphal, M., Soffietti, R., Reifenberger, G., & Wick, W. (2021). EANO guidelines on the diagnosis and treatment of diffuse gliomas of adulthood. *Nat Rev Clin Oncol*, *18*(3), 170-186. https://doi.org/10.1038/s41571-020-00447-z

Wessel, S. R., Mohni, K. N., Luzwick, J. W., Dungrawala, H., & Cortez, D. (2019). Functional Analysis of the Replication Fork Proteome Identifies BET Proteins as PCNA Regulators. *Cell Rep*, *28*(13), 3497-3509 e3494. https://doi.org/10.1016/j.celrep.2019.08.051

Wesseling, P., & Capper, D. (2018). WHO 2016 Classification of gliomas. *Neuropathol Appl Neurobiol*, *44*(2), 139-150. https://doi.org/10.1111/nan.12432

Wick, W., Roth, P., Hartmann, C., Hau, P., Nakamura, M., Stockhammer, F., Sabel, M. C., Wick, A., Koeppen, S., Ketter, R., Vajkoczy, P., Eyupoglu, I., Kalff, R., Pietsch, T., Happold, C., Galldiks, N., Schmidt-Graf, F., Bamberg, M., Reifenberger, G., Platten, M., von Deimling, A., Meisner, C., Wiestler, B., Weller, M., & Neurooncology Working Group of the German Cancer, S. (2016). Long-term analysis of the NOA-04 randomized phase III trial of sequential radiochemotherapy of anaplastic glioma with PCV or temozolomide. *Neuro Oncol*, *18*(11), 1529-1537. https://doi.org/10.1093/neuonc/now133

Wilsker, D., Petermann, E., Helleday, T., & Bunz, F. (2008). Essential function of Chk1 can be uncoupled from DNA damage checkpoint and replication control. *Proc Natl Acad Sci U S A*, *105*(52), 20752-20757. https://doi.org/10.1073/pnas.0806917106

Wolf, C., Rapp, A., Berndt, N., Staroske, W., Schuster, M., Dobrick-Mattheuer, M., Kretschmer, S., Konig, N., Kurth, T., Wieczorek, D., Kast, K., Cardoso, M. C., Gunther, C., & Lee-Kirsch, M. A. (2016). RPA and Rad51 constitute a cell intrinsic mechanism to protect the cytosol from self DNA. *Nat Commun*, *7*, 11752. https://doi.org/10.1038/ncomms11752

Xie, L., Pi, X., Mishra, A., Fong, G., Peng, J., & Patterson, C. (2012). PHD3-dependent hydroxylation of HCLK2 promotes the DNA damage response. *J Clin Invest*, *122*(8), 2827-2836. https://doi.org/10.1172/JCI62374

Xie, S., Mortusewicz, O., Ma, H. T., Herr, P., Poon, R. Y., Helleday, T., & Qian, C. (2015). Timeless Interacts with PARP-1 to Promote Homologous Recombination Repair. *Mol Cell*, *60*(1), 163-176. https://doi.org/10.1016/j.molcel.2015.07.031

Xu, W., Yang, H., Liu, Y., Yang, Y., Wang, P., Kim, S. H., Ito, S., Yang, C., Wang, P., Xiao, M. T., Liu, L. X., Jiang, W. Q., Liu, J., Zhang, J. Y., Wang, B., Frye, S., Zhang, Y., Xu, Y. H., Lei, Q. Y., Guan, K. L., Zhao, S. M., & Xiong, Y. (2011). Oncometabolite 2-hydroxyglutarate is a competitive inhibitor of alpha-ketoglutarate-dependent dioxygenases. *Cancer Cell*, *19*(1), 17-30. https://doi.org/10.1016/j.ccr.2010.12.014

Yan, H., Parsons, D. W., Jin, G., McLendon, R., Rasheed, B. A., Yuan, W., Kos, I., Batinic-Haberle, I., Jones, S., Riggins, G. J., Friedman, H., Friedman, A., Reardon, D., Herndon, J., Kinzler, K. W., Velculescu, V. E., Vogelstein, B., & Bigner, D. D. (2009). IDH1 and IDH2 mutations in gliomas. *N Engl J Med*, *360*(8), 765-773. https://doi.org/10.1056/NEJMoa0808710

Yang, R., Chen, L. H., Hansen, L. J., Carpenter, A. B., Moure, C. J., Liu, H., Pirozzi, C. J., Diplas, B. H., Waitkus, M. S., Greer, P. K., Zhu, H., McLendon, R. E., Bigner, D. D., He, Y., & Yan, H. (2017). Cic Loss Promotes Gliomagenesis via Aberrant Neural Stem Cell Proliferation and Differentiation. *Cancer Res*, *77*(22), 6097-6108. https://doi.org/10.1158/0008-5472.CAN-17-1018

Yang, Y. G., Lindahl, T., & Barnes, D. E. (2007). Trex1 exonuclease degrades ssDNA to prevent chronic checkpoint activation and autoimmune disease. *Cell*, *131*(5), 873-886. https://doi.org/10.1016/j.cell.2007.10.017

Yoshizawa-Sugata, N., & Masai, H. (2007). Human Tim/Timeless-interacting protein, Tipin, is required for efficient progression of S phase and DNA replication checkpoint. *J Biol Chem*, *282*(4), 2729-2740. https://doi.org/10.1074/jbc.M605596200

Young, L. M., Marzio, A., Perez-Duran, P., Reid, D. A., Meredith, D. N., Roberti, D., Star, A., Rothenberg, E., Ueberheide, B., & Pagano, M. (2015). TIMELESS Forms a Complex with PARP1 Distinct from Its Complex with TIPIN and Plays a Role in the DNA Damage Response. *Cell Rep*, *13*(3), 451-459. https://doi.org/10.1016/j.celrep.2015.09.017

Yu, Y., Villanueva-Meyer, J., Grimmer, M. R., Hilz, S., Solomon, D. A., Choi, S., Wahl, M., Mazor, T., Hong, C., Shai, A., Phillips, J. J., Wainer, B. H., McDermott, M., Haas-Kogan, D., Taylor, J. W., Butowski, N., Clarke, J. L., Berger, M. S., Molinaro, A. M., Chang, S. M., Costello, J. F., & Oberheim Bush, N. A. (2021). Temozolomide-induced hypermutation is associated with distant recurrence and reduced survival after high-grade transformation of low-grade IDH-mutant gliomas. *Neuro Oncol*, *23*(11), 1872-1884. https://doi.org/10.1093/neuonc/noab081

Zhang, J., Stevens, M. F., & Bradshaw, T. D. (2012). Temozolomide: mechanisms of action, repair and resistance. *Curr Mol Pharmacol*, *5*(1), 102-114. https://doi.org/10.2174/1874467211205010102

Zhang, P., Xia, Q., Liu, L., Li, S., & Dong, L. (2020). Current Opinion on Molecular Characterization for GBM Classification in Guiding Clinical Diagnosis, Prognosis, and Therapy. *Front Mol Biosci*, *7*, 562798. https://doi.org/10.3389/fmolb.2020.562798

Zhao, Z., Zhang, K. N., Wang, Q., Li, G., Zeng, F., Zhang, Y., Wu, F., Chai, R., Wang, Z., Zhang, C., Zhang, W., Bao, Z., & Jiang, T. (2021). Chinese Glioma Genome Atlas (CGGA): A Comprehensive Resource with Functional Genomic Data from Chinese Glioma Patients. *Genomics Proteomics Bioinformatics*, *19*(1), 1-12. https://doi.org/10.1016/j.gpb.2020.10.005